Fluorescent sensor development through surface functionalisation

The University of Adelaide
School of Physical Sciences

Submitted in fulfilment of the degree

Doctor of Philosophy (Chemistry)

Patrick Keith Capon

B. Sc. (Advanced), M. Phil (Chemical Science)

Supervisors: Prof. Andrew Abell and Dr Malcolm Purdey

April 2021

Table of Contents

Declaration

I certify that this work contains no material which has been accepted for the award of any other degree or diploma in my name, in any university or other tertiary institution and, to the best of my knowledge and belief, contains no material previously published or written by another person, except where due reference has been made in the text. In addition, I certify that no part of this work will, in the future, be used in a submission in my name, for any other degree or diploma in any university or other tertiary institution without the prior approval of the University of Adelaide and where applicable, any partner institution responsible for the joint-award of this degree. I acknowledge that copyright of published works contained within this thesis resides with the copyright holder(s) of those works.

I also give permission for the digital version of my thesis to be made available on the web, via the University's digital research repository, the Library Search and also through web search engines, unless permission has been granted by the University to restrict access for a period of time. I acknowledge the support I have received for my research from through the provision of the MF and MH Joyner Scholarship in Science, the Norman and Patricia Polglase Supplementary Scholarship, and the fee-offset component of the Australian Government Research Training Program. I also acknowledge support from the Australian Research Council Centre of Excellence for Nanoscale BioPhotonics through the provision of travel funding.

Patrick K. Capon, 26th of April 2021

Abstract

The research undertaken in this thesis is concerned with the attachment of fluorophores to both optical fibres and nanodiamonds to provide sensing devices with application to biological sensing. Fluorescent sensors are commonly used to detect biological analytes through a change in fluorescence, a concept introduced in **Chapter 1**. However, the successful application of fluorescent sensors to biological systems is inhibited by a number of challenges, including delivery of the fluorophore to the measurement site, photobleaching, and fluorophore cell permeability. Chapter 1 introduces optical fibres and nanodiamonds as solid supports for attachment of fluorophores to overcome these challenges.

Chapter 2 presents a new fibre functionalisation architecture for dual imaging and sensing within a single optical fibre probe. The fluorescent pH sensor, 5(6)carboxy-SNARF2, was reacted with the *N*-terminus of a silk-binding peptide to form an amide bond and provide the peptide SBP-SNARF. A fluorescence polarisation assay showed this peptide to bind with a K_d of 36 μM when added to aqueous silk fibroin protein. Fibre probes were prepared by dip-coating the fibre tip into the silk and peptide mixture, which provided a uniform silk coating (determined by scanning electron microscopy) that was stable to repeated washing in water and did not affect the imaging light emitted. This allows concurrent optical coherence tomography (OCT) imaging and pH sensing, which was demonstrated in an *in vitro* fertilisation (IVF) setting. Specifically, the probe detected a change in pH of 0.04 in cumulus-oocyte complexes after metabolic stimulation with $CoCl_2$ to produce lactic acid, with the distance between the probe tip and the oocyte monitored by simultaneous OCT acquisitions. Notably, OCT imaging of an ovary revealed the presence/absence of an oocyte within an ovarian follicle, an important first step toward improving IVF patient outcomes by limiting the number of follicle punctures required to collect oocytes. Collectively, these results demonstrate the utility of the new fibre coating system to enable simultaneous OCT imaging and sensing, which provides significant insight into complex biological systems.

Chapter 3 reports the detection of AlexaFluor-532 tagged streptavidin through its binding to D-biotin, which was reacted with the *N*-terminus of a silk-binding peptide to form the complex

SBP-Biotin. This complex then adheres to a silk-coated fibre tip to provide an optical fibre probe for streptavidin, which is stable to repeated washing and long-term exposure to water. The probes were prepared by two methods that either distribute the SBP-Biotin throughout the silk fibroin matrix, or isolate the SBP-Biotin to the exterior of the silk layer. Only probes with surface bound SBP-Biotin successfully detected streptavidin, with a fluorescence-based detection limit of 15 mg/mL. Atomic absorption spectroscopy revealed that silk coating formation was inhibited by a lithium concentration of 200 ppm, however reduction to less than 20 ppm by dialysis re-enabled fibre coating. Together, Chapters 2 and 3 demonstrate that judicious preparation of optical fibre probes provides an opportunity for a wide array of fibre-based sensors using the silk fibroin and silk-binding peptide-based fibre functionalisation architecture described herein.

Chapter 4 explores functionalisation of carboxylic acid laden nanodiamonds (NDs) through amide bond formation. This was first probed using an analytical high pressure liquid chromatography system to quantify the amount of 4-fluorobenzylamine attached to NDs. However, it was found that 4-fluorobenzylamine did not bind to NDs. Next, ^{1}H nuclear magnetic resonance spectroscopy was employed to determine that the amount of diamino-PEG molecules attached to the NDs varied between 0 and 0.2 mmol/g. This indicated an inconsistent yield from the amidation reactions, which was investigated in more detail across ten separate amidation reactions between 4-cyanobenzylamine and NDs. However, none of these reactions resulted in an observable loading of 4-cyanobenzylamine, and it was concluded that amide bond formation is not an effective strategy for ND functionalisation.

Chapter 5 presents four carbon-binding peptides (**1-DLC**, **2-CN**, **3-DF** and **4-GF**) for ND functionalisation. Retention of each peptide on NDs was assessed by colourimetric assay and their presence confirmed through infrared spectroscopy and thermogravimetric analysis. **1-DLC** was found to be the most well-retained peptide, at 87% and 35% on detonation and high-pressure high-temperature NDs respectively. This interaction was determined to be predominantly electrostatic, while **2-CN** bound through non-polar interactions. Both **1-DLC** and **2-CN** coatings improved the colloidal stability of detonation NDs in aqueous solution, however neither peptide

affected the colloidal stability of high-pressure, high-temperature NDs. This study provides a new, highly adaptable approach to functionalise NDs using carbon-binding peptides.

Chapter 6 presents the synthesis of 4-aminobutanenitrile, an important synthetic intermediate for neurological disorder therapeutics, including Parkinson's and Alzheimer's diseases. Preparation of 4-aminobutanenitrile by Co(II) catalysed reduction, or a one-pot Staudinger reduction, of 4-azidobutanenitrile was low yielding. The reported Staudinger reaction was investigated through ^{1}H-NMR analysis to reveal formation of the iminophosphorane intermediate after 22 h at rt, and increasing the temperature to 40 °C promoted hydrolysis of this intermediate to the desired amine. The Staudinger reduction was performed using pyridine solvent in place of THF, with water added 3 h after reaction initiation. These conditions gave rise to 4-aminobutanenitrile in 69% yield and 94% purity (calculated by qHNMR) without chromatography. However, 4-aminobutanenitrile was found to be unstable at rt, and cyclised to 2-aminopyrroline over several days. This was circumvented by preparation of the hydrochloride salt, which was shown to be stable at rt. Hence, 4-aminobutanitrile is best stored as the corresponding hydrochloride salt.

Acknowledgments

My first thanks are to my supervisors Prof. Andrew Abell and Dr. Malcolm Purdey. They have provided an immense amount of guidance and advice that can't be listed here. Andrew in particular has given me the confidence to trust in my own judgment when planning projects, a skill that I am very thankful for. My coffee catch ups with Malcolm were always exciting and refreshing, and I would return to the office re-invigorated and inspired to strive to achieve the best possible outcome.

Thanks are also due to the numerous Abell lab members who have been present during my PhD. I have thoroughly enjoyed my time working with all of them in a positive and supportive environment. Special mention to the founding members of 'Beer Club', a Friday tradition which was a fantastic way to end the week. These include Dion Turner, Rouven Becker, Kathryn Palasis, and Aimee Horsfall. Particular thanks also to KP, the other of the 'three amigos' who was there for the entire time and is now a life-long friend. Even if I had to listen to DJ Kathode a little too much around Christmas time ☺

I was lucky enough to work in the ARC Centre for Nanoscale BioPhotonics, where I met a wide range of incredible people and scientists. In particular I worked closely with Dr. Jiawen Li, Dr. Erik Schartner, Dr. Kylie Dunning, Suliman Yagoub, Dr. Philipp Reineck, Dr. Asma Khalid, and Prof. Robert McLaughlin, as well as our director Prof. Mark Hutchinson and events manager Mel Trebilcock. I am extremely fortunate to have met such an array of excellent role models, and I look forward to continuing these connections as I move into my future career.

I would also like to thank my friends and family from outside the lab, who kept everything in perspective and continually challenged me to ensure I translated my research outcomes into something that can make a real impact in the world. Thanks to my 'in-laws' Paul and Marianne for their support and for having us at their little slice of paradise for numerous visits across the years. In my masters thesis I wrote that my parents Deb and David have supported me immeasurably for as long as I can remember, and this certainly hasn't changed! Thank you for everything!

Lastly, thanks are due to my partner Aimee, who has been there for the entire journey and arguably finished two PhDs to my one. Her unending support and loyalty have held me up and kept me moving forward through difficult times. We have also shared a lot of great times together during our PhDs which have made it a particularly special journey. Thank you.

Abbreviations

αMEM Eagle's minimum essential medium alpha formulation

AAS Atomic absorption spectroscopy

ACN Acetonitrile

Ahx Aminohexanoic acid

ANFF Australian National Fabrication Facility

APTES 3-(Aminopropyl)triethoxysilane

ARC Australian Research Council

Arg Arginine

Asn Asparagine

Asp Aspartic acid

ATR Attenuated total reflectance

Boc Tertiary-butyloxycarbonyl (protecting group)

BODIPY Boron dipyrromethene (4,4-difluoro-4-bora-3a,4a-diaza-s-indacene)

BLiSS Brisbane Life Sciences Symposium

BSA Bovine serum albumin

BTFFH Bis(tetramethylene) fluoroformamidinium hexafluorophosphate

CDI 1,1'-Carbonyl diimidazole

CN Carbon nanotube

CNBP Centre of Excellence for Nanoscale BioPhotonics

CNF Carboxy naphthofluorescein

COC Cumulus-oocyte complex

CPF1 Carboxy peroxyfluor-1

Cys Cysteine

DBP Diamond-binding peptide

DCC N,N'-dicyclohexylcarbodiimide

DCF Double-clad fibre

DCM Dichloromethane

DF Diamond film

DHE Dihydroethidium

DIC N,N'-diisopropylcarbodiimide

DIPEA N,N-diisopropyl ethylamine

DLC Diamond-like carbon

DLS Dynamic light scattering

DMF N,N-dimethylformamide

DMSO Dimethylsulfoxide

DND Detonation nanodiamond

DODT 2,2'-(Ethylenedioxy)diethanethiol

DSS Sodium trimethylsilylpropanesulfonate

EDC 1-Ethyl-3-(3-dimethylaminopropyl) carbodiimide

EDX Energy dispersive X-ray

EEPF1 2-Ethoxy(2-ethoxyethoxy) peroxyfluor-1

ESI Electrospray ionisation

FBA 4-Fluorobenzylamine

FCR2 Flavin Coumarin Redox sensor 2

Fmoc Fluorenylmethyloxycarbonyl (protecting group)

FTIR Fourier-transform infrared

FRET Förster resonance energy transfer

GF Graphite film

GFP Green fluorescent protein

Gln Glutamine

Glu Glutamic acid

Gly Glycine

GRIN Gradient index

HATU 2-(1H-7-azabenzotriazole-1-yl) -oxy-1,1,3,3-tetramethyluronium hexafluorophosphate

HEPES 4-(2-Hydroxyethyl)piperazine-1-ethanesulfonic acid

His Histidine

HPLC High performance liquid chromatography

HPHT High pressure high temperature

HRMS High resolution mass spectrometry

ICYRAM International Conference for Young Researchers on Advanced Materials

Ile Isoleucine

IPAS Institute for Photonics and Advanced Sensing

IVF *In vitro* fertilisation

Leu Leucine

Lys Lysine

MAS NMR Magic angle spinning nuclear magnetic resonance

Met Methionine

NCF No core fibre

ND Nanodiamond

NHMRC National Health and Medical Research Council

NHS N-hydroxy succinimide

NMR Nuclear magnetic resonance

NV Nitrogen vacancy

Oxyma Ethyl cyanohydroxyiminoacetate

OCT Optical coherence tomography

Pbf pentamethyl-2,3-dihydrobenzofuran-5-Sulfonyl (protecting group)

PBS Phosphate buffer solution

PEG Polyethylene glycol

PF1 Peroxyfluor-1

Phe Phenylalanine

ppm Parts per million

Pro Proline

PTFE Polytetrafluoroethylene

QMS Quadrupole mass spectrometer

ROS Reactive oxygen species

RP Reverse phase

rt room temperature

SBP Silk-binding peptide

SE Standard error of the mean

Ser Serine

SNARF Seminaphthorhodafluor

SNAFL Seminaphthofluorescein

SPPS Solid phase peptide synthesis

T3P Propylphosphonic acid anhydride

TAMRA Tetramethylrhodamine

tBu Tertiary butyl (protecting group)

TFA Trifluoroacetic acid

TGA Thermogravimetric analysis

THF Tetrahydrofuran

Thr Threonine

TIPS Triisopropylsilane

TMS Tetramethylsilane

TNBS 2,4,6-Trinitrobenzenesulfonic acid

TOF Time of flight

Trp Tryptophan

Trt Trityl (protecting group)

Tyr Tyrosine

UV Ultra-violet

v/v Volume per volume

Val Valine

XPS X-ray photoelectron spectroscopy

ZP Zeta potential

ZPL Zero phonon line

List of publications

The following publications comprise full chapters in this thesis:

- **Patrick K. Capon**, Thomas D. Avery, Malcolm S. Purdey, Andrew D. Abell, An improved synthesis of 4-aminobutanenitrile from 4-azidobutanenitrile, and comments on room temperature stability, *Synthetic Communications*, **2020**, 51, 3, 428-436, doi.org/10.1080/00397911.2020.1832527

- **Patrick K. Capon**, Jiawen Li, Aimee J. Horsfall, Suliman Yagoub, Erik P. Schartner, Asma Khalid, Rodney W. Kirk, Malcolm S. Purdey, Kylie R. Dunning, Robert A. McLaughlin, Andrew D. Abell, A Silk-based Functionalization Architecture for Single Fibre Imaging and Sensing, *Advanced Functional Materials*, March 29th, **2021**, 2010713, doi.org/10.1002/adfm.202010713

- **Patrick K. Capon**, Aimee J. Horsfall, Jiawen Li, Erik P. Schartner, Asma Khalid, Malcolm S. Purdey, Robert A. McLaughlin, Andrew D. Abell, Protein detection enabled using functionalised silk-binding peptides on a silk-coated optical fibre, *RSC Advances*, **2021**, 11, 22334-22342, doi.org/10.1039/D1RA03584C

- **Patrick K. Capon**, Aimee J. Horsfall, Wioleta Kowalczyk, Philipp Reineck, Marco D. Torelli, Olga A. Shendarova, Malcolm S. Purdey, Andrew D. Abell, Investigation of diamond-binding peptides for nanodiamond functionalisation, *in preparation for submission to the Journal of Physical Chemistry C*, **2021**

The following publication contains other work by the author that is described in this thesis (Chapter 1 and introduction to Chapter 4):

- Malcolm S. Purdey, **Patrick K. Capon**, Benjamin J. Pullen, Philipp Reineck, Nisha Schwarz, Peter J. Psaltis, Stephen J. Nicholls, Brant C. Gibson, Andrew D. Abell, An organic fluorophore-nanodiamond hybrid sensor for photostable imaging and orthogonal, on-demand biosensing, *Scientific Reports*, **2017**, 7, 15967, doi.org/10.1038/s41598-017-15772-0

List of conference and workshop presentations

Talks:

- "A new peptide-based functionalisation method for optical fibres", 36th European Peptide Symposium and International Peptide Symposium, accepted for September 2020 postponed due to COVID-19
- "Perfect Peptides for Surface Functionalisation", ARC CNBP annual conference, June 2020
- "Perfect Peptides for Fibre Functionalisation", IPAS seminar, February 2020
- "Peptides for Optical Fibre Functionalisation", IPAS student talks competition, February 2020
- "Silk coated optical fibre for fluorescent sensing", ARC CNBP research challenges meeting, December 2019
- "Surface Functionalisation - A Chemist's Perspective", ARC CNBP seminar, May 2019
- "Nanodiamond-Fluorophore Hybrids for Biological Sensing", ICYRAM, November 2018
- "A Nanodiamond-Fluorophore Hybrid for Hydrogen Peroxide Sensing", IPAS seminar, April 2018
- "Nanodiamond-Fluorophore Hybrids for Biological Sensing", ARC CNBP annual conference, October 2017

Posters:

- “How to Functionalise a Nanodiamond”, online gif poster for ARC CNBP annual conference, June 2020
- “Silk for Coating Optical Fibres”, online gif poster for ARC CNBP annual conference, June 2020
- “Optical Fibre Functionalisation with Peptide Based pH Sensors”, BioPhotonics Careers Workshop, Swinburne University, November 2019
- “Optical Fibre Functionalisation with Peptide Based pH Sensors”, ARC CNBP annual conference, October 2019
- “Dual Imaging and Sensing Fibres for pH Measurement”, BLiSS Adelaide conference, September 2019
- “Approaches to Surface Functionalisation with Fluorophores”, ARC CNBP annual conference, November 2018
- “A Multimodal Nanodiamond Based Sensing Platform”, ARC CNBP annual conference, October 2017
- “Nanodiamond-fluorophore Hybrid Sensors”, ARC CNBP mid-year workshop, July 2017

Chapter 1: Introduction

1.1 Detection of biological analytes

Biological analytes such as metal ions, reactive oxygen or nitrogen species, proteins, and other biomolecules are central to life, but are typically too small to directly image through electron or optical microscopy. One approach to overcome this limitation is to use compounds that fluoresce on exposure to such analytes.[1] These compounds are generally referred to as fluorophores or fluorescent sensors and have emission wavelengths that cover most of the visible spectrum.[2] A second approach is to use solid devices that can be directly inserted into the biological system to detect the desired analyte. For example, optical fibre-based sensors can detect proteins based on changes in refractive index at the fibre tip,[3,4] or nanodiamonds can be added to a biological system to monitor environmental variables such as temperature or magnetic fields.[5-8] The combination of these two approaches provides an opportunity to develop composite sensing devices, which possess the inherent advantages of both the organic fluorophore and solid material components. This thesis is concerned with the development of such composite sensing devices through surface functionalisation chemistry and characterisation of the resultant devices.

1.1.1 Organic fluorescent sensors

Two fluorophores that are frequently applied in biological systems due to their high quantum yields are fluorescein and rhodamine. These compounds bear hydroxy or amino functional groups at the 3'- and 6'-positions on a xanthene scaffold, respectively (Scheme 1.1). The quantum yield, excitation wavelength, and emission wavelength of rhodamines can be tuned to suit the desired application by modification of the 3'- and 6'-amines.[9-12] A benzoic acid moiety is also attached at the 1-position of the xanthene scaffold, with an *o*-carboxylic acid that exists in equilibrium between a ring-opened, fluorescent quinoid form, and a non-fluorescent ring-closed spirolactam. The

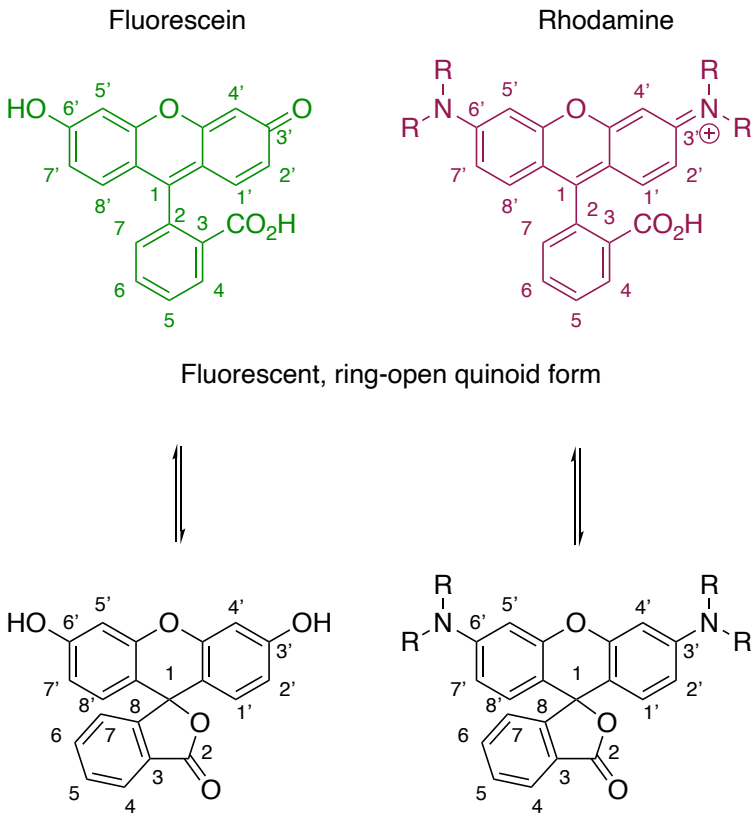

Scheme 1.1. Equilibrium between the fluorescent, ring-opened quinoid forms and the non-fluorescent, ring-closed spirolactam forms of fluorescein (green) and rhodamine (purple). The R groups on the rhodamine are typically alkyl chains.

spirolactam form is non-fluorescent due to interruption of the conjugation in the xanthene scaffold. This equilibrium between fluorescent quinoid and non-fluorescent spirolactam forms is affected by solvent polarity and pH for both fluorescein and rhodamine.[13-15] This pH dependent behaviour can be exploited to provide a fluorescent pH sensor. For example, Choudary *et al*. used a fluorescein dye to determine the pH of milk and thus predict a shelf life for the milk sample.[16]

1.1.2 Classes of fluorescent sensors

Fluorescent sensors can be separated into three categories: turn-on, turn-off, or ratiometric sensors. This classification is dependent on the sensor's behaviour upon exposure to the desired analyte.[2,17] Turn-on sensors fluoresce when exposed to the analyte, while turn-off sensors will reduce in fluorescence output (also referred to as fluorescence quenching). Turn-on sensors are more desirable than turn-off sensors, as there is an intense signal emitted against a dark background, which maximises the fluorescence signal to noise ratio.[15] These turn-on sensors can

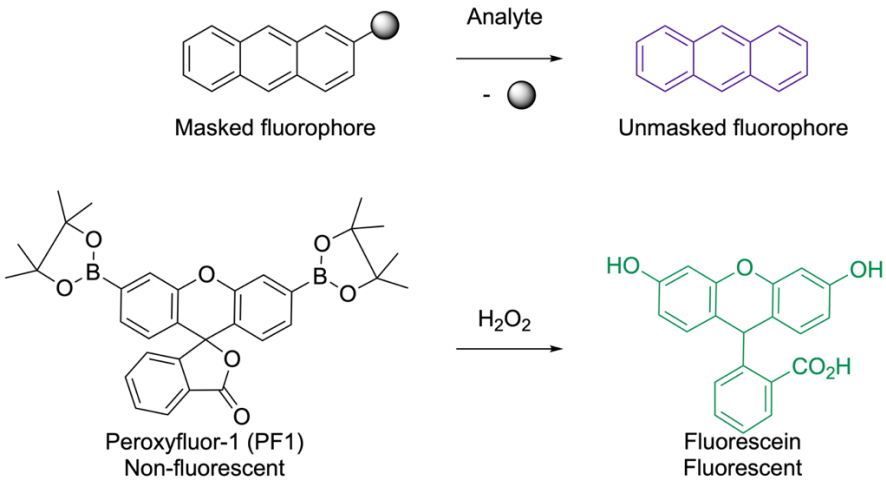

Scheme 1.2. Top, a general approach to prepare a turn-on fluorescent sensor where a masking group is released on reaction with the analyte, to reveal the unmasked fluorophore. **Bottom**, the irreversible turn-on fluorescent sensor PF1 which reacts with H_2O_2 to reveal fluorescein.

be synthesised by the addition of a masking group to a fluorescent scaffold, which results in a molecule that fluoresces after it has reacted with the analyte (Scheme 1.2, top). Turn-on sensors prepared in this manner are irreversible, as the masking group cannot be replaced after reaction with the analyte. An example of this irreversible approach is the family of H_2O_2 sensors produced by the Chang group, where the 3' or 6' hydroxyl groups on a fluorescein scaffold were masked with a boronate ester (Scheme 1.2, middle).[18-20] This ester is selectively cleaved upon reaction with H_2O_2 to unmask fluorescein, and therefore provides detection of H_2O_2 through collection of the resultant fluorescence emitted by the unmasked fluorescein.[21-23]

A reversible turn-on sensor can be prepared through the use of an analyte binding group, in contrast to a reactive masking group for irreversible sensors. These compounds selectively bind to the desired analyte, which causes a change in fluorescence. This type of turn-on sensor is reversible if the analyte is subsequently removed from the sensor. A reversible sensor can be used repeatedly in the same system, in contrast to a single-use irreversible sensor.

The third class of fluorescent sensors alongside turn-on and turn-off sensors is ratiometric sensors. This type of sensor has two emission maxima that respond to external stimuli in a predictable manner. For example, the seminaphthorhodafluor (SNARF) and seminaphthofluorescein (SNAFL) families of benzoxanthene based dyes reported by Whitaker *et al*. respond ratiometrically to pH.[24] These dyes exist in a pH dependent equilibrium between

multiple charge states, and the ring-opened fluorescent quinoid or ring-closed non-fluorescent spirolactam forms, as shown in Figure 1.1. Ratiometric sensors provide an advantage over turn-on or turn-off sensors as they can be internally calibrated to minimise experimental errors, such as an inconsistent distribution of the sensor within a sample. This is particularly advantageous in biological applications, as a ratiometric sensor can provide quantitative analyte measurement without the need for the addition of an external standard. For example, the ratiometric pH sensor carboxy-napthofluorescein (CNF, see Figure 1.1, top left) has been used to measure pH levels in human tissue samples,[25] as well as the pH change due to metabolic flux in cumulus-oocyte complexes.[26]

1.1.3 Challenges facing organic fluorescent sensors

The application of fluorescent sensors to a biological system can be inhibited by a number of challenges including cell permeability, specific targeting, and photobleaching. First, a sensor designed to measure an analyte within a cell must be cell permeable, unless it is directly injected. This generally requires a synthetic modification to the sensor molecule to impart cell permeability. For example, the H_2O_2 sensor EEPF1 was prepared by attachment of the hydrophilic compound 2-(2-ethoxyethoxy)ethanol to the 5/6 position carboxylic acid on carboxy-PF1 (Scheme 1.3).[23] Both c-PF1 and EEPF1 were added to spermatozoa cells and fluorescence spectra collected, with EEPF1 observed to detect more H_2O_2 produced within the sperm cells, likely due to improved cell permeability.[23] However, this approach is not amenable to all fluorescent sensors, as many fluorophores do not possess a convenient functional group that is available for derivatisation.

Another challenge for fluorescent sensors is to specifically target the area of interest *in vitro* or *in vivo*. The complexity of biological systems can often result in delivery of the fluorophore to an area away from the intended sensing site. For example, the fluorescent sensor may be captured in organelles within a cell.[27-29] In some cases, the fluorescent sensor can be synthetically modified with a targeting group to alleviate this issue and control localisation of the sensor to the desired area. For example, attachment of a triphenylphosphonium moiety to a fluorescent sensor

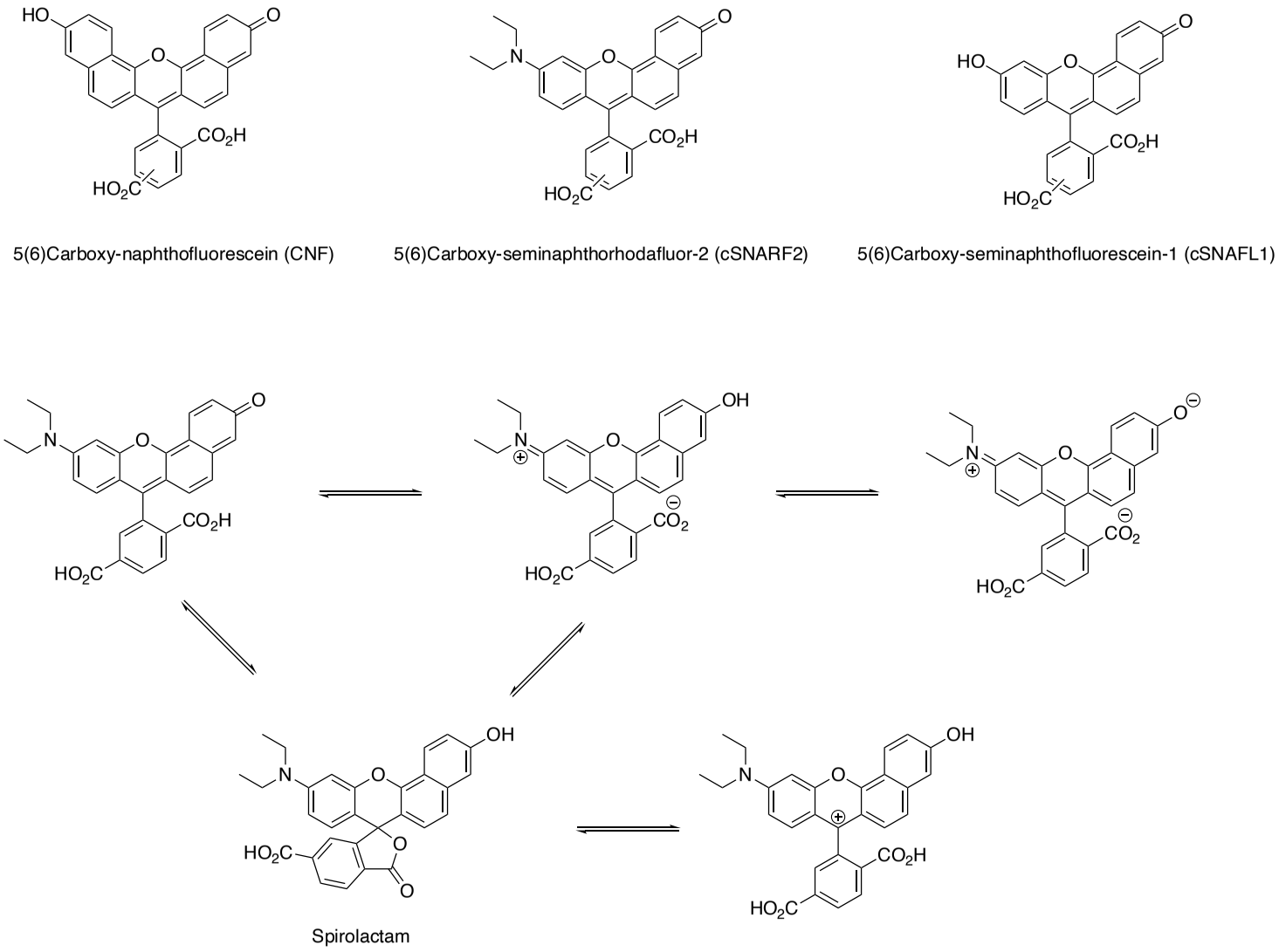

Figure 1.1. Top, the ratiometric fluorescent sensors CNF, cSNARF2, and cSNAFL1 (left to right). **Bottom**, The species present in the pH dependent equilibrium of the cSNARF2 system, including the non-fluorescent spirolactam form.

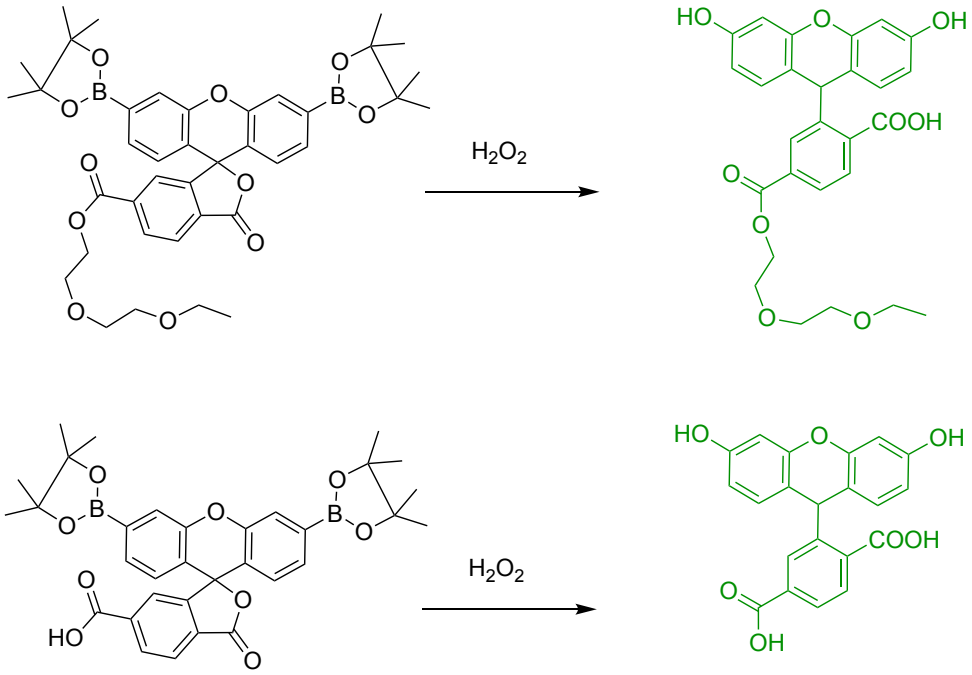

Scheme 1.3. Reaction of the fluorescent sensors EEPF1 (top) and cPF1 (bottom) with H_2O_2. Note that both compounds are 5/6 carboxy isomers, but only the 6 position is shown for clarity.[23]

is a commonly encountered modification which selectively directs the sensor toward mitochondria,[30-34] while addition of a morpholine group can provide specific targeting to the lysosome (Figure 1.2).[35,36] The weakly basic nature of the morpholine aids in probe diffusion across the cell membrane, but subsequent protonation of the morpholine inside the acidic lysosome causes the probe to become trapped.[37,38] Hence, the sensor now cannot diffuse away from the fluorescence measurement site. However, these types of synthetic modification can affect the fluorescence of the final compound. Therefore, the attachment of targeting groups to a fluorescent sensor is limited to modifications that do not adversely impact the fluorescence output of the sensor.

A further challenge in fluorescent sensing is photobleaching, where the emitted fluorescence intensity reduces exponentially under extended exposure to excitation light (see Figure 1.3). The rate at which a fluorophore photobleaches is dependent on the fluorescent scaffold in question. For example, a fluorescein derivative will photobleach faster than its related rhodamine counterpart.[40] Photobleaching can be particularly problematic when a high intensity

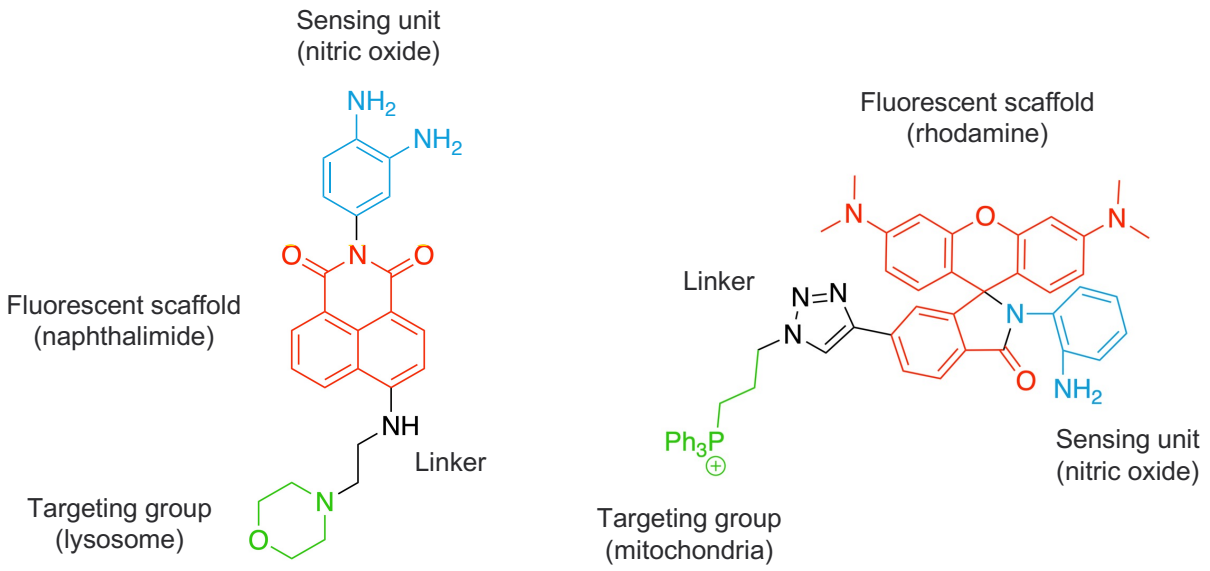

Figure 1.2. Schematic of two complex fluorescent sensors consisting of a fluorophore scaffold (red), targeting group (green), and a sensing unit (blue). **Left**, A nitric oxide sensor targeted to the lysosome. **Right**, A nitric oxide sensor targeted to mitochondria. Structures reproduced based on references 35 and 39.

light source is used, such as in confocal microscopy experiments,[41] and can make quantitative measurements difficult to obtain. For example, a measurement taken at the start of an experiment may have a higher fluorescence intensity than a measurement taken some time later. These negative effects of photobleaching can be reduced to an extent by minimising exposure of the fluorophore to excess light.[42] However, this reduction is limited as photobleaching can occur before any measurements are made, due to the light exposure required to find the region of interest and obtain the best focal plane in microscopy experiments.

The impact of photobleaching can also be reduced by synthetic modification of the fluorophore. For example, the JaneliaFluor™ series of dyes possess an azetidine in place of the traditional N,N' dialkylamine at the 3' and 6' positions on a rhodamine backbone. This has been shown to provide increased photostability, as well as impart control over excitation and emission wavelengths.[9,10] Despite these efforts, even the most photostable of organic fluorophores continue to suffer from photobleaching. For example, Reineck *et al*. demonstrated that AlexaFluor-647, touted by Thermofisher as one of the most photostable fluorophores, will photobleach down to less than 10% of the original fluorescence intensity within one minute under 10.67 Wcm^{-2} of

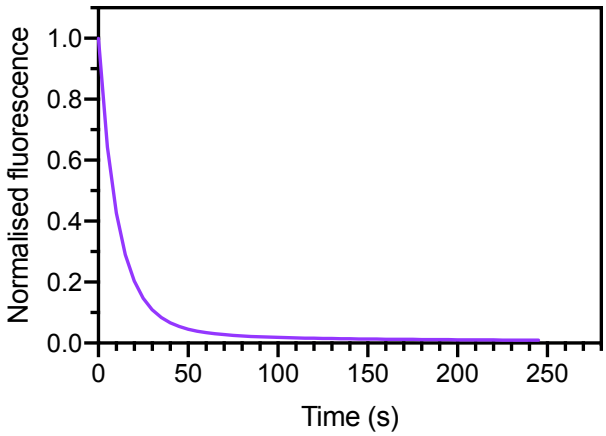

Figure 1.3. Normalised fluorescence intensity of AlexaFluor-647 647 (ex. 640 nm, em. 692 nm) under constant illumination at 10.67 Wcm^{-2}. The dye was dissolved in water at ~8 nM and fluorescence emission collected every 5 s. Reproduced from reference 43.

irradiation (Figure 1.3).[43] This is a commonly encountered irradiation power in fluorescence microscopy, which shows that photobleaching remains a significant challenge in the field of fluorescence based sensing, and requires new approaches to circumvent or avoid.

1.2 Solid supports for fluorescent sensors

Preparation of a sensing device through attachment of a fluorescent sensor to a solid support can provide a solution to the challenges of precise targeting *in vitro* or *in vivo* and photobleaching as discussed in section 1.1.3. These sensing devices combine the advantages of organic fluorescent sensors and the solid support used. For example, attachment of a fluorescent sensor to an optical fibre provides spatial control over the delivery and collection of light for analyte detection, while the use of specialised nanoparticles can provide precise targeting without requiring synthetic modification of the base fluorophore.

The attachment of a fluorescent sensor to a solid support occurs through a process known as surface functionalisation. There are a number of routes to functionalise a surface, including silanisation,[44] electrografting,[45] polymer growth,[46,47] plasma coatings,[48] direct coupling reactions,[49] and non-covalent coatings.[50,51] These techniques are dependent on the functional groups present on the surface in question. For example, covalent functionalisation with silane reagents requires a hydroxylated surface to form O-Si-O bonds,[52,53] and is commonly performed on glass

samples[25,54] or silica nanoparticles.[55,56] In this thesis the surface functionalisation of fluorophores onto two solid support materials, optical fibres and nanodiamonds, is investigated in detail.

1.2.1 Optical fibres

Optical fibres are an excellent base material for attachment of a fluorophore, to provide an optical fibre probe capable of detecting biological analytes. Optical fibres are light-weight, flexible materials comprised of an inner core and at least one outer cladding, where the inner core has a higher refractive index than the cladding.[57] The material used is generally soft glass, however optical fibres made from other materials such as polymers are commercially available.[58,59] Light can propagate within the fibre until reaching the tip due to total internal reflection, caused by the difference in refractive index between the core and cladding (Figure 1.4A). This total internal reflection allows optical fibres to transmit light over extremely long distances, a property commonly exploited in telecommunications.[60] This property is also advantageous for optical fibre sensors, as the distal tip of the fibre sensor can be placed in one location, while the proximal end of the fibre is connected to a light source and detector kept in a separate location at a relatively large distance away.[61] This allows sensing to occur at the fibre tip in difficult to reach locations,[62,63] while the spectrometer and other equipment remain at a distance. Optical fibres are also largely inert to chemical environments, and do not carry any current. These properties are advantageous for application of fibre sensors in hazardous or reactive environments, such as highly corrosive sewer waste,[63] highly volatile liquids,[61] or high temperature environments.[64,65]

Another advantage of attaching fluorescent sensors to optical fibres is to allow collection of fluorescence spectra in areas that are not typically accessible to fluorescence microscopy.[66] Optical fibre sensors can be used in ultra-small volumes,[67] and incorporated into clinical needles for minimally invasive spectroscopy to be conducted inside the body.[68,69] These properties can be further enhanced by manipulation of the cladding surrounding the fibre core, or direct modification of the core structure. For example, addition of a second cladding around the fibre core, to provide a double-clad fibre (Figure 1.4B), allows the combination of two distinct light sources in a single fibre.[68,70] This was demonstrated by Li *et al*., who prepared a double-clad fibre capable of

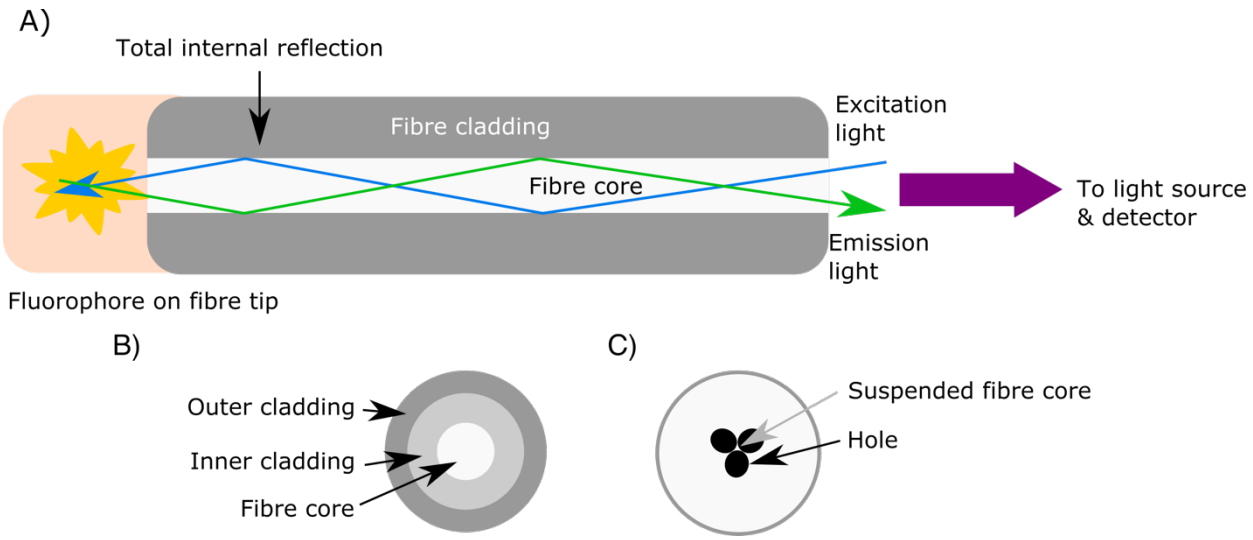

Figure 1.4. A) Diagram of an optical fibre with the fibre core (white) and fibre cladding (grey) shown. Light is carried through the fibre by total internal reflection, shown by the excitation (blue) and emission (green) light rays. The fluorescent sensor is attached to the distal end of the fibre while the proximal end is connected to a light source and spectrometer. **B)** Cross-section of a double-clad fibre, showing the fibre core, outer and inner cladding. **C)** Cross-section of a suspended-core fibre, where the core is thinly suspended between three holes in the fibre core.

concurrent optical coherence tomography (OCT) imaging and temperature sensing.[70] Meanwhile, suspended-core or micro-structured optical fibres (Figure 1.4C) have proven advantageous in chemical sensing applications,[71-74] with fibres used to make measurements on sample volumes as low as 30 nanolitres.[75,76]

Optical fibre functionalisation

A common approach to prepare an optical fibre sensor is to coat the fibre tip in a polymer matrix, within which the fluorophore is embedded (Figure 1.5). One such fibre sensor was prepared by attachment of the ratiometric pH sensor CNF (see Figure 1.1 above) to an optical fibre tip to provide a pH sensing device, where CNF was encapsulated within a poly(acrylamide) matrix on the optical fibre tip.[25,26] The resulting device has been shown to be capable of measuring pH near highly sensitive cumulus-oocyte complexes (COCs),[26] and to determine the difference between cancerous and non-cancerous tissue.[25] Attachment to the optical fibre alleviated the challenge of specifically targeting the CNF fluorescent sensor to the desired sensing location in both cases, and mitigated the need to release the free CNF molecule into solution, thus potentially avoiding toxicity effects or systemic distribution of the CNF throughout each system. A key challenge of this approach is to ensure a sufficient fluorophore concentration to obtain a high signal to noise ratio.

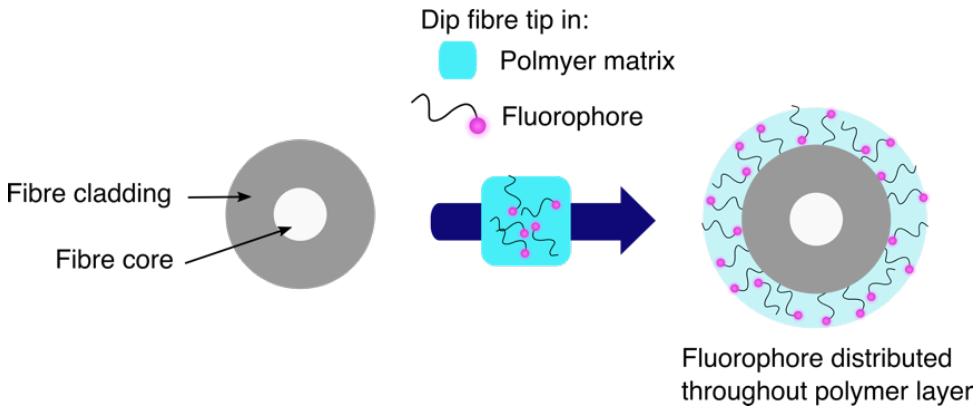

Figure 1.5. Preparation of an optical fibre sensor by coating the fibre tip in a polymer matrix, within which the fluorophore is embedded. The fibre is shown as an end-on cross section.

A similar fibre functionalisation approach as described for CNF was used to produce an optical fibre sensor for dual H_2O_2 and pH sensing. Here, the ratiometric pH sensor SNARF-2 (see Figure 1.1 above) and the turn-on H_2O_2 sensor carboxy-PF1 (see Scheme 1.3 above) were combined within a poly(acrylamide) matrix, that was subsequently attached to the fibre tip. This allowed for sensing of two parameters with a single fibre probe. Functionalisation of optical fibres with fluorescent sensors specific for detection of aluminium,[44] mercury,[77] pyridine vapour,[78] or temperature[79] has also been reported (Table 1.1). In each case, the optical fibre provides additional capabilities beyond that of the fluorescent sensor alone. Specifically, the aluminium sensor was produced using a suspended-core fibre, which provided access to small sample volumes that are not compatible with standard fluorescent imaging.[44] The mercury sensor was prepared as a prototype for deployment to agricultural areas, where use of an optical fibre allowed miniaturisation of the sensing system into a transportable device.[77] The pyridine vapour sensor exploits the advantage of optical fibres carrying light over long distances. This allows physical separation of the optical fibre tip sensor from the detector and the person operating the sensor, which is particularly important when sensing toxic compounds such as pyridine.[78] Finally, the temperature sensor was able to be employed at temperatures up to 600 K as the optical fibre remains stable in high temperature environments.[79]

Table 1.1. Summary of optical fibre sensors prepared by attachment of a fluorophore to an optical fibre tip.

Fibre	Fluorophore (analyte)	Functionalisation method	Application	Advantage of fibre	Reference
Double-clad	Tellurite glass (temperature)	Molten glass on tip	Imaging and sensing in rat brains	Allows OCT imaging	Li *et al*. 2018 #70
Suspended core	Spiropyran (lithium)	Silanisation	Proof-of-concept	Low volume measurement	Heng *et al*. #80
Single mode	CNF (pH) & cPF1 (H_2O_2)	Polyacrylamide coating from silane layer	Proof-of-concept	Concurrent measurement	Purdey *et al*. #81
Single mode	CNF (pH)	Polyacrylamide coating from silane layer	Cancer detection	Adaptable to surgery	Schartner *et al*. #25
Single mode	CNF (pH)	Polyacrylamide coating from silane layer	Assessment of cumulus-oocyte complexes	Non-invasive addition of fluorophore to IVF set up	McLennan *et al*. #26
Suspended core	Lumogallion derivative (aluminium)	Polyallylamine hydrochloride coating	Proof-of-concept	Low volume measurement	Warren-Smith *et al*. #44
Single mode	Coumarin with azathia crown ether (mercury)	Silanisation	Proof-of-concept	Can produce portable device	Nguyen *et al*. #77
Single mode	β-$Co(py)_2Cl_2$ complex (pyridine)	Polyvinyl chloride coating	Air quality monitoring	Can use in toxic environments	Elosua *et al*. #78
Single mode	Upconversion nanoparticle doped with Er^{3+} (temperature)	Polydimethylsiloxane coating	Temperature sensing	Can use in high temperature environments	Kumar *et al*. #79

In summary, optical fibres are an ideal solid support for attachment of a fluorescent sensor to provide an optical fibre-based sensing device. These devices can overcome a number of challenges in fluorescent sensing, including precise light delivery and collection, and specific tissue targeting. The optical fibre also allows measurements to be made in extreme environments, such as deep within tissue, at high temperatures, or near highly toxic compounds. Finally, the optical fibre microstructure can be customised to suit the desired sensing application. Overall, optical fibre sensors are robust devices, and the design of the final sensing device can be modified for compatibility with a wide array of fluorescent sensors.

1.2.2 Nanodiamonds

An alternative solid support material for fluorescent sensors is nanodiamond (ND), which is defined as diamond material that has at least one dimension less than 100 nm in length. NDs are a versatile material that have found application in fields including drug delivery,[82-85] cell/tissue labelling,[86-88] and advanced optics.[89-93] In general, NDs have been shown to be biocompatible in cell uptake experiments,[94,95] however the long term exposure effects remain undetermined.[5] Nanodiamonds can be used to overcome the fluorescence sensing challenges of specific targeting and photobleaching detailed in section 1.1.3.

Nanodiamonds may contain defects in the carbon lattice, which impart additional properties on the bulk material. The defect can be due to elements including N, Si, Ge, Sn, and Pb.[96] The focus in this thesis is on the fluorescent nitrogen-vacancy (NV) centre, which emits broadly in the 600-700 nm region with excitation near 550 nm (Figure 1.6A). This fluorescence is responsive to both ambient temperature and local magnetic fields.[7] The fluorescence intensity is dependent on the NV charge state, at either 0 or -1, where the NV^0 peak emission (or zero phonon line, ZPL) is approximately 600 nm, while the NV^- ZPL is at approximately 690 nm, and of much higher intensity (Figure 1.6A).[97] It is desirable for the NV centre to be predominantly in the NV^- charge state as most fluorescence based applications of NV-NDs require high signal intensity. Furthermore, the NV centre fluorescence is highly photostable, with no loss in fluorescence output during extended periods of excitation (Figure 1.6B).[43]

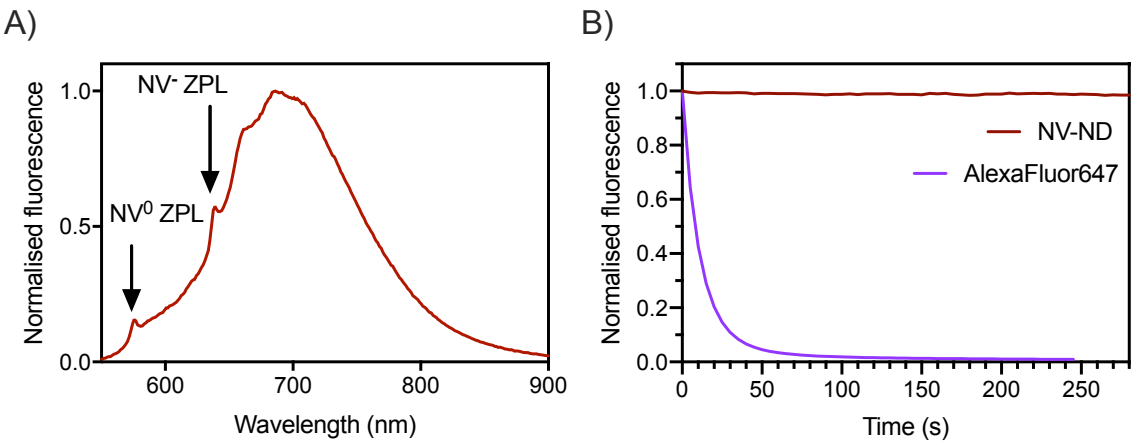

Figure 1.6. A) Fluorescence from a nitrogen-vacancy centre containing nanodiamond (NV-ND), with the zero phonon lines (ZPL) marked for the two NV charge states. Excitation wavelength 550 nm, data provided by Dr. Philipp Reineck, RMIT University. **B)** Normalised fluorescence intensity of AlexaFluor-647 (ex. 640 nm, em. 692 nm) and NV-NDs (ex. 560 nm, em. 692 nm), under constant illumination at 10.67 Wcm^{-2}. The AlexaFluor was dissolved in water at 8 nM, and the NV-NDs dispersed in water at 40 mg/mL, with fluorescence collected every 5 s. Reproduced from reference 43.

The extended photostability of the NV centre in NDs provides an opportunity to circumvent the challenge of photobleaching in application of organic fluorophores to biological sensing. A hybrid nanoparticle can be prepared by attachment of an organic fluorophore to the ND surface. This attachment is dependent on the precise nature of the functional groups present on the ND surface, which can include amines, carboxylic acids, alcohols, or halides.[49] The functionalised ND particles can then be tracked by the NV fluorescence within a biological system,[88] while the surface bound fluorophore is available for sensing on-demand. Photobleaching of the organic fluorophore is therefore avoided with appropriate choice of an organic fluorophore that has an absorbance profile distinct from the NV excitation wavelength of ~550 nm. For example, this requirement is filled by coumarin- or fluorescein-based sensor molecules, which have maximum absorbance at approximately 400 and 490 nm respectively (Figure 1.7). Meanwhile a rhodamine-based sensor molecule would be a poor choice for attachment to NDs, as its maximum absorbance is at 560 nm, and therefore it would still be photobleached by excitation of the NV centre (Figure 1.7).

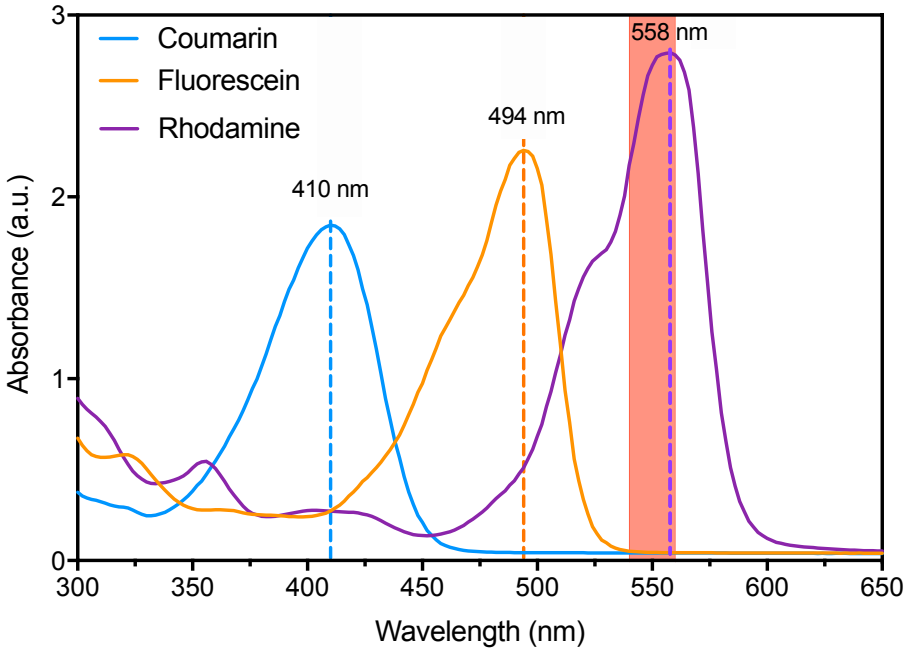

Figure 1.7. Plot of absorbance spectra for 7-diethylamino-4-methylcoumarin (Coumarin 1, blue), 5(6)-carboxyfluorescein (orange), and rhodamine B (purple) with absorbance maxima marked by the dashed lines. The major band for excitation of the nitrogen vacancy centre in nanodiamonds is shown by the red box (540 to 560 nm). Each fluorophore was at a concentration of 1 mM in DMSO, absorbance spectra were collected in a 96-well clear bottom plate on a BioTeK Synergy H4 plate reader with a Xenon light source.

A small number of proof-of-concept studies on attachment of fluorophores to NDs have been reported previously. For example, Hens *et al*. produced conjugates of amine-terminated NDs (with no NV centre) and the fluorophore carboxy-tetramethylrhodamine (TAMRA). The ND-TAMRA nanoparticles were coated onto silicon tip arrays and shown to be detectable through the TAMRA fluorescence with a fluorescence microscope.[98] The fluorophore pyrene has also been attached to NDs by several groups, where the pyrene is subsequently detectable by confocal microscopy.[99,100] Finally, Huang and Chang non-covalently coated NDs in poly-L-lysine through electrostatic interactions, then attached the fluorophore AlexaFluor-488 by NHS/EDC mediated amide formation between the fluorophore's carboxylic acid and the lysine amine.[101]

The above examples were all performed on ND samples that do not contain NV centres, and thus are still susceptible to photobleaching of the attached organic fluorophore. Recently, Purdey *et al*. reported attachment of the organic H_2O_2 sensor cPF1 (see Scheme 1.3 above) to NDs that were engineered to contain a large number of NV centres (Figure 1.8).[102] These hybrid H_2O_2 sensing nanoparticles were tracked via the NV fluorescence in macrophage cells over 18 h,

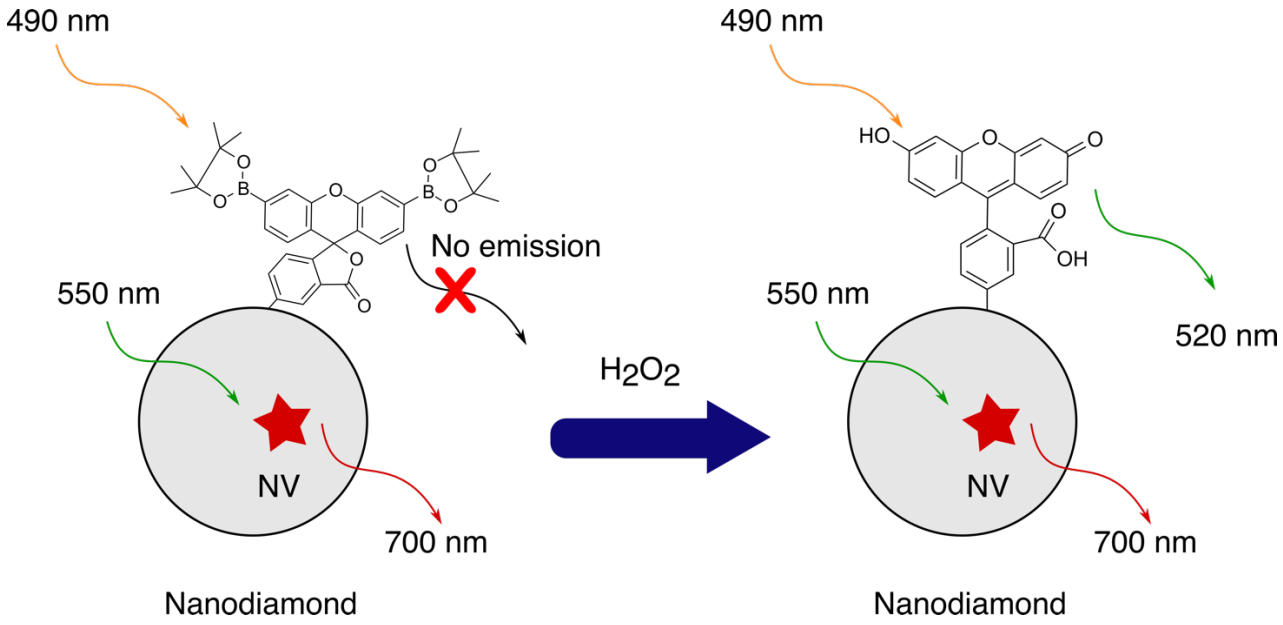

Figure 1.8. Attachment of the fluorescent hydrogen peroxide (H_2O_2) sensor carboxy-PF1 to a nitrogen vacancy (NV) containing nanodiamond to overcome photobleaching of carboxy-PF1. **Left**, the NV centre fluoresces around 700 nm upon excitation at 550 nm, and in the absence of H_2O_2 the carboxy-PF1 is non-fluorescent. This allows tracking of the hybrid nanoparticles without photobleaching the carboxy-PF1. **Right**, upon reaction with H_2O_2 the carboxy-PF1 is unmasked to reveal carboxy-fluorescein, which emits light at 520 nm when excited at 490 nm. Only one NV centre and one fluorophore are shown for clarity. Figure adapted from reference 101.

without photobleaching the cPF1 fluorophore. This allowed measurement of the basal levels of H_2O_2 production within the macrophages without the impact of photobleaching. This work was the first example of a hybrid nanoparticle that combines the advantage of highly photostable NV centres in NDs with a traditional organic fluorescent sensor.

1.2.3 Characterisation of surface functionalised materials

It is critical to thoroughly characterise the final sensing device prepared by surface functionalisation of an organic fluorescent sensor onto a solid support, including determination of the precise nature of the bonding present at the surface. This provides a clear understanding of the benefits and limitations of the sensing device for application to biological sensing. It is critical to note here that incomplete characterisation does not necessarily detract from the demonstrated application of the final material. Even with the precise nature of the bond between solid support and surface loaded molecule unknown, the described application of the resulting hybrid material remains valid. Instead, the major limitation of these less well-characterised devices is their reproducibility in other research laboratories.

Optical fibres

Optical fibres are typically functionalised through polymer coatings or silanisation chemistry as described in section 1.2.1 and Table 1.1. Generally, the precise nature of the bond between an optical fibre surface and the coating is not known, and is instead interrogated by techniques such as resistance to washing in solvent and exposure to harsh environments. The functionalised optical fibres can be analysed by techniques such as scanning electron microscopy (SEM), fluorescence spectroscopy, and profiling of the light beam exiting the fibre tip. SEM gives an indication of the surface topology of the functionalised fibre tip when compared to a bare fibre tip and can be used to measure the thickness of a tip coating.[103] The optical properties of a fibre such as reflectivity, refractive index, and the width of the light beam are also strongly affected by the fibre coating.[65,104]

Characterisation of functionalised nanodiamonds

Generally, multiple techniques are required to definitively characterise a functionalised ND. However, there is no defined minimum requirement for this characterisation in the ND literature.[105] The techniques employed may include spectroscopic methods such as Fourier-transform infrared (FTIR) spectroscopy, X-ray photoelectron spectroscopy (XPS), magic angle spinning nuclear magnetic resonance (MAS NMR) spectroscopy, Raman spectroscopy, and fluorescence spectroscopy, or analytical methods such as thermogravimetric analysis (TGA), dynamic light scattering (DLS) and zeta potential (ZP) measurements.

These characterisation techniques are rarely able to definitively prove the precise nature of the bond between a solid support and the surface loaded molecule when used on an individual basis, as a covalent bond and non-covalent surface coatings can provide similar – if not identical – results. For example, peaks observed in the FTIR spectrum of a functionalised ND that were not present in the unreacted ND spectrum, and are consistent with the molecule in question, are assigned to the surface bound molecule.[106] However, this approach is additive in nature and does not prove the type of bond that is present between the ND and new compound. Rather, it only confirms that both components were present in the interrogated sample. Precise characterisation

by FTIR can be difficult as the carboxyl region in the ND FTIR spectra typically contains common diamond peaks that can confuse interpretation.[106]

The combination of two orthogonal techniques is required to probe the bonding between ND and surface loaded molecule. For example, a spectroscopic technique such as FTIR is complementary to an analytical method such as TGA, which measures the mass of a sample while heating from ambient to high temperatures of up to 600-900 °C. This provides greater insight into the presence or absence of a covalent bond compared to the use of two similar spectroscopic techniques. For example, FTIR and Raman spectroscopy both rely on the vibrational modes of bonds. Therefore, using only these two techniques to demonstrate covalent functionalisation of a ND should be considered unreliable.

1.3 Thesis outline

This thesis describes research toward overcoming the current challenges in the field of fluorescence-based sensing including location specific targeting, cell permeability, and photobleaching. Attachment of fluorescent sensors to a solid support is presented as a potential solution to these challenges. The required chemistry to attach fluorescent sensors to two solid supports, optical fibres (**Chapters 2** and **3**) or nanodiamonds (**Chapters 4 and 5**), is discussed in detail, with a new surface functionalisation system presented for each material.

Chapter 2 presents a new fibre functionalisation architecture to provide optical fibres which are capable of dual imaging and sensing. The fibre is coated in silk fibroin protein and a silk-binding peptide with the pH sensor covalently bound to the peptide. The design, synthesis, and characterisation of this new fibre coating is presented along with application of the fibre probe to conduct dual imaging and sensing of cumulus-oocyte complexes in an *in vitro* fertilisation context.

Chapter 3 details the expansion of the silk fibroin protein and silk-binding peptide fibre functionalisation architecture into protein sensing. A model biotin and streptavidin system is used, where D-biotin is attached to the silk-binding peptide coated on the optical fibre tip. The influence of the precise position of the silk-binding peptide with respect to the silk fibroin coating on the

optical fibre on protein sensing is investigated, through the development of two complementary coating procedures.

Chapter 4 explores the functionalisation of nanodiamonds through covalent bond formation. First, two methods are developed toward quantification of the number of reactive sites available on carboxylated nanodiamonds. Next, attempts to covalently functionalise carboxylated nanodiamonds *via* amide bond formation with an amine bearing a nitrile handle for spectroscopic identification are presented.

Chapter 5 presents a new approach to non-covalently functionalise nanodiamonds utilising four carbon binding peptides, which bind to diamond-like carbon, carbon nanotubes, diamond film, and graphite film, respectively. The synthesis of these four peptides is presented alongside characterisation of their adherence to both detonation nanodiamond and high-pressure high-temperature synthesised nanodiamonds.

In **Chapter 6**, the synthesis and stability of 4-aminobutanenitrile, an amine first designed for use in **Chapter 4**, is discussed. Literature methods to prepare 4-aminobutanenitrile from 4-azidobutanenitrile are attempted and optimised to provide 4-aminobutanenitrile in greater yield with a simplified work-up procedure. The subsequent room temperature stability is also discussed, and stability increased by conversion of 4-aminobutanenitrile to the corresponding hydrochloride salt.

Finally in **Chapter 7**, the research presented in **Chapters 1** to **5** is summarised, and future directions of this work are discussed.

1.4 References

(1) Lavis, L. D.; Raines, R. T. Bright Ideas for Chemical Biology. *ACS Chem. Biol.* **2008**, *3* (3), 142-155. https://doi.org/10.1021/cb700248m.

(2) Chan, J.; Dodani, S. C.; Chang, C. J. Reaction-Based Small-Molecule Fluorescent Probes for Chemoselective Bioimaging. *Nat. Chem.* **2012**, *4* (12), 973-984. https://doi.org/10.1038/nchem.1500.

(3) Urrutia, A.; Bojan, K.; Marques, L.; Mullaney, K.; Goicoechea, J.; James, S.; Clark, M.; Tatam, R.; Korposh, S. Novel Highly Sensitive Protein Sensors Based on Tapered Optical Fibres Modified with Au-Based Nanocoatings https://www.hindawi.com/journals/js/2016/8129387/ (accessed Jan 4, 2021). https://doi.org/10.1155/2016/8129387.

(4) Wang, W.; Mai, Z.; Chen, Y.; Wang, J.; Li, L.; Su, Q.; Li, X.; Hong, X. A Label-Free Fiber Optic SPR Biosensor for Specific Detection of C-Reactive Protein. *Sci. Rep.* **2017**, *7* (1), 16904. https://doi.org/10.1038/s41598-017-17276-3.

(5) Schrand, A. M.; Hens, S. A. C.; Shenderova, O. A. Nanodiamond Particles: Properties and Perspectives for Bioapplications. *Crit. Rev. Solid State Mater. Sci.* **2009**, *34* (1-2), 18-74. https://doi.org/10.1080/10408430902831987.

(6) Mochalin, V. N.; Shenderova, O.; Ho, D.; Gogotsi, Y. The Properties and Applications of Nanodiamonds. *Nat. Nanotechnol.* **2012**, *7* (1), 11-23. https://doi.org/10.1038/nnano.2011.209.

(7) Doherty, M. W.; Manson, N. B.; Delaney, P.; Jelezko, F.; Wrachtrup, J.; Hollenberg, L. C. L. The Nitrogen-Vacancy Colour Centre in Diamond. *Phys. Rep.* **2013**, *528* (1), 1-45. https://doi.org/10.1016/j.physrep.2013.02.001.

(8) Torelli, M. D.; Nunn, N. A.; Shenderova, O. A. A Perspective on Fluorescent Nanodiamond Bioimaging. *Small* **2019**, 1902151. https://doi.org/10.1002/smll.201902151.

(9) Grimm, J. B.; English, B. P.; Chen, J.; Slaughter, J. P.; Zhang, Z.; Revyakin, A.; Patel, R.; Macklin, J. J.; Normanno, D.; Singer, R. H.; Lionnet, T.; Lavis, L. D. A General Method to Improve Fluorophores for Live-Cell and Single-Molecule Microscopy. *Nat. Methods* **2015**, *12* (3), 244-250. https://doi.org/10.1038/nmeth.3256.

(10) Grimm, J. B.; Muthusamy, A. K.; Liang, Y.; Brown, T. A.; Lemon, W. C.; Patel, R.; Lu, R.; Macklin, J. J.; Keller, P. J.; Ji, N.; Lavis, L. D. A General Method to Fine-Tune Fluorophores for Live-Cell and in Vivo Imaging. *Nat. Methods* **2017**, *14* (10), 987-994. https://doi.org/10.1038/nmeth.4403.

(11) Zheng, Q.; Ayala, A. X.; Chung, I.; Weigel, A. V.; Ranjan, A.; Falco, N.; Grimm, J. B.; Tkachuk, A. N.; Wu, C.; Lippincott-Schwartz, J.; Singer, R. H.; Lavis, L. D. Rational Design of Fluorogenic and Spontaneously Blinking Labels for Super-Resolution Imaging. *ACS Cent. Sci.* **2019**, *5* (9), 1602-1613. https://doi.org/10.1021/acscentsci.9b00676.

(12) Jun, J. V.; Chenoweth, D. M.; Petersson, E. J. Rational Design of Small Molecule Fluorescent Probes for Biological Applications. *Org. Biomol. Chem.* **2020**, *18* (30), 5747-5763. https://doi.org/10.1039/D0OB01131B.

(13) Martin, M. M.; Lindqvist, L. The PH Dependence of Fluorescein Fluorescence. *J. Lumin.* **1975**, *10* (6), 381-390. https://doi.org/10.1016/0022-2313(75)90003-4.

(14) Adamczyk, M.; Grote, J. Synthesis of Probes with Broad PH Range Fluorescence. *Bioorg. Med. Chem. Lett.* **2003**, *13* (14), 2327-2330. https://doi.org/10.1016/S0960-894X(03)00411-6.

(15) Lavis, L. D. Teaching Old Dyes New Tricks: Biological Probes Built from Fluoresceins and Rhodamines. *Annu. Rev. Biochem.* **2017**, *86* (1), 825-843. https://doi.org/10.1146/annurev-biochem-061516-044839.

(16) Choudhary, S.; Joshi, B.; Pandey, G.; Joshi, A. Application of Single and Dual Fluorophore-Based PH Sensors for Determination of Milk Quality and Shelf Life Using a Fibre Optic Spectrophotometer. *Sens. Actuators B Chem.* **2019**, *298*, 126925. https://doi.org/10.1016/j.snb.2019.126925.

(17) Fernández, A.; Vendrell, M. Smart Fluorescent Probes for Imaging Macrophage Activity. *Chem. Soc. Rev.* **2016**, *45* (5), 1182-1196. https://doi.org/10.1039/C5CS00567A.

(18) Chang, M. C. Y.; Pralle, A.; Isacoff, E. Y.; Chang, C. J. A Selective, Cell-Permeable Optical Probe for Hydrogen Peroxide in Living Cells. *J. Am. Chem. Soc.* **2004**, *126* (47), 15392-15393. https://doi.org/10.1021/ja0441716.

(19) Dickinson, B. C.; Chang, C. J. A Targetable Fluorescent Probe for Imaging Hydrogen Peroxide in the Mitochondria of Living Cells. *J. Am. Chem. Soc.* **2008**, *130* (30), 9638-9639. https://doi.org/10.1021/ja802355u.

(20) Dickinson, B. C.; Huynh, C.; Chang, C. J. A Palette of Fluorescent Probes with Varying Emission Colors for Imaging Hydrogen Peroxide Signaling in Living Cells. *J. Am. Chem. Soc.* **2010**, *132* (16), 5906-5915. https://doi.org/10.1021/ja1014103.

(21) Lippert, A. R.; Van de Bittner, G. C.; Chang, C. J. Boronate Oxidation as a Bioorthogonal Reaction Approach for Studying the Chemistry of Hydrogen Peroxide in Living Systems. *Acc. Chem. Res.* **2011**, *44* (9), 793-804. https://doi.org/10.1021/ar200126t.

(22) Srikun, D.; Albers, A. E.; Chang, C. J. A Dendrimer-Based Platform for Simultaneous Dual Fluorescence Imaging of Hydrogen Peroxide and PH Gradients Produced in Living Cells. *Chem. Sci.* **2011**, *2* (6), 1156. https://doi.org/10.1039/c1sc00064k.

(23) Purdey, M. S.; Connaughton, H. S.; Whiting, S.; Schartner, E. P.; Monro, T. M.; Thompson, J. G.; Aitken, R. J.; Abell, A. D. Boronate Probes for the Detection of Hydrogen Peroxide Release from Human Spermatozoa. *Free Radic. Biol. Med.* **2015**, *81*, 69-76. https://doi.org/10.1016/j.freeradbiomed.2015.01.015.

(24) Whitaker, J. E.; Haugland, R. P.; Prendergast, F. G. Spectral and Photophysical Studies of Benzo[c]Xanthene Dyes: Dual Emission PH Sensors. *Anal. Biochem.* **1991**, *194* (2), 330-344. https://doi.org/10.1016/0003-2697(91)90237-N.

(25) Schartner, E. P.; Henderson, M. R.; Purdey, M.; Dhatrak, D.; Monro, T. M.; Gill, P. G.; Callen, D. F. Cancer Detection in Human Tissue Samples Using a Fiber-Tip PH Probe. *Cancer Res.* **2016**, *76* (23), 6795-6801. https://doi.org/10.1158/0008-5472.CAN-16-1285.

(26) McLennan, H. J.; Saini, A.; Sylvia, G. M.; Schartner, E. P.; Dunning, K. R.; Purdey, M. S.; Monro, T. M.; Abell, A. D.; Thompson, J. G. A Biophotonic Approach to Measure PH in Small Volumes in Vitro: Quantifiable Differences in Metabolic Flux around the Cumulus-Oocyte-Complex (COC). *J. Biophotonics* **2020**, *13* (3), e201960038. https://doi.org/10.1002/jbio.201960038.

(27) Cunningham, C. W.; Mukhopadhyay, A.; Lushington, G. H.; Blagg, B. S. J.; Prisinzano, T. E.; Krise, J. P. Uptake, Distribution and Diffusivity of Reactive Fluorophores in Cells: Implications toward Target Identification. *Mol. Pharm.* **2010**, *7* (4), 1301-1310. https://doi.org/10.1021/mp100089k.

(28) Jones, L. H.; Beal, D.; Selby, M. D.; Everson, O.; Burslem, G. M.; Dodd, P.; Millbank, J.; Tran, T.-D.; Wakenhut, F.; Graham, E. J. S.; Targett-Adams, P. In-Cell Click Labelling of Small Molecules to Determine Subcellular Localisation. *J. Chem. Biol.* **2011**, *4* (2), 49-53. https://doi.org/10.1007/s12154-010-0047-1.

(29) Ghosh, B.; Jones, L. H. Target Validation Using In-Cell Small Molecule Clickable Imaging Probes. *MedChemComm* **2014**, *5* (3), 247-254. https://doi.org/10.1039/C3MD00277B.

(30) Murphy, M. P. Targeting Lipophilic Cations to Mitochondria. *Biochim. Biophys. Acta BBA - Bioenerg.* **2008**, *1777* (7), 1028-1031. https://doi.org/10.1016/j.bbabio.2008.03.029.

(31) Dodani, S. C.; Leary, S. C.; Cobine, P. A.; Winge, D. R.; Chang, C. J. A Targetable Fluorescent Sensor Reveals That Copper-Deficient SCO1 and SCO2 Patient Cells Prioritize Mitochondrial Copper Homeostasis. *J. Am. Chem. Soc.* **2011**, *133* (22), 8606-8616. https://doi.org/10.1021/ja2004158.

(32) Lee, M. H.; Han, J. H.; Lee, J.-H.; Choi, H. G.; Kang, C.; Kim, J. S. Mitochondrial Thioredoxin-Responding Off-On Fluorescent Probe. *J. Am. Chem. Soc.* **2012**, *134* (41), 17314-17319. https://doi.org/10.1021/ja308446y.

(33) Cheng, G.; Fan, J.; Sun, W.; Sui, K.; Jin, X.; Wang, J.; Peng, X. A Highly Specific BODIPY-Based Probe Localized in Mitochondria for HClO Imaging. *Analyst* **2013**, *138* (20), 6091-6096. https://doi.org/10.1039/C3AN01152F.

(34) Yu, H.; Zhang, X.; Xiao, Y.; Zou, W.; Wang, L.; Jin, L. Targetable Fluorescent Probe for Monitoring Exogenous and Endogenous NO in Mitochondria of Living Cells. *Anal. Chem.* **2013**, *85* (15), 7076-7084. https://doi.org/10.1021/ac401916z.

(35) Yu, H.; Xiao, Y.; Jin, L. A Lysosome-Targetable and Two-Photon Fluorescent Probe for Monitoring Endogenous and Exogenous Nitric Oxide in Living Cells. *J. Am. Chem. Soc.* **2012**, *134* (42), 17486-17489. https://doi.org/10.1021/ja308967u.

(36) Du, C.; Fu, S.; Wang, X.; Sedgwick, A. C.; Zhen, W.; Li, M.; Li, X.; Zhou, J.; Wang, Z.; Wang, H.; Sessler, J. L. Diketopyrrolopyrrole-Based Fluorescence Probes for the Imaging of Lysosomal Zn2+ and Identification of Prostate Cancer in Human Tissue. *Chem. Sci.* **2019**, *10* (22), 5699-5704. https://doi.org/10.1039/C9SC01153F.

(37) Xu, W.; Zeng, Z.; Jiang, J.-H.; Chang, Y.-T.; Yuan, L. Discerning the Chemistry in Individual Organelles with Small-Molecule Fluorescent Probes. *Angew. Chem. Int. Ed.* **2016**, *55* (44), 13658-13699. https://doi.org/10.1002/anie.201510721.

(38) Li, X.; Zhao, R.; Wang, Y.; Huang, C. A New GFP Fluorophore-Based Probe for Lysosome Labelling and Tracing Lysosomal Viscosity in Live Cells. *J. Mater. Chem. B* **2018**, *6* (41), 6592-6598. https://doi.org/10.1039/C8TB01885E.

(39) Trinh, N.; Jolliffe, K. A.; New, E. Dual-Functionalisation of Fluorophores for the Preparation of Targeted and Selective Probes. *Angew. Chem. Int. Ed.* **2020**, *59* (46), 20290. https://doi.org/10.1002/anie.202007673.

(40) Lakowicz, J. R. *Principles of Fluorescence Spectroscopy*, 3rd ed.; Springer: New York, 2006.

(41) Bernas, T.; Zarębski, M.; Cook, R. R.; Dobrucki, J. W. Minimizing Photobleaching during Confocal Microscopy of Fluorescent Probes Bound to Chromatin: Role of Anoxia and Photon Flux. *J. Microsc.* **2004**, *215* (3), 281-296. https://doi.org/10.1111/j.0022-2720.2004.01377.x.

(42) Hoebe, R. A.; Van Oven, C. H.; Gadella, T. W. J.; Dhonukshe, P. B.; Van Noorden, C. J. F.; Manders, E. M. M. Controlled Light-Exposure Microscopy Reduces Photobleaching and Phototoxicity in Fluorescence Live-Cell Imaging. *Nat. Biotechnol.* **2007**, *25* (2), 249-253. https://doi.org/10.1038/nbt1278.

(43) Reineck, P.; Francis, A.; Orth, A.; Lau, D. W. M.; Nixon-Luke, R. D. V.; Rastogi, I. D.; Razali, W. A. W.; Cordina, N. M.; Parker, L. M.; Sreenivasan, V. K. A.; Brown, L. J.; Gibson, B. C. Brightness and Photostability of Emerging Red and Near-IR Fluorescent Nanomaterials for Bioimaging. *Adv. Opt. Mater.* **2016**, *4* (10), 1549-1557. https://doi.org/10.1002/adom.201600212.

(44) Warren-Smith, S. C.; Heng, S.; Ebendorff-Heidepriem, H.; Abell, A. D.; Monro, T. M. Fluorescence-Based Aluminum Ion Sensing Using a Surface-Functionalized Microstructured Optical Fiber. *Langmuir* **2011**, *27* (9), 5680-5685. https://doi.org/10.1021/la2002496.

(45) Bélanger, D.; Pinson, J. Electrografting: A Powerful Method for Surface Modification. *Chem. Soc. Rev.* **2011**, *40* (7), 3995-4048. https://doi.org/10.1039/C0CS00149J.

(46) Song, A.; Parus, S.; Kopelman, R. High-Performance Fiber-Optic PH Microsensors for Practical Physiological Measurements Using a Dual-Emission Sensitive Dye. *Anal. Chem.* **1997**, *69* (5), 863-867. https://doi.org/10.1021/ac960917+.

(47) Kostecki, R.; Ebendorff-Heidepriem, H.; V, S. A.; McAdam, G.; Davis, C.; Monro, T. M. Novel Polymer Functionalization Method for Exposed-Core Optical Fiber. *Opt. Mater. Express* **2014**, *4* (8), 1515-1525. https://doi.org/10.1364/OME.4.001515.

(48) Bachhuka, A.; Heng, S.; Vasilev, K.; Kostecki, R.; Abell, A.; Ebendorff-Heidepriem, H. Surface Functionalization of Exposed Core Glass Optical Fiber for Metal Ion Sensing. *Sensors* **2019**, *19* (8), 1829. https://doi.org/10.3390/s19081829.

(49) Krueger, A.; Lang, D. Functionality Is Key: Recent Progress in the Surface Modification of Nanodiamond. *Adv. Funct. Mater.* **2012**, *22* (5), 890-906. https://doi.org/10.1002/adfm.201102670.

(50) Wang, X.; Meier, R. J.; Schmittlein, C.; Schreml, S.; Schäferling, M.; Wolfbeis, O. S. A Water-Sprayable, Thermogelating and Biocompatible Polymer Host for Use in Fluorescent Chemical Sensing and Imaging of Oxygen, PH Values and Temperature. *Sens. Actuators B Chem.* **2015**, *221*, 37-44. https://doi.org/10.1016/j.snb.2015.05.082.

(51) Sarkar, P. K.; Halder, A.; Adhikari, A.; Polley, N.; Darbar, S.; Lemmens, P.; Pal, S. K. DNA-Based Fiber Optic Sensor for Direct in-Vivo Measurement of Oxidative Stress. *Sens. Actuators B Chem.* **2018**, *255*, 2194-2202. https://doi.org/10.1016/j.snb.2017.09.029.

(52) McIntire, T. M.; Smalley, S. R.; Newberg, J. T.; Lea, A. S.; Hemminger, J. C.; Finlayson-Pitts, B. J. Substrate Changes Associated with the Chemistry of Self-Assembled Monolayers on Silicon. *Langmuir* **2006**, *22* (13), 5617-5624. https://doi.org/10.1021/la060153l.

(53) Zhu, M.; Lerum, M. Z.; Chen, W. How To Prepare Reproducible, Homogeneous, and Hydrolytically Stable Aminosilane-Derived Layers on Silica. *Langmuir* **2012**, *28* (1), 416-423. https://doi.org/10.1021/la203638g.

(54) Mohamad, F.; G. Tanner, M.; Choudhury, D.; R. Choudhary, T.; C. Wood, H. A.; Harrington, K.; Bradley, M. Controlled Core-to-Core Photo-Polymerisation - Fabrication of an Optical Fibre-Based PH Sensor. *Analyst* **2017**, *142* (19), 3569-3572. https://doi.org/10.1039/C7AN00454K.

(55) Wisser, F. M.; Abele, M.; Gasthauer, M.; Müller, K.; Moszner, N.; Kickelbick, G. Detection of Surface Silanol Groups on Pristine and Functionalized Silica Mixed Oxides and Zirconia. *J. Colloid Interface Sci.* **2012**, *374* (1), 77-82. https://doi.org/10.1016/j.jcis.2012.01.015.

(56) Kunc, F.; Balhara, V.; Brinkmann, A.; Sun, Y.; Leek, D. M.; Johnston, L. J. Quantification and Stability Determination of Surface Amine Groups on Silica Nanoparticles Using Solution NMR. *Anal. Chem.* **2018**, *90* (22), 13322-13330. https://doi.org/10.1021/acs.analchem.8b02803.

(57) Utzinger, U.; Richards-Kortum, R. R. Fiber Optic Probes for Biomedical Optical Spectroscopy. *J. Biomed. Opt.* **2003**, *8* (1), 121-147. https://doi.org/10.1117/1.1528207.

(58) Tao, G.; Stolyarov, A. M.; Abouraddy, A. F. Multimaterial Fibers. *Int. J. Appl. Glass Sci.* **2012**, *3* (4), 349-368. https://doi.org/10.1111/ijag.12007.

(59) Addanki, S.; Amiri, I. S.; Yupapin, P. Review of Optical Fibers-Introduction and Applications in Fiber Lasers. *Results Phys.* **2018**, *10*, 743-750. https://doi.org/10.1016/j.rinp.2018.07.028.

(60) Essiambre, R.-J.; Tkach, R. W.; Ryf, R. Chapter 1 - Fiber Nonlinearity and Capacity: Single-Mode and Multimode Fibers. In *Optical Fiber Telecommunications (Sixth Edition)*; Kaminow, I. P., Li, T., Willner, A. E., Eds.; Optics and Photonics; Academic Press: Boston, 2013; pp 1-43. https://doi.org/10.1016/B978-0-12-396960-6.00001-8.

(61) Culshaw, B. Optical Fiber Sensor Technologies: Opportunities and - Perhaps - Pitfalls. *J. Light. Technol.* **2004**, *22* (1), 39.

(62) Pal, A.; Dhar, A.; Ghosh, A.; Sen, R.; Hooda, B.; Rastogi, V.; Ams, M.; Fabian, M.; Sun, T.; Grattan, K. T. V. Sensors for Harsh Environment: Radiation Resistant FBG Sensor System. *J. Light. Technol.* **2017**, *35* (16), 3393-3398. https://doi.org/10.1109/JLT.2016.2598666.

(63) Rente, B.; Fabian, M.; Chen, Y.; Vorreiter, L.; Bustamante, H.; Sun, T.; Grattan, K. T. V. In-Sewer Field-Evaluation of an Optical Fibre-Based Condition Monitoring System. *IEEE Sens. J.* **2020**, *20* (6), 2976-2981. https://doi.org/10.1109/JSEN.2019.2956826.

(64) Warren-Smith, S. C.; Nguyen, L. V.; Lang, C.; Ebendorff, H.; Monro, T. M. Temperature Sensing up to 1300°C Using Suspended-Core Microstructured Optical Fibers. *Opt. Express* **2016**, 6.

(65) Warren-Smith, S. C.; Schartner, E. P.; Nguyen, L. V.; Otten, D. E.; Yu, Z.; Lancaster, D. G.; Ebendorff-Heidepriem, H. Stability of Grating-Based Optical Fiber Sensors at High Temperature. *IEEE Sens. J.* **2019**, *19* (8), 2978-2983. https://doi.org/10.1109/JSEN.2019.2890847.

(66) Li, J.; Ebendorff-Heidepriem, H.; Gibson, B. C.; Greentree, A. D.; Hutchinson, M. R.; Jia, P.; Kostecki, R.; Liu, G.; Orth, A.; Ploschner, M.; Schartner, E. P.; Warren-Smith, S. C.; Zhang, K.; Tsiminis, G.; Goldys, E. M. Perspective: Biomedical Sensing and Imaging with Optical Fibers—Innovation through Convergence of Science Disciplines. *APL Photonics* **2018**, *3* (10), 100902. https://doi.org/10.1063/1.5040861.

(67) Binetti, L.; Villar, I. D.; Dissanayake, K. P.; Stankiewicz, A.; Sun, T.; Grattan, K. T. V.; Alwis, L. S. M. Monitoring of the Critical Meniscus of Very Low Liquid Volumes Using an Optical Fiber Sensor. *IEEE Sens. J.* **2020**, *20* (20), 12232-12240. https://doi.org/10.1109/JSEN.2020.2999537.

(68) Scolaro, L.; Lorenser, D.; Madore, W.-J.; Kirk, R. W.; Kramer, A. S.; Yeoh, G. C.; Godbout, N.; Sampson, D. D.; Boudoux, C.; McLaughlin, R. A. Molecular Imaging Needles: Dual-Modality Optical Coherence Tomography and Fluorescence Imaging of Labeled Antibodies Deep in Tissue. *Biomed. Opt. Express* **2015**, *6* (5), 1767-1781. https://doi.org/10.1364/BOE.6.001767.

(69) Ramakonar, H.; Quirk, B. C.; Kirk, R. W.; Li, J.; Jacques, A.; Lind, C. R. P.; McLaughlin, R. A. Intraoperative Detection of Blood Vessels with an Imaging Needle during Neurosurgery in Humans. *Sci. Adv.* **2018**, *4* (12), eaav4992. https://doi.org/10.1126/sciadv.aav4992.

(70) Li, J.; Schartner, E.; Musolino, S.; Quirk, B. C.; Kirk, R. W.; Ebendorff-Heidepriem, H.; McLaughlin, R. A. Miniaturized Single-Fiber-Based Needle Probe for Combined Imaging and Sensing in Deep Tissue. *Opt. Lett.* **2018**, *43* (8), 1682. https://doi.org/10.1364/OL.43.001682.

(71) Monro, T. M.; Belardi, W.; Furusawa, K.; Baggett, J. C.; Broderick, N. G. R.; Richardson, D. J. Sensing with Microstructured Optical Fibres. *Meas. Sci. Technol.* **2001**, *12* (7), 854-858. https://doi.org/10.1088/0957-0233/12/7/318.

(72) Monro, T. M.; Warren-Smith, S.; Schartner, E. P.; François, A.; Heng, S.; Ebendorff-Heidepriem, H.; Afshar, S. Sensing with Suspended-Core Optical Fibers. *Opt. Fiber Technol.* **2010**, *16* (6), 343-356. https://doi.org/10.1016/j.yofte.2010.09.010.

(73) Schartner, E. P.; Ebendorff-Heidepriem, H.; Warren-Smith, S. C.; White, R. T.; Monro, T. M. Driving down the Detection Limit in Microstructured Fiber-Based Chemical Dip Sensors. *Sensors* **2011**, *11* (3), 2961-2971. https://doi.org/10.3390/s110302961.

(74) Frazão, O.; Silva, R. M.; Ferreira, M. S.; Santos, J. L.; Lobo Ribeiro, A. B. Suspended-Core Fibers for Sensing Applications. *Photonic Sens.* **2012**, *2* (2), 118-126. https://doi.org/10.1007/s13320-012-0058-3.

(75) Schartner, E. P.; Jin, D.; Ebendorff-Heidepriem, H.; Piper, J. A.; Lu, Z.; Monro, T. M. Lanthanide Upconversion within Microstructured Optical Fibers: Improved Detection Limits for Sensing and the Demonstration of a New Tool for Nanocrystal Characterization. *Nanoscale* **2012**, *4* (23), 7448-7451. https://doi.org/10.1039/C2NR32583G.

(76) Heng, S.; Nguyen, M.-C.; Kostecki, R.; M. Monro, T.; D. Abell, A. Nanoliter-Scale, Regenerable Ion Sensor: Sensing with a Surface Functionalized Microstructured Optical Fibre. *RSC Adv.* **2013**, *3* (22), 8308-8317. https://doi.org/10.1039/C3RA40321A.

(77) Nguyen, T. H.; Sun, T.; Grattan, K. T. V. A Turn-On Fluorescence-Based Fibre Optic Sensor for the Detection of Mercury. *Sensors* **2019**, *19* (9), 2142. https://doi.org/10.3390/s19092142.

(78) Elosua, C.; Bariain, C.; Matias, I. R.; Rodriguez, A.; Colacio, E.; Salinas-Castillo, A.; Segura-Carretero, A.; Fernandez-Gutiérrez, A. Pyridine Vapors Detection by an Optical Fibre Sensor. *Sensors* **2008**, *8* (2), 847-859. https://doi.org/10.3390/s8020847.

(79) Kumar, R.; Binetti, L.; Nguyen, T. H.; Alwis, L. S. M.; Sun, T.; Grattan, K. T. V. Optical Fibre Thermometry Using Ratiometric Green Emission of an Upconverting Nanoparticle-Polydimethylsiloxane Composite. *Sens. Actuators Phys.* **2020**, *312*, 112083. https://doi.org/10.1016/j.sna.2020.112083.

(80) Heng, S.; McDevitt, C. A.; Stubing, D. B.; Whittall, J. J.; Thompson, J. G.; Engler, T. K.; Abell, A. D.; Monro, T. M. Microstructured Optical Fibers and Live Cells: A Water-Soluble, Photochromic Zinc Sensor. *Biomacromolecules* **2013**, *14* (10), 3376-3379. https://doi.org/10.1021/bm401040v.

(81) Purdey, M.; Thompson, J.; Monro, T.; Abell, A.; Schartner, E. A Dual Sensor for PH and Hydrogen Peroxide Using Polymer-Coated Optical Fibre Tips. *Sensors* **2015**, *15* (12), 31904-31913. https://doi.org/10.3390/s151229893.

(82) Guan, B.; Zou, F.; Zhi, J. Nanodiamond as the PH-Responsive Vehicle for an Anticancer Drug. *Small* **2010**, *6* (14), 1514-1519. https://doi.org/10.1002/smll.200902305.

(83) Xiao, J.; Duan, X.; Yin, Q.; Zhang, Z.; Yu, H.; Li, Y. Nanodiamonds-Mediated Doxorubicin Nuclear Delivery to Inhibit Lung Metastasis of Breast Cancer. *Biomaterials* **2013**, *34* (37), 9648-9656. https://doi.org/10.1016/j.biomaterials.2013.08.056.

(84) Jeong, S. H.; Lim, D.; Kim, K.; Kang, E.; Lim, S.; Ricci, J.; Sung, S.; Kwon, M. Comprehensive Evaluation of Carboxylated Nanodiamond as a Topical Drug Delivery System. *Int. J. Nanomedicine* **2016**, 2381. https://doi.org/10.2147/IJN.S104859.

(85) Li, L.; Tian, L.; Wang, Y.; Zhao, W.; Cheng, F.; Li, Y.; Yang, B. Smart PH-Responsive and High Doxorubicin Loading Nanodiamond for in Vivo Selective Targeting, Imaging, and Enhancement of Anticancer Therapy. *J. Mater. Chem. B* **2016**, *4* (29), 5046-5058. https://doi.org/10.1039/C6TB00266H.

(86) Smith, B. R.; Niebert, M.; Plakhotnik, T.; Zvyagin, A. V. Transfection and Imaging of Diamond Nanocrystals as Scattering Optical Labels. *J. Lumin.* **2007**, *127* (1), 260-263. https://doi.org/10.1016/j.jlumin.2007.02.044.

(87) Chang, B.-M.; Lin, H.-H.; Su, L.-J.; Lin, W.-D.; Lin, R.-J.; Tzeng, Y.-K.; Lee, R. T.; Lee, Y. C.; Yu, A. L.; Chang, H.-C. Highly Fluorescent Nanodiamonds Protein-Functionalized for Cell Labeling and Targeting. *Adv. Funct. Mater.* **2013**, *23* (46), 5737-5745. https://doi.org/10.1002/adfm.201301075.

(88) Su, L.-J.; Wu, M.-S.; Hui, Y. Y.; Chang, B.-M.; Pan, L.; Hsu, P.-C.; Chen, Y.-T.; Ho, H.-N.; Huang, Y.-H.; Ling, T.-Y.; Hsu, H.-H.; Chang, H.-C. Fluorescent Nanodiamonds Enable Quantitative Tracking of Human Mesenchymal Stem Cells in Miniature Pigs. *Sci. Rep.* **2017**, *7* (1), 45607. https://doi.org/10.1038/srep45607.

(89) Fang, C.-Y.; Vaijayanthimala, V.; Cheng, C.-A.; Yeh, S.-H.; Chang, C.-F.; Li, C.-L.; Chang, H.-C. The Exocytosis of Fluorescent Nanodiamond and Its Use as a Long-Term Cell Tracker. *Small* **2011**, *7* (23), 3363-3370. https://doi.org/10.1002/smll.201101233.

(90) Tisler, J.; Reuter, R.; Lämmle, A.; Jelezko, F.; Balasubramanian, G.; Hemmer, P. R.; Reinhard, F.; Wrachtrup, J. Highly Efficient FRET from a Single Nitrogen-Vacancy Center in Nanodiamonds to a Single Organic Molecule. *ACS Nano* **2011**, *5* (10), 7893-7898. https://doi.org/10.1021/nn2021259.

(91) Zhang, X.-Q.; Lam, R.; Xu, X.; Chow, E. K.; Kim, H.-J.; Ho, D. Multimodal Nanodiamond Drug Delivery Carriers for Selective Targeting, Imaging, and Enhanced Chemotherapeutic Efficacy. *Adv. Mater.* **2011**, *23* (41), 4770-4775. https://doi.org/10.1002/adma.201102263.

(92) Zhang, T.; Cui, H.; Fang, C.-Y.; Cheng, K.; Yang, X.; Chang, H.-C.; Forrest, M. L. Targeted Nanodiamonds as Phenotype-Specific Photoacoustic Contrast Agents for Breast Cancer. *Nanomed.* **2015**, *10* (4), 573-587. https://doi.org/10.2217/nnm.14.141.

(93) Pichot, V.; Guerchoux, M.; Muller, O.; Guillevic, M.; Fioux, P.; Merlat, L.; Spitzer, D. Nanodiamond Coating by Polyethylenimine for Optical Limitation. *Diam. Relat. Mater.* **2019**, *95*, 55-59. https://doi.org/10.1016/j.diamond.2019.04.001.

(94) Ho, D. Beyond the Sparkle: The Impact of Nanodiamonds as Biolabeling and Therapeutic Agents. *ACS Nano* **2009**, *3* (12), 3825-3829. https://doi.org/10.1021/nn9016247.

(95) Hemelaar, S.; Saspaanithy, B.; L'Hommelet, S.; Perona Martinez, F.; van der Laan, K.; Schirhagl, R. The Response of HeLa Cells to Fluorescent NanoDiamond Uptake. *Sensors* **2018**, *18* (2), 355. https://doi.org/10.3390/s18020355.

(96) Bradac, C.; Gao, W.; Forneris, J.; Trusheim, M. E.; Aharonovich, I. Quantum Nanophotonics with Group IV Defects in Diamond. *Nat. Commun.* **2019**, *10* (1), 5625. https://doi.org/10.1038/s41467-019-13332-w.

(97) Reineck, P.; Trindade, L. F.; Havlik, J.; Stursa, J.; Heffernan, A.; Elbourne, A.; Orth, A.; Capelli, M.; Cigler, P.; Simpson, D. A.; Gibson, B. C. Not All Fluorescent Nanodiamonds Are Created Equal: A Comparative Study. *Part. Part. Syst. Charact.* **2019**, *36* (3), 1900009. https://doi.org/10.1002/ppsc.201900009.

(98) Hens, S. C.; Cunningham, G.; Tyler, T.; Moseenkov, S.; Kuznetsov, V.; Shenderova, O. Nanodiamond Bioconjugate Probes and Their Collection by Electrophoresis. *Diam. Relat. Mater.* **2008**, *17* (11), 1858-1866. https://doi.org/10.1016/j.diamond.2008.03.020.

(99) Barras, A.; Lyskawa, J.; Szunerits, S.; Woisel, P.; Boukherroub, R. Direct Functionalization of Nanodiamond Particles Using Dopamine Derivatives. *Langmuir* **2011**, *27* (20), 12451-12457. https://doi.org/10.1021/la202571d.

(100) Barras, A.; Szunerits, S.; Marcon, L.; Monfilliette-Dupont, N.; Boukherroub, R. Functionalization of Diamond Nanoparticles Using "Click" Chemistry. *Langmuir* **2010**, *26* (16), 13168-13172. https://doi.org/10.1021/la101709q.

(101) Huang, L. L.-C.; Chang, H.-C. Adsorption and Immobilization of Cytochrome c on Nanodiamonds. *Langmuir* **2004**, *20*, 5879-5884. https://doi.org/10.1021/la0495736.

(102) Purdey, M. S.; Capon, P. K.; Pullen, B. J.; Reineck, P.; Schwarz, N.; Psaltis, P. J.; Nicholls, S. J.; Gibson, B. C.; Abell, A. D. An Organic Fluorophore-Nanodiamond Hybrid Sensor for Photostable Imaging and Orthogonal, on-Demand Biosensing. *Sci. Rep.* **2017**, *7* (1), 15967. https://doi.org/10.1038/s41598-017-15772-0.

(103) Khalid, A.; Peng, L.; Arman, A.; Warren-Smith, S. C.; Schartner, E. P.; Sylvia, G. M.; Hutchinson, M. R.; Ebendorff-Heidepriem, H.; McLaughlin, R. A.; Gibson, B. C.; Li, J. Silk: A Bio-Derived Coating for Optical Fiber Sensing Applications. *Sens. Actuators B Chem.* **2020**, *311*, 127864. https://doi.org/10.1016/j.snb.2020.127864.

(104) Gouveia, C. A. J.; Baptista, J. M.; Jorge, P. A. S. Refractometric Optical Fiber Platforms for Label Free Sensing. *Curr. Dev. Opt. Fiber Technol.* **2013**. https://doi.org/10.5772/55376.

(105) Reina, G.; Zhao, L.; Bianco, A.; Komatsu, N. Chemical Functionalization of Nanodiamonds: Opportunities and Challenges Ahead. *Angew. Chem. Int. Ed.* **2019**, *58* (50), 17918-17929. https://doi.org/10.1002/anie.201905997.

(106) Petit, T.; Puskar, L. FTIR Spectroscopy of Nanodiamonds: Methods and Interpretation. *Diam. Relat. Mater.* **2018**, *89*, 52-66. https://doi.org/10.1016/j.diamond.2018.08.005.

Chapter 2: A silk-based functionalisation architecture for single fibre imaging and sensing

This chapter consists of a publication submitted to Advanced Functional Materials in December 2020 and accepted in March 2021.

Advanced Functional Materials, 2021, 2010713

Patrick K. Capon, Jiawen Li, Aimee J. Horsfall, Suliman Yagoub, Erik P. Schartner, Asma Khalid, Rodney W. Kirk, Malcolm S. Purdey, Kylie R. Dunning, Robert A. McLaughlin, Andrew D. Abell

Statement of Authorship

Title of Paper	A Silk-based Functionalization Architecture for Single Fiber Imaging and Sensing
Publication Status	☐ Published ☒ Accepted for Publication ☐ Submitted for Publication ☐ Unpublished and Unsubmitted work written in manuscript style
Publication Details	**Patrick K. Capon**, Jiawen Li, Aimee J. Horsfall, Suliman Yagoub, Erik P. Schartner, Asma Khalid, Rodney W. Kirk, Malcolm S. Purdey, Kylie R. Dunning, Robert A. McLaughlin, Andrew D. Abell, A Silk-based Functionalization Architecture for Single Fiber Imaging and Sensing, *submitted to Advanced Functional Materials*, **2020**

Principal Author

Name of Principal Author (Candidate)	Patrick Capon		
Contribution to the Paper	Conceptualised and conducted the full research project, including data collection and analysis. Wrote and edited the manuscript.		
Overall percentage (%)	60		
Certification:	This paper reports on original research I conducted during the period of my Higher Degree by Research candidature and is not subject to any obligations or contractual agreements with a third party that would constrain its inclusion in this thesis. I am the primary author of this paper.		
Signature		Date	11/01/2021

Co-Author Contributions

By signing the Statement of Authorship, each author certifies that:

i. the candidate's stated contribution to the publication is accurate (as detailed above);

ii. permission is granted for the candidate in include the publication in the thesis; and

iii. the sum of all co-author contributions is equal to 100% less the candidate's stated contribution.

Name of Co-Author	Jiawen Li		
Contribution to the Paper	Co-first author, conceptualised and conducted the full research project, including data collection and analysis. Wrote and edited the manuscript.		
Signature		Date	11/1/2021

Name of Co-Author	Aimee Horsfall		
Contribution to the Paper	Conceptualised the peptide system and aided in synthesis. Assisted with experiment design and data analysis. Designed the table of contents image and edited the manuscript.		
Signature		Date	12/01/2021

Name of Co-Author	Suliman Yagoub		
Contribution to the Paper	Aided in design and preparation of IVF experiments, conducted IVF experiments alongside Patrick and Jiawen. Assisted with data analysis and edited the manuscript.		
Signature		Date	12/01/2021

Name of Co-Author	Erik Schartner		
Contribution to the Paper	Assisted with design and preparation of the fibre laser system, including troubleshooting. Provided resources for the laser system and wrote custom LabView software. Edited the manuscript.		
Signature		Date	18/1/2021

Name of Co-Author	Asma Khalid		
Contribution to the Paper	Involved with research conceptualisation and provided the silk materials required.		
Signature		Date	13-01-2021

Name of Co-Author	Rodney Kirk		
Contribution to the Paper	Wrote custom C++ software for the optical coherence tomography system.		
Signature		Date	12/01/2021

Name of Co-Author	Malcolm Purdey		
Contribution to the Paper	Aided in project conceptualisation and data analysis, and co-supervised Patrick during his PhD. Edited the manuscript.		
Signature		Date	11/01/2021

Name of Co-Author	Kylie Dunning		
Contribution to the Paper	Aided in design and preparation of IVF experiments, and provided the required resources. Supervised Suliman during his PhD degree, and edited the manuscript.		
Signature		Date	13/01/2021

Name of Co-Author	Robert McLaughlin			
Contribution to the Paper	Aided in design and preparation of the full research project, and provided resources for the fibre optical coherence tomography system. Aided in writing the manuscript and edited the manuscript.			
Signature			Date	13 January 2021

Name of Co-Author	Andrew Abell			
Contribution to the Paper	Aided in design and preparation of the full research project, and provided resources for all chemical synthesis. Aided in writing the manuscript and edited the manuscript. Supervised Patrick and Aimee during PhD degrees.			
Signature			Date	13/01/2021

2.1 Abstract

A new fibre functionalisation architecture for single-fibre imaging and sensing is presented. 5(6)Carboxy-SNARF2 (a fluorescent pH sensor) is attached to a silk-binding peptide and the complex added to aqueous silk fibroin protein. These bind with a K_d of 36 μM as determined by a fluorescence polarisation assay. The fibre is dip-coated into the silk and peptide mixture, and scanning electron microscopy images reveal a uniform silk coating on the fibre tip. The coating is stable to repeated washes and does not affect the imaging light emitted from the fibre, which allows concurrent optical coherence tomography (OCT) imaging and pH sensing. Oocytes were metabolically stimulated with $CoCl_2$ to produce lactic acid, and a pH reduction of 0.04 was measured using the probe. The distance between fibre tip and oocyte was monitored by simultaneous OCT acquisitions to precisely position the probe. Lastly, OCT imaging of an ovary revealed the presence/absence of an oocyte within a follicle, an important step toward improving patient outcomes during IVF, by limiting the number of invasive follicle punctures required. These results demonstrate the utility of this new coating to enable simultaneous OCT imaging and sensing, which provides significant insight into complex biological systems.

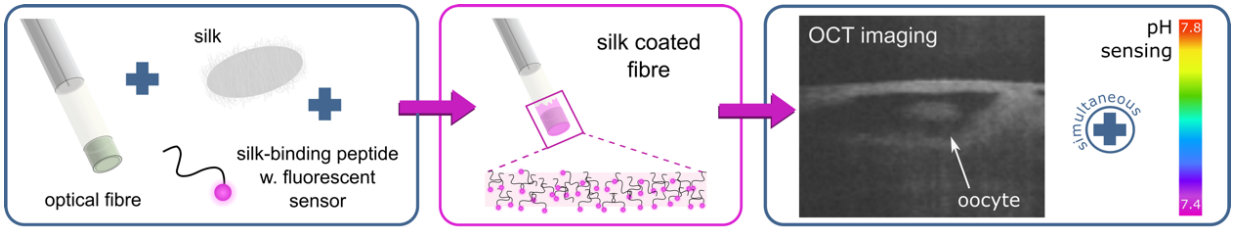

A new architecture is presented for coating optical fibres. A silk-binding peptide anchors a fluorescent pH sensor to the silk fibroin coated fibre, which allows dual depth-resolved imaging through optical coherence tomography (OCT) and pH sensing. These new probes are demonstrated in an *in vitro* fertilization setting to perform dual OCT imaging and pH sensing on cumulus-oocyte complexes.

2.2 Introduction

Optical fibres are a highly adaptable base material for light-based analysis of biological samples by spectroscopy and imaging.[1,2] Their small size allows delivery of light in difficult to access locations,[3] such as deep within the body, with a high degree of spatio-temporal control.[4] Sensing capability is typically provided by an attached organic fluorophore that changes its emission on contact with an analyte, with a number of these sensing-only fibre probes reported.[5,6] One such fibre probe for pH measurement is now commercially available and has been approved for use in humans for intravascular blood gas monitoring.[7,8] The local environment surrounding the fibre tip can also be optically imaged by an imaging fibre bundle, to provide further capability. This combination of imaging and sensing has been used to detect acetylcholine release from enzymes,[9] L-glutamate within insect oesophageal nerves,[10] and changes in pH caused by fertilisation of sea urchin eggs.[11] However, these analyses are currently limited to superficial imaging only, and are unable to visualise tissue structure below the external surface of the sample.

We recently reported an optical coherence tomography (OCT) imaging fibre probe incorporating specialised tellurite glass to provide a single fibre probe capable of temperature sensing and OCT imaging. Coating the optical fibre tip with tellurite glass allowed temperature sensing without the need for any further fibre functionalisation.[12] Meanwhile, OCT provides enhanced imaging with depth-resolved, volumetric information of tissue at micrometre resolution.[13-15] This level of imaging, compared with superficial imaging, provides significantly enhanced analysis of the environment surrounding the fibre tip, in which sensing is conducted. However, an organic fluorophore (sensing component) needs to be attached to the optical fibre tip if this advanced OCT imaging approach is to be generally applicable to sensing a range of analytes in complex biological systems.

A single layer of a fluorophore directly attached to the fibre tip does not provide sufficient fluorescence signal for sensing.[16] Instead, a number of methods have been developed for attaching an increased quantity of organic fluorophores to an optical fibre tip, for example by plasma deposition,[17] silanisation,[18-20] polyelectrolyte layering,[21] or by growth of an organic

polymer.[22-25] These approaches generally require long reaction times,[20] repetitive layering,[18,21] and/or extreme temperatures.[17] Importantly, they are not compatible with the design of an OCT fibre probe, which requires a coating that does not detrimentally alter the shape of the imaging light beam. Such functionalisation also typically renders the fibre tip opaque, confounding OCT imaging which requires the tip to remain optically clear for imaging. As an additional complexity, the fibre coating must be biocompatible if the probe is to be applied in vivo.

Here we present a solution to these problems with a new fibre functionalisation architecture that allows for simultaneous OCT imaging and fluorescence-based pH-sensing within a single fibre probe of less than 0.2 mm diameter. The new coating allows functional attachment of 5(6)-carboxyseminaphthorhodafluor-2 (SNARF-2, an organic fluorophore able to sense changes in pH)[26] to the fibre via a silk-based matrix, while retaining OCT imaging capability. The composite structure remains intact over extended immersion in solution, and the coated fibre probes are compatible with acquisition of high-quality OCT images. We demonstrate that this new fibre functionalisation architecture can be used in an *in vitro* fertilisation (IVF) setting, with collection of the first single-fibre OCT images alongside pH sensing.

2.3 Results and discussion

2.3.1 System design

The new fibre functionalisation architecture presented here was produced by coating a custom-built OCT imaging probe with a mixture of silk fibroin protein and a silk-binding peptide (SBP)[27] in a simple all in one dipping process.[28] A fluorescent sensor (SNARF-2) was covalently attached to the SBP, which then binds to the silk fibroin (Figure 2.1, see the Supporting Information for synthetic procedures). Silk fibroin is an optically transparent material,[29,30] known to be biocompatible when used as surgical mesh and sutures,[31-34] and is therefore an ideal material to prepare an optical fibre capable of imaging and sensing. SNARF-2 was chosen as the fluorescent sensor component as its 540 nm excitation does not cause significant autofluorescence in most tissues,[35] and the closely related SNARF-1 has been applied to in vivo animal experiments.[36,37]

The OCT imaging probe (with a full width half maximum beam waist of approximately 10 μm) was prepared by splicing a 180 μm length of gradient index (GRIN) fibre and a 420 μm length of no-core fibre onto the distal end of a 1.5 m double-clad-fibre (DCF) using an automated glass processor with an in-line cleaver (see Experimental Section 2.5.2).[38] The DCF allows OCT and fluorescence sensing signals to be captured simultaneously,[12,38] where the light for OCT is transmitted and collected through the DCF core, whilst the fluorescence excitation and emission light is carried through the core and inner cladding of the same fibre, respectively. An integrated OCT and fluorescence system, consisting of two light sources and detectors (see Experimental Section 2.5.2 and Supporting Information Figure S2.4 for full details), was connected to the proximal end of the DCF (see Figure 2.1) to allow dual OCT imaging and fluorescence sensing.

A literature SBP (Figure 2.1)[27] was chosen for study and synthesised by standard solid phase peptide synthesis protocols as detailed in the Supporting Information. In the first instance, a commercially available and highly fluorescent fluorophore 5(6)carboxy-tetramethylrhodamine (TAMRA) was attached to the *N*-terminus of the SBP via a 6-aminohexanoic acid (Ahx) linker, prior to cleavage of the peptide from the resin, to give the final peptide conjugate **SBP-TAMRA** (see Figure 2.1). This fluorophore was chosen in order to study the SBP and silk fibroin interaction, with the Ahx linker separating the fluorophore from the silk-binding sequence. Custom-built OCT imaging probes (see above) were then dip-coated once in an aqueous mixture of silk fibroin and **SBP-TAMRA** to provide a silk coated fibre (see Experimental Section 2.5.4) capable of dual OCT imaging and fluorescence collection.

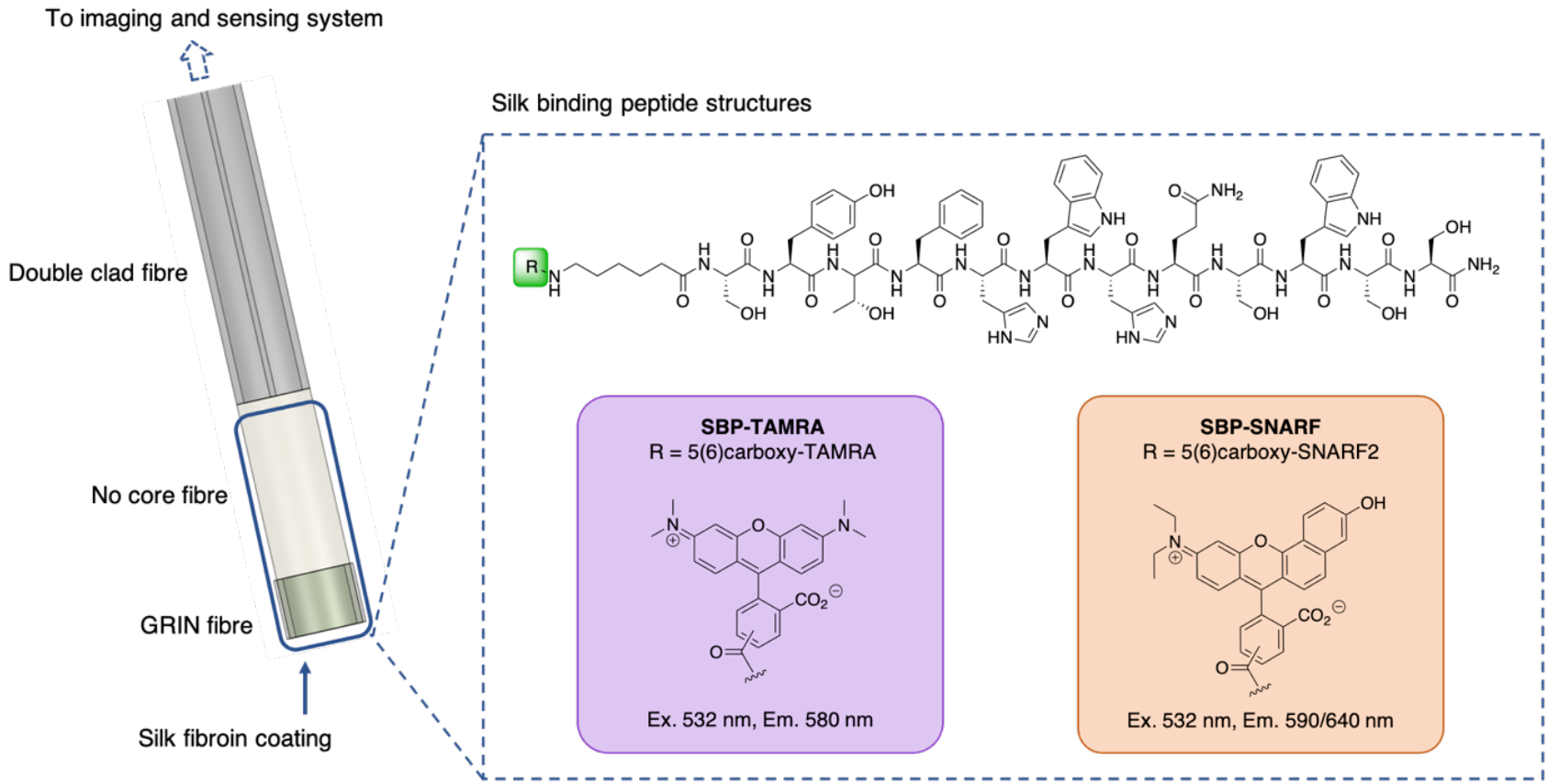

Figure 2.1. Left, Schematic of the OCT imaging probe that was prepared, consisting of double-clad fibre (DCF), with sections of no core fibre and gradient refractive index (GRIN) fibre attached to the distal end of the DCF. The proximal end is connected to the light source and detector. The silk coating on the fibre probe is indicated by the blue box, with the functionalised silk-binding peptides (SBPs) highlighted. **Right**, Structure of the SBPs studied, where the SBP amino acid sequence is SYTFHWHQSWSS,[27] and where R = 5(6)carboxy-tetramethylrhodamine (purple) to provide **SBP-TAMRA** and R=5(6)carboxy-seminaphthorhodafluor-2 (orange) to provide **SBP-SNARF**. Optical and scanning electron microscope images of the fibre probes are shown in Figure 2.2 and Figure 2.5.

2.3.2 Characterisation of silk coated fibres

The binding affinity between the SBP and silk fibroin was determined in order to characterise the new fibre functionalisation architecture. This was carried out by adding **SBP-TAMRA** (4 μM) to silk fibroin (0 to 300 μM) and measuring the resultant fluorescence polarisation (see Experimental Section 2.5.3 and Supporting Information Figure S2.5) to give a K_d of 35.9 μM. This is in agreement with the surface binding affinities for a range of solid binding peptides reported in literature,[39] as such the SBP clearly immobilises the TAMRA fluorophore onto silk fibroin.

Double-clad optical fibres were coated with silk fibroin, in the absence of SBP (see Experimental Section 2.5.4), and the resulting silk coated fibres were analysed by scanning electron microscopy (SEM), in secondary electron (SE) mode, to determine if the fibre surface topology is altered by the silk fibroin coating (Figure 2.2). Previous work from our co-authors has shown the silk fibroin coating on an optical fibre is 1-3 μm in thickness by analysis of SEM images in MATLAB.[28] The SEM images collected here revealed a smooth surface across the entire coated fibre tip (Figure 2.2B), similar to the bare fibre (Figure 2.2A). The surface topology of these coated fibres was further investigated using an optical profiler (see Experimental section 2.5.5) to collect 3D contour plots of the fibre tip (Figure 2.2D and Figure 2.2E). The plots for the bare fibre and coated fibre appeared similar, with a calculated mean roughness (S_a parameter) of 0.15 μm and 0.19μm respectively. The mean roughness of a 50 × 50 μm region at the fibre centre (where the imaging and fluorescence light exits) was also calculated and found to be 0.04 μm and 0.06 μm respectively. This similarity in optical fibre surfaces found by SEM and optical profiling indicates that the silk fibroin coating does not alter the fibre tip surface topology.

The presence of the silk coating on the fibre tip was next validated by acquiring energy dispersive X-ray (EDX) spectra from both coated and bare optical fibres, on the scanning electron microscope (Figure 2.2C). The silk coated fibre tip exhibited Kμ emission lines for C (0.27 keV) and N (0.39 keV), where EDX spectra contain emission lines characteristic to each element present. C and N were not observed on the bare fibre, which consists of a core, inner-and outer-cladding which predominantly consist of SiO_2 (Figure 2.2F).[40] A corresponding reduction in intensity for both Si (1.74 keV) and O (0.52 keV) Kμ emission lines was observed for the silk

coated fibre compared to the bare fibre. This reduction in Si and O emission was expected for the silk coated fibre compared to a bare fibre, as the electron beam must first penetrate the silk coating before any Si or O is encountered. The observed C and N Kμ emission, along with the reduction of Si and O Kμ emission, is consistent with the presence of a silk coating on the fibre tip, as the bare fibre does not contain C or N. These observations were consistent across multiple spectral collection positions on the fibre tips (see Supporting Information Figure S2.6).

The approximate atomic composition of each fibre tip surface was calculated from the resultant EDX spectra using the inbuilt Aztec program. The C (9.1 to 52%) and N (0.7 to 21%) content was observed to increase for the silk fibroin coated fibre compared to the bare fibre. The C to N ratio for the coated fibre was approximately 5:2, which is in agreement with the atomic composition of silk fibroin.[33] Furthermore, the relative atomic percentages of Si and O were reduced from 35% to 0% and 55% to 27%, respectively. This further confirms the presence of the silk fibroin layer on the fibre tip.

2.3.3 Optical properties of silk coated fibres

The impact of the new fibre functionalisation architecture on the light beam exiting the fibre probes was investigated using a beam profiling setup (Figure 2.2G-I, see Experimental Section 2.5.5). First, an uncoated fibre probe was mounted on a custom holder in front of a CMOS camera. The light exiting the fibre tip was collected by the camera, and the beam profile diameter measured in both the horizontal (x) and vertical (y) directions, perpendicular to the propagation of the light beam (z). The camera was then incrementally translated away from the fibre tip in the z direction with a motorised linear stage, and beam profile diameters measured over a distance of 0-1 mm between fibre tip and camera. This process was repeated for a fibre probe that was coated in silk fibroin using the new fibre functionalisation architecture. The resultant beam diameters for the silk fibroin coated fibre were similar to the uncoated fibre over the full range of measurements (Figure 2.2I). Furthermore, there was no clear change in the intensity profiles acquired at the beam waist from the uncoated and silk coated fibre probes (Figure 2.2G and 2.2H). This similarity in optical properties of the uncoated and coated fibre probes indicates that the silk fibroin coating has negligible effect on the light exiting the fibre tip. These results are in agreement with previous

literature which has shown that silk is optically transparent in visible and near infrared range.[29,30] Hence the new fibre functionalisation architecture presented is compatible with OCT imaging, as the coating does not affect the imaging component of the fibre probe. In contrast, coating a fibre with polyacrylamide degrades the OCT imaging beam due to optical scatterers in the coating, as shown in the Supporting Information (Figure S2.7).

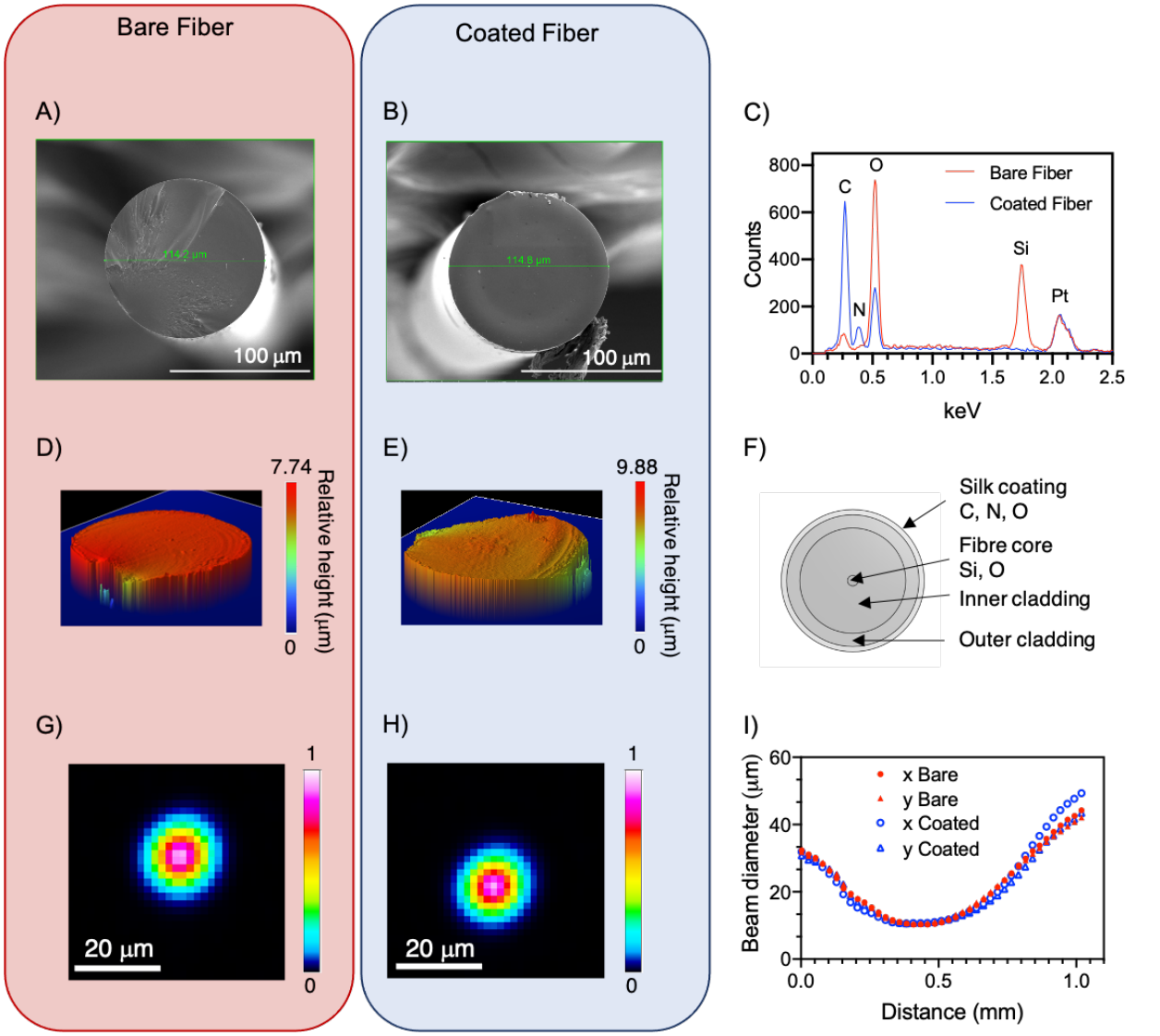

Figure 2.2. Characterisation of bare fibers (A,D, G, red box) and silk-coated fibers (B, E, H, blue box). **A)** and **B)** Scanning electron microscopy (SEM) images of bare and silk-coated fiber tips showing the smooth surface obtained. **C)** Energy dispersive X-ray (EDX) spectra obtained with characteristic elemental emissions marked. The coated fiber (blue) clearly contains more C and N than the bare fiber (red), and less O and Si. The Pt signal is from the sample preparation. **D)** and **E)** 3D contour plots of bare and silk-coated fiber tips showing the surface height, relative to the microscope objective position. The major low points observed are due to the fiber cleaving process. **F)** Cross-section of the optical fiber showing the elemental composition of the silk coating and the fiber core, along with the fiber cladding. The elemental composition of the cladding is not known (proprietary), but only Si and O were observed by EDX spectroscopy. **G)** and **H)** 2D beam intensity profile acquired at the beam waist for a bare (red) and a silk-coated (blue) fiber with the relative light intensity shown by the colored heatmap. **I)** The measured beam diameter in the x (circles) and y (triangles) directions for a bare fiber (red, filled) and a silk-coated fiber (blue, open), plotted against the distance between the fiber tip and camera.

2.3.4 Adherence of silk binding peptides to silk coated fibres

The aqueous stability of coated fibre probes produced with the new fibre functionalisation architecture was investigated in a series of fibre washing experiments. OCT imaging probes, prepared and functionalised with **SBP-TAMRA** as described earlier, were washed by dipping the fibre tips in water. The fibre probes were connected to the integrated OCT and fluorescence system to collect fluorescence spectra before and after washing the fibres in water (see Experimental Section 2.5.2 for the system description).

First, three fibre probes were washed by submerging their tips in water for 30 seconds, then the fibre probes removed from solution. This washing process was repeated three times to simulate repeated fibre sensor measurements, with fluorescence spectra collected using the fibre-coupled OCT and fluorescence system before the first wash and following the third wash. The fluorescence retention (%) was determined by comparison of the pre- and post-wash fluorescence intensity, with the silk fibroin and **SBP-TAMRA** coated fibres observed to have 100% fluorescence retention (Figure 2.3A, solid blue bar, see Supporting Information Figure S2.6 for full spectra). This shows that **SBP-TAMRA** is retained within the silk coating on an optical fibre probe when repeatedly washed with water, as there was no measurable reduction in fluorescence observed after washing. As a control, three fibre probes were coated with silk fibroin and free TAMRA (see Experimental Section 2.5.4), where the free TAMRA replaced **SBP-TAMRA**, to investigate if TAMRA can bind to the silk coated fibre without the SBP present. Three such control fibre probes were washed with water (as before) and fluorescence spectra collected. Comparison of the post-wash and pre-wash fluorescence spectra from these control fibres revealed a 98% reduction in fluorescence after washing (Figure 2.3A, striped blue bar). A second set of three control fibres were dipped in **SBP-TAMRA** in the absence of silk fibroin, to investigate if the **SBP-TAMRA** binds to bare fibres. These control fibres also revealed a 97% reduction in fluorescence after washing (see Supporting Information Figure S2.8). This clearly demonstrates that the TAMRA fluorophore must be attached to an SBP to be retained on the silk coated fibre probe, and that the new fibre functionalisation architecture is compatible with repeated insertion and removal of the fibre probe from solution.

Next, the submersion time of the coated fibre tips in water was increased from 30 s to 18 h to investigate the longer-term stability of **SBP-TAMRA** within the silk fibroin coating. Three optical fibre probes were coated with silk and **SBP-TAMRA** and soaked in water for 18 h, with fluorescence spectra collected before and after the 18 h soak (see Supporting Information Figure S2.6 for full spectra). Comparison of the post-wash and pre-wash spectra revealed that the TAMRA fluorescence was unchanged after the 18 h, showing that **SBP-TAMRA** was not removed from the optical fibre probe after 18 h in water (Figure 2.3A, solid purple bar). Three control fibre probes, coated with silk fibroin and free TAMRA (as before), were also soaked in water for 18 h. A 96% loss of the original fluorescence signal was observed for these control fibre probes (Figure 2.3A, striped purple bar). These results demonstrate that the SBP is critical to retain the TAMRA fluorophore within the silk fibroin coating when the coated fibre probe is soaked in water for up to 18 h. As such, the silk fibroin and SBP based fibre functionalisation architecture is compatible with exposure of the fibre probe to liquid environments over extended time periods.

2.3.5 Dual optical coherence tomography imaging and pH sensing

We next demonstrated the capability of our new fibre functionalisation architecture to produce an optical fibre compatible with both OCT imaging and pH sensing. The fluorescent pH sensor 5(6)carboxy-seminaphthorhodafluor-2 (SNARF-2) was chosen for this study, as it provides a ratiometric response to pH within the biologically relevant window of pH 6-8.[26] SNARF-2 was attached to the *N*-terminus of the SBP, via an Ahx linker, prior to cleavage of the peptide from the resin to give the final peptide conjugate **SBP-SNARF** (see Figure 2.1 and Supporting Information for synthetic procedures). An OCT imaging fibre probe was then dip coated in silk fibroin and **SBP-SNARF**, in the same manner as described for **SBP-TAMRA**, to provide a single fibre capable of OCT imaging and pH sensing, herein referred to as the OCTpH probe (see Experimental Section 2.5.4).

Characterisation of pH sensing

The pH dependent response of the OCTpH probe was first characterised by collecting fluorescence spectra in 4-(2-hydroxyethyl)-1-piperazine ethanesulfonic acid (HEPES) buffer over a pH range of 6.8 to 7.8 (Figure 2.3B, see Experimental Section 2.5.1 for buffer preparation). The OCTpH probe was submerged into each buffer solution, and fluorescence spectra collected using the fibre-coupled OCT and fluorescence system described in Experimental Section 2.5.2. The resultant spectra exhibited two emission maxima at 590 nm and 640 nm, with the ratio between the two peak regions (590/640 nm) observed to be dependent on buffer pH (Figure 2.3B). This pH dependent behaviour is consistent with the literature reports for free SNARF-2,[23,26] which indicates that attachment of SNARF-2 to the SBP does not alter the fluorescence of the SNARF-2 component. The fluorescence ratio obtained from an OCTpH probe can therefore be used to calculate the pH of an unknown solution, such as the media surrounding an oocyte during IVF, by reference to a known calibration curve.

The reproducibility of the OCTpH probe fluorescence, and hence the resultant pH measurement, was validated by repeated interrogation in five HEPES buffers between pH 7.21 and 7.75 (Figure 2.3C). The OCTpH probe was submerged into each buffer solution and fluorescence spectra collected with the fibre-coupled OCT and fluorescence system. The first five measurements were made in order from the lowest pH (7.218) to highest pH (7.752) and the fluorescence ratio (590/640 nm) calculated. The next set of five measurements were collected from highest to lowest pH to test if the measurement order influenced the resultant fluorescence spectra. A third set of five measurements was finally collected from lowest to highest pH again, for a total of 15 buffer measurements and 45 individual SNARF-2 fluorescence excitation events. There was no change observed in the calculated fluorescence ratio for each individual buffer solution across all measurements (see Figure 2.3C). Furthermore, the buffer solution measurement order (low to high or high to low pH) did not affect the resultant fluorescence ratio. Therefore, the fluorescence response of the OCTpH probe is consistent within the pH range of 7.21 to 7.75 for up to 15 measurements, and the OCTpH probe can reliably determine an unknown pH in this range with reference to a calibration curve.

Finally, the extended photostability of the SNARF-2 fluorophore on an OCTpH probe was investigated by performing 300 individual fluorescence excitation events with the fibre-coupled OCT and fluorescence system. The resultant fluorescence spectra were collected and the fluorescence ratio (590/640 nm peak ratio) calculated. This ratio was observed to increase rapidly over the first 50 irradiation events, followed by a slower increase for the remaining 250 irradiation events (see Figure 2.3D). A concurrent reduction in the total fluorescence intensity was also observed, indicating that some photobleaching of SNARF-2 occurred. The two emission maxima of SNARF-2 are known to photobleach at different rates due to the relative stability of the molecular species involved in each peak, which is consistent with the observed increase in peak ratio.[26] These peak ratio and photobleaching observations are also in agreement with recent data on the structurally related pH sensitive fluorophore carboxynaphthofluorescein deployed on an optical fibre.[25] The effect of photobleaching was minimised in subsequent experiments by irradiating all OCTpH probes 100 times prior to collecting fluorescence measurements, similar to the protocol reported by McLennan et al.[25]

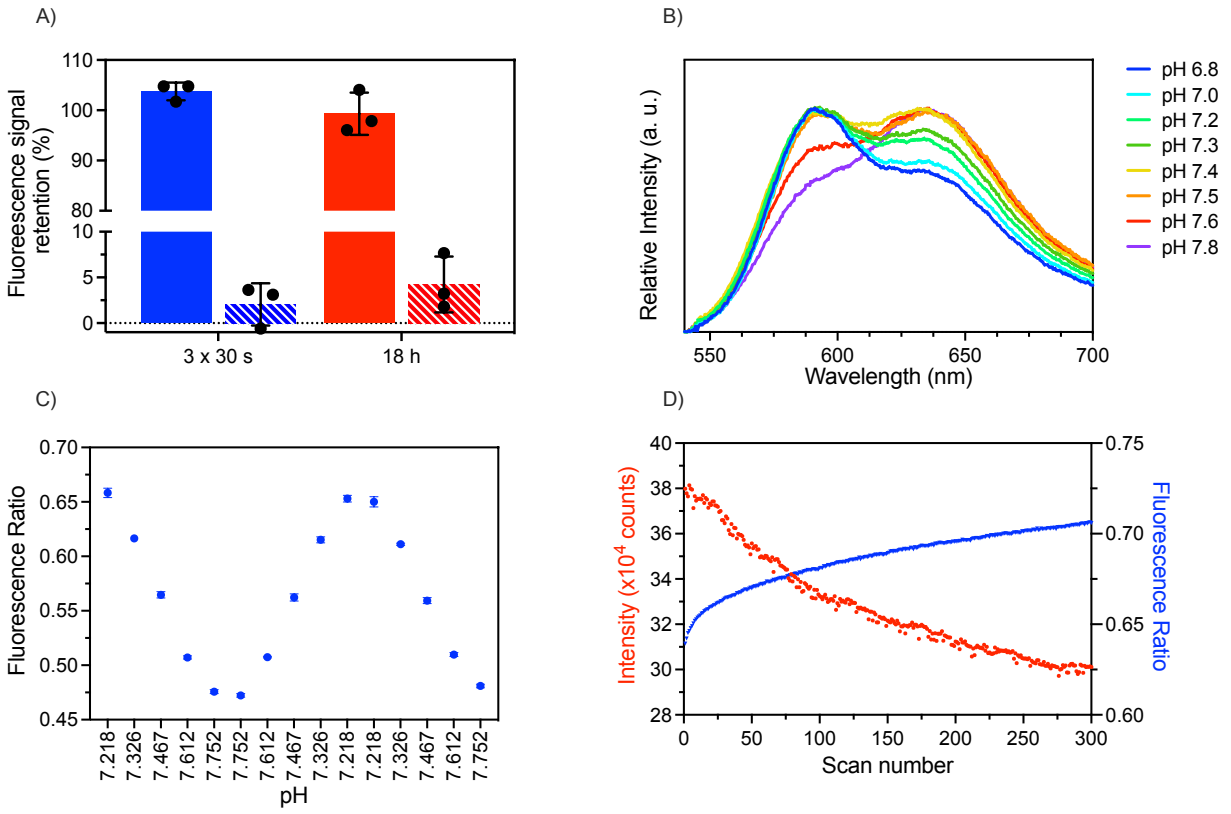

Figure 2.3. A) Fluorescence signal retention (the percentage change to the fluorescence signal obtained after washing compared to the signal before washing) for **SBP-TAMRA** (solid bars) compared to free TAMRA (striped bars). The fiber probes were washed by dipping three times in distilled water for 30 s, or left to soak for 18 h. The results from three individual probes per washing condition are plotted as mean μ standard deviation. **SBP-TAMRA** was retained under all conditions, while free TAMRA was washed away. Excitation 532 nm, emission integrated between 570-600 nm to minimise noise. **B)** Fluorescence emission spectra for **SBP-SNARF** attached to an OCTpH probe in HEPES buffer ranging from pH 6.8 to 7.8, normalised to the highest intensity peak. The peak at 590 nm decreases as pH increases, while the peak at 640 nm increases with pH. **C)** The calculated fluorescence ratio obtained from one OCTpH probe in HEPES buffer ranging from pH 7.218 to 7.752, monitored over fifteen measurements with the order of the middle five measurements reversed. Three spectra were collected per buffer measurement for a total of 45 excitation events. Each buffer measurement is plotted as mean ± standard deviation. **D)** Total integrated fluorescence intensity (red) and calculated fluorescence ratio (590/640 nm, blue) over 300 individual excitation events for one OCTpH probe. The fluorescence ratio is calculated between the integrated ranges of 575-620 nm and 620-690 nm to minimise noise.

Application to *in vitro* fertilisation

The OCTpH probe was applied in an IVF setting using a mouse model, which is a standard model for human IVF.[41] **SBP-SNARF** provides pH measurement at the fibre tip, where the pH near an oocyte is an important indicator of oocyte maturity,[25,42,43] while the OCT component provides concurrent depth resolved imaging of the environment surrounding the fibre tip.

First, a mouse ovary was imaged using an OCTpH probe to establish the ability of the probe to reveal subsurface structures. The ovary was held in a petri dish on a heated microscope stage as the OCTpH probe was manually translated over the tissue to acquire a 2D OCT image (see Experimental Section 2.5.6 and 2.5.7). The resulting image revealed two follicles within the ovary that were well resolved from the surrounding follicular and stromal tissue, with a cumulus-oocyte complex (COC) observed in only one follicle (Figure 2.4). The OCTpH probe can therefore determine which follicles contain COCs through depth resolved imaging. This level of spatial detail in imaging is not possible with existing tools such as transvaginal ultrasound, which has approximately 20 times poorer resolution than the OCT system.[44,45] Accurate identification of follicles containing COCs has the potential to improve clinical practice, limiting the number of invasive ovarian punctures required to obtain sufficient oocytes for IVF. This may in turn reduce patient complications from the oocyte pick up process including pain, bleeding and pelvic infections.[46]

Next, an OCTpH probe was used to perform simultaneous OCT imaging and pH measurement of cumulus-oocyte complexes (COCs) collected from ovarian follicles (Figure 2.5). A COC is the collective term for the oocyte and the group of cumulus cells around the oocyte, which act as nurse cells during the oocyte maturation process.[43] Measurement of the pH near a COC is important as the local pH is an indicator of oocyte maturation. This may aid in selection of the optimal oocyte for later fertilisation and implantation,[25,42,43] as metabolic activity of an oocyte has been shown to be indicative of developmental capacity.[47] Here, the OCTpH probe was held

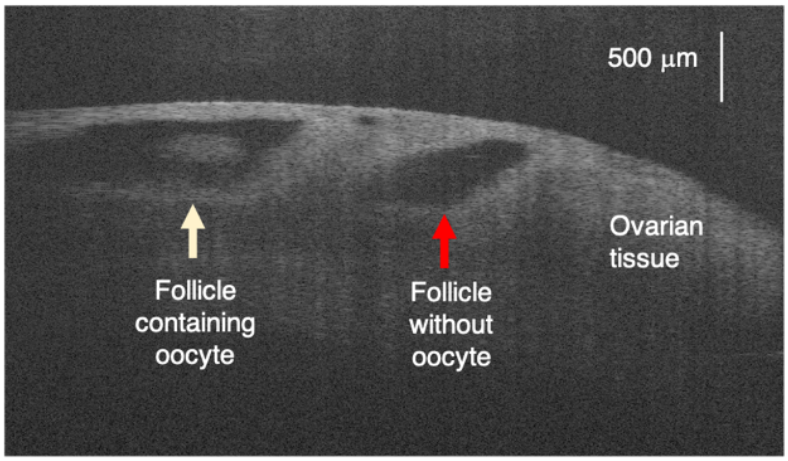

Figure 2.4. OCT image acquired of a mouse ovary (light grey area), with two follicles observed. The white arrow indicates a follicle that contains an oocyte while the red arrow indicates a follicle without an oocyte. Scale bar 500 µm.

in a micromanipulator and COCs contained in a petri dish on a heated microscope stage (see Experimental Section 2.5.8), with OCT images and fluorescence spectra acquired using the fibre-coupled OCT and fluorescence system. A group of 20 COCs were treated with $CoCl_2$ to stimulate metabolism,[25] including lactic acid production, while a second group of 20 COCs were left untreated (this treatment was blinded with respect to $CoCl_2$ presence/absence). The pH of each group was calculated through calibration curves constructed from pH adjusted culture media (see Experimental Section 2.5.8), where a reduction in pH of 0.04 was measured for the $CoCl_2$ treated group (Figure 2.5A). This reduction in pH is consistent with an increase in lactic acid production, and is in agreement with previous studies involving pH detection near COCs with an optical fibre pH sensor prepared by attachment of carboxynaphthofluorescein to the fibre tip.[25] Furthermore, the OCT imaging clearly resolved the oocyte from the surrounding cumulus cells (Figure 2.5C), showing the high level of detail obtained through OCT imaging. Together these results indicate that the OCTpH probe is able to determine key oocyte maturation criteria, which may aid in selection of the ideal oocyte for IVF.

Finally, an OCTpH probe was used to determine the distance between the fibre tip and an individual COC, as the oocyte pick up process requires precise positioning of the aspiration needle (Figure 2.5D-F). OCT images were collected using the fibre-coupled OCT and fluorescence system while the probe was slowly moved toward the COC using the

micromanipulator. An interface (black to white colour change) was observed in the OCT images due to the refractive index difference between the culture media and the edge of the oocyte (Figure 2.5E). This interface was observed to move toward the fibre tip while the probe was moved toward the COC, and therefore reflects the distance between the fibre tip and the oocyte (Figure 2.5F). This demonstrates that the OCTpH probe can provide precise measurement of the fibre tip position near an individual COC, which will aid in both oocyte analysis and subsequent oocyte pick up.

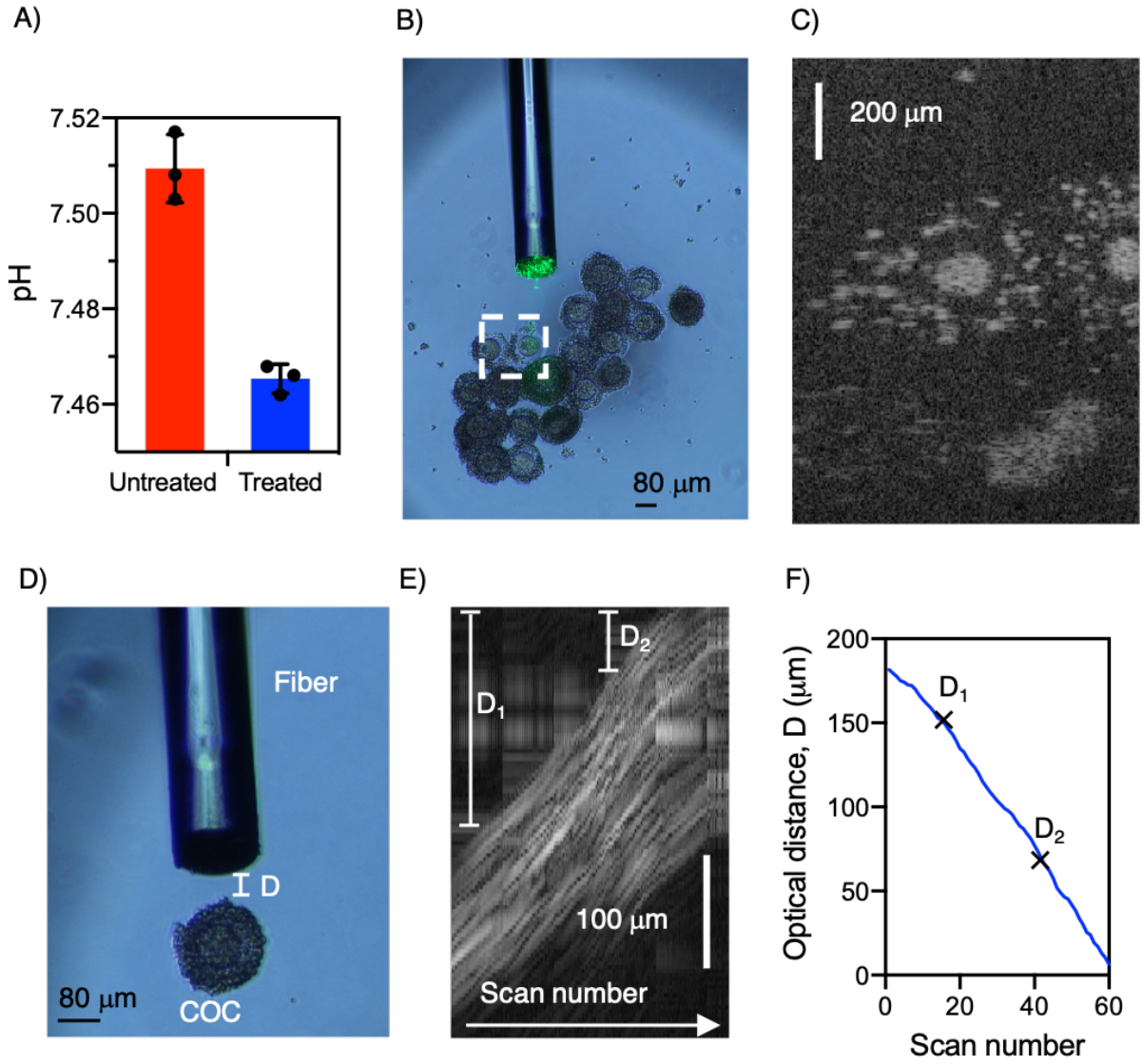

Figure 2.5. A) Using an OCTpH probe, pH values were calculated for cumulus-oocyte complexes (COCs) that were treated with 100 m µM CoCl2 (blue), or left untreated (red). Data presented as mean ± standard deviation, n = 20 COCs per treatment group, 3 measurements per group. **B)** Optical microscope image of the OCTpH probe near a group of COCs at 10x magnification, with the approximate OCT field of view marked by the white box. The fiber coupled 532 nm laser is switched on, causing the green light. Scale bar 80 µm. **C)** OCT image acquired of the COCs showing clear resolution of the cumulus cells (small circular structures) surrounding the oocytes (large circular structures). Scale bar 200 µm. **D)** Optical image of the OCTpH probe near a single cumulus oocyte complex (COC), with the optical distance, D, between fiber tip and oocyte marked in white, at 10x magnification. Scale bar 80 µm. **E)** Composite image obtained from a series of OCT scans generated as the OCTpH probe was moved toward a COC. The white striated structure corresponds to the COC. As the scan number increases, the fiber is moved toward the COC. This results in the white interface (against a black background) shifting toward the top right of the image (i.e., toward the fiber tip), and a reduction in the distance D. Scale bar 100 µm. **F)** Plot of optical distance D against scan number as the OCTpH probe is moved toward the oocyte, with the approximate positions of D1 and D2 from 5E marked by a black cross.

2.4 Conclusion

Here we have presented a new fibre functionalisation architecture to produce a single fibre probe capable of dual depth-resolved imaging and fluorescence-based sensing. The architecture consists of three simple components: a silk-binding peptide, an organic fluorophore (sensor) and silk fibroin protein. The fluorophore is covalently attached to the *N*-terminus of the silk-binding peptide via simple amide bond formation, with an alkyl chain linker, to provide the sensing component. This complex is added to an aqueous solution of silk fibroin protein, to which it associates. The fibre is then dipped in the resultant mixture to coat the fibre tip. The custom-built fibre probe is capable of optical coherence tomography imaging, an imaging technique that provides depth resolved, sub-surface images of tissue microarchitecture. The resulting functionalised probe has been used to obtain a clear snapshot of the tissue microstructure at the same location as analyte detection. This simultaneous information provides superior insight into complex biological systems, which are known to have a heterogenous distribution of analytes,[48,49] over sensing-only fibres, or sensing fibres that are only capable of superficial imaging.

The beam profiles from coated and uncoated fibre probes were compared, and it was determined that the silk coating does not affect the optical properties of the custom OCT imaging probes. Furthermore, a series of wash-out experiments using the model peptide **SBP-TAMRA** demonstrated that the silk coating is robust and the fluorescent component is retained on the fibre tip for up to 18 h when left submerged in solution. Finally, we applied this new fibre functionalisation architecture to produce a fibre probe capable of dual OCT imaging and pH sensing. The ratiometric fluorescent pH sensor SNARF-2 was attached to the SBP and subsequently coated onto OCT fibre probes to provide an OCTpH probe. This probe presents an advance over the pH sensors currently in clinical use that do not provide an indication of the tissue microstructure around the probe tip, and are therefore subject to measurement variations due to misplacement of the probe.[7,8] In contrast, the OCTpH probes presented here can simultaneously acquire micron-scale images of the nearby tissue microstructure during pH measurement, enabling a real-time assessment that the correct tissue structures are being sampled. We

demonstrated this in a model application of IVF, where the oocytes within ovarian follicles were resolved by OCT imaging for the first time.

A pH change of 0.04 units was also observed in COCs that were metabolically stimulated with $CoCl_2$ alongside OCT imaging, demonstrating that an OCTpH probe is capable of dual imaging and pH sensing in a complex biological system. These results are an important step toward improving the highly invasive collection of oocytes from ovarian follicles, through an increased understanding of the ovarian tissue microstructure. Furthermore, future integration of the OCTpH probe into clinical aspiration needles will provide depth-resolved OCT images to guide the accurate positioning of the aspiration needle to the oocyte (potentially avoiding blood vessels[15] or follicles devoid of oocytes), alongside determining of oocyte maturity through concurrent pH measurement. This imaging is complementary to, and of greater resolution that the current ultrasound guidance used in the clinic.

Our approach to covalently attach the sensor to the SBP *N*-terminus via an amide bond is amenable to the attachment of a wide range of other sensors. A large number of commercial sensors contain amine-reactive groups,[50] and we therefore expect to see our technology applied to other fields that require high quality depth-resolved imaging alongside sensing information. In summary, we have clearly shown that the use of both silk fibroin and an SBP bound sensor is a robust and reliable coating method for producing optical fibre sensors capable of dual OCT imaging and fluorescence-based sensing, a technique which is ready for expansion into further imaging and sensing applications.

2.5 Experimental

2.5.1 General materials

All reagents and solvents were purchased from Merck/Sigma-Aldrich unless otherwise specified, at the highest purity level available and used as received. were ≥99% 5(6)-carboxytetramethylrhodamine (TAMRA), Oxyma, and all Fmoc-protected building blocks including 6-Fmoc-Ahx-OH, Fmoc-Ser(tBu)-OH, Fmoc-Tyr(tBu)-OH, Fmoc-Thr(tBu)-OH, Fmoc-His(Trt)-OH, Fmoc-Phe-OH, Fmoc-Trp(Boc)-OH and Fmoc-Glu(tBu)-OH were purchased from Chem-Impex International and used as received. All amino acids were the L isomer.

^{1}H NMR spectra were recorded on an Agilent 500 MHz or a Varian Inova 600 MHz instrument in d_6-DMSO, d_6-acetone, CD_3OD, or $CDCl_3$ as indicated, and referenced to the solvent residual peak. Chemical shifts are reported in ppm (δ). Resonances are reported as s (singlet), br. s (broad singlet), d (doublet), t (triplet) or m (multiplet, range given).

Aqueous silk fibroin was obtained as per previous protocols by boiling and de-gumming *Bombyx mori* cocoons in an alkaline solution of 0.02 M sodium carbonate for 30 min.[28,51] The silk fibroin was rinsed thoroughly with water and dissolved in 9.3 M aq. LiBr. The solution was then dialysed in water using a dialysis cassette with a 3500 Da molecular cut off for 48 h. After dialysis, the fibroin solution was transferred into a centrifuge tube and centrifuged for 2 h at 9000 rpm. The purified supernatant silk solution was stored at 4 °C.

All reference pH values were obtained by recording the solution pH at 37 °C with a glass electrode pH meter (InLab MicroPro-ISM electrode, Seven Excellence S400 pH meter, manufacturer stated accuracy ±0.002 pH units, Mettler Toledo, Switzerland).

A series of 4-(2-hydroxyethyl)-1-piperazine ethanesulfonic (HEPES) acid buffers were prepared for initial **SBP-SNARF** validation. HEPES acid (238 mg, 1.00 mmol) and sodium chloride (875 mg, 15.0 mmol) were dissolved in distilled water (100 mL) to provide HEPES buffer at a concentration of 10 mM and 300 osmolarity. The bulk buffer was split into eight samples, and pH adjusted using 1 M HCl or NaOH to obtain pH values of 6.80, 7.03, 7.21, 7.34, 7.41, 7.50, 7.64, and 7.78.

2.5.2 Optical fibre set up

Prior to dip-coating in the silk solution, a 180 μm length of gradient index (GRIN) fibre (DrakaElite 100/125μm, Drake Communications, USA) and a 420 μm length of no-core fibre (NCF125, Success Prime Corporation, Taiwan) was spliced onto a connectorised double-clad-fibre (DCF13, Thorlabs, USA) by using an automated glass processor with an in-line cleaver (Vytran GPX3800, Thorlabs, USA), to create an OCT imaging probe with a full width half maximum beam waist of approximately 10 μm (see Figure 2.1 and 2.2).[38]

A dual OCT imaging and fluorescence sensing system was developed in order to collect fluorescence spectra from the SBP and silk fibroin coated optical fibres at the same time as acquiring OCT images. The OCT imaging subsystem was modified from a commercial OCT scanner (Telesto II, Thorlabs GmbH, Germany). The central wavelength is 1300 nm with a manufacturer-specified axial resolution of 5.5 μm (in air). The fluorescence sensing subsystem and the OCT imaging subsystem were coupled together with a custom module (Castor Optics, Canada) including a wavelength division multiplexer (WDM) and a DCF coupler. The DCF allows OCT and fluorescence sensing signals to be captured simultaneously,[12] where the light for OCT is transmitted and collected through the DCF core. Meanwhile a 532 nm laser (CrystaLaser, USA) was used to excite the relevant fluorophore (TAMRA or SNARF-2) on the fibre tip, with excitation and emission light delivered and collected through the core and the inner cladding of the same fibre respectively. The laser power at the fibre tip was measured to be 2.7 mW. A shutter (LS6, Uniblitz, USA) and shutter driver (VCM-D1, Uniblitz, USA) system were installed to minimise excess exposure to excitation light, with custom LabVIEW software (National Instruments Corp, USA) used to synchronise the Ocean Optics spectrometer acquisition with a 100 ms shutter opening for each collection. A dark spectrum was also acquired immediately after each measurement with the shutter closed to remove the effects of ambient light from the experiment. The fluorescence signal was collected through the inner cladding of the DCF, passed through a long pass filter to remove the excitation light (532 nm, Semrock, USA), and measured with a portable spectrometer (Ocean Optics, USA). See Supporting Information Figure S2.4 for a diagram of the full system.

2.5.3 Binding affinity

The dissociation constant (K_d) between **SBP-TAMRA** and silk fibroin was determined measurement of **SBP-TAMRA** fluorescence polarisation, as a function of silk fibroin concentration. All fluorescence polarisation values were measured (from the top) with a BioTeK Synergy H4 Plate Reader using a filter set with an excitation wavelength of 485 ± 20 nm and emission wavelength of 620 ± 40 nm, with a Xenon light source and gain set to 70. The plate used was a black polystyrene, clear bottomed, tissue culture treated polystyrene 96-well plate (Corning Inc. costar® 3605).

Aqueous silk fibroin was mixed with **SBP-TAMRA** (4 μM) at concentrations of 300.0, 150.0, 75.00, 37.50, 18.75, 9.375, 4.688, 2.344, and 0 μM. The silk fibroin concentrations were calculated based on an average molecular weight of 100 kDa. The mixture was plated in triplicate into the 96-well plate fluorescence polarisation data collected. A one site model, including a non-specific adsorption factor, was used to fit the fluorescence polarisation data with GraphPad Prism 8 software, to give a calculated K_d of 35.9 μM for **SBP-TAMRA** to silk fibroin (see Supporting Information Figure S2.5).

2.5.4 Fibre coating

A mixture of aqueous silk fibroin (65 mg/mL, 100 μL, average molecular weight 100kDa), distilled water (80 μL), and peptide (**SBP-TAMRA** or **SBP-SNARF**, 100 μM, 20 μL) was gently mixed by pipette until homogeneous. 1-2 mm of the OCT capable optical fibre tip (as described in section 2.3.1 above) was dipped into the silk mixture for 30 s, then removed. The silk fibroin coated fibre was then dipped into 90% aq. HPLC grade methanol for 10 s to convert the silk secondary structure from the silk I α-helix to the silk II β-sheet,[52,53] then the fibre removed and dried in air for at least 10 s before use.

The functionalised SBP was replaced with free TAMRA (100 μM, 20 μL) or water (20 μL) for control experiments to demonstrate the importance of the SBP component in retention of the fluorophore within the silk fibroin coating (see Figure 2.3).

The fibre dip-coating time was optimised to 30 s and silk fibroin concentration to 32.5 mg/mL, and the peptide concentration (SBP-TAMRA or SBP-SNARF) of 100 μM was chosen to maximise the fluorescence response of the final probe. This concentration is the solubility limit of the peptides in water and therefore cannot be exceeded.

2.5.5 Optical fibre characterisation

The OCT capable fibre, prepared as described in Experimental Section 2.5.2, was mounted onto custom designed holder-stage units to ensure that the optical beam from the probe was incident normal to the CMOS chip (WinCamD-XHR-1310, DataRay Inc., USA). Beam profiles were collected while the camera was moved axially away (i.e., in the direction of the light beam) by a linear translation stage (M2DU-50, DataRay Inc., USA) to step through the imaging beam waist at a distance of 0 to 1 mm (See Figure 2.2).

Scanning electron microscopy (SEM, see Figure 2.2) of the silk coated fibres was performed on a Quanta 450 scanning electron microscope in secondary electron (SE) mode, with energy dispersive X-ray (EDX) spectra also collected. Samples were dry loaded onto adhesive carbon tabs on aluminium stubs and coated with a 5 nm Pt coating. The electron beam voltage was held at 5.00 keV for SE and EDX measurements, with a working distance between 9.5 and 10.5 mm, spot size of 4, and images taken at 1500x (end on). EDX spectra were collected with an Oxford Instruments Ultim Max 170 EDX attachment on the Quanta 450 and analysed using the inbuilt Aztec software (Oxford Instruments).

3D contour plots of the optical fibre tips were collected using a Bruker Contour GT optical profilometer equipped with a 20x objective (see Figure 2.2). A section of bare or silk-coated fibre was attached to a metal mount with sticky tape such that the fibre tip was pointing directly up toward the microscope objective. The mean roughness parameter S_a was calculated for each fibre using the Vision64 program.

2.5.6 *In vitro* fertilisation experiments

Eagle's minimum essential medium alpha formulation (αMEM) was prepared from powder containing Earle's salts and non-essential amino acids and excluding L-glutamine, phenol red and

sodium bicarbonate to use as culture media for the IVF experiments. Fresh sodium bicarbonate, gentamicin, and glutamax were added to supplement the media, and HEPES acid and HEPES salt (sodium) were added to stabilise the pH without gas buffering. Bovine serum albumin (BSA, MP Biomedicals, Solon, Ohio, 3 mg/mL) was added fresh to the media immediately before use for each replicate.

Fresh αMEM as prepared above, was added to five separate Eppendorf tubes each containing 500 µL to obtain the pH calibration standard solutions. Two tubes were treated with 1 M HCl (2.5 µL or 5 µL), two were treated with 1 M NaOH (2.5 µL or 5 µL), and then all tubes were made up to a final volume of 505 µL using distilled water.

All experiments were approved by The University of Adelaide Animal Ethics Committee (M-2018-008) and were conducted in accordance with the Australian Code of Practice for the Care and Use of Animals for Scientific Purposes. Pre-pubertal CBA × C57Bl/6 F1 hybrid mice (3-4 weeks old) at 9 to 11 g were housed within the Laboratory Animal Services (University of Adelaide, Australia) under controlled temperature, and photoperiod (12 h light:12 h dark) with water and feed provided ad libitum. Pre pubertal female mice were hyperstimulated with 5 IU equine chorionic gonadotropin (eCG; Folligon, Intervet, Boxmeer, The Netherlands) via intra-peritoneal administration. 46 h later mice were culled via cervical dislocation. Two 1 mL insulin needles were used to puncture the ovarian follicles to harvest the immature COCs, which were randomly allocated to the blinded treatment groups (untreated and treated with 100 µM $CoCl_2$). Ovaries that were not punctured were harvested placed in 5 mL round bottom Eppendorf tubes containing 2 mL of αMEM handling medium with BSA that had been pre-heated at 37 °C for 2 h.

A Nikon Eclipse TE2000-E inverse microscope (Nikon Instruments, Inc., Melville, New York) with a Nikon Digital Sight DS-U3 camera attached and Nikon NIS Elements Freeware v4 32 bit was used to visualise the probe and COCs. An Eppendorf TransferMan NK2 micro-manipulator (Eppendorf, Hamburg, Germany) was used to position the OCTpH probe in the 25 µL drops of culture medium. Optical images were taken at 10x magnification.

2.5.7 Ovary imaging

The dual OCT imaging and fluorescence system described in section 4.2 was used for ovary imaging. Custom software allowing simultaneous acquisition of both imaging and sensing channels was implemented in the C++ language. An excised ovary was placed into a petri dish on a heating stage set at 37 °C ± 0.5 °C. By manually translating the fibre probe, a 2D image was acquired showing the tissue microarchitecture immediately adjacent to the distal end of the fibre probe (see Figure 2.4).

2.5.8 Dual OCT imaging and pH sensing of cumulus-oocyte complexes

Immature COCs, collected as described above, were randomly allocated to blinded 25 µL drops of culture media under paraffin oil (20 COCs per drop). COCs were cultured in the presence (treated) or absence (untreated) of 100 µM $CoCl_2$. COCs were incubated at 37 °C for 4 h, then moved to the heated microscope stage for OCT imaging and pH sensing measurements, where the probe was moved between drops using a micro-manipulator. A 2D OCT image of the COCs was obtained in the same manner as described for the ovary imaging (see Figure 2.5C). The distance between the fibre tip and an individual COC was measured by acquisition of continuous OCT A-scans in M-mode imaging while the fibre was moved toward to the oocyte (see Figure 2.5E). In the M-mode imaging, OCT A-scans were acquired at a frequency of 5.5 kHz to avoid oversampling.

Fluorescence spectra were collected using the fibre-coupled laser system as described above, where the OCTpH probe was first pre-bleached for 100 irradiations as discussed in the main text. The total intensity was integrated between the two ranges of 575-620 nm and 620-690 nm, and the fluorescence ratio calculated. A calibration curve for fluorescence ratio to pH was constructed using 25 µL drops of the calibration media (preparation described in Experimental Section 2.5.6) in the same petri dish as the COCs. Fluorescence spectra were then collected in the COC containing drops, blinded with respect to the presence or absence of $CoCl_2$. The pH of each drop was calculated from the calibration curve, then assigned to the $CoCl_2$ treated or untreated group before being unblinded (see Figure 2.5A).

2.6 Acknowledgements

PKC and JL contributed equally to this work. The authors acknowledge helpful discussions with Dr. Georgina Sylvia, Dr. Hanna McLennan, and Dr. Anwar Sunna, and support from the Australian National Fabrication Facility (ANFF) Optofab node director Prof. Heike Ebendorff-Heidepriem in submission to this ANFF special issue. PKC would like to thank Adelaide Microscopy and Ken Neubauer for assistance with SEM and EDX analysis, Philip Clements for assistance with NMR collection and analysis, and Alson Ng for assistance with the optical profilometer measurements. This work is supported by the Australian Research Council (ARC) Centre of Excellence for Nanoscale BioPhotonics (CE140100003). The IVF component of this work was supported in part by Cook Medical Pty Ltd and an ARC Linkage grant (LP 110200736). PKC acknowledges PhD scholarship support from MF and MH Joyner, and Patricia and Norman Polglase. JL is supported by a Postdoctoral Fellowship (102093) from the National Heart Foundation and an NHMRC Ideas grant (2001646). AJH is supported by an Australian Government Research Training Program Stipend. SY acknowledges PhD support from the CNBP and the Robinson Research Institute. EPS is supported by an ARC linkage grant LP150100657. AK acknowledges an RMIT Vice Chancellor's Research Fellowship for supporting silk fibroin research. KRD is supported by a Mid-career Fellowship from the Hospital Research Foundation (C-MCF-58-2019). RAM is supported by an NHMRC Development grant (APP1178912) and an NHMRC Ideas grant (2002254). This work was performed in part at the Optofab node of the ANFF utilising Commonwealth and SA State Government funding.

2.7 Conflicts of interest

RAM and RWK are co-founders and directors of Miniprobes Pty Ltd., a company that develops novel optical imaging systems. Miniprobes Pty Ltd. did not contribute to this study.

2.8 References

(1) U. Utzinger, R. R. Richards-Kortum, Fiber optic probes for biomedical optical spectroscopy. *J. Biomed. Opt.* **2003**, *8*, 121. https://doi.org/10.1117/1.1528207

(2) J. Li, H. Ebendorff-Heidepriem, B. C. Gibson, A. D. Greentree, M. R. Hutchinson, P. Jia, R. Kostecki, G. Liu, A. Orth, M. Ploschner, E. P. Schartner, S. C. Warren-Smith, K. Zhang, G. Tsiminis, E. M. Goldys, Perspective: Biomedical sensing and imaging with optical fibers—Innovation through convergence of science disciplines. *APL Photonics* **2018**, *3*, 100902. https://doi.org/10.1063/1.5040861

(3) L. Binetti, I. D. Villar, K. P. Dissanayake, A. Stankiewicz, T. Sun, K. T. V. Grattan, L. S. M. Alwis, Monitoring of the Critical Meniscus of Very Low Liquid Volumes Using an Optical Fiber Sensor. *IEEE Sens. J.* **2020**, *20*, 12232. https://doi.org/10.1109/JSEN.2020.2999537

(4) J. Li, B. C. Quirk, P. B. Noble, R. W. Kirk, D. D. Sampson, R. A. McLaughlin, Flexible needle with integrated optical coherence tomography probe for imaging during transbronchial tissue aspiration. *J. Biomed. Opt.* **2017**, *22*, 106002. https://doi.org/10.1117/1.JBO.22.10.106002

(5) X. Wang, O. S. Wolfbeis, Fiber-Optic Chemical Sensors and Biosensors (2013–2015). *Anal. Chem.* **2016**, *88*, 203. https://doi.org/10.1021/acs.analchem.5b04298

(6) X. Wang, O. S. Wolfbeis, Fiber-Optic Chemical Sensors and Biosensors (2015–2019). *Anal. Chem.* **2020**, *92*, 397. https://doi.org/10.1021/acs.analchem.9b04708

(7) J. L. Gehrich, D. W. Lubbers, N. Opitz, D. R. Hansmann, W. W. Miller, J. K. Tusa, M. Yafuso, Optical Fluorescence and Its Application to an Intravascular Blood Gas Monitoring System. *IEEE Trans. Biomed. Eng.* **1986**, *BME-33*, 117. https://doi.org/10.1109/TBME.1986.325886

(8) M. Ganter, A. Zollinger, Continuous intravascular blood gas monitoring: development, current techniques, and clinical use of a commercial device. *BJA: Br. J. Anaesth.* **2003**, *91*, 397. https://doi.org/10.1093/bja/aeg176

(9) K. S. Bronk, K. L. Michael, Paul. Pantano, D. R. Walt, *Combined Imaging and Chemical Sensing Using a Single Optical Imaging Fiber. Chem.* **1995**, *67*, 2750. https://doi.org/10.1021/ac00113a005

(10) J. P. Issberner, C. L. Schauer, B. A. Trimmer, D. R. Walt, Combined imaging and chemical sensing of l-glutamate release from the foregut plexus of the Lepidopteran, Manduca sexta. *J. Neurosci. Methods* **2002**, *120*, 1. https://doi.org/10.1016/S0165-0270(02)00165-6

(11) K. L. Michael, D. R. Walt, Combined Imaging and Chemical Sensing of Fertilization-Induced Acid Release from Single Sea Urchin Eggs. *Anal. Biochem.* **1999**, *273*, 168. https://doi.org/10.1006/abio.1999.4173

(12) J. Li, E. Schartner, S. Musolino, B. C. Quirk, R. W. Kirk, H. Ebendorff-Heidepriem, R. A. McLaughlin, Miniaturized single-fiber-based needle probe for combined imaging and sensing in deep tissue. *Opt. Lett.* **2018**, *43*, 1682. https://doi.org/10.1364/OL.43.001682

(13) Stephen A. Boppart, Brett E. Bouma, Costas Pitris, James F. Southern, Mark E. Brezinski, James G. Fujimoto, In vivo cellular optical coherence tomography imaging. *Nat. Med.* **1998**, *4*, 861. https://doi.org/10.1038/nm0798-861

(14) B. E. Bouma, M. Villiger, K. Otsuka, W.-Y. Oh, Intravascular optical coherence tomography. *Biomed. Opt. Express* **2017**, *8*, 2660. https://doi.org/10.1364/BOE.8.002660

(15) H. Ramakonar, B. C. Quirk, R. W. Kirk, J. Li, A. Jacques, C. R. P. Lind, R. A. McLaughlin, Intraoperative detection of blood vessels with an imaging needle during neurosurgery in humans. *Sci. Adv.* **2018**, *4*, eaav4992. https://doi.org/10.1126/sciadv.aav4992

(16) M. S. Purdey, E. P. Schartner, M. L. Sutton-McDowall, L. J. Ritter, J. Thompson, T. M. Monro, A. D. Abell, Localised hydrogen peroxide sensing for reproductive health. PRoc. SPIE 9506, *Optical Sensors 2015*, **2015**, p. 950614. https://doi.org/10.1117/12.2178680

(17) A. Bachhuka, S. Heng, K. Vasilev, R. Kostecki, A. Abell, H. Ebendorff-Heidepriem, Surface Functionalization of Exposed Core Glass Optical Fiber for Metal Ion Sensing. *Sensors* **2019**, *19*, 1829. https://doi.org/10.3390/s19081829

(18) S. C. Warren-Smith, S. Heng, H. Ebendorff-Heidepriem, A. D. Abell, T. M. Monro, Fluorescence-Based Aluminum Ion Sensing Using a Surface-Functionalized Microstructured Optical Fiber. *Langmuir* **2011**, *27*, 5680. https://doi.org/10.1021/la2002496

(19) S. Heng, M.-C. Nguyen, R. Kostecki, T. M. Monro, A. D. Abell, Nanoliter-scale, regenerable ion sensor: sensing with a surface functionalized microstructured optical fibre. *RSC Adv.* **2013**, *3*, 8308. https://doi.org/10.1039/C3RA40321A

(20) T. H. Nguyen, T. Sun, K. T. V. Grattan, A Turn-On Fluorescence-Based Fibre Optic Sensor for the Detection of Mercury. *Sensors* **2019**, *19*, 2142. https://doi.org/10.3390/s19092142

(21) J.-D. Hong, E.-S. Park, A.-L. Park, Effects of Added Salt on Photochemical Isomerization of Azobenzene in Alternate Multilayer Assemblies: Bipolar Amphiphile−Polyelectrolyte. *Langmuir* **1999**, *15*, 6515. https://doi.org/10.1021/la990265v

(22) C. Elosua, C. Bariain, I. R. Matias, A. Rodriguez, E. Colacio, A. Salinas-Castillo, A. Segura-Carretero, A. Fernandez-Gutiérrez, Pyridine Vapors Detection by an Optical Fibre Sensor. *Sensors* **2008**, *8*, 847. https://doi.org/10.3390/s8020847

(23) M. Purdey, J. Thompson, T. Monro, A. Abell, E. Schartner, A Dual Sensor for pH and Hydrogen Peroxide Using Polymer-Coated Optical Fibre Tips. *Sensors* **2015**, *15*, 31904. https://doi.org/10.3390/s151229893

(24) E. P. Schartner, M. R. Henderson, M. Purdey, D. Dhatrak, T. M. Monro, P. G. Gill, D. F. Callen, Cancer Detection in Human Tissue Samples Using a Fiber-Tip pH Probe. *Cancer Res.* **2016**, *76*, 6795. https://doi.org/10.1158/0008-5472.CAN-16-1285

(25) H. J. McLennan, A. Saini, G. M. Sylvia, E. P. Schartner, K. R. Dunning, M. S. Purdey, T. M. Monro, A. D. Abell, J. G. Thompson, A biophotonic approach to measure pH in small volumes in vitro: Quantifiable differences in metabolic flux around the cumulus-oocyte-complex (COC). *J. Biophotonics* **2020**, *13*, e201960038. https://doi.org/10.1002/jbio.201960038

(26) J. E. Whitaker, R. P. Haugland, F. G. Prendergast, Spectral and photophysical studies of benzo[c]xanthene dyes: Dual emission pH sensors. *Anal. Biochem.* **1991**, *194*, 330. https://doi.org/10.1016/0003-2697(91)90237-N

(27) Y. Nomura, V. Sharma, A. Yamamura, Y. Yokobayashi, Selection of silk-binding peptides by phage display. *Biotechnol. Lett.* **2011**, *33*, 1069. https://doi.org/10.1007/s10529-011-0519-6

(28) A. Khalid, L. Peng, A. Arman, S. C. Warren-Smith, E. P. Schartner, G. M. Sylvia, M. R. Hutchinson, H. Ebendorff-Heidepriem, R. A. McLaughlin, B. C. Gibson, J. Li, Silk: A bio-derived coating for optical fiber sensing applications. *Sens. Actuators B Chem.* **2020**, *311*, 127864. https://doi.org/10.1016/j.snb.2020.127864

(29) H. Perry, A. Gopinath, D. L. Kaplan, L. D. Negro, F. G. Omenetto, Nano- and Micropatterning of Optically Transparent, Mechanically Robust, Biocompatible Silk Fibroin Films. *Adv. Mater.* **2008**, *20*, 3070. https://doi.org/https://doi.org/10.1002/adma.200800011

(30) K. Min, M. Umar, S. Ryu, S. Lee, S. Kim, Silk protein as a new optically transparent adhesion layer for an ultra-smooth sub-10 nm gold layer. *Nanotechnology* **2017**, *28*, 115201. https://doi.org/10.1088/1361-6528/aa5aaa

(31) G. H. Altman, F. Diaz, C. Jakuba, T. Calabro, R. L. Horan, J. Chen, H. Lu, J. Richmond, D. L. Kaplan, Silk-based biomaterials. *Biomaterials* **2003**, *24*, 401. https://doi.org/10.1016/S0142-9612(02)00353-8

(32) C. Vepari, D. L. Kaplan, Silk as a biomaterial. *Prog. Polym. Sci.* **2007**, *32*, 991. https://doi.org/10.1016/j.progpolymsci.2007.05.013

(33) A. R. Murphy, D. L. Kaplan, Biomedical applications of chemically-modified silk fibroin. *J. Mater. Chem.* **2009**, *19*, 6443. https://doi.org/10.1039/b905802h

(34) C. Holland, K. Numata, J. Rnjak-Kovacina, F. P. Seib, The Biomedical Use of Silk: Past, Present, Future. *Adv. Healthc. Mater.* **2019**, *8*, 1800465. https://doi.org/10.1002/adhm.201800465

(35) M. Monici, Cell and tissue autofluorescence research and diagnostic applications. In *Biotechnology Annual Review*, Elsevier, **2005**, pp. 227-256.

(36) V. Estrella, T. Chen, M. Lloyd, J. Wojtkowiak, H. H. Cornnell, A. Ibrahim-Hashim, K. Bailey, Y. Balagurunathan, J. M. Rothberg, B. F. Sloane, J. Johnson, R. A. Gatenby, R. J. Gillies, Acidity Generated by the Tumor Microenvironment Drives Local Invasion. *Cancer Res.* **2013**, *73*, 1524. https://doi.org/10.1158/0008-5472.CAN-12-2796

(37) M. Anderson, A. Moshnikova, D. M. Engelman, Y. K. Reshetnyak, O. A. Andreev, Probe for the measurement of cell surface pH in vivo and ex vivo. *Proc. Natl. Acad. Sci.* **2016**, *113*, 8177. https://doi.org/10.1073/pnas.1608247113

(38) L. Scolaro, D. Lorenser, W.-J. Madore, R. W. Kirk, A. S. Kramer, G. C. Yeoh, N. Godbout, D. D. Sampson, C. Boudoux, R. A. McLaughlin, Molecular imaging needles: dual-modality optical coherence tomography and fluorescence imaging of labeled antibodies deep in tissue. *Biomed. Opt. Express* **2015**, *6*, 1767. https://doi.org/10.1364/BOE.6.001767

(39) A. Care, P. L. Bergquist, A. Sunna, Solid-binding peptides: smart tools for nanobiotechnology. *Trends Biotechnol.* **2015**, *33*, 259. https://doi.org/10.1016/j.tibtech.2015.02.005

(40) Thorlabs - DCF13 Double-clad fibre, Ø105 µm core, Ø125 µm cladding, Single mode (core): 0.12 NA, 1250 - 1600 nm; Multimode (cladding): 0.2NA, 400-2200nm.

(41) M. Myers, K. L. Britt, N. G. M. Wreford, F. J. P. Ebling, J. B. Kerr, Methods for quantifying follicular numbers within the mouse ovary. *Reproduction* **2004**, *127*, 569. https://doi.org/10.1530/rep.1.00095

(42) G. FitzHarris, J. M. Baltz, Regulation of intracellular pH during oocyte growth and maturation in mammals. *Reproduction* **2009**, *138*, 619. https://doi.org/10.1530/REP-09-0112

(43) D. Richani, K. R. Dunning, J. G. Thompson, R. B. Gilchrist, Metabolic co-dependence of the oocyte and cumulus cells: essential role in determining oocyte developmental competence. *Hum. Reprod. Update* **2020**, dma0043. https://doi.org/10.1093/humupd/dmaa043

(44) T. Boissenot, A. Bordat, E. Fattal, N. Tsapis, Ultrasound-triggered drug delivery for cancer treatment using drug delivery systems: From theoretical considerations to practical applications. *J. Controlled Release* **2016**, *241*, 144. https://doi.org/10.1016/j.jconrel.2016.09.026

(45) E. Di Naro, L. Raio, A. Basso, M. R. Catalano, In *Pick Up and Oocyte Management* (Eds.: Malvasi, A.; Baldini, D.), Springer International Publishing, Cham, **2020**, pp. 49-72. https://doi.org/

(46) A. K. Ludwig, M. Glawatz, G. Griesinger, K. Diedrich, M. Ludwig, Perioperative and post-operative complications of transvaginal ultrasound-guided oocyte retrieval: prospective study of >1000 oocyte retrievals. *Hum. Reprod.* **2006**, *21*, 3235. https://doi.org/10.1093/humrep/del278

(47) R. Singh, K. D. Sinclair, Metabolomics: Approaches to assessing oocyte and embryo quality. *Theriogenology* **2007**, *68*, S56. https://doi.org/10.1016/j.theriogenology.2007.04.007

(48) D. E. Clapham, Calcium Signaling. *Cell* **2007**, *131*, 1047. https://doi.org/10.1016/j.cell.2007.11.028

(49) N. W. Lutz, Y. L. Fur, J. Chiche, J. Pouysségur, P. J. Cozzone, Quantitative In Vivo Characterization of Intracellular and Extracellular pH Profiles in Heterogeneous Tumors: A Novel Method Enabling Multiparametric pH Analysis. *Cancer Res.* **2013**, *73*, 4616. https://doi.org/10.1158/0008-5472.CAN-13-0767

(50) invitrogen, In *The Molecular Probes Handbook: A Guide to Fluorescent Probes and Labelling Technologies*, Thermofisher, **2010**.

(51) A. Khalid, R. Lodin, P. Domachuk, H. Tao, J. E. Moreau, D. L. Kaplan, F. G. Omenetto, B. C. Gibson, S. Tomljenovic-Hanic, Synthesis and characterization of biocompatible nanodiamond-silk hybrid material. *Biomed. Opt. Express* **2014**, *5*, 596. https://doi.org/10.1364/BOE.5.000596

(52) D. Huemmerich, U. Slotta, T. Scheibel, Processing and modification of films made from recombinant spider silk proteins. *Appl. Phys. A* **2006**, *82*, 219. https://doi.org/10.1007/s00339-005-3428-5

(53) Y. Qi, H. Wang, K. Wei, Y. Yang, R.-Y. Zheng, I. S. Kim, K.-Q. Zhang, A Review of Structure Construction of Silk Fibroin Biomaterials from Single Structures to Multi-Level Structures. *Int. J. Mol. Sci.* **2017**, *18*, 237. https://doi.org/10.3390/ijms18030237

(54) R. Hirayama, M. Kawase, T. Kimachi, K. Tanaka, F. Yoneda, The autorecycling oxidation of benzylamine by synthetic 8-hydroxy-5-deazaflavin derivatives. *J. Heterocycl. Chem.* **1989**, *26*, 1255. https://doi.org/10.1002/jhet.5570260509

(55) D. Srikun, A. E. Albers, C. J. Chang, A dendrimer-based platform for simultaneous dual fluorescence imaging of hydrogen peroxide and pH gradients produced in living cells. *Chem. Sci.* **2011**, *2*, 1156. https://doi.org/10.1039/c1sc00064k

(56) W. S. Hancock, J. E. Battersby, A new micro-test for the detection of incomplete coupling reactions in solid-phase peptide synthesis using 2,4,6-trinitrobenzene-sulphonic acid. *Anal. Biochem.* **1976**, *71*, 260. https://doi.org/10.1016/0003-2697(76)90034-8

Supporting Information

S2.1 Synthesis of 5(6)-carboxySNARF2

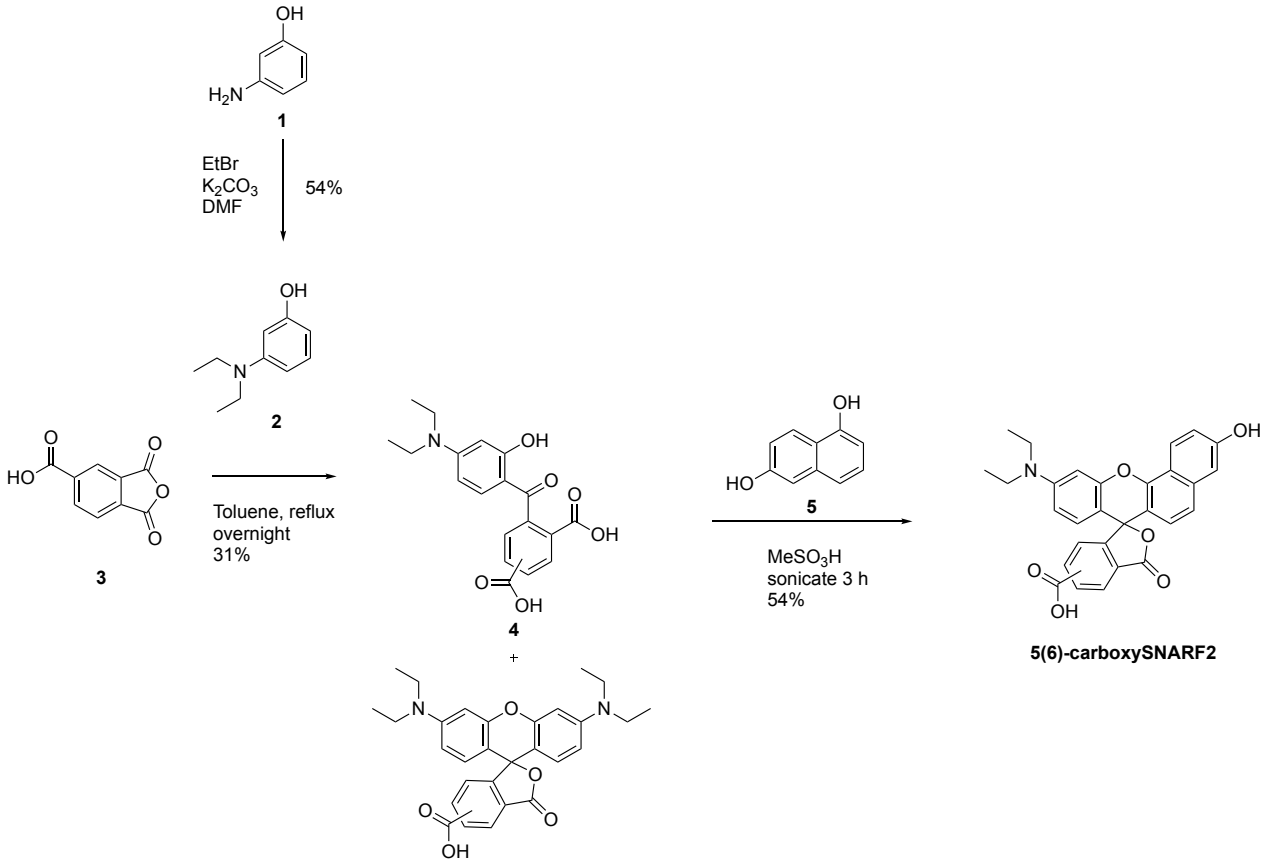

Scheme S2.1. Synthetic pathway to 5(6)-carboxySNARF2. No yield was recorded for the 5(6)-carboxy-rhodamine B by-product.

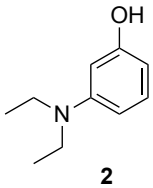

2

3-Aminophenol (**1**, 4.00 g, 37.0 mmol, 1.00 equiv) was dissolved in DMF (25 mL) and K_2CO_3 (10.7 g, 77.7 mmol, 2.10 equiv) added. Ethylbromide (5.76 mL, 77.7 mmol, 2.10 equiv) was added and the reaction mixture heated at 100 °C for 3 h then cooled to rt. Water (200 mL) was added and

the mixture was extracted with diethyl ether (3 × 100 mL). The combined organic layers were dried over $MgSO_4$, filtered, and solvent removed from the filtrate under reduced pressure to give a dark green-brown oil (5 g). The crude oil was purified in portions (1.0 g) by flash column chromatography on silica (9:1 to 4:1 (v/v) petroleum spirit/ethyl acetate) to give 3-diethylaminophenol (**2**) as a blue oil (0.67 g, 4.0 mmol, 54%). NMR was consistent with literature:[54] ^{1}H NMR (500 MHz, $CDCl_3$) δ 7.06 (t, *J* = 8.1 Hz, 1H), 6.28 (d, *J* = 8.3 Hz, 1H), 6.18 (s, 1H), 6.12 (d, *J* = 7.8 Hz, 1H), 4.58 (s, 1H), 3.33 (q, *J* = 7.0 Hz, 4H), 1.16 (t, *J* = 7.1 Hz, 6H) ppm.

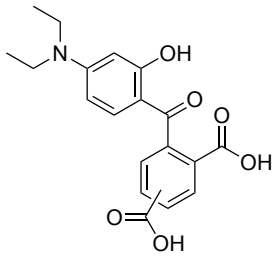

4

3-Diethylaminophenol (**2**, 1.33 g, 8.00 mmol, 1.00 equiv) and 1,2,4-benzenetricaboxylic anhydride (**3**, 1.55 g, 8.00 mmol, 1.00 equiv) were dissolved in toluene (100 mL). The reaction mixture was heated to reflux overnight, cooled to rt and the solid precipitate was collected by vacuum filtration. This was washed extensively with dichloromethane, then the residue dissolved in methanol. The methanol was removed under reduced pressure and the resultant solid purified by squat column chromatography on silica (1% (v/v) acetic acid/ethyl acetate) to remove 5(6)-carboxy-rhodamine B. The enriched solid was taken up in ethyl acetate (40 mL) and extracted with 1 M sodium hydroxide (2 × 30 mL) to remove starting material **3**. The combined aqueous phases were acidified to pH 1 with 32% hydrochloric acid, and the resulting yellow precipitate isolated by filtration. The acidified aqueous layer was extracted with ethyl acetate (2 × 30 mL) and the combined organic layers were dried over $MgSO_4$ and filtered. Solvent was removed from the filtrate under reduced pressure to give a yellow solid, which was combined with the yellow precipitate obtained earlier, to give a mixture of 2-(4-(diethylamino)-2-hydroxybenzoyl) terephthalic acid and 4-(4-(diethylamino)-2-hydroxybenzoyl)isophthalic acid (**4**) as a yellow solid (0.88 g, 2.5 mmol, 31%). NMR was consistent with a mixture of the two structural isomers with the carboxylic acid at the 5 or 6 position, as per literature:[55] ^{1}H NMR (500 MHz, d_6-acetone) δ

8.72 (d, *J* = 1.6 Hz, 1H), 8.32 (dd, *J* = 7.9, 1.7 Hz, 1H), 8.24 (dd, *J* = 8.1, 1.7 Hz, 1H), 8.00 (d, *J* = 1.7 Hz, 1H), 7.56 (d, *J* = 7.9 Hz, 1H), 6.89 (d, *J* = 9.2 Hz, 1H), 6.24-6.17 (m, 2H), 6.13-6.09 (m, 2H), 3.47 (q, *J* = 7.1 Hz, 8H), 1.18 (t, *J* = 7.1 Hz, 12H) ppm.

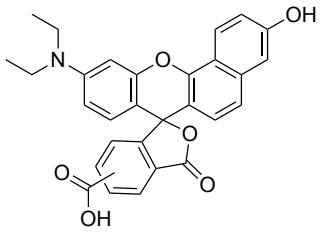

5(6)-carboxySNARF2

The isomeric mixture of **4** (500 mg, 1.38 mmol, 1.00 equiv) and 1,6-dihydroxynapthalene (**5**, 263 mg, 13.8 mmol, 10.0 equiv) were added to an 8 mL capacity glass vial with a screw cap. Methanesulfonic acid (6.0 mL) was added and the sealed vial was sonicated for 3 h. The resulting dark mixture was poured onto an ice-water slurry (150 mL) and the purple precipitate collected by gravity filtration. The crude solid was purified by flash column chromatography on silica (1% (v/v) acetic acid/ethyl acetate to 10% (v/v) methanol/ethyl acetate) to give 5(6)-carboxySNARF2 as a purple solid (368 mg, 0.76 mmol, 54%). NMR was consistent with a mixture of the two structural isomers with the carboxylic acid at the 5 or 6 position, as per literature:[55] ^{1}H NMR (500 MHz, d_6-acetone) δ 8.61-8.54 (m, 1H), 8.50 (dd, *J* = 8.9, 3.7 Hz, 1H), 8.40-8.31 (m, 2H), 8.16-8.10 (m, 1H), 7.85 (s, 1H), 7.37 (d, *J* = 8.8 Hz, 2H), 7.32 (dd, *J* = 9.1, 2.5 Hz, 2H), 7.24 (t, *J* = 2.5 Hz, 2H), 7.16-7.06 (m, 1H), 6.81 (t, *J* = 2.3 Hz, 2H), 6.75 (dd, *J* = 8.7, 3.1 Hz, 2H), 6.70 (dd, *J* = 8.9, 2.7 Hz, 2H), 3.48 (q, *J* = 7.0 Hz 8H), 1.20 (t, *J* = 7.1 Hz, 12H). MS (ESI+) expected $[M+H]^+$ for $C_{29}H_{23}NO_6$ 482.2, found 482.3.

S2.2 Peptide synthesis

General SPPS procedure

Peptides were assembled by solid phase peptide synthesis (SPPS) using a standard Fmoc/tBu protocol, as follows. Rink Amide PL resin (645 mg, 0.20 mmol, 0.31 mmol/g, Agilent) was swollen in 1:1 (v/v) DCM/DMF (10 mL) for 15 min, the solution was drained and the resin washed with DMF (3 × 8 mL). The resin-bound Fmoc protecting group was then removed by treatment of the resin with 20% (v/v) piperidine in DMF (8 mL) for 10 min, with intermittent stirring. The resulting

solution was drained and the resin successively washed with DMF (3 × 8 mL), DCM (3 × 8 mL), and DMF (3 × 8 mL). A solution of the relevant *N*-terminally Fmoc-protected building block (5 equiv), HATU (5 equiv) and DIPEA (10 equiv) in DMF (10 mL) was added to the resin and allowed to react for 1 h, with intermittent stirring. The resulting solution was drained and the resin successively washed with DMF (3 × 8 mL), DCM (3 × 8 mL), and DMF (3 × 8 mL). The *N*-terminal Fmoc group was subsequently removed by treatment of the resin with 20% (v/v) piperidine in DMF (10 mL) for 10 min with intermittent stirring. A TNBS test (see below) was used to verify that each coupling/deprotection step was successful, with retreatment as necessary. Successive couplings and Fmoc-deprotections were repeated to achieve the desired peptide sequence. After the final Fmoc-deprotection with 20% (v/v) piperidine in DMF (10 mL) for 10 min, the solution was drained and the resin washed with DMF (3 × 5 mL) and DCM (3 × 5 mL) and then washed with diethyl ether (3 × 8 mL) to deswell the resin, and air-dried with vacuum.

*TNBS Test:[56] A small spatula of swollen resin was removed and 1 drop each of TNBS solution (100 µL 5% (w/v) picrylsulfonic acid in H_2O added to 900 µL of DMF) and DIPEA solution (100 µL in 900 µL of DMF) were added, and the resin allowed to develop for 1 min. Clear/yellow beads indicated no free amine (negative, observed post successful coupling), and red/orange beads showed free amine (positive, observed post successful deprotection).

General resin cleavage procedure

The peptide was cleaved from the dried resin (and all amino acid side chains simultaneously deprotected) by addition of a cleavage cocktail consisting of 92.5:2.5:2.5:2.5 (v/v) trifluoroacetic acid/triisopropylsilane/2,2'-(ethylenedioxy)diethanethiol/water (10 mL), and the suspension was placed on a table rocker for 1 h. The solution was pipetted away from the resin and concentrated to 1-1.5 mL under a stream of N_2. Diethyl ether (10 mL) was added to the concentrated solution and the mixture cooled at -20°C overnight. The resulting precipitate was pelleted by centrifugation (7,800 rpm, 15 min) and the supernatant decanted. The remaining solid was dried under a stream of N_2, dissolved in 1:1 (v/v) acetontrile:water, syringe filtered (20 µm PTFE syringe filter) and lyophilised to give the crude peptide as a fluffy solid.

General peptide purification and characterisation procedure

Crude peptides were purified by semi-preparative RP-HPLC on a Gilson GX-Prep RP-HPLC system equipped with a Phenomenex Luna™ 5 µm Peptide XB-C18 100 Å 10 × 250 mm column over a linear 25-50% gradient of ACN (B) in water (A) with 0.1% trifluoroacetic acid over 25 min. Pure fractions were combined and lyophilised to give the final product. Product purity was confirmed to be >85% by analytical RP-HPLC on an Agilent Infinity 1260 analytical HPLC equipped with a Phenomenex Luna™ C18(2) 100 Å 4.6 × 250 mm column over a linear gradient of 5-50% B over 15 min and visualised at 220 nm. Product identity was confirmed by high resolution mass spectrometry on an Agilent 6230 ESI MS.

SBP: H-SYTFHWHQSWSS-NH_2

The peptide with sequence SYTFHWHQSWSS (**SBP**)[27] was assembled on resin as per the *'General SPPS procedure'* and then cleaved from the resin as described in *'General resin cleavage procedure'*, detailed above. The crude peptide was purified as per the '*General peptide purification and characterisation procedure*' as detailed above, to provide **SBP** as a white solid. Analytical HPLC 98% purity (220 nm). HRMS (ESI+) expected $[M+H]^+$ for $C_{79}H_{101}N_{21}O_{20}$ 1664.7595, found $[M+H]^+$ 1664.7588.

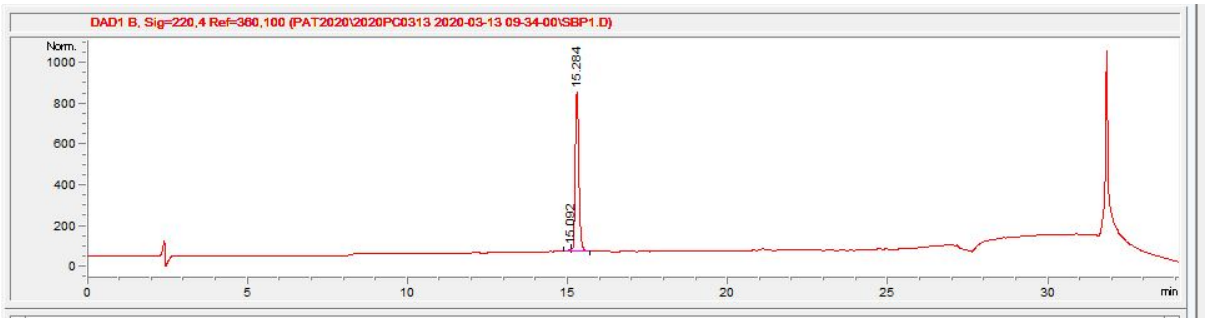

Figure S2.1. Analytical HPLC trace for the SBP run over a linear gradient of 5-50% ACN in H_2O with 0.1% TFA, from 5 min to 20 min, visualised at 220 nm.

SBP-TAMRA: TAMRA-Ahx-SYTFHWHQSWSS-NH2

The peptide with sequence Ahx-SYTFHWHQSWSS was assembled on resin as per the *'General SPPS procedure'*. Following *N*-terminal Fmoc deprotection, a portion of the peptide-loaded resin (0.05 mmol) was transferred to a microwave vial (7 mL capacity) using DMF (1-2 mL). A solution of 5(6)-carboxyTAMRA (64.6 mg, 0.15 mmol, 3 equiv), 1,3-diisopropylcarbodiimide (23.2 µL, 0.15

mmol, 3 equiv) and Oxyma (21.3 mg, 0.15 mmol, 3 equiv) in DMF (2 mL) was added, then DMF was used to rinse the fluorophore into the reaction vessel, to make a final reaction volume of 5 mL. The reaction vessel was heated by microwave irradiation to 60 °C for 30 min then cooled to rt. The resultant solution was drained and the resin washed extensively with DMF (5 × 10 mL) and DCM (5 × 5 mL) until no colour remained in the washings. No TNBS test was performed due to the residual purple/pink colour of the resin. The resin was then deswelled with diethyl ether (3 × 5 mL) and the crude peptide was cleaved from the resin and simultaneously globally deprotected according to the *'General resin cleavage procedure'* above. The crude peptide was purified as per the '*General peptide purification and characterisation procedure*' as detailed above, to provide **SBP-TAMRA** as a purple solid. Analytical HPLC 87% purity (220 nm). HRMS (ESI+) expected $[M+3H]^{3+}$ for $C_{104}H_{121}N_{23}O_{24}$ 692.9732, found $[M+3H]^{3+}$ 692.9732.

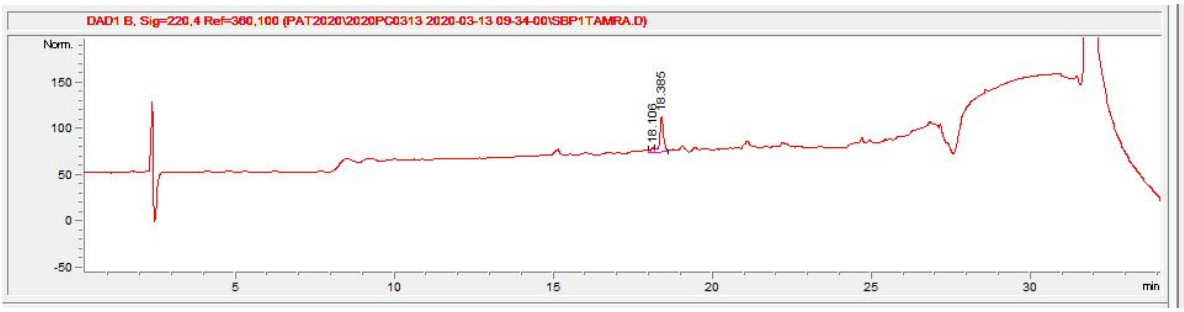

Figure S2.2. Analytical HPLC trace for SBP-TAMRA run over a linear gradient of 5-50% ACN in H_2O with 0.1% TFA, from 5 min to 20 min, visualised at 220 nm.

SBP-SNARF: SNARF-Ahx-SYTFHWHQSWSS-NH2

The peptide with sequence Ahx-SYTFHWHQSWSS was assembled on resin as per the *'General SPPS procedure'.* Following *N*-terminal Fmoc deprotection, a portion of the peptide-loaded resin (0.05 mmol) was transferred to a microwave vial (7 mL capacity) using DMF (1-2 mL). A solution of 5(6)-carboxySNARF (72.0 mg, 0.15 mmol, 3 equiv), 1,3-Diisopropylcarbodiimide (23.2 µL, 0.15 mmol, 3 equiv) and Oxyma (21.3 mg, 0.15 mmol, 3 equiv) in DMF (2 mL) was added, then DMF was used to rinse the fluorophore into the reaction vessel, to make a final reaction volume of 5 mL. The reaction vessel was heated by microwave irradiation to 60°C for 30 min then cooled to rt. The resultant solution was drained and the resin washed extensively with DMF (5 × 10 mL) and DCM (5 × 5 mL) until no colour remained in the washings. No TNBS test was performed due to the residual purple/pink colour of the resin. The resin was then deswelled with diethyl ether

(3 × 5 mL) and the crude peptide was cleaved from the resin and simultaneously globally deprotected according to the *'General resin cleavage procedure'* above. The crude peptide was purified as per the '*General peptide purification and characterisation procedure*' as detailed above, to provide **SBP-SNARF** as a purple solid. Analytical HPLC 93% purity (220 nm). HRMS (ESI+) expected $[M+3H]^{3+}$ for $C_{108}H_{122}N_{22}O_{25}$ 709.9730, found $[M+3H]^{3+}$ 709.9733.

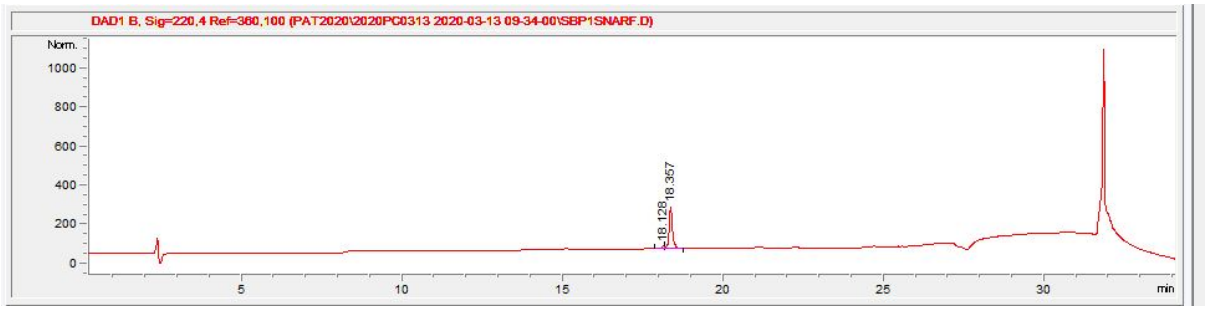

Figure S2.3. Analytical HPLC trace for SBP-SNARF run over a linear gradient of 5-50% ACN in H_2O with 0.1% TFA, from 5 min to 20 min, visualised at 220 nm.

S2.3 Laser system set up

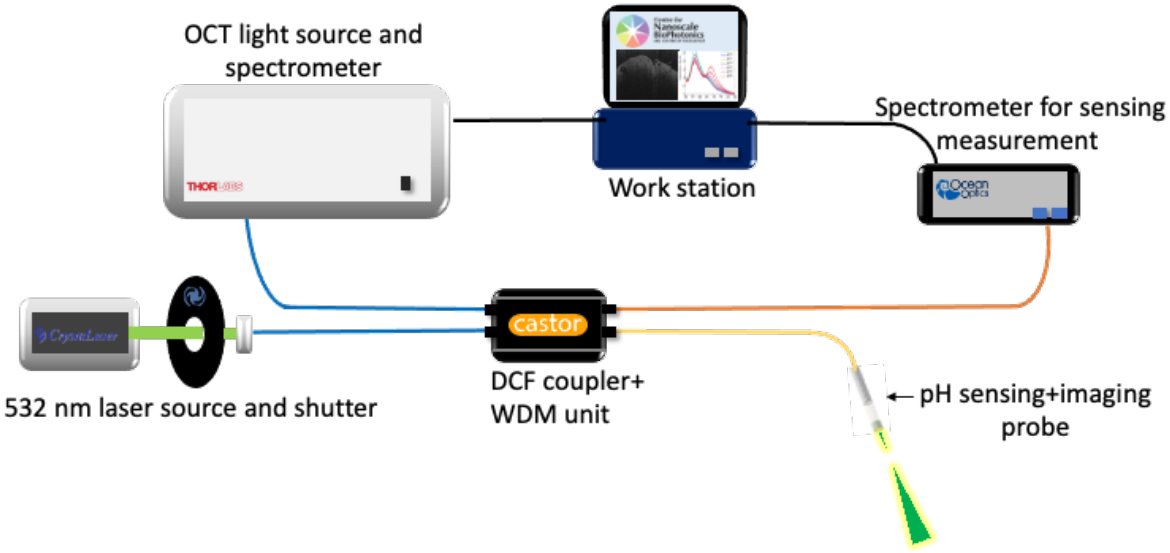

Figure S2.4. Schematic of the laser set up used. Blue line: single-mode fibre; orange line: multimode fibre; yellow line: double-clad fibre (DCF). WDM: Wavelength division multiplexer.

S2.4 Dissociation constant determination

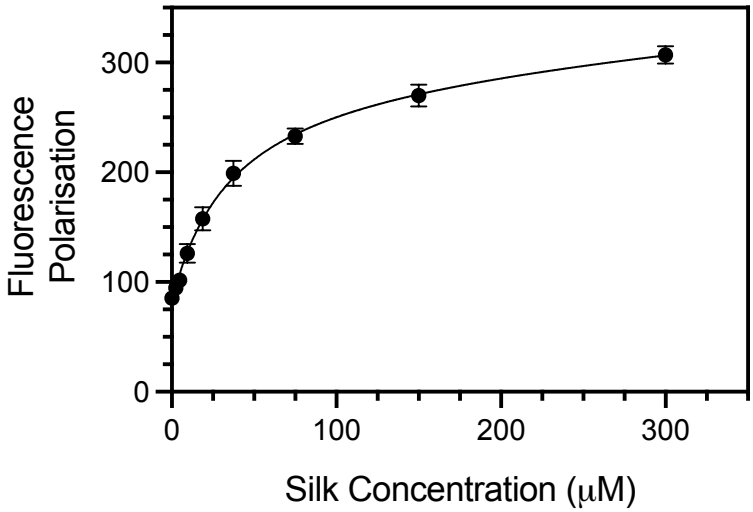

Y=Bmax*X/(Kd+X) + NS*X + Background

	Fluorescence Polarisation
Best-fit values	
Bmax	213.6
Kd	35.89
NS	0.1138
Background	81.57
95% CI (profile likelihood)	
Bmax	181.1 to 259.3
Kd	25.15 to 52.36
NS	-0.01124 to 0.2160
Background	74.72 to 88.20

Figure S2.5. Plot of fluorescence polarisation **of SBP-TAMRA** against silk fibroin concentration. A one site model, including a non-specific adsorption factor, was used to fit the data with GraphPad Prism 8 software, fitting parameters are shown in the table. The K_d was determined to be 35.9 μM with a 95% confidence interval of 25.2 to 52.4 μM. Error bars are standard deviations.

S2.5 Additional EDX spectra

As detailed in the main text, additional EDX spectra were collected at three locations for a bare fibre and a silk-coated fibre.

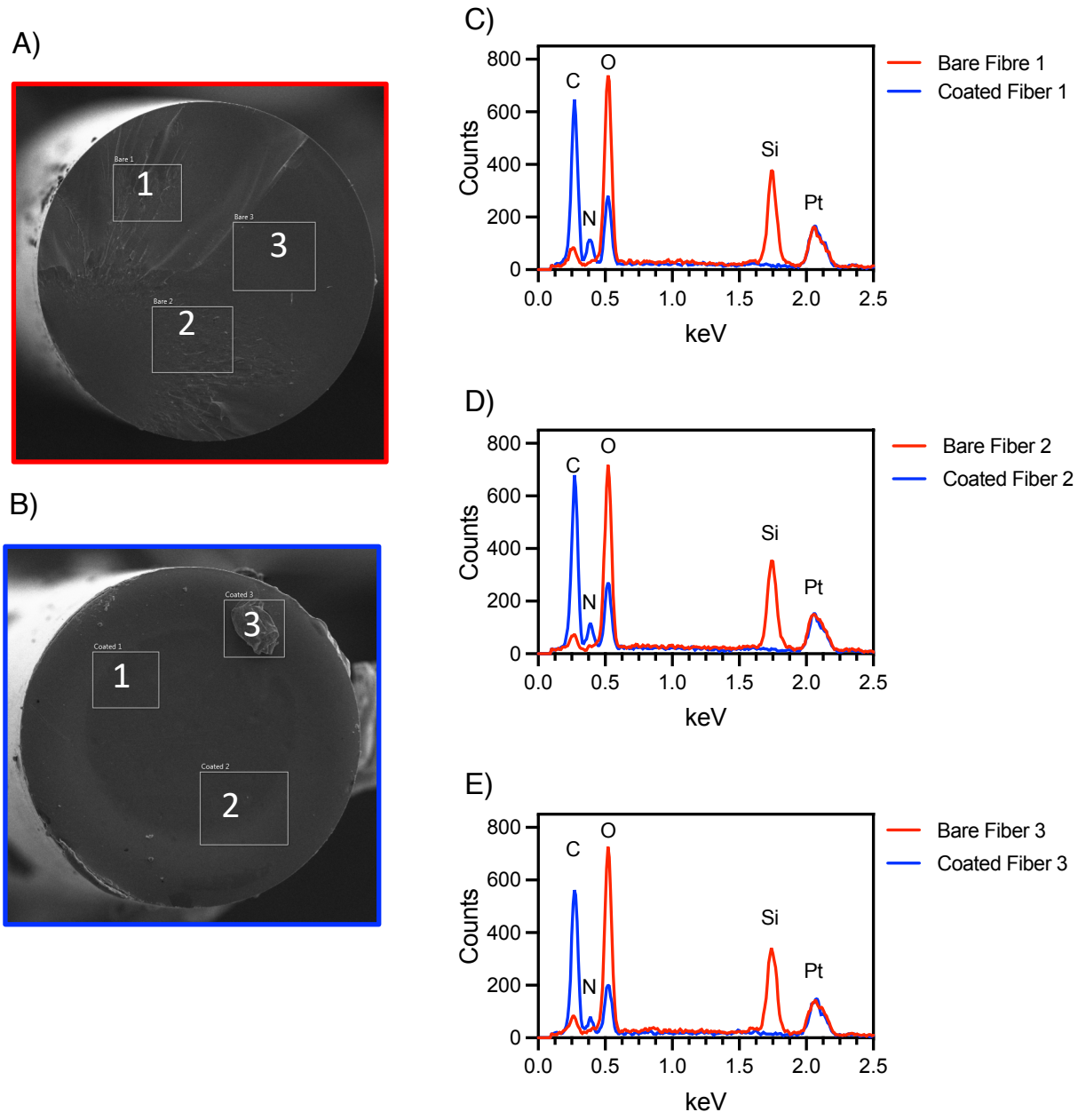

Figure S2.6. SEM images of **A)** a bare fibre and **B)** a silk-coated fibre, with positions marked where EDX spectra were collected, which are compared in **C)**, **D)**, and **E)** respectively. Note the Pt signal is from the sample preparation.

S2.6 Polyacrylamide coating on OCT-capable fibres

During preliminary work in this study a double-clad fibre was coated with polyacrylamide, following the procedures described in our previous publications (Figure S2.7A).[23-25] This fibre probe was connected to the integrated OCT and fluorescence system to collect an OCT image (Figure S2.7B). The reflection from the surface of a detector card (red arrows, visible near IR detector card, VRC2,Thorlabs, USA) is difficult to resolve from the noise generated by the polyacrylamide coating. This suggests that the existing technology of polyacrylamide coatings to attach a fluorophore to an optical fibre tip is not compatible with the design of an OCT fibre probe as the polymer degrades the imaging beam.

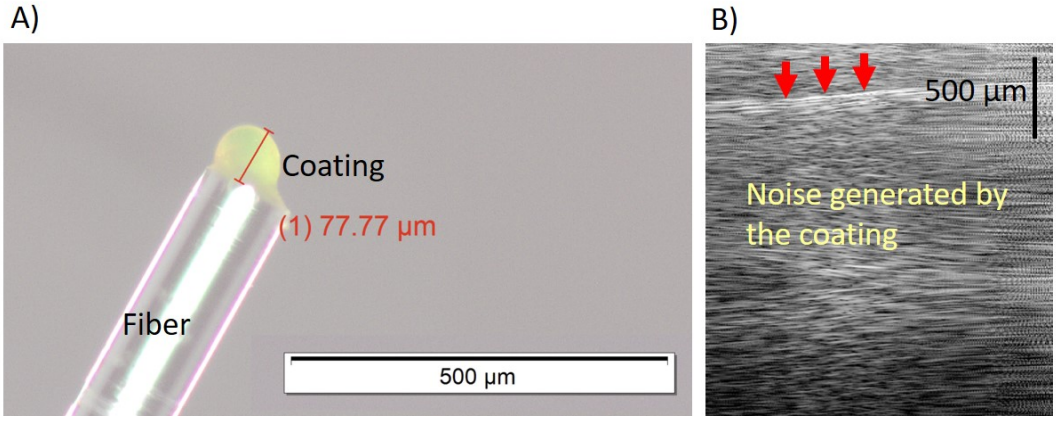

Figure S2.7. A) Optical microscopic image at 2.5x magnification showing a ~78 µm polyacrylamide coating on a double-clad optical fibre. **B)** OCT image generated using the polyacrylamide-coated fibre shown in A; Red arrows point to the signal from a visible near infrared detector card (VRC2, Thorlabs, USA). Strong noise was generated by the polyacrylamide coating, rendering it incompatible with OCT imaging.

S2.7 Additional data for SBP-TAMRA adherence experiments

The fluorescence retention of additional control fibres which were coated with **SBP-TAMRA** in the absence of silk fibroin is provided below.

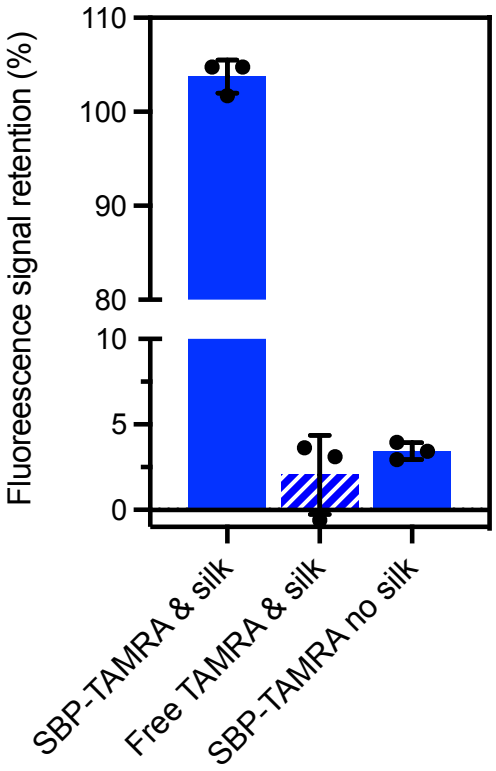

Figure S2.8. Fluorescence signal retention (the percentage change to the fluorescence signal obtained after washing compared to the signal before washing) for fibres coated with silk fibroin and **SBP-TAMRA** (solid bar, left) compared to coated with free TAMRA (striped bar), and SBP-TAMRA in the absence of silk fibroin (solid bar, right). The fibre probes were washed by dipping three times in distilled water for 30 s.

Full spectra are provided below for all washing experiments as detailed in the main text (Figure 2.3).

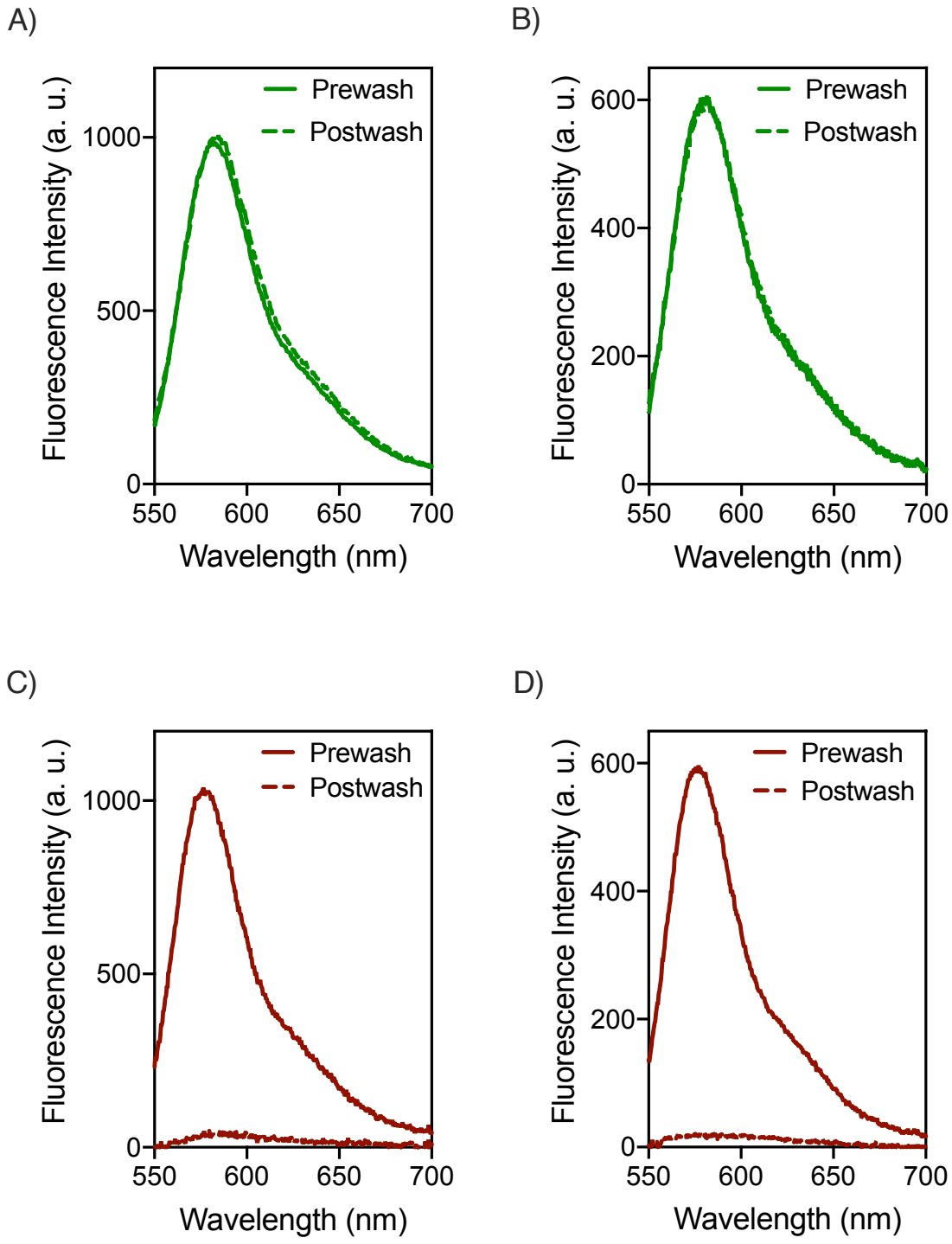

Figure S2.9. Normalised fluorescence spectra for fibres coated in silk fibroin with SBP-TAMRA (green) or free TAMRA (red). **A)** SBP-TAMRA washed 3 × 30 s, **B)** SBP-TAMRA washed 18 h, C) free TAMRA washed 3 × 30 s, D) free TAMRA washed 18 h. Excitation 532 nm.

S2.8 SBP-SNARF ratiometric response to pH

As detailed in the main text, the ratio between the 580 nm and 640 nm fluorescence peaks of SNARF gives an inverse response to pH (see Figure 2.3 in the manuscript). The calibration curves for three OCTpH probes in HEPES buffer are given below. Each fibre has a slightly different calibration curve due to inherent difference in the optical fibre background signal, and thus each fibre must be individually calibrated before use.

	Fibre 1	Fibre 2	Fibre 3
Equation	Y = -0.5161*X + 4.332	Y = -0.4023*X + 3.498	Y = -0.3845*X + 3.262

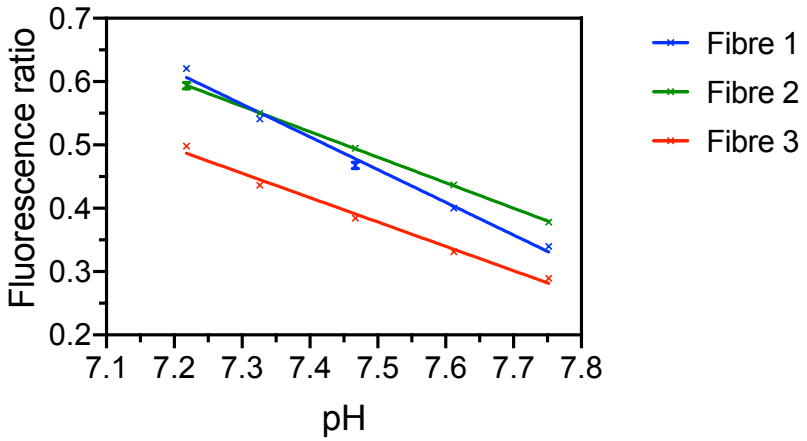

Figure S2.10. Ratiometric response of OCTpH probes to pH, calculated by the ratio of the 580 nm to 640 nm fluorescence peaks. Error bars are standard deviations, however no error bars are visible for most data points as they are smaller than the symbol size.

Chapter 3: Protein detection enabled using functionalised silk-binding peptides on a silk-coated optical fibre

This chapter consists of a publication submitted to RSC Advances in March 2021 and accepted in June 2021. The publication is entitled “Protein detection enabled using functionalised silk-binding peptides on a silk-coated optical fibre”.

RSC Advances, **2021**, 11, 22334-22342

Patrick K. Capon, Aimee J. Horsfall, Jiawen Li, Erik P. Schartner, Asma Khalid, Malcolm S. Purdey, Robert A. McLaughlin, Andrew D. Abell

Statement of Authorship

Title of Paper	Protein detection enabled using functionalised silk-binding peptides on a silk-coated optical fibre
Publication Status	☐ Published ☐ Accepted for Publication ☒ Submitted for Publication ☐ Unpublished and Unsubmitted work written in manuscript style
Publication Details	**Patrick K. Capon**, Aimee J. Horsfall, Jiawen Li, Erik P. Schartner, Asma Khalid, Malcolm S. Purdey, Robert A. McLaughlin, Andrew D. Abell, Protein detection enabled using functionalised silk-binding peptides on a silk-coated fibre, RSC Advances, 2021

Principal Author

Name of Principal Author (Candidate)	Patrick Capon		
Contribution to the Paper	Conceptualised and conducted the full research project, including data collection and analysis. Wrote and edited the manuscript.		
Overall percentage (%)	70		
Certification:	This paper reports on original research I conducted during the period of my Higher Degree by Research candidature and is not subject to any obligations or contractual agreements with a third party that would constrain its inclusion in this thesis. I am the primary author of this paper.		
Signature		Date	15/02/2021

Co-Author Contributions

By signing the Statement of Authorship, each author certifies that:

i. the candidate's stated contribution to the publication is accurate (as detailed above)

ii. permission is granted for the candidate in include the publication in the thesis; and

iii. the sum of all co-author contributions is equal to 100% less the candidate's stated contribution.

Name of Co-Author	Aimee Horsfall		
Contribution to the Paper	Conceptualised the peptide system and aided in synthesis. Assisted with experiment design, data analysis, and figure preparation. Edited the manuscript.		
Signature		Date	22/02/2021

Name of Co-Author	Jiawen Li		
Contribution to the Paper	Assisted with the optical fibre system preparation. Edited the manuscript.		
Signature		Date	15/2/2021

Name of Co-Author	Erik Schartner		
Contribution to the Paper	Assisted with design and preparation of the fibre laser system, including troubleshooting. Provided resources for the laser system and wrote custom LabView software. Edited the manuscript.		
Signature		Date	16/2/21

Name of Co-Author	Asma Khalid		
Contribution to the Paper	Involved with research conceptualisation and provided the silk materials required.		
Signature		Date	17/02/2021

Name of Co-Author	Malcolm Purdey		
Contribution to the Paper	Aided in project conceptualisation and data analysis, and co-supervised Patrick during his PhD. Edited the manuscript.		
Signature		Date	15/02/2021

Name of Co-Author	Robert McLaughlin		
Contribution to the Paper	Aided in design and preparation of the research, and provided resources for the fibre system. Aided in writing the manuscript and edited the manuscript.		
Signature		Date	22 February 2021

Name of Co-Author	Andrew Abell		
Contribution to the Paper	Aided in design and preparation of the full research project, and provided resources for all chemical synthesis. Aided in writing the manuscript and edited the manuscript. Supervised Patrick and Aimee during PhD degrees.		
Signature		Date	15/02/2021

3.1 Abstract

We report the detection of AlexaFluor-532 tagged streptavidin by its binding to D-biotin that is functionalised onto an optical fibre, via incorporation in a silk fibroin fibre coating. The D-biotin was covalently attached to a silk-binding peptide to provide SBP-Biotin, which adheres the D-biotin to the silk-coated fibre tip. These optical fibre probes were prepared by two methods. The first involves dip-coating the fibre tip into a mixture of silk fibroin and SBP-Biotin, which distributes the SBP-Biotin throughout the silk coating (method A). The second method uses two steps, where the fibre is first dip-coated in silk only, then SBP-Biotin added in a second dip-coating step. This isolates SBP-Biotin to the outer surface of the silk layer (method B). A series of fluorescence measurements revealed that only the surface bound SBP-Biotin detects streptavidin with a detection limit of 15 mg/mL. The fibre coatings are stable to repeated washing and long-term exposure to water. Formation of silk coatings on fibres using commercial aqueous silk fibroin was found to be inhibited by a lithium concentration of 200 ppm, as determined by atomic absorption spectroscopy. This was reduced to less than 20 ppm by dialysis against water, and was found to successfully form a coating on optical fibres.

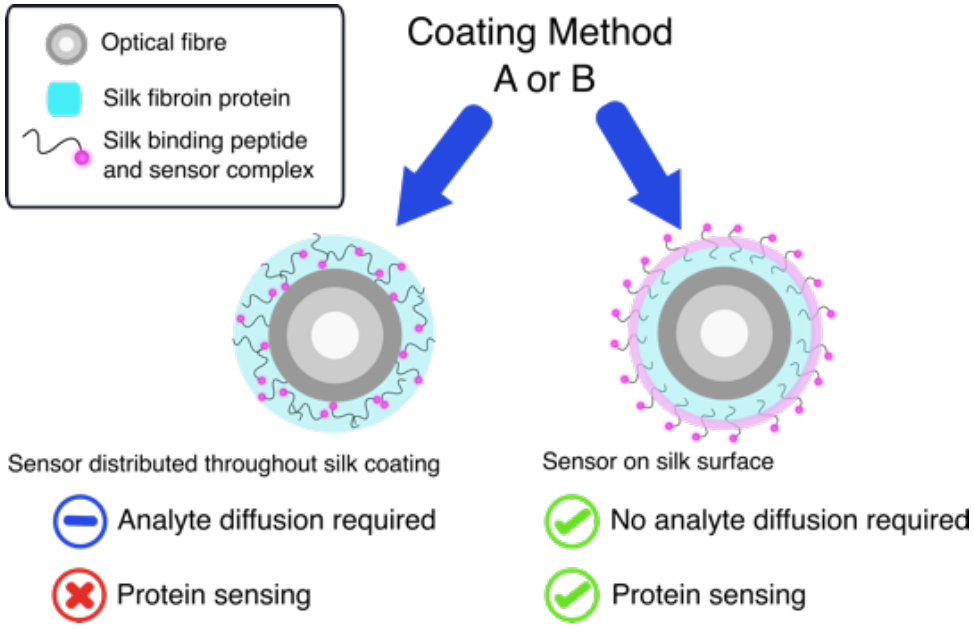

Sensor molecule location on an optical fibre probe is controlled by our two coating methods, which dictates suitability for protein sensing.

3.2 Introduction

A wide range of fluorescent molecules are available for the detection of biological analytes, which function by measuring a change in fluorescence output on binding.[1-4] However, the associated sensing experiments are often limited to *in vitro* studies, as minimally invasive delivery of light to an *in vivo* site is challenging. This is largely due to the low penetration of light through tissue.[5] One solution is to use an optical fibre to deliver excitation light, and collect the subsequent fluorescence emission from the location of the fluorophore.[6-10] Furthermore, an optical fibre-based probe can be prepared by coating the fibre tip in a matrix, such as a polymer or electrolyte layer, within which a fluorescent sensor molecule is embedded.[11-13] Production of such an optical fibre probe provides advantages of small device size,[14] precise spatio-temporal control of the fibre tip,[10] and delivery of light in difficult to reach locations,[15] such as those required for *in vivo* studies.[16,17]

Optical fibre probes have been developed for a number of applications, including the detection of biological analytes such as metal ions,[18-21] small biomolecules,[22,23] and pH measurement.[24-27] However, there are few reports on the detection of proteins and other large biomolecules using such systems.[28,29] This is a significant limitation since biological processes and associated disease states are invariably controlled by these large biomolecules.[30,31] Advances are required in optical fibre coating procedures if this unmet need is to be realised.[32] Such an advance must address the key problem that the large size of a protein may limit its diffusion into a fibre coating matrix, and hence limit its ability to reach the embedded sensor molecule. This contrasts small analytes that readily diffuse through the matrix. Here we present a new coating procedure to prepare such an optical fibre probe for protein sensing and demonstrate it with the detection of streptavidin using D-biotin adhered to the fibre tip. Specifically, D-biotin is attached to a silk-binding peptide (SBP) by an amide coupling to provide SBP-Biotin. This peptide conjugate is then immobilised onto an optical fibre by incorporation into a silk fibroin layer on the fibre tip. Two coating methods were developed to investigate if fibres bearing surface bound SBP-Biotin, or those with SBP-Biotin incorporated throughout the silk matrix, were able to detect streptavidin in solution. We show that this control over the SBP-Biotin location is critical for

successful streptavidin detection. Our new fibre coating technology paves the way for development of further fluorescence based optical fibre probes for protein sensing *in vivo*.

3.3 Results and discussion

3.3.1 System design and fibre preparation

The new coating procedure developed here for production of optical fibre probes to sense protein was demonstrated with a proof-of-concept system that exploits the strong, highly specific, interaction between biotin and streptavidin.[33] D-Biotin was covalently attached to the *N*-terminus of a silk-binding peptide (SBP, sequence SYTFHWHQSWSS)[34] by a diisopropylcarbodiimide and Oxyma mediated amide coupling to provide SBP-Biotin (Figure 3.1). The SBP was selected for use here as we have previously shown that it binds to silk fibroin coatings on optical fibres.[35] Optical fibres were coated with silk fibroin and the new peptide SBP-Biotin to provide an optical fibre probe for streptavidin, where the streptavidin is detected through collection of the fluorescence signal from an AlexaFluor-532 tag. This fibre coating was carried out by either a one-step or two-step process, referred to as methods A and B (see Figure 3.1 and the Supporting Information). Method A involves submersion of the optical fibre tip in an aqueous mixture of both silk fibroin and SBP-Biotin in a single silk-coating step. The silk fibroin was then cured by dipping the functionalised optical fibre tip in methanol.[36] This results in distribution of SBP-Biotin throughout the silk fibroin coating (Figure 3.1, Method A). In contrast, method B involves two distinct fibre coating steps. First, the fibre tip was dipped into an aqueous solution of silk fibroin, which results in formation of a silk layer on the fibre tip, that was then cured in methanol.[36] The silk-coated fibre was subsequently dipped in a separate aqueous solution of SBP-Biotin. This two-step process, with SBP-Biotin added last, results in localisation of the SBP-Biotin to the exterior of the silk fibroin coating (Figure 3.1, Method B).

It was expected that the large size of streptavidin (~52.8 kDa) would preclude its diffusion through the silk fibroin matrix, and thus not reach the majority of the SBP-Biotin sensor component embedded within the silk fibroin through fibre coating method A. However, isolation of SBP-Biotin to the exterior of the silk coating, achieved through coating fibres with silk fibroin using method B,

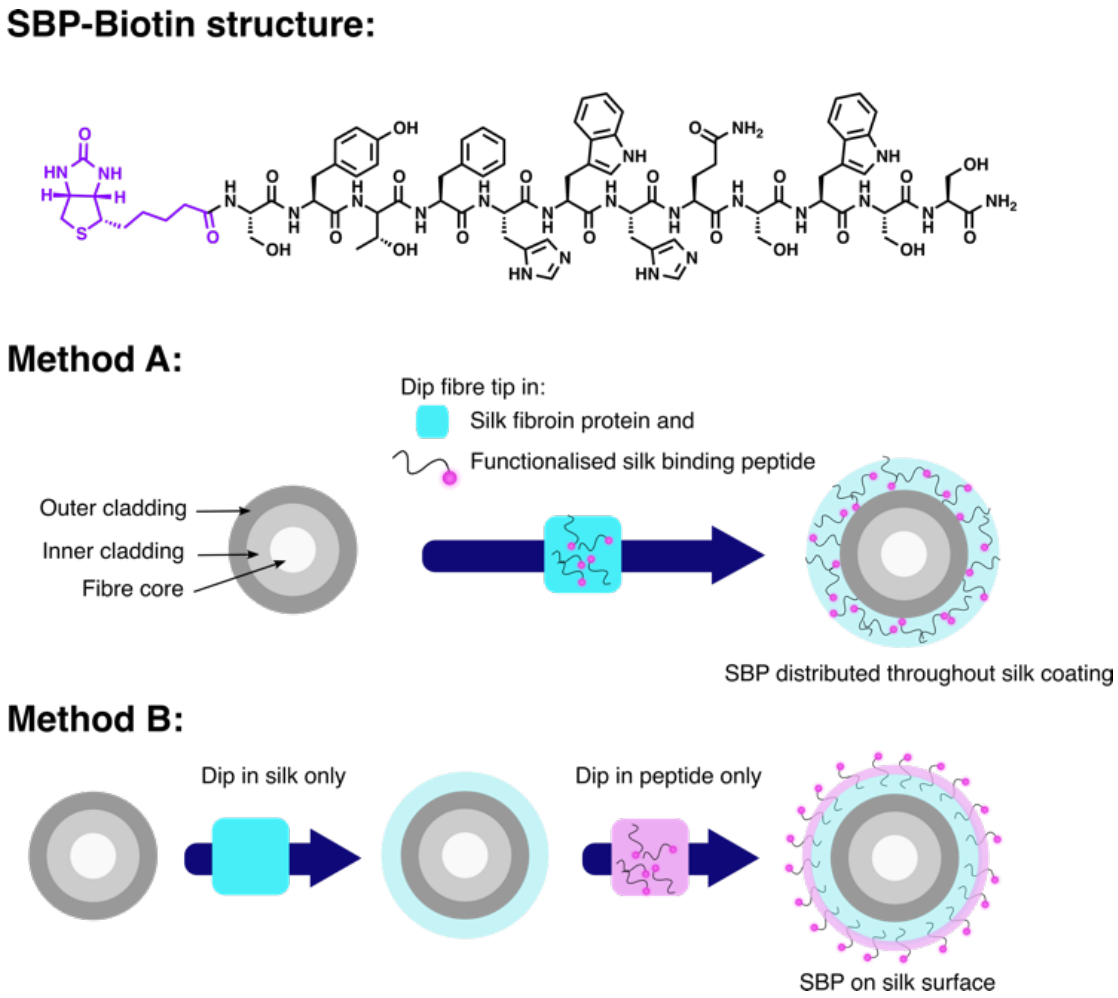

Figure 3.1. Top, Structure of the functionalised silk-binding peptide, SBP-Biotin, prepared by N-terminal attachment of D-Biotin (purple) to a SBP (black). **Middle**, Fibre coating method A is a single step process, where the optical fibre tip (shown as an end on cross section) is dipped into an aqueous mixture of silk fibroin protein (light blue) and SBP-Biotin. The fibre is then removed and dipped in 90% aqueous methanol. This provides a fibre probe with the SBP-Biotin distributed throughout the silk fibroin layer. **Bottom**, Method B consists of two fibre dip coating steps, where the optical fibre tip is first dipped in a solution of silk fibroin only followed by 90% methanol (shown by the blue coating). The silk coated fibre tip is then dipped in an aqueous solution of the SBP-Biotin to provide a fibre probe with the SBP-Biotin decorated on the outer surface of the silk fibroin coating (shown by the purple layer).

was expected to allow the streptavidin to access and bind D-Biotin, as diffusion through the silk matrix is not required. Thus, fibre probes bearing surface bound SBP-Biotin were expected to result in superior detection of streptavidin compared to those with SBP-Biotin distributed throughout the silk layer.

3.3.2 Detection of fluorescently tagged streptavidin

The detection of streptavidin with SBP-Biotin coated fibres prepared by method A or B was investigated to determine which coating method was more effective for detection of streptavidin in solution. First, all fibres used for sensing were connected to a fibre-coupled laser system and

baseline (i.e. uncoated fibre) fluorescence spectra collected (ex. 532 nm, see Experimental section and Figure S3.3 in the Supporting Information). Three optical fibres were then coated with SBP-Biotin by method A, and three optical fibres were coated with SBP-Biotin by method B. Additionally, three control fibres were prepared by coating the fibre with silk fibroin only, to determine if the streptavidin bound non-specifically to the silk fibroin layer in the absence of SBP-Biotin (see Experimental section). Each fibre was dipped in a solution of AlexaFluor-532 tagged streptavidin (30 μg/mL in 100 mM phosphate buffer at pH 7.2) for 30 seconds. Fluorescence spectra were collected for each fibre and are labelled as 'pre-wash' in Figure 3.2. The intensity of all spectra was integrated between 565 and 600 nm to minimise noise. All fibres were then washed three times by submerging the fibre tip in phosphate buffer (100 mM, pH 7.2) for 30 seconds per wash. Fluorescence spectra were again collected for each fibre and are labelled as 'washed' in Figure 3.2. The baseline, pre-wash, and washed spectra were compared for each fibre coating method to determine which set of fibres was successful in detection of the AlexaFluor-532 tagged streptavidin.

The pre-wash spectra for the control fibres (no SBP-Biotin present) had an average integrated intensity of 135,000 counts, indicating that AlexaFluor-532 tagged streptavidin was present on the fibre tips (Figure 3.2, white bars, also see Supporting Information Figures S3.5 to S3.8). After washing, the fluorescence intensity was reduced to 2,400 counts, which indicates that streptavidin was removed. This suggests the streptavidin was non-specifically bound to the silk fibroin layer on the control fibres. The washed fluorescence intensity for the fibres coated with silk fibroin and SBP-Biotin by method A was similarly reduced in comparison to the pre-wash intensity (203,000 reduced to 4,200 counts, Figure 3.2 blue bars). The washed intensity was of similar magnitude to the baseline intensity, which indicates that there was no detectable streptavidin remaining on the fibre tip. This shows that when SBP-Biotin is embedded within the silk matrix on the fibre tip (method A), it does not selectively bind to fluorescently tagged streptavidin. This observation is consistent with the hypothesis that streptavidin cannot diffuse through the silk fibroin coating to reach the majority of the embedded SBP-Biotin. In contrast, the post-wash fluorescence intensity observed for the fibres coated with silk fibroin and SBP-Biotin by method B was significantly greater than the baseline intensity (24,400 vs 2,200 counts, Figure 3.2 red

bars). As the washing process was shown to remove any non-specifically bound streptavidin on the control and method A coated fibres, the fluorescence signal remaining after washing is attributed to AlexaFluor-532 tagged streptavidin that is bound to SBP-Biotin. Hence, streptavidin binds to SBP-Biotin that is decorated on the outside of the silk fibroin coating on an optical fibre tip (method B). Finally, we investigated if streptavidin could be removed from these fibres by washing with sodium dodecyl sulfate (SDS), which is known to denature streptavidin.[37] The fibres were washed three times by dipping the fibre tips in 2% v/v aqueous SDS for 30 seconds per wash. Fluorescence spectra were collected, with the resulting integrated intensity found to be 2,400 counts (Figure 3.2, 'Washed SDS'). Thus, it is clear that streptavidin is removed from the optical fibre tip by washing the fibre with SDS.

In summary, optical fibre probes with SBP-Biotin isolated to the exterior of the silk fibroin layer on the fibre tip were able to detect AlexaFluor-532 tagged streptavidin (method B). However, fibres with SBP-Biotin distributed throughout the silk fibroin layer were not able to detect streptavidin (method A). This is consistent with the hypothesis that streptavidin cannot diffuse through the silk fibroin matrix to reach the embedded SBP-Biotin sensor component. The preparation of SBP-Biotin and silk fibroin coated fibres by method B is thus optimum for detection of streptavidin. Our SBP-Biotin and streptavidin model system demonstrates that coating method B is amenable to sensing large analytes such as proteins, while coating method A is not suitable.

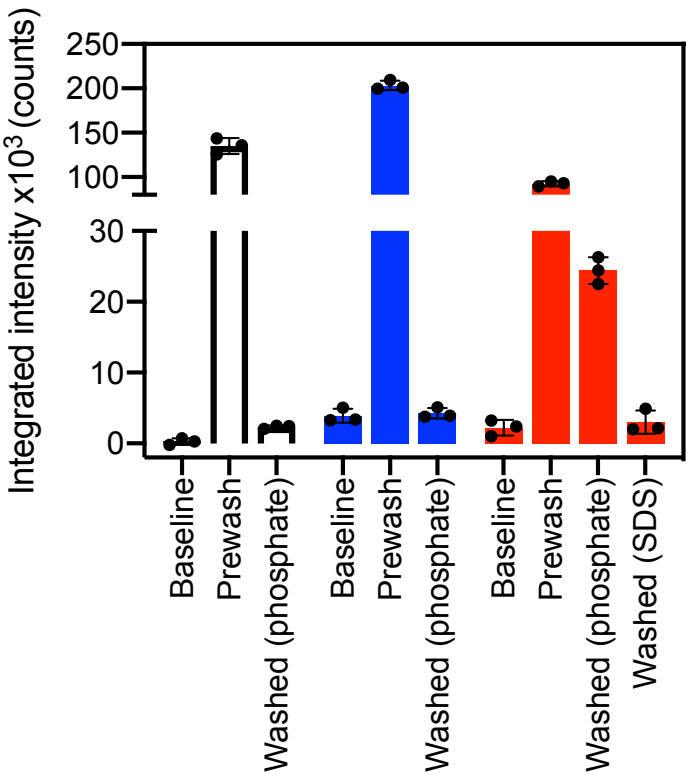

Figure 3.2. Sensing of AlexaFluor-532 tagged streptavidin with SBP-Biotin coated fibre probes. One fibre is shown for each coating type, plotted as the mean ±standard deviation of three individual fluorescence reads. Data for all three fibres for each fibre coating type is available in the Supporting Information. **Left**, white; a control fibre coated with silk fibroin only, where all prewash fluorescence was lost upon washing with phosphate buffer (100 mM, pH 7.2). **Middle**, blue; a fibre coated with SBP-Biotin and silk fibroin by method A, where all prewash fluorescence was again lost upon washing with phosphate buffer. **Right**, red; a fibre coated with SBP-Biotin and silk fibroin by method B, where approximately 30% of the prewash signal was retained after washing with phosphate buffer, then all fluorescence removed by further washing of the fibre with aqueous sodium dodecyl sulfate (SDS, 2%). The excitation wavelength for all spectra was 532 nm, with intensity integrated between 565 and 600 nm for each fluorescence spectrum.

3.3.3 Limit of detection for streptavidin with SBP-Biotin coated fibres

An approximate concentration limit for detection of AlexaFluor-532 tagged streptavidin using SBP-Biotin coated fibre probes was determined. Three fibre probes prepared by method B were dipped into a solution of AlexaFluor-532 tagged streptavidin at 7.8 µg/mL (100 mM phosphate buffer, pH 7.2). The fibres were washed once by dipping for 30 seconds in phosphate buffer (100 mM, pH 7.2) to remove any non-specifically bound streptavidin, then fluorescence spectra were collected and the integrated intensity plotted (Figure 3.3, blue bars). Some variability in the integrated intensity was apparent between fibre probes, where the AlexaFluor-532 fluorescence intensity (blue) was well separated from the baseline intensity (white) for fibres #1 and #3, but fibre #2 was within error of the baseline intensity (Figure 3.3). Therefore, fibre #2 was not able to

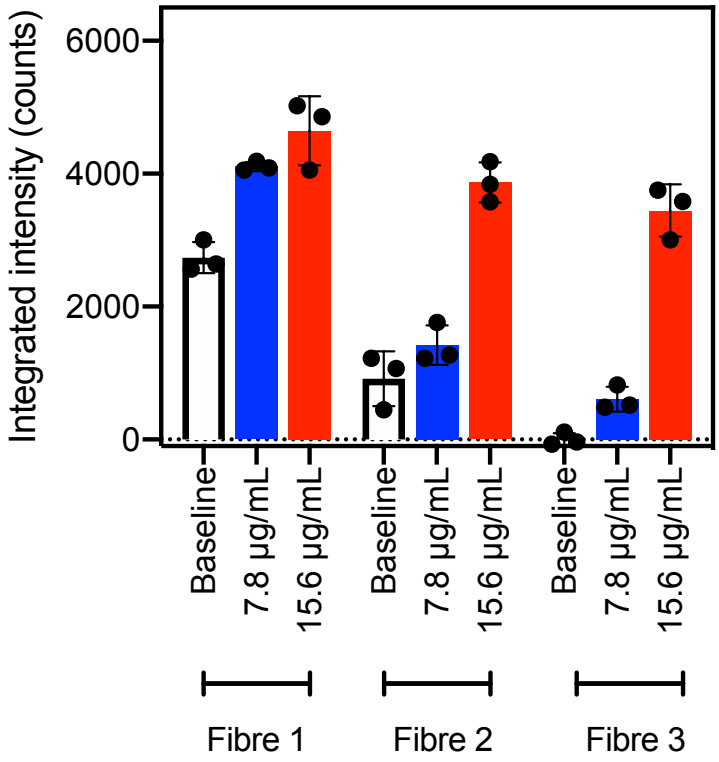

Figure 3.3. Integrated intensity between 565 and 600 nm for fibre probes coated with silk fibroin and SBP-Biotin by method B. White, the baseline signal obtained before exposure to streptavidin; blue, signal after dipping in AlexaFluor-532 tagged streptavidin at 7.8 µg/mL; and red, signal after dipping in AlexaFluor-532 tagged streptavidin at 15 µg/mL. The excitation wavelength was 532 nm for all spectra, data is plotted as mean standard deviation of three reads.

distinguish between the streptavidin solution (7.8 µg/mL) and the baseline fluorescence of the fibre.

The same three fibre probes coated with SBP-Biotin by method B were next washed three times in 2% aqueous SDS to remove all bound streptavidin, as shown by the earlier results in the streptavidin detection experiments. These fibres were then dipped in a second solution of AlexaFluor-532 tagged streptavidin at a higher concentration of 15 µg/mL for 30 seconds, then washed once with phosphate buffer. Fluorescence spectra were collected and the resultant integrated intensity (Figure 3.3, red bars) was found to be clearly distinguished from the baseline signal (Figure 3.3, white bars) for all three fibres. Therefore, all three fibres can detect streptavidin at a concentration of 15 µg/mL.

In summary, optical fibre probes coated with SBP-Biotin with method B were able to detect streptavidin at 15 µg/mL. Fibres #1 and #3 also detected streptavidin at 7.8 µg/mL, however fibre

#2 could not distinguish between a 7.8 µg/mL streptavidin sample and a baseline measurement. The detection limit of AlexaFluor-532 tagged streptavidin using optical fibre probes coated with SBP-Biotin by method B was thus determined to be 15 µg/mL in accordance with the definition by Armbruster and Pry of "the lowest analyte concentration likely to be reliably distinguished from the blank and at which detection is feasible".[38] Recently reported surface plasmon resonance based optical fibre probes for streptavidin[39] and C-reactive protein[40] have a comparable detection limit of 0.1 to 20 µg/mL, suggesting that silk fibroin and SBP coatings prepared by method B are a viable option for the production of optical fibre probes for protein sensing.

3.3.4 Retention of method B coatings on fibres

The stability of coatings prepared by method B to repeated submersion in water was investigated to simulate repeated usage of the optical fibre probes. A model SBP was prepared where D-Biotin was replaced by the fluorophore 5(6)-carboxyTAMRA to provide the functionalised SBP, SBP-TAMRA (see Experimental section).[35] This allowed the stability of the coating to be monitored by collection of the TAMRA fluorescence signal, where a loss of fluorescence implies a loss of SBP-TAMRA from the fibre tip. SBP-TAMRA directly replaced SBP-Biotin in the procedure for coating method B, which resulted in isolation of SBP-TAMRA to the outer surface of the silk layer on the optical fibre. Fluorescence spectra were collected using the described fibre-coupled laser and spectrometer system (Supporting Information Figure S3.3).

First, three control fibres were prepared with free TAMRA used in place of SBP-TAMRA, to demonstrate the necessity of the SBP component for retention of TAMRA on the silk coated fibre (see Experimental section). These control fibres were coated by method B such that the free TAMRA was isolated to the silk surface. Fluorescence spectra were collected, then the fibres were washed by submerging the fibre tips three times in water for 30 seconds. Fluorescence spectra were collected again and the percentage fluorescence retention calculated (Figure 3.4, see Supporting Information Figures S3.10 and S3.11 for full spectra). This showed that only 5% of the fluorescence signal was retained after washing (Figure 3.4, striped blue bar). Next, the fluorescence retention of three fibres bearing surface bound SBP-TAMRA (method B) was calculated through the same washing and fluorescence spectra collection procedure. In this case,

90% of the fluorescence signal obtained before washing was retained after washing in water (Figure 3.4, solid blue bar). The optical fibres functionalised by method B are thus stable to repeated submersion in water, with minimal SBP-TAMRA removed. Therefore, the SBP is required to retain TAMRA on optical fibres coated by method B.

Next, the long-term adherence of the silk coatings on optical fibres was investigated. A set of three control fibres (coated with free TAMRA only) and three SBP-TAMRA coated fibres were prepared by method B and fluorescence spectra acquired, and the fibre tips were soaked in water overnight. Fluorescence spectra were collected again after this soak and the fluorescence retention calculated (Figure 3.4, see Supporting Information Figure S3.10 and S3.11 for full spectra). Only 3% of the original fluorescence signal was retained after soaking the control fibres (Figure 3.4, striped red bar), while 68% was retained for the SBP-TAMRA coated fibres (Figure 3.4, solid red bar). This demonstrates that the method B coating of silk fibroin and SBP-TAMRA is stable on the fibre for extended periods of time, while free TAMRA is not. Overall, these washing experiments demonstrate that silk fibroin and SBP-TAMRA coatings prepared by method B remain adhered to the optical fibre under repeated or prolonged exposure to water. These results are in agreement with the observed stability of fibres coated with SBP-TAMRA by method A (Supporting Information Figure S3.9).[35]

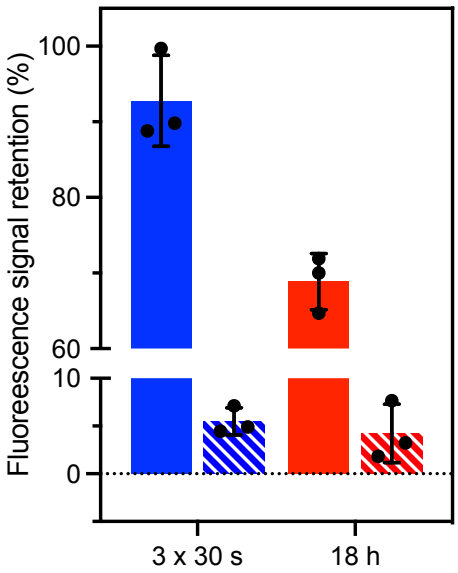

Figure 3.4. Percentage fluorescence retention on method B coated fibres, calculated from comparison of the integrated intensity (570 to 600 nm) of fluorescence spectra obtained before and after washing each fibre. Each point shown is the average of three spectra for one fibre, with a total of three fibres plotted per bar as mean μ standard deviation. The solid bars represent fibres coated with silk fibroin and SBP-TAMRA, while the striped bars represent fibres coated with silk fibroin and free TAMRA. Fibres were washed in water for 3 × 30 s (blue) or soaked overnight (red). All spectra were collected with an excitation wavelength of 532 nm.

3.3.5 Comparison of silk fibroin sources

The silk fibroin used here was prepared in-house or purchased from Merck as a 50 mg/mL aqueous solution (Supelco 5154-20mL). The crude in-house silk fibroin was extracted from *Bombyx mori* cocoons following reported protocols,[41,42] then purified from 6.3 M LiBr solution by dialysis against water to provide aqueous silk fibroin at 65 mg/mL. This in-house prepared silk fibroin is known to provide a coating of silk fibroin and SBP-TAMRA on optical fibres, as shown in our previous work.[35,42] We therefore attempted to use the commercial silk fibroin in the same manner to allow a direct comparison of the two silk sources. Optical fibre tips were dip-coated in a mixture of commercial silk fibroin and SBP-TAMRA according to method A, which should result in distribution of the SBP-TAMRA throughout the silk layer. Fluorescence spectra were collected, however there was no signal observed corresponding to SBP-TAMRA. This result was consistently observed over multiple optical fibres, which suggests that the commercial silk fibroin cannot form a coating on optical fibres.

Table 3.1. Summary of atomic absorption spectroscopy results for lithium concentration of in-house and commercially prepared silk fibroin samples.

Sample	Approximate lithium concentration (ppm)
In-house silk fibroin solution	20.0
Merck silk fibroin solution	200
Dialysed Merck silk fibroin solution	<1

Given the observed difference in preparation of optical fibres coatings between silk samples, we sought to further characterise the two silk fibroin solutions. As the final silk fibroin processing step is dialysis from LiBr, we hypothesised a difference in lithium salt content may affect the production of a silk coating on the fibres. Therefore, atomic absorption spectroscopy (AAS) was conducted on both silk samples to investigate their lithium content (at 50 mg/mL, see Experimental section and Figure S3.4). The commercial silk fibroin sample was found to contain a 10-fold higher lithium concentration than the in-house silk fibroin sample (200 vs 20.0 ppm, see Table 3.1). The commercial sample was then further dialysed against 1 L of water for 48 h with the water changed every ~12 h, and the resulting dialysed silk solution analysed by AAS to find <1 ppm lithium (Table 3.1).

The dialysed commercial silk fibroin was then used to coat fibres, in order to investigate if the lowered lithium content in this silk sample affected silk coating production. An optical fibre was dip-coated in a mixture of dialysed commercial silk fibroin and SBP-TAMRA according to method A, then fluorescence spectra collected. A fluorescence signal from SBP-TAMRA was observed, of similar magnitude to that obtained using the in-house silk fibroin. This indicated that the silk coating was successfully formed using the dialysed commercial silk fibroin. Overall, it was found that the as-received commercial silk fibroin cannot form a coating on optical fibres, which is likely due to the observed increase in lithium content. Therefore, we recommend that the lithium content of aqueous silk fibroin solutions is tested, and additional dialysis conducted to reduce the lithium concentration below 20 ppm before attempting to coat optical fibres.

3.4 Conclusion

We have described the preparation of a fluorescence based fibre probe for the detection of streptavidin, enabled by attachment of D-biotin to the fibre tip. D-Biotin was attached to the *N*-terminus of a silk-binding peptide (SBP) by an amide coupling reaction to provide SBP-Biotin. The SBP was selected as it is known to bind to a silk fibroin coating on optical fibres, which therefore ensures that SBP-Biotin is adhered to the silk coated fibre tip. We developed two methods to prepare these optical fibre probes in order to control the location of SBP-Biotin: either distributed throughout the silk coating (method A), or isolated to the outer surface of the silk layer (method B). These methods were shown to form a silk coating that is stable to repeated or long-term exposure to water. The detection of streptavidin with optical fibre probes prepared by these two methods was compared in order to investigate the diffusion of streptavidin through the silk matrix. It was found that only fibres bearing SBP-Biotin on the outer surface of the silk layer were able to detect streptavidin, with the experimental limit of detection found to be 15 μg/mL. This comparison demonstrates that the precise location of the sensor component (SBP-Biotin in our model), with respect to the fibre coating, is a critical design consideration for preparation of optical fibre probes for protein sensing.

The coating of optical fibres with in-house prepared or commercial silk fibroin was also compared to allow wider access to our fibre coating technology. We determined that the commercial silk fibroin did not successfully form a coating on optical fibres, however this was rectified by dialysis against water. Analysis by atomic absorption spectroscopy suggested that a low lithium content (≤20 ppm) in the silk solution was an important factor in forming a silk fibroin coating on optical fibres. Therefore, our fibre coating technology requires that the lithium content of all aqueous silk fibroin solutions is checked prior to coating optical fibres, and dialysis be performed to reduce the lithium content below 20 ppm.

We have presented a new approach to prepare optical fibre probes for protein sensing, and detected streptavidin using fibre probes coated with SBP-Biotin as a model system. However, the SBP-Biotin sensor component can be easily substituted for other sensors, through covalent attachment of the sensor to the *N*-terminus of the SBP. This will enable development of optical

fibre probes for other protein analytes using our silk coating technology. The fibre coating must be prepared following method B, developed here to isolate the sensor component to the external surface of the silk layer, as we have shown that only these fibres are amenable to protein sensing.

3.5 Acknowledgements

The authors acknowledge support from the ARC Centre of Excellence for Nanoscale Biophotonics (CE140100003). PKC would like to thank Matthew Bull for running the atomic absorption spectroscopy experiments, and acknowledges PhD scholarship support from the MF and MH Joyner Scholarship in Science and the Norman and Patricia Polglase Supplementary Scholarship. AJH acknowledges PhD scholarship support from a Research Training Program Stipend (RTPS). JL is supported by a Postdoctoral Fellowship (102093) from the National Heart Foundation and an NHMRC Ideas grant (2001646). EPS is supported by an ARC Linkage grant (LP 150100657). AK acknowledges an RMIT Vice Chancellor's Research Fellowship for supporting silk fibroin research. RAM is supported by an NHMRC Development grant (APP1178912) and an NHMRC Ideas grant (2002254). This work was performed in part at the Optofab node of the Australian National Fabrication Facility utilising Commonwealth and SA State Government funding.

3.6 Conflicts of interest

RAM is a co-founder and the director of Miniprobes Pty Ltd., a company that develops novel optical imaging systems. Miniprobes Pty Ltd. did not contribute to this study.

3.7 References

(1) Chan, J.; Dodani, S. C.; Chang, C. J. Reaction-Based Small-Molecule Fluorescent Probes for Chemoselective Bioimaging. *Nat. Chem.* **2012**, *4* (12), 973-984. https://doi.org/10.1038/nchem.1500.

(2) Fernández, A.; Vendrell, M. Smart Fluorescent Probes for Imaging Macrophage Activity. *Chem. Soc. Rev.* **2016**, *45* (5), 1182-1196. https://doi.org/10.1039/C5CS00567A.

(3) Liu, H.-W.; Chen, L.; Xu, C.; Li, Z.; Zhang, H.; Zhang, X.-B.; Tan, W. Recent Progresses in Small-Molecule Enzymatic Fluorescent Probes for Cancer Imaging. *Chem. Soc. Rev.* **2018**, *47* (18), 7140-7180. https://doi.org/10.1039/C7CS00862G.

(4) Kaur, A.; New, E. J. Bioinspired Small-Molecule Tools for the Imaging of Redox Biology. *Acc. Chem. Res.* **2019**, *52* (3), 623-632. https://doi.org/10.1021/acs.accounts.8b00368.

(5) Jacques, S. L. Optical Properties of Biological Tissues: A Review. *Phys. Med. Biol.* **2013**, *58* (11), R37-R61. https://doi.org/10.1088/0031-9155/58/11/R37.

(6) Chu, C.-S.; Lo, Y.-L.; Sung, T.-W. Review on Recent Developments of Fluorescent Oxygen and Carbon Dioxide Optical Fiber Sensors. *Photonic Sens.* **2011**, *1* (3), 234-250. https://doi.org/10.1007/s13320-011-0025-4.

(7) Stevens, O.; Petterson, I. E. I.; Day, J. C. C.; Stone, N. Developing Fibre Optic Raman Probes for Applications in Clinical Spectroscopy. *Chem. Soc. Rev.* **2016**, *45* (7), 1919-1934. https://doi.org/10.1039/C5CS00850F.

(8) Addanki, S.; Amiri, I. S.; Yupapin, P. Review of Optical Fibers-Introduction and Applications in Fiber Lasers. *Results Phys.* **2018**, *10*, 743-750. https://doi.org/10.1016/j.rinp.2018.07.028.

(9) Canales, A.; Park, S.; Kilias, A.; Anikeeva, P. Multifunctional Fibers as Tools for Neuroscience and Neuroengineering. *Acc. Chem. Res.* **2018**, *51* (4), 829-838. https://doi.org/10.1021/acs.accounts.7b00558.

(10) Li, J.; Schartner, E.; Musolino, S.; Quirk, B. C.; Kirk, R. W.; Ebendorff-Heidepriem, H.; McLaughlin, R. A. Miniaturized Single-Fiber-Based Needle Probe for Combined Imaging and Sensing in Deep Tissue. *Opt. Lett.* **2018**, *43* (8), 1682. https://doi.org/10.1364/OL.43.001682.

(11) Song, A.; Parus, S.; Kopelman, R. High-Performance Fiber-Optic PH Microsensors for Practical Physiological Measurements Using a Dual-Emission Sensitive Dye. *Anal. Chem.* **1997**, *69* (5), 863-867. https://doi.org/10.1021/ac960917+.

(12) Sarkar, P. K.; Halder, A.; Adhikari, A.; Polley, N.; Darbar, S.; Lemmens, P.; Pal, S. K. DNA-Based Fiber Optic Sensor for Direct in-Vivo Measurement of Oxidative Stress. *Sens. Actuators B Chem.* **2018**, *255*, 2194-2202. https://doi.org/10.1016/j.snb.2017.09.029.

(13) François, A.; Foo, H. T. C.; Monro, T. M. Polyelectrolyte Multilayers for Surface Functionalization: Advantages and Challenges. In *Advanced Photonics*; OSA: Barcelona, 2014; p JTu4C.1. https://doi.org/10.1364/BGPP.2014.JTu4C.1.

(14) Kopelman, R.; Dourado, S. Is Smaller Better?--Scaling of Characteristics with Size of Fiber-Optic Chemical and Biochemical Sensors. In *Chemical, Biochemical, and Environmental Fiber Sensors VIII*; International Society for Optics and Photonics, 1996; Vol. 2836, pp 2-11. https://doi.org/10.1117/12.260577.

(15) Rente, B.; Fabian, M.; Chen, Y.; Vorreiter, L.; Bustamante, H.; Sun, T.; Grattan, K. T. V. In-Sewer Field-Evaluation of an Optical Fibre-Based Condition Monitoring System. *IEEE Sens. J.* **2020**, *20* (6), 2976-2981. https://doi.org/10.1109/JSEN.2019.2956826.

(16) Musolino, S.; Schartner, E. P.; Tsiminis, G.; Salem, A.; Monro, T. M.; Hutchinson, M. R. Portable Optical Fiber Probe for in Vivo Brain Temperature Measurements. *Biomed. Opt. Express* **2016**, *7* (8), 3069-3077. https://doi.org/10.1364/BOE.7.003069.

(17) Li, J.; Ebendorff-Heidepriem, H.; Gibson, B. C.; Greentree, A. D.; Hutchinson, M. R.; Jia, P.; Kostecki, R.; Liu, G.; Orth, A.; Ploschner, M.; Schartner, E. P.; Warren-Smith, S. C.; Zhang, K.; Tsiminis, G.; Goldys, E. M. Perspective: Biomedical Sensing and Imaging with Optical Fibers—Innovation through Convergence of Science Disciplines. *APL Photonics* **2018**, *3* (10), 100902. https://doi.org/10.1063/1.5040861.

(18) Nguyen, T. H.; Sun, T.; Grattan, K. T. V. A Turn-On Fluorescence-Based Fibre Optic Sensor for the Detection of Mercury. *Sensors* **2019**, *19* (9), 2142. https://doi.org/10.3390/s19092142.

(19) Bachhuka, A.; Heng, S.; Vasilev, K.; Kostecki, R.; Abell, A.; Ebendorff-Heidepriem, H. Surface Functionalization of Exposed Core Glass Optical Fiber for Metal Ion Sensing. *Sensors* **2019**, *19* (8), 1829. https://doi.org/10.3390/s19081829.

(20) Warren-Smith, S. C.; Heng, S.; Ebendorff-Heidepriem, H.; Abell, A. D.; Monro, T. M. Fluorescence-Based Aluminum Ion Sensing Using a Surface-Functionalized Microstructured Optical Fiber. *Langmuir* **2011**, *27* (9), 5680-5685. https://doi.org/10.1021/la2002496.

(21) Heng, S.; Nguyen, M.-C.; Kostecki, R.; M. Monro, T.; D. Abell, A. Nanoliter-Scale, Regenerable Ion Sensor: Sensing with a Surface Functionalized Microstructured Optical Fibre. *RSC Adv.* **2013**, *3* (22), 8308-8317. https://doi.org/10.1039/C3RA40321A.

(22) Bronk, K. S.; Michael, K. L.; Pantano, Paul.; Walt, D. R. Combined Imaging and Chemical Sensing Using a Single Optical Imaging Fiber. *Anal. Chem.* **1995**, *67* (17), 2750-2757. https://doi.org/10.1021/ac00113a005.

(23) Issberner, J. P.; Schauer, C. L.; Trimmer, B. A.; Walt, D. R. Combined Imaging and Chemical Sensing of L-Glutamate Release from the Foregut Plexus of the Lepidopteran, Manduca Sexta. *J. Neurosci. Methods* **2002**, *120* (1), 1-10. https://doi.org/10.1016/S0165-0270(02)00165-6.

(24) Michael, K. L.; Walt, D. R. Combined Imaging and Chemical Sensing of Fertilization-Induced Acid Release from Single Sea Urchin Eggs. *Anal. Biochem.* **1999**, *273* (2), 168-178. https://doi.org/10.1006/abio.1999.4173.

(25) Purdey, M.; Thompson, J.; Monro, T.; Abell, A.; Schartner, E. A Dual Sensor for PH and Hydrogen Peroxide Using Polymer-Coated Optical Fibre Tips. *Sensors* **2015**, *15* (12), 31904-31913. https://doi.org/10.3390/s151229893.

(26) Schartner, E. P.; Henderson, M. R.; Purdey, M.; Dhatrak, D.; Monro, T. M.; Gill, P. G.; Callen, D. F. Cancer Detection in Human Tissue Samples Using a Fiber-Tip PH Probe. *Cancer Res.* **2016**, *76* (23), 6795-6801. https://doi.org/10.1158/0008-5472.CAN-16-1285.

(27) McLennan, H. J.; Saini, A.; Sylvia, G. M.; Schartner, E. P.; Dunning, K. R.; Purdey, M. S.; Monro, T. M.; Abell, A. D.; Thompson, J. G. A Biophotonic Approach to Measure PH in Small Volumes in Vitro: Quantifiable Differences in Metabolic Flux around the Cumulus-Oocyte-Complex (COC). *J. Biophotonics* **2020**, *13* (3), e201960038. https://doi.org/10.1002/jbio.201960038.

(28) Benito-Peña, E.; Valdés, M. G.; Glahn-Martínez, B.; Moreno-Bondi, M. C. Fluorescence Based Fiber Optic and Planar Waveguide Biosensors. A Review. *Anal. Chim. Acta* **2016**, *943*, 17-40. https://doi.org/10.1016/j.aca.2016.08.049.

(29) Mowbray, S. E.; Amiri, A. M. A Brief Overview of Medical Fiber Optic Biosensors and Techniques in the Modification for Enhanced Sensing Ability. *Diagnostics* **2019**, *9* (1), 23. https://doi.org/10.3390/diagnostics9010023.

(30) Goehler, H.; Lalowski, M.; Stelzl, U.; Waelter, S.; Stroedicke, M.; Worm, U.; Droege, A.; Lindenberg, K. S.; Knoblich, M.; Haenig, C.; Herbst, M.; Suopanki, J.; Scherzinger, E.; Abraham, C.; Bauer, B.; Hasenbank, R.; Fritzsche, A.; Ludewig, A. H.; Buessow, K.; Coleman, S. H.; Gutekunst, C.-A.; Landwehrmeyer, B. G.; Lehrach, H.; Wanker, E. E. A Protein Interaction Network Links GIT1, an Enhancer of Huntingtin Aggregation, to Huntington's Disease. *Mol. Cell* **2004**, *15* (6), 853-865. https://doi.org/10.1016/j.molcel.2004.09.016.

(31) Gonzalez, M. W.; Kann, M. G. Chapter 4: Protein Interactions and Disease. *PLOS Comput. Biol.* **2012**, *8* (12), e1002819. https://doi.org/10.1371/journal.pcbi.1002819.

(32) Leca-Bouvier, B.; Blum, L. J. Biosensors for Protein Detection: A Review. *Anal. Lett.* **2005**, *38* (10), 1491-1517. https://doi.org/10.1081/AL-200065780.

(33) N. M. Green, *Adv. Protein Chem.,* **1975**, *29*, 85-133, https://doi.org/10.1016/S0065-3233(08)60411-8.

(34) Nomura, Y.; Sharma, V.; Yamamura, A.; Yokobayashi, Y. Selection of Silk-Binding Peptides by Phage Display. *Biotechnol. Lett.* **2011**, *33* (5), 1069-1073. https://doi.org/10.1007/s10529-011-0519-6.

(35) Capon, P. K.; Li, J.; Horsfall, A. J.; Yagoub, S.; Schartner, E. P.; Khalid, A.; Kirk, R. W.; Purdey, M. S.; Dunning, K. R.; McLaughlin, R. A.; Abell, A. D. A Silk-Based Functionalization Architecture for Single Fiber Imaging and Sensing. *Adv. Funct. Mater.* **2021**, 2010713. https://doi.org/10.1002/adfm.202010713.

(36) Huemmerich, D.; Slotta, U.; Scheibel, T. Processing and Modification of Films Made from Recombinant Spider Silk Proteins. *Appl. Phys. A* **2006**, *82* (2), 219-222. https://doi.org/10.1007/s00339-005-3428-5.

(37) Cheah, J. S.; Yamada, S. A Simple Elution Strategy for Biotinylated Proteins Bound to Streptavidin Conjugated Beads Using Excess Biotin and Heat. *Biochem. Biophys. Res. Commun.* **2017**, *493* (4), 1522-1527. https://doi.org/10.1016/j.bbrc.2017.09.168.

(38) Urrutia, A.; Bojan, K.; Marques, L.; Mullaney, K.; Goicoechea, J.; James, S.; Clark, M.; Tatam, R.; Korposh, S. Novel Highly Sensitive Protein Sensors Based on Tapered Optical Fibres Modified with Au-Based Nanocoatings https://www.hindawi.com/journals/js/2016/8129387/ (accessed Jan 4, 2021). https://doi.org/10.1155/2016/8129387.

(39) Wang, W.; Mai, Z.; Chen, Y.; Wang, J.; Li, L.; Su, Q.; Li, X.; Hong, X. A Label-Free Fiber Optic SPR Biosensor for Specific Detection of C-Reactive Protein. *Sci. Rep.* **2017**, *7* (1), 16904. https://doi.org/10.1038/s41598-017-17276-3.

(40) Khalid, A.; Lodin, R.; Domachuk, P.; Tao, H.; Moreau, J. E.; Kaplan, D. L.; Omenetto, F. G.; Gibson, B. C.; Tomljenovic-Hanic, S. Synthesis and Characterization of Biocompatible Nanodiamond-Silk Hybrid Material. *Biomed. Opt. Express* **2014**, *5* (2), 596-608. https://doi.org/10.1364/BOE.5.000596.

(41) Khalid, A.; Peng, L.; Arman, A.; Warren-Smith, S. C.; Schartner, E. P.; Sylvia, G. M.; Hutchinson, M. R.; Ebendorff-Heidepriem, H.; McLaughlin, R. A.; Gibson, B. C.; Li, J. Silk: A Bio-Derived Coating for Optical Fiber Sensing Applications. *Sens. Actuators B Chem.* **2020**, *311*, 127864. https://doi.org/10.1016/j.snb.2020.127864.

Supporting Information

S3.1 General materials

All reagents and solvents were purchased from Merck unless otherwise specified, at the highest purity level available. D-biotin (≥97.5%), 5(6)-carboxytetramethylrhodamine (TAMRA, ≥99%), Oxyma, and all Fmoc-protected building blocks including 6-(Fmoc-amino)hexanoic acid (Fmoc-Ahx-OH), Fmoc-Ser(tBu)-OH, Fmoc-Tyr(tBu)-OH, Fmoc-Thr(tBu)-OH, Fmoc-His(Trt)-OH, Fmoc-Trp(Boc)-OH and Fmoc-Glu(tBu)-OH were purchased from ChemImpex International. All amino acids were the L isomer. Streptavidin AlexaFluor-532 conjugate was purchased from ThermoFisher (S11224). Phosphate buffer solution (100 mM) was prepared from sodium phosphate salts and adjusted to pH 7.2 with aqueous solutions of 0.1 M HCl and 0.1 M NaOH.

Aqueous silk fibroin was prepared at RMIT University according to previously reported protocols[1,2] and shipped to the University of Adelaide on ice. Alternatively, aqueous silk fibroin was purchased from Merck at 50 mg/mL and stored at -80 °C (Supelco 5154-20mL). Aliquots (1 mL) were thawed overnight at 4 °C then dialysed in water for 48 h (water changed every ~12 h) using CelluSep T2 regenerated cellulose tubular membrane dialysis tubing with a 6000-8000 Da molecular weight cut off, wall thickness 30 μm, and flat width 32 mm.[1,2] After dialysis, the silk fibroin solution was stored at 4 °C. Any solids that formed during storage were removed by centrifugation at 7800 rpm for 10 min and the supernatant retained.

S3.2 Peptide synthesis

General SPPS procedure

Peptides were assembled by solid phase peptide synthesis (SPPS) using a standard Fmoc/tBu protocol, as follows:

Rink Amide PL resin (645 mg, 0.2 mmol, 0.31 mmol/g, Agilent) was swollen in 1:1 (v/v) DCM/DMF (10 mL) for 15 min, then the solution drained and the resin washed with DMF (3 × 8 mL). The resin-bound Fmoc protecting group was then removed by treatment of the resin with 20% (v/v) piperidine in DMF (8 mL) for 10 min, with intermittent stirring. The resulting solution was drained and the resin washed with DMF (3 × 8 mL), DCM (3 × 8 mL), and DMF (3 × 8 mL). A solution of the relevant *N*-terminally Fmoc-protected building block (5 equiv), HATU (5 equiv) and DIPEA (10 equiv) in DMF (10 mL) was added to the resin and allowed to react for 1 h, with intermittent stirring. The solution was drained and the resin washed successively with DMF (3 × 8 mL), DCM (3 × 8 mL), and DMF (3 × 8 mL). The *N*-terminal Fmoc group was subsequently removed by treatment of the resin with 20% (v/v) piperidine in DMF (8 mL) for 10 min with intermittent stirring. A TNBS test (see below) was used to verify that each coupling/deprotection step was successful, with retreatment as necessary. Successive couplings and Fmoc-deprotections were repeated to achieve the desired peptide sequence. After the final Fmoc-deprotection with 20% (v/v) piperidine in DMF (8 mL) for 10 min, the solution was drained and the resin washed with DMF (3 × 8 mL) and DCM (3 × 8mL) and then washed with diethyl ether (3 × 8 mL) to deswell the resin, and air-dried with suction.

TNBS Test:[3] A small spatula of swollen resin was removed and 1 drop each of TNBS solution (100 µL 5% (w/v) picrylsulfonic acid in H_2O added to 900 µL of DMF) and DIPEA solution (100 µL in 900 µL of DMF) were added, and the resin allowed to develop for 1 min. Clear/yellow beads indicated no free amine (negative, observed post successful coupling), and red/orange beads showed free amine (positive).

General resin cleavage procedure

The peptide was cleaved from the dried resin (and all amino acid side chains simultaneously deprotected) by treatment of this resin with a cleavage cocktail consisting of 92.5:2.5:2.5:2.5 (v/v) trifluoroacetic acid/triisopropylsilane/2,2'-(ethylenedioxy)diethanethiol/water (10 mL), and the suspension was placed on a table rocker for 1 h. The solution was pipetted away from the resin and concentrated to 1-1.5 mL under a stream of N_2. Diethyl ether (10 mL) was added and the mixture cooled at -20 °C overnight. The resulting precipitate was pelleted by centrifugation (7800 rpm, 15 min) and the supernatant decanted. The solid was dried under a stream of N_2, dissolved in 1:1 (v/v) acetonitrile:water, syringe filtered (20 µm PTFE syringe filter) and lyophilised to give the crude peptide as a fluffy solid.

General peptide purification and characterisation

Crude peptides were purified by semi-preparative RP-HPLC on a Gilson GX-Prep RP-HPLC system equipped with a Phenomenex Aeris™ 5 µm Peptide XB-C18 100 Å 10 × 250 mm column over a linear 25-50% gradient of ACN (B) in water (A) with 0.1% trifluoroacetic acid, over 25 min, at 4 mL/min and visualised at 220 and 254 nm. Pure fractions were combined and lyophilised to give the final product. Product purity was confirmed to be >85% by analytical RP-HPLC on an Agilent Infinity 1260 analytical HPLC equipped with a Phenomenex Luna™ C18(2) 100 Å 4.6 × 250 mm column over a linear gradient of 5-50% B over 15 min, at 1.5 mL/min and visualised at 220 nm. Product identity was confirmed by high resolution mass spectrometry on an Agilent 6230 ESI MS.

SBP-Biotin: D-biotin-SYTFHWHQSWSS-NH_2

The peptide with sequence SYTFHWHQSWSS was assembled on resin as per the *General SPPS procedure*. Following *N*-terminal deprotection, a portion of the peptide-loaded resin (0.05 mmol) was swollen in 1:1 (v/v) DCM/DMF (5 mL) and washed with DMF (3 × 5 mL). A solution of D-biotin (61.1 mg, 0.25 mmol, 5 equiv), HATU (95.0 mg, 0.25 mmol, 5 equiv) and DIPEA (174 µL, 0.5 mmol, 10 equiv) in DMF (5 mL) was added to the resin and stirred intermittently for 4 h at rt. The solution was drained and the resin washed with DMF (3 × 5 mL), DCM (3 × 5 mL), and DMF (3 × 5 mL). Coupling was verified by TNBS test, then the resin was deswelled with diethyl ether

(3 × 5 mL) and air-dried with suction. The crude peptide was simultaneously cleaved from the resin and globally deprotected as per the *General resin cleavage procedure*, then purified as per the *General peptide purification and characterisation procedure*, to provide SBP-Biotin as a white solid. Analytical RP-HPLC (220 nm) 92%. HRMS (ESI+) expected $[M+3H]^{3+}$ for $C_{89}H_{115}N_{23}O_{22}S$ (1889.8308): 630.9516, found $[M+3H]^{3+}$ 630.9510.

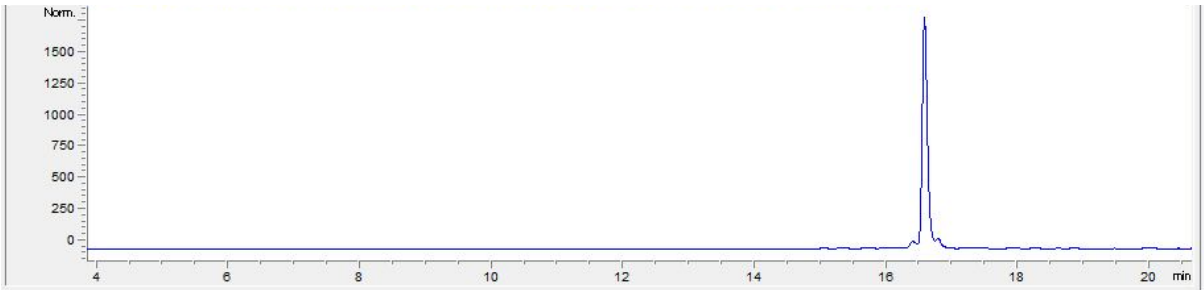

Figure S3.1. Analytical HPLC trace for SBP-Biotin run over a linear gradient of 5-50% ACN in H_2O with 0.1% TFA, from 5 min to 20 min, visualized at 220 nm.

SBP-TAMRA: TAMRA-Ahx-SYTFHWHQSWSS-NH_2

The peptide with sequence Ahx-SYTFHWHQSWSS was assembled on resin as per the *General SPPS procedure*. Following *N*-terminal deprotection, a portion of the resin-bound peptide (0.05 mmol) was transferred to a microwave vial (7 mL capacity) using DMF (1-2 mL). A solution of 5(6)-carboxyTAMRA (64.6 mg, 0.15 mmol, 3 equiv), 1,3-diisopropylcarbodiimide (23.2 µL, 0.15 mmol, 3 equiv) and Oxyma (21.3 mg, 0.15 mmol, 3 equiv) in DMF (2 mL) was added, then DMF was used to rinse the fluorophore into the reaction vessel to obtain a final reaction volume of 5 mL. The reaction vessel was heated by microwave irradiation to 60 °C for 30 min then cooled to rt. The resultant contents of the microwave vessel were transferred to a fritted syringe and the solution drained, then the resin washed extensively with DMF (5 × 10 mL) and DCM (5 × 5 mL) until no colour remained in the washings. The resin was then washed with diethyl ether (3 × 5 mL) and air-dried with suction. The crude peptide was simultaneously cleaved from the resin and globally deprotected according to the *General resin cleavage procedure*. The crude peptide was purified as per the *General peptide purification and characterisation procedure*, to provide SBP-TAMRA as a purple solid.[4] Analytical RP-HPLC (220 nm) 87%. HRMS (ESI+) expected $[M+3H]^{3+}$ for $C_{104}H_{121}N_{23}O_{24}$ (2075.8955): 692.9732, found $[M+3H]^{3+}$ 692.9732.

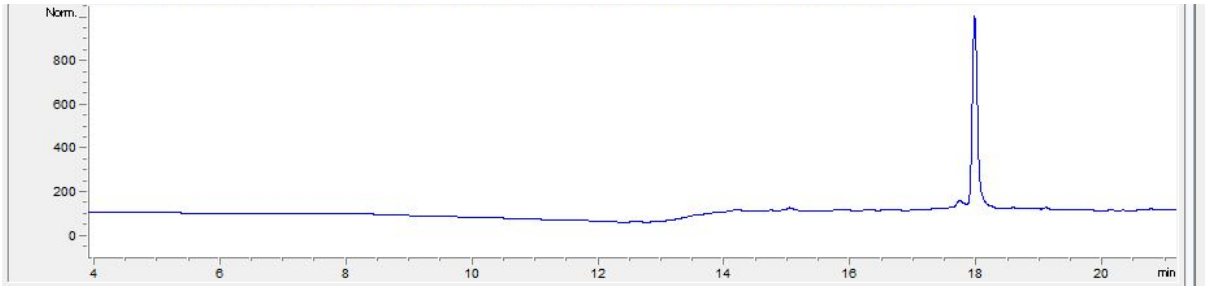

Figure S3.2. Analytical HPLC trace for SBP-TAMRA run over a linear gradient of 5-50% ACN in H_2O with 0.1% TFA, from 5 min to 20 min, visualized at 220 nm.

S3.3 Fibre coating

Method A

A mixture of aqueous silk fibroin (65 mg/mL, 100 µL), distilled water (80 µL), and functionalised peptide (SBP-TAMRA or SBP-Biotin, 100 µM, 20 µL) was gently pipetted until homogeneous. Double-clad fibre (DCF) was cleaved with a fibre cleaver (LDC401A, Thorlabs, USA) to expose a fresh section of DCF tip, and 1-2 mm of the fibre tip was dipped into the silk mixture for 30 s. The silk fibroin coated DCF was then dipped into 90% aq. HPLC grade methanol for 10 s to convert the silk fibroin from the silk I α-helix to the silk II β-sheet,[5,6] then removed and dried in air for at least 10 s before use.

The control fibres coated with silk fibroin only, for use in the streptavidin detection experiments, were also prepared according to Method A with the functionalised SBP replaced with water (20 µL).

Method B

Aqueous silk fibroin (65 mg/mL, 100 µL) was diluted with water (100 µL) and the mixture was gently pipetted until homogenous. DCF was cleaved with a fibre cleaver (LDC401A, Thorlabs, USA) to expose a fresh section of DCF tip and 1-2 mm of the fibre tip was dipped into the mixture and held for 30 s. The coated fibre was dipped into 90% aq. HPLC grade methanol for 10 s to convert the silk fibroin from the silk I α-helix to the silk II β-sheet,[5,6] then the silk fibroin coated fibre was removed and dried in air for 10 s. The fibre was then dipped into functionalised SBP (SBP-TAMRA or SBP-Biotin, 10 µM, 200 µL) for 30 s and dried in air for at least 10 s before use.

The functionalised SBP was replaced with free TAMRA (10 μM, 200 μL) to prepare the control fibres used in the silk coating retention experiments.

Silk fibroin only

Control fibres for the protein detection model system were prepared by coating with silk fibroin only. Aqueous silk fibroin (65 mg/mL, 100 μL) was diluted with water (100 μL) and the mixture was gently pipetted until homogenous. DCF was cleaved with a fibre cleaver (LDC401A, Thorlabs, USA) to expose a fresh section of DCF tip and 1-2 mm of the fibre tip was dipped into the mixture and held for 30 s. The coated fibre was dipped into 90% aq. HPLC grade methanol for 10 s to convert the silk fibroin from silk I to silk II,[5] then the silk fibroin coated fibre was dried in air for 10 s.

S3.4 Optical fibre sensing system

An optical fibre sensing system was built in order to stimulate fluorescence emission and collect fluorescence spectra from the SBP and silk fibroin coated optical fibres. Double-clad fibre (DCF13, Thorlabs, USA, 9 μm core diameter, 105 μm inner cladding, 125 μm outer cladding) was used to fabricate the fibre sensors. A 532 nm laser (CrystaLaser, USA, 25 mW, model CL532-025) was coupled into the core of the DCF to excite the relevant fluorophore (TAMRA or AlexaFluor™ 532) located on the fibre tip. The fluorescence signal was then collected through the inner cladding of the DCF, passed through a long pass filter to remove the excitation light (532 nm, Semrock 532 LP EdgeBasic, USA), and measured with a portable spectrometer (Ocean Optics QE65000, USA). See Figure S3.3 below for a diagram of the system. The laser power at the fibre tip was measured to be 2.7 mW. A shutter (LS6 & VCM-D1, Uniblitz, USA) was installed to minimise excess exposure of the fluorophore to excitation light, with custom LabVIEW software (National Instruments Corp, USA) used to synchronise the Ocean Optics spectrometer acquisition with a 100 ms shutter opening for each collection. A dark spectrum was also acquired immediately after each measurement with the laser shutter closed to remove the effects of ambient light from the experiment. Before collecting fluorescence spectra, uncoated fibres were connected to the system and a background spectrum collected. This background spectrum was subtracted from all

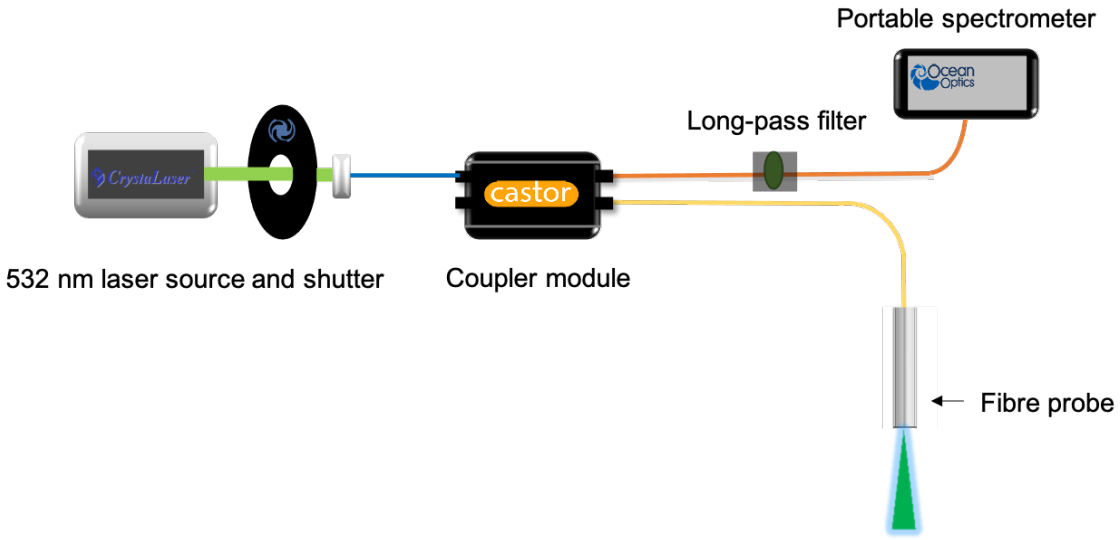

Figure S3.3. Schematic of the optical fibre coupled laser and spectrometer used for fluorescence spectra collection. Blue: single-mode fibre, orange: multimode fibre, yellow: double-clad fibre.

subsequent spectra. The total intensity was integrated between 570 and 600 nm for TAMRA spectra, and between 565 and 600 nm for AlexaFluor-532 spectra. The resultant integrated intensities were plotted and compared as described in the main text.

S3.5 Atomic absorption spectroscopy

Atomic absorption spectroscopy (AAS) was used to determine the lithium concentration in aqueous silk fibroin solutions. A standard curve for Li between 1 and 100 ppm was prepared from stock solutions of LiOH in distilled water. Three samples of aqueous silk fibroin solutions were prepared at 50 mg/mL: the in-house silk fibroin, the Merck silk fibroin as received, and a dialysed sample of the Merck silk fibroin. The Merck silk fibroin was dialysed against 1 L of water for 48 h with the water changed every ~12 h, using CelluSep T2 regenerated cellulose tubular membrane dialysis tubing with a 6000-8000 Da molecular weight cut off, wall thickness 30 µm, and flat width 32 mm. The three silk fibroin samples were diluted 10-fold, then run on a Varian Spectra AA 250+ Atomic Absorption Spectrophotometer. The lithium concentration (ppm) was calculated for each sample with reference to the standard curve (see Table 3.1 in the main text).

S3.6 Silk fibroin concentration

Processed silk fibroin is stable under refrigeration at ~4 °C for 3-4 months, after which severe aggregation occurs. This results in a thick silk gel that is not easily handled and cannot be disaggregated. The aggregation process can be slowed by storage at -80 °C, and by

centrifugation of the silk fibroin sample when small aggregates are observed in solution. However, removal of these aggregates changes the concentration of the remaining silk fibroin supernatant. Therefore, a calibration curve for silk fibroin concentration was constructed based on absorbance at 205 nm, which is predominantly from amide bonds,[7] to ensure that all silk solutions were used at the same concentration.

Freshly prepared aqueous silk fibroin at 65 mg/mL (calculated by the dry weight of silk fibroin) was diluted to 60, 55, 50, 45, 40, and 35 mg/mL, then each stock solution was further diluted in water 200-fold and the absorbance at 205 nm measured three times per sample on a Thermofisher Nanodrop 2000 UV/Vis Spectrophotometer. This absorbance was plotted against the stock concentration, and a calibration curve calculated using GraphPad Prism 9 with a forced y-intercept of 0 (Figure S3.4, Equation S3.1). Absorbance at 205 nm was chosen over than the traditional 280 nm wavelength used for proteins,[8] as silk fibroin predominantly consists of the amino acids glycine (46 mol %) alanine (30 mol %), and serine (12 mol %), which do not have a strong absorbance at 280 nm.[6,9] There is also minimal tryptophan (0.2 mol %) or tyrosine (5.3 mol %) present to contribute to absorption at 280 nm.[9]

The concentration of all silk fibroin solutions used in this work were calculated with reference to this calibration curve to ensure fibre coating results were comparable. Note that these concentrations are relative to the original 65 mg/mL sample, as the extinction coefficient of the silk fibroin was not calculated.

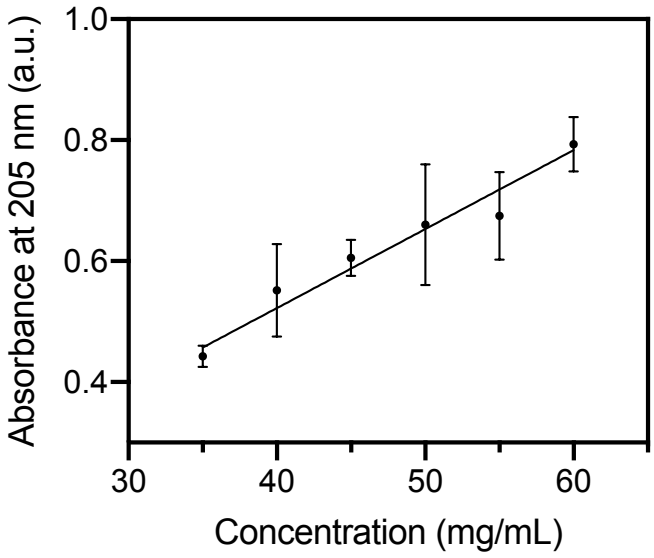

Figure S3.4. Calibration curve for silk fibroin absorbance at 205 nm against concentration (mg/mL). The equation of best fit was calculated using GraphPad Prism 9 linear regression with a y intercept set to 0, to give absorbance = 0.01306 * concentration (in mg/mL). Goodness of fit (Sy.x) 0.05892. Data is plotted as mean μ standard deviation of three reads.

$$A_{205\,nm} = 0.01306 \times Silk\ concentration\ in \frac{mg}{mL} \qquad S3.1$$

S3.7 Detection of fluorescently tagged streptavidin

Optical fibres were coated with silk fibroin and SBP-Biotin by method A or B, then used to detect AlexaFluor-532 tagged streptavidin as detailed in the main text. Figure 3.2 shows the integrated intensity between 565 and 600 nm for one fibre of each coating type: one coated with silk fibroin only, one coated with silk fibroin and SBP-Biotin by method A, and one coated with silk fibroin and SBP-Biotin by method B. Additional plots for all three fibres prepared by each coating type are provided here, along with sample full spectra.

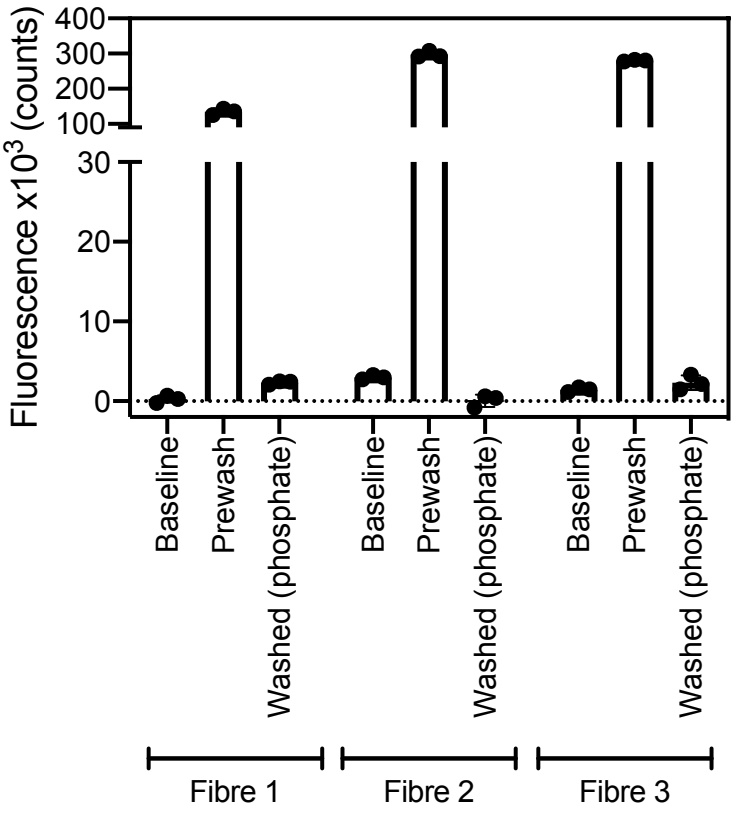

Figure S3.5. SBP-Biotin sensing of AlexaFluor-532 tagged streptavidin. Each point is the integrated intensity between 565 and 600 nm for a single spectrum. All fibres are control fibres coated with silk fibroin only, where all prewash fluorescence was lost upon washing with phosphate buffer (100 mM, pH 7.2). Excitation for all fibres was at 532 nm, data is plotted as mean μ standard deviation of three reads.

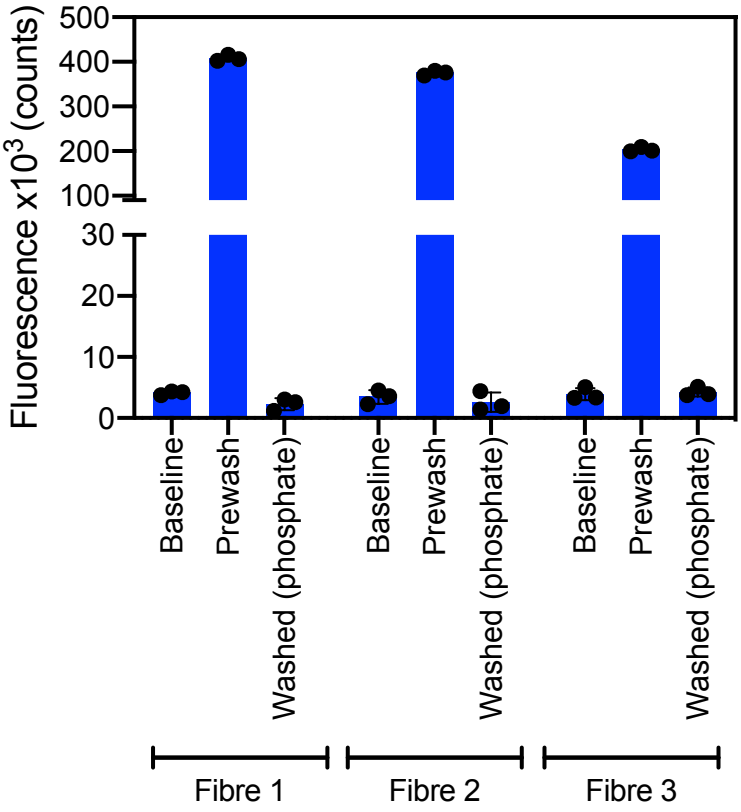

Figure S3.6. SBP-Biotin sensing of AlexaFluor-532 tagged streptavidin. Each point is the integrated intensity between 565 and 600 nm for a single spectrum. All fibres were coated with silk fibroin and SBP-Biotin by method A, where all prewash fluorescence was lost upon washing with phosphate buffer (100 mM, pH 7.2). Excitation for all fibres was at 532 nm, data is plotted as mean μ standard deviation of three reads.

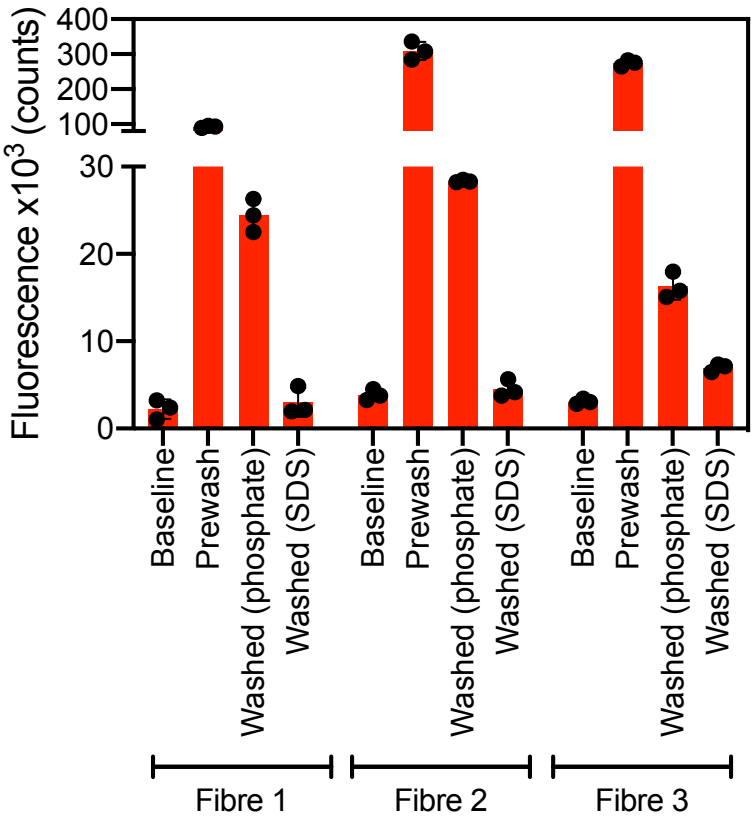

Figure S3.7. SBP-Biotin sensing of AlexaFluor-532 tagged streptavidin. Each point is the integrated intensity between 565 and 600 nm for a single spectrum. All fibres were coated with silk fibroin and SBP-Biotin by method B. Washing with phosphate buffer(100 mM, pH 7.2) did not remove all prewash fluorescence. Washing with 2% aqueous sodium dodecyl sulfate (SDS) removed all fluorescence. Excitation for all fibres was at 532 nm, data is plotted as mean μ standard deviation of three reads.

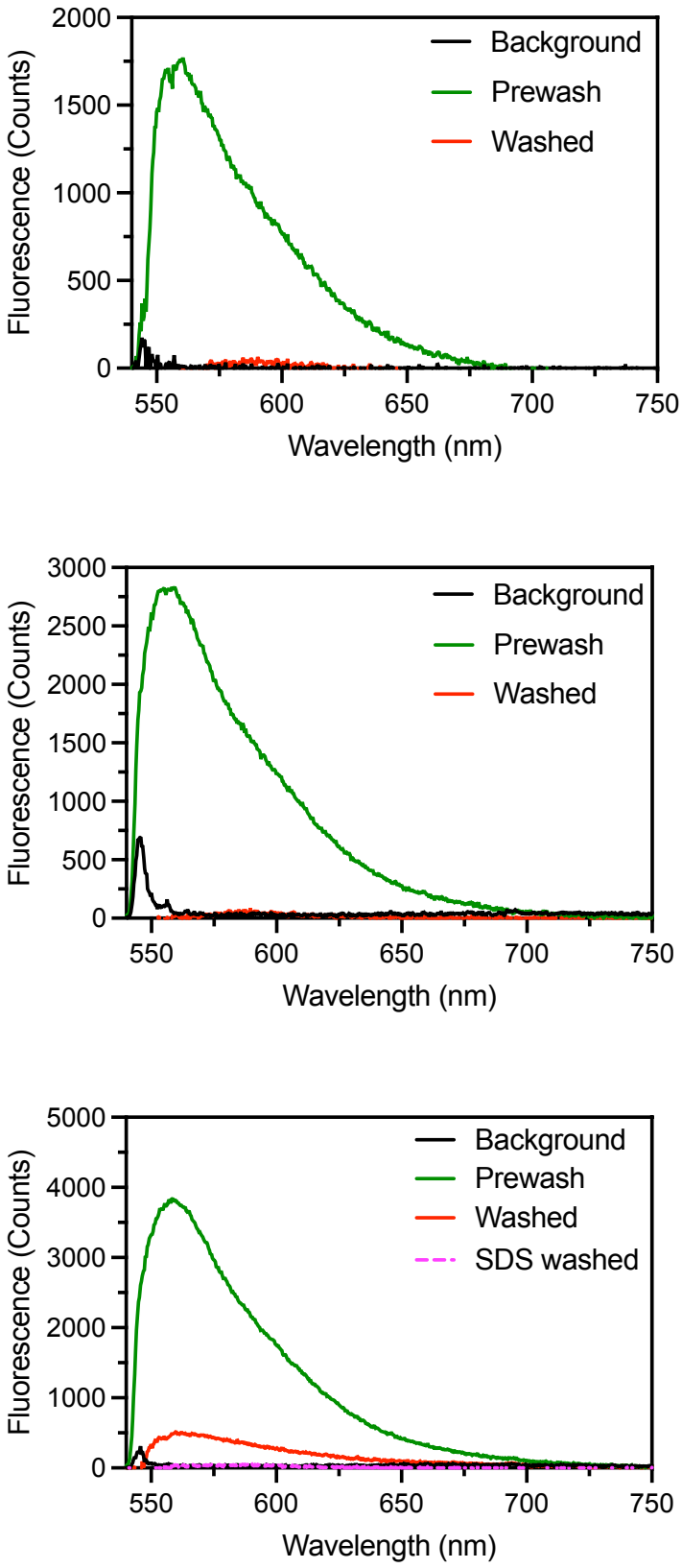

Figure S3.8. Sample full spectra for an optical fibre coated with **top)** silk fibroin only, **middle)** silk fibroin and SBP-Biotin by method A, and **bottom)** silk fibroin and SBP-Biotin by method B. Black) background fluorescence before exposure to AlexaFluor-532 tagged streptavidin. Green) Fluorescence spectrum after dipping in streptavidin solution. Red) Fluorescence spectrum after washing 3 × 30 s in phosphate buffer (100 mM, pH 7.2). Pink, dashed) Fluorescence spectrum after washing 3 × 30 s in sodium dodecyl sulfate (SDS, 2% aqueous). Excitation wavelength for all spectra was 532 nm.

S3.8 Retention of SBP-TAMRA on optical fibres

Optical fibres were coated with silk fibroin and SBP-TAMRA or free TAMRA by method B, then washed by submerging the fibre tips in water on a short term (3 × 30 s) or a long term (18 h) basis as detailed in the main text. The calculated fluorescence retention shown in Figure 3.4 for the method B coated fibres is replotted here with comparison to the method A coatings.[4] Sample full spectra are also provided for each coating type.

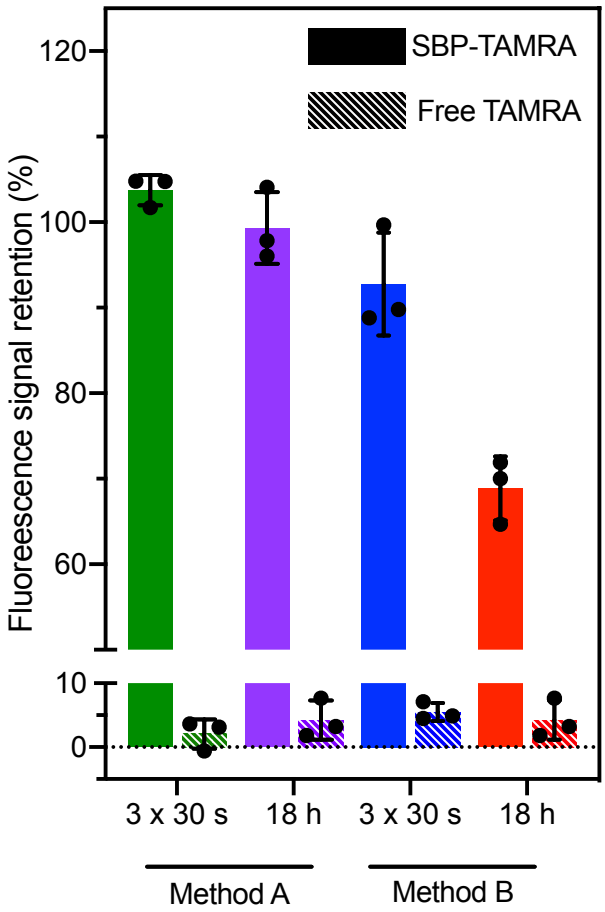

Figure S3.9. Percentage fluorescence retention on silk fibroin coated fibres, calculated from comparison of the integrated intensity (570 to 600 nm) of fluorescence spectra obtained before and after washing each fibre. Each point shown is the average of three spectra for one fibre, with a total of three fibres plotted per bar as mean μ standard deviation. The solid bars represent fibres coated with silk fibroin and SBP-TAMRA, while the striped bars represent fibres coated with silk fibroin and free TAMRA. **Left**, fibres coated by method A and washed in water for 3 × 30 s (green) or soaked overnight (purple). **Right**, fibres coated by method B washed in water 3 × 30 s (blue) or soaked overnight (red). All spectra were collected with an excitation wavelength of 532 nm.

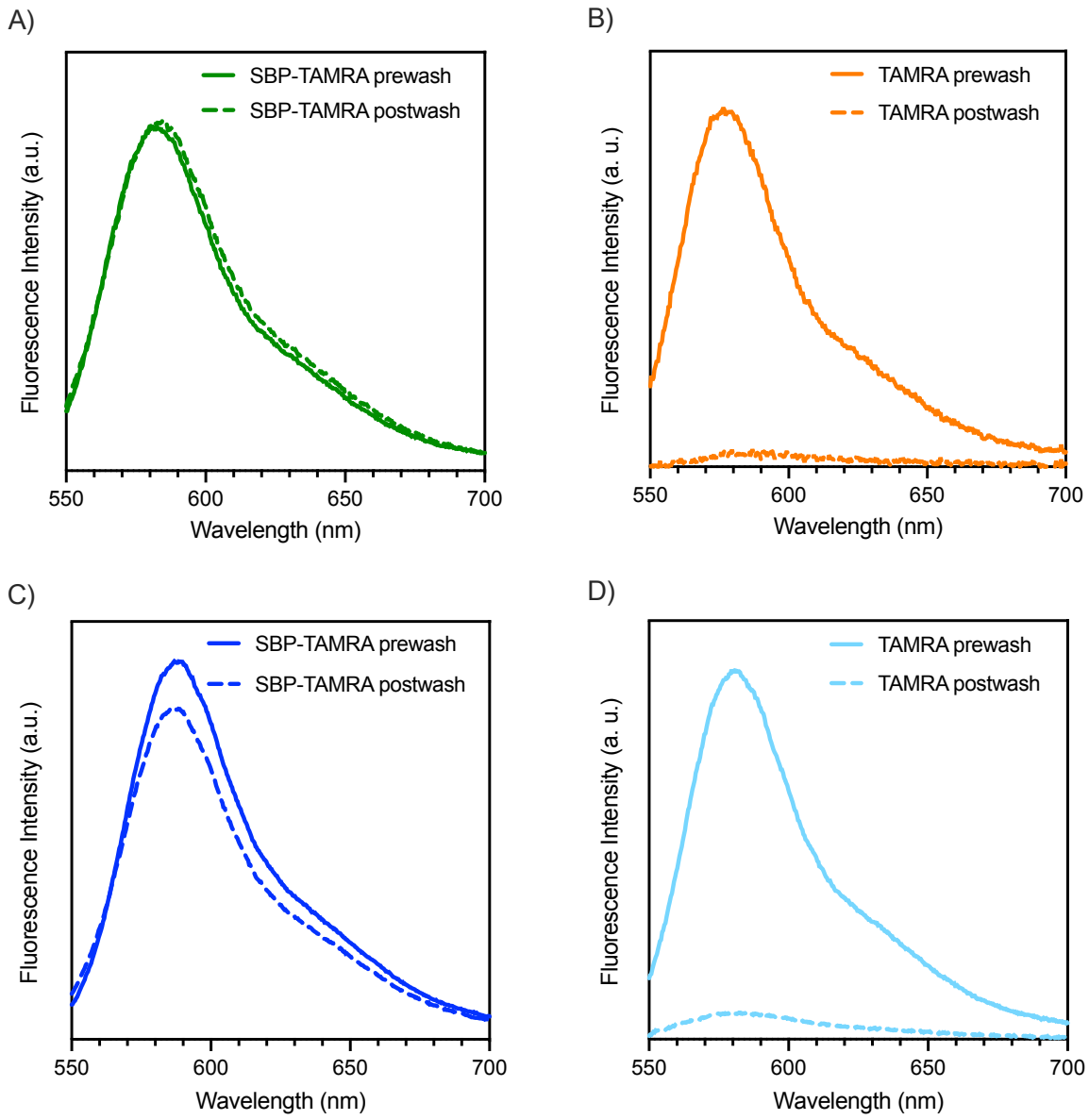

Figure S3.10. Full spectra obtained for sample optical fibres, coated with silk fibroin and SBP-TAMRA or free TAMRA then washed 3 × 30 s in water. Excitation at 532 nm for all spectra.

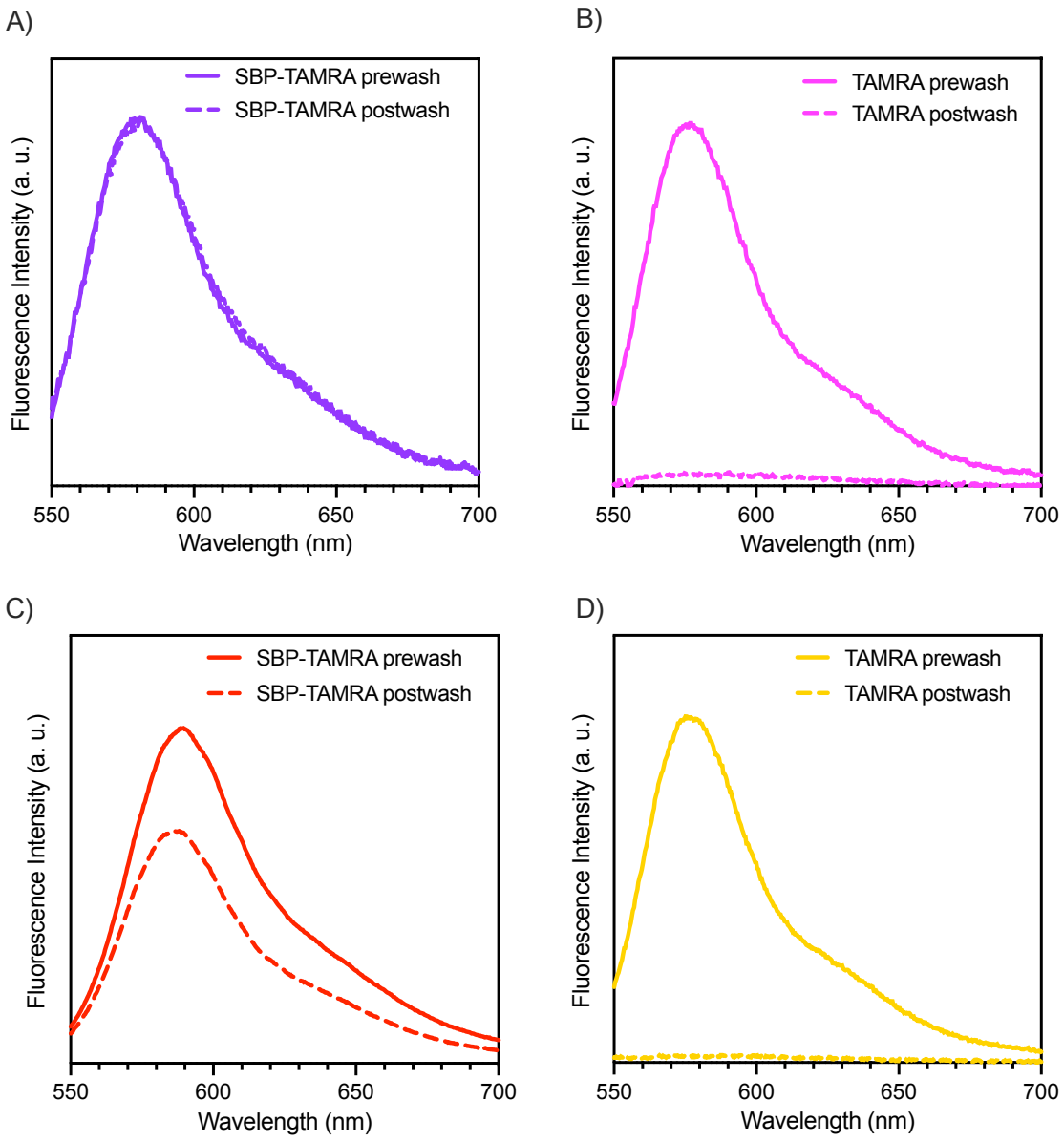

Figure S3.11. Full spectra obtained for sample optical fibres, coated with silk fibroin and SBP-TAMRA or free TAMRA then soaked in water for 18 h. Excitation at 532 nm for all spectra.

S3.9 Supplementary references

(1) Khalid, A.; Lodin, R.; Domachuk, P.; Tao, H.; Moreau, J. E.; Kaplan, D. L.; Omenetto, F. G.; Gibson, B. C.; Tomljenovic-Hanic, S. Synthesis and Characterization of Biocompatible Nanodiamond-Silk Hybrid Material. *Biomed. Opt. Express* **2014**, *5* (2), 596-608. https://doi.org/10.1364/BOE.5.000596.

(2) Khalid, A.; Peng, L.; Arman, A.; Warren-Smith, S. C.; Schartner, E. P.; Sylvia, G. M.; Hutchinson, M. R.; Ebendorff-Heidepriem, H.; McLaughlin, R. A.; Gibson, B. C.; Li, J. Silk: A Bio-Derived Coating for Optical Fiber Sensing Applications. *Sens. Actuators B Chem.* **2020**, *311*, 127864. https://doi.org/10.1016/j.snb.2020.127864.

(3) Hancock, W. S.; Battersby, J. E. A New Micro-Test for the Detection of Incomplete Coupling Reactions in Solid-Phase Peptide Synthesis Using 2,4,6-Trinitrobenzene-Sulphonic Acid. *Anal. Biochem.* **1976**, *71* (1), 260-264. https://doi.org/10.1016/0003-2697(76)90034-8.

(4) Capon, P. K.; Li, J.; Horsfall, A. J.; Yagoub, S.; Schartner, E. P.; Khalid, A.; Kirk, R. W.; Purdey, M. S.; Dunning, K. R.; McLaughlin, R. A.; Abell, A. D. A Silk-Based Functionalization Architecture for Single Fiber Imaging and Sensing. Adv. Funct. Mater. 2021, 2010713. https://doi.org/10.1002/adfm.202010713.

(5) Huemmerich, D.; Slotta, U.; Scheibel, T. Processing and Modification of Films Made from Recombinant Spider Silk Proteins. *Appl. Phys. A* **2006**, *82* (2), 219-222. https://doi.org/10.1007/s00339-005-3428-5.

(6) Qi, Y.; Wang, H.; Wei, K.; Yang, Y.; Zheng, R.-Y.; Kim, I. S.; Zhang, K.-Q. A Review of Structure Construction of Silk Fibroin Biomaterials from Single Structures to Multi-Level Structures. *Int. J. Mol. Sci.* **2017**, *18* (3). https://doi.org/10.3390/ijms18030237.

(7) Anthis, N. J.; Clore, G. M. Sequence-Specific Determination of Protein and Peptide Concentrations by Absorbance at 205 Nm. *Protein Sci.* **2013**, *22* (6), 851-858. https://doi.org/10.1002/pro.2253.

(8) Christa M. Stoscheck. [6] Quantitation of Protein. *Methods Enzymol.* **1990**, *182*, 50-68. https://doi.org/10.1016/0076-6879(90)82008-P.

(9) Murphy, A. R.; Kaplan, D. L. Biomedical Applications of Chemically-Modified Silk Fibroin. *J. Mater. Chem.* **2009**, *19* (36), 6443. https://doi.org/10.1039/b905802h.

Chapter 4: Covalent functionalisation of nanodiamonds

4.1 Introduction

Nanodiamonds (NDs) are a versatile material with application in fields such as drug delivery,[1-4] sensing,[5] cell/tissue labelling,[6-8] and advanced optics.[9-13] Surface functionalisation of a ND with an organic molecule provides a hybrid nanomaterial that bears the properties of both components. For example, attachment of a drug molecule to a ND bearing a nitrogen-vacancy centre (NV, see Chapter 1) provides a conjugate nanoparticle that can be detected by the NV fluorescence, while the drug enacts its therapeutic action at the hybrid nanoparticle's location. Surface functionalisation of NDs is defined in this thesis as '*the attachment of an additional compound to the nanodiamond surface through covalent or non-covalent bonding*'. Hence, this definition excludes surface *modifications*, such as a reaction to obtain hydroxylated NDs from carboxylated NDs. This is an important distinction, as there is a large body of research on surface *modification*, while there is less research on surface *functionalisation*.

4.1.1 Nanodiamond surfaces

The ND surface can be modified to bear a wide array of functional groups including amines, alcohols, and carboxylic acids.[14] Amines are the least commonly encountered surface functional group on NDs, as there is no direct synthetic route to graft amines on the ND surface. Instead of a surface *modification*, the surface of the ND must be *functionalised* in order to obtain an aminated surface. Such functionalisation methods include silanisation or diazotisation.[15] The aminated NDs can then be further functionalised. For example, Barras *et al*. reported a dicyclohexylcarbodiimide (DCC) mediated coupling of 4-azidobenzoic acid onto commercial amine decorated detonation NDs (DNDs) as a model system for subsequent Huisgen cyclisation reactions.[16] More recently,

Gaur and coworkers used C-N cross couplings to generate secondary amines on DNDs, the first demonstration of this chemistry on NDs.[17]

Beyond aminated NDs, hydroxyl-terminated NDs provide a good handle for further surface functionalisation to be conducted. Commercial 'as synthesised' NDs can be modified to bear hydroxy surface groups by treatment with reducing agents such as $LiAlH_4$, $NaBH_4$, or BH_3. This area of research has been led by the Krueger group, who found that BH_3 in THF was the optimal reducing agent to prepare hydroxylated NDs, as it does not leave residual metal (ie Li, Al or Na) on the NDs.[15] Hydroxylated NDs can be functionalised using the silane chemistry developed for glass modification, based on the Stöber process.[15,18,19] Alternatively, the hydroxyl group can react to form an ester bond with acyl chlorides,[20,21] poly(glycerol),[22] or glycidol.[23,24]

An alternative handle for ND surface functionalisation is a carboxylic acid. A fully carboxylated surface is typically obtained by treatment of 'as synthesised' NDs with strongly oxidising mixtures, frequently acids. The exact treatment conditions used vary between laboratories, but are most commonly a mixture of HNO_3 and H_2SO_4 heated at 70-80 °C for 18-72 h. Carboxylated NDs can be reacted with amines through the use of coupling agents such as EDC/NHS or DCC,[7,25-27] or *via* an acyl chloride intermediate.[28,29] The use of more recently developed coupling agents such as HATU or OxymaPure®,[30,31] or acyl fluoride forming reagents,[32,33] has not yet been reported for functionalisation of carboxylated NDs.

4.1.2 Quantification of nanodiamond functionalisation

Quantification of the amount of reagent bound to NDs is critical as it directly affects application of the functionalised NDs. For example, the exact number of drug molecules attached to an ND will impact on the drug delivery system's efficacy. Techniques including TGA, UV-Vis absorbance, and the Kaiser test can be used to determine the quantitative surface loading of an organic molecule adhered to a ND (Table 4.1, also see Chapter 1). However, there is considerable variability in the stoichiometry of ND functionalisation reactions in literature to date, and further investigation is clearly required.

Table 4.1. Summary of quantitative techniques for calculation of the loading of organic molecules on nanodiamonds, sorted by the ND surface functional group. #The Kaiser test is only applicable to surface bearing free amines. *The Boehm titration is only applicable to the calculation of surface carboxylic acids and is therefore a theoretical maximum for attachment of organic molecules to those carboxylic acids.

Functional group	Technique	Calculated loading (mmol/g)	Reference(s)
OH	Kaiser test#	0.15-1	Jarre *et al*. #34
OH	TGA	0.2 to 1.5	Krüger *et al*. #15,18,35
OH	TGA	0.15-0.5	Barras *et al*. #16,36
OH	UV-Vis	0.27	Barras *et al*. #36
CO_2H	Boehm titration*	0.52	Schmidlin *et al*. #37
CO_2H	TGA	0.9	Cheng *et al*. #38

4.2 Quantification using unreacted reagent

The techniques employed to characterise or calculate surface loadings of functionalised NDs presented in literature to date (Table 4.1) have focused on the ND itself, but neglected the presence of any unreacted reagent after the functionalisation reaction. There is untapped potential in this unreacted reagent, as examining the amount consumed in the reaction provides an alternative route to determine the surface loading of an ND. This enables quantification of ND functionalisation without relying on the use of a destructive analytical technique on the final nanomaterial. Critically, this approach is orthogonal to the currently existing spectroscopic (e.g FTIR, Raman) and analytical (e.g TGA, titration) techniques that use the solid ND component of the ND functionalisation reaction.

The unreacted reagent is typically separated from the functionalised ND sample by centrifugation. The centrifuged NDs form a pellet at the base of the centrifuge tube while the unreacted reagent remains dissolved in the supernatant. This provides an opportunity to develop new techniques to calculate surface loading of functionalised NDs based on the unreacted reagent (Scheme 4.1 below)

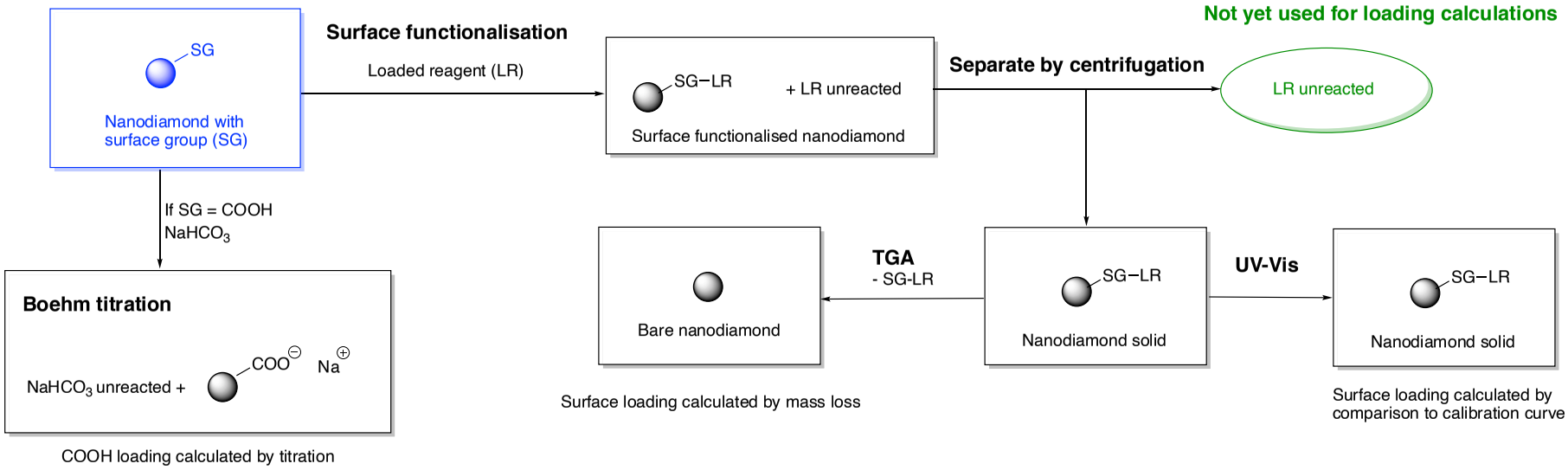

Scheme 4.1. Summary of the methods to determine loading of a reagent on nanodiamonds (NDs), starting from NDs with a terminal surface group for attachment (blue). If the surface group is a carboxylic acid, the Boehm titration can be used. Otherwise, the amount of reagent attached to the NDs can be calculated by thermogravimetric analysis, Kaiser test (free amines only), or UV-Vis absorbance. The unreacted reagent that is separated by centrifugation is yet to be used for loading calculations.

4.2.1 High-performance liquid chromatography system

Quantification of the unreacted reagent remaining in solution after a ND functionalisation reaction was first investigated using analytical reverse phase high-performance liquid chromatography (RP-HPLC). 4-Fluorobenzylamine was chosen as a model compound as the primary amine is available to form an amide bond with carboxylic acids on the ND surface (Scheme 4.2), and it has a distinct peak in analytical HPLC traces (Figure 4.1). Fluorobenzene was also added to the reaction mixture as an internal standard which does not participate in the coupling reaction. The appended fluorine present in both 4-fluorobenzylamine and fluorobenzene was selected to allow ^{19}F NMR-based confirmation of the HPLC quantification results. Unfortunately, the capability to perform ^{19}F NMR was out of commission for the duration of this study. Thus, the discussion in this thesis is limited to analytical HPLC only.

Pure samples of 4-fluorobenzylamine and fluorobenzene (1 mM in ACN) were first subjected to analytical RP-HPLC, with a 0-100% gradient of ACN over 15 min (see Experimental section 4.4.2). The resulting chromatograms (Figure 4.1) revealed that 4-fluorobenzylamine eluted at 12.3 min (82% ACN) and fluorobenzene eluted at 19 min (93% ACN). The coupling agents DIC and Oxyma were also subjected to analytical RP-HPLC, and Oxyma was found to elute at 10.9 min (73% ACN). DIC was not detected as it does not absorb at any of the wavelengths available on the HPLC instrument (220, 254, 280 nm). The peak observed in each analyte's chromatogram (4-fluorobenzylamine, fluorobenzene or Oxyma) was integrated, then divided by the integral of the fluorobenzene peak (the internal standard) to calculate relative response factors of 1.1 and 9.8 for 4-fluorobenzylamine and Oxyma, respectively (Table 4.2).[39]

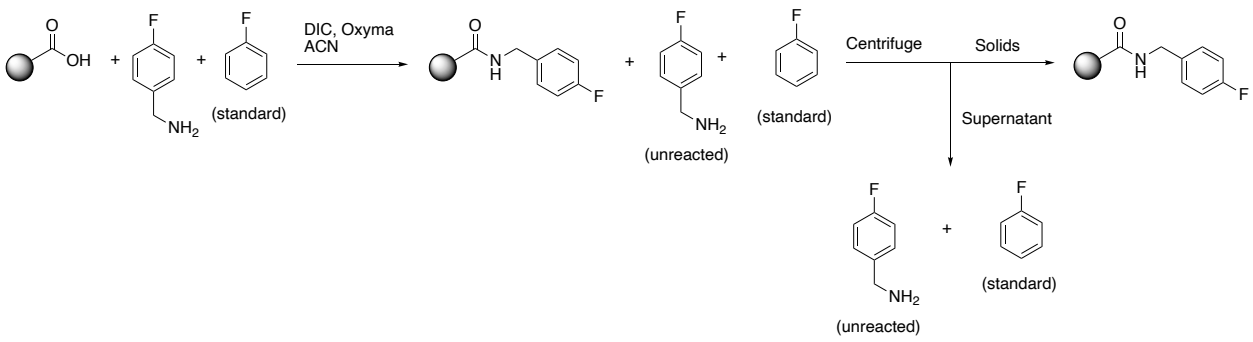

Scheme 4.2. General scheme for quantification of the amount of 4-fluorobenzylamine attached to carboxylated NDs through DIC/Oxyma coupling.

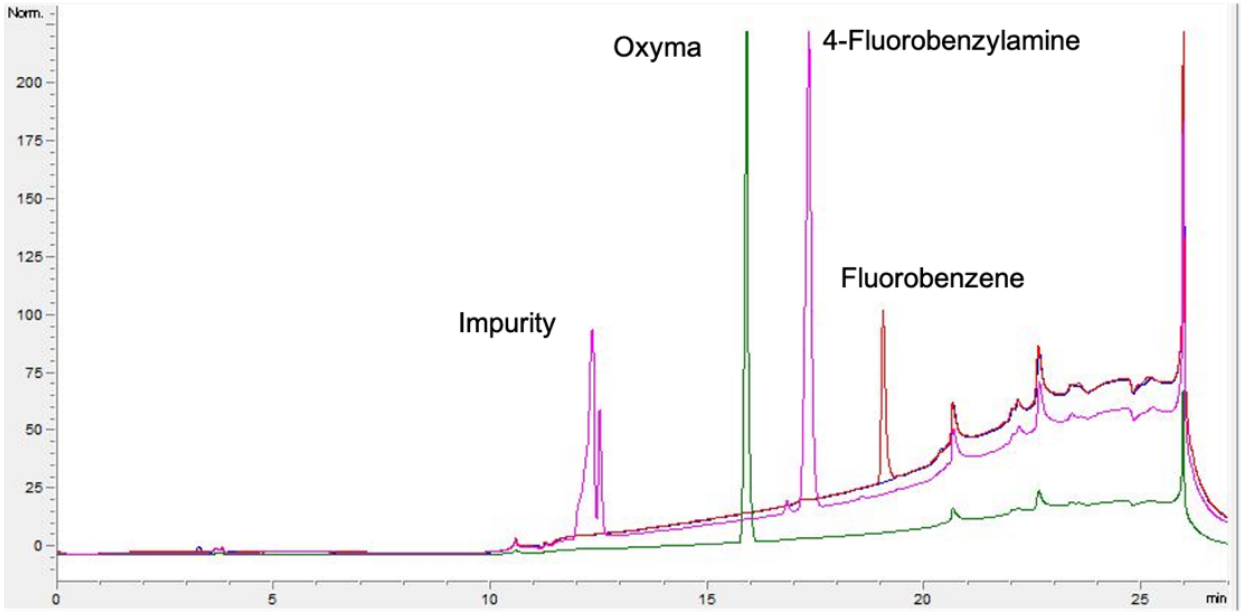

Figure 4.1. RP-HPLC chromatograms for 4-fluorobenzylamine (pink), fluorobenzene (red), Oxyma (green), and a blank (methanol, brown, largely underneath the red fluorobenzene signal) all visualised at 220 nm. An impurity from the column is present in all samples at ~12.5 min.

Table 4.2. The integrated RP-HPLC peak areas and calculated relative response factors for 4-fluorobenzylamine, fluorobenzene, and Oxyma.

Compound	Concentration (mM)	HPLC peak area	Relative Response
4-Fluorobenzylamine	1	537.8	1.1
Fluorobenzene	1	485.2	1.0
Oxyma	1	4774	9.8

The relative response factor calculated for 4-fluorobenzylamine by RP-HPLC was verified using six standard solutions of 4-fluorobenzylamine at concentrations of 0.25, 0.50, 1.0, 2.0, 3.0, and 4.0 mM in ACN. The internal standard fluorobenzene (2 mM) was added to each standard solution, then each mixture was subjected to analytical RP-HPLC and the resulting chromatogram collected. The observed peaks in the chromatogram were assigned to 4-fluorobenzylamine or fluorobenzene based on elution time, then integrated. This integral was used to back-calculate the concentration of 4-fluorobenzylamine in each sample according to the method of Magee and Herd.[39] The difference between the calculated concentration and known concentration was determined for each standard solution (Table 4.3). An average difference between HPLC calculated concentration and known standard concentration of 1% was observed across the six

Table 4.3. Calculated concentration of 4-fluorobenzylamine by analytical RP-HPLC for standard solutions at 0.25, 0.50, 1.0, 2.0, 3.0, and 4.0 mM in ACN.

Compound	Calculated Concentration (mM)	Integrated peak area	Response	Relative Response	Difference to known concentration (mM)
0.25 mM standard solution					
4-Fluorobenzylamine	0.27	127	466	1.108	+0.02
Fluorobenzene	2	841	421	1	NA
0.50 mM standard solution					
4-Fluorobenzylamine	0.52	242	468	1.108	+0.02
Fluorobenzene	2	844	422	1	NA
1.0 mM standard solution					
4-Fluorobenzylamine	1.01	1193	1181	1.108	+0.01
Fluorobenzene	2	2131	1066	1	NA
2.0 mM standard solution					
4-Fluorobenzylamine	1.96	933	475	1.108	-0.04
Fluorobenzene	2	857	429	1	NA
3.0 mM standard solution					
4-Fluorobenzylamine	2.98	1410	474	1.108	-0.02
Fluorobenzene	2	855	427	1	NA
4.0 mM standard solution					
4-Fluorobenzylamine	3.98	1921	482	1.108	-0.02
Fluorobenzene	2	870	435	1	NA

samples, which indicates that the analytical RP-HPLC quantification method is valid for determining the concentration of 4-fluorobenzylamine in solution.

Once verified, the RP-HPLC quantification method was employed for two identical amide coupling reactions between 4-fluorobenzylamine and carboxylated high-pressure high-temperature (HPHT) NDs. 4-fluorobenzylamine (2.7 mM) was added to a suspension of carboxylated HPHT NDs (1.0 mg), fluorobenzene (2.0 mM), DIC (2.0 mM), and Oxyma (2.0 mM) in ACN (final volume 1.0 mL, see Experimental section 4.4.4). The reaction suspension was sonicated for 6 h at rt. At the 3 h mark, an aliquot (300 µL) was removed and centrifuged (14,800 rpm, 20 min) to separate the ND pellet from the supernatant, while the remaining 700 µL continued to be sonicated. The isolated supernatant was immediately subjected to analytical RP-HPLC, with three independent injections (3 × 20 µL) performed. The remaining reaction

suspension after 6 h was centrifuged and this isolated supernatant also analysed by RP-HPLC. The concentration of 4-fluorobenzylamine calculated from the 3 h and 6 h timepoint chromatograms is shown in Table 4.4 below.

The initial solution of 4-fluorobenzylamine prepared at 2.7 mM was also analysed by RP-HPLC to provide a 0 h reaction timepoint. This sample was calculated to be 2.58 mM by RP-HPLC, which is slightly lower than the known 2.7 mM starting concentration. The remaining calculated 4-fluorobenzylamine concentrations were 2.84 mM at 3 h and 3.33 mM at 6 h for reaction 1, and 2.99 mM at 3 h and 3.05 mM at 6 h for reaction 2. This indicated that there was an error in the RP-HPLC quantification procedure due to the calculated increase over time in 4-fluorobenzylamine present, which is not consistent with the reaction conditions employed.

The calculated increase in 4-fluorobenzylamine concentration while the ND functionalisation reaction proceeded was further investigated by checking the reproducibility of the RP-HPLC peak integral from the internal standard, fluorobenzene. A solution of fluorobenzene (2 mM in ACN, 20 µL) was injected into the RP-HPLC system every hour, and a chromatogram collected. As analysis of one sample takes 30 minutes, 4-fluorobenzylamine (2 mM in ACN, 20 µL) was injected between each fluorobenzene sample injection. The integral of the 4-fluorobenzylamine peak remained steady over 10 h, with a slight increase from 1035 to 1070 units (3%, Figure 4.2). This may be due to evaporation of a small amount of ACN, which would cause the concentration of 4-fluorobenzylamine to increase in the sample vial. In contrast, the integral of the fluorobenzene decreased significantly over 10 h from 1006 to 890 units (12%, Figure 4.2). This decrease over time would therefore result in an increasing over-estimate when calculating an unknown concentration with reference to the internal standard. This is consistent with the calculated increase in 4-fluorobenzylamine concentration over 6 h time scale ND coupling reactions performed. Hence, fluorobenzene was found to be an unsuitable internal standard and the RP-HPLC method developed here was deemed unsuitable for quantification of the amount of 4-fluorobenzylamine loaded on NDs.

Table 4.4. Calculated concentration of 4-fluorobenzylamine at 0, 3, and 6 h timepoints for two coupling reactions on carboxylated HPHT NDs.

Sample	Time	Concentration (mM)	Standard deviation (mM)
Initial	0 h	2.58	0.03
Reaction 1	3 h	2.85	0.04
	6 h	3.33	0.36
Reaction 2	3 h	2.99	0.16
	6 h	3.05	0.12

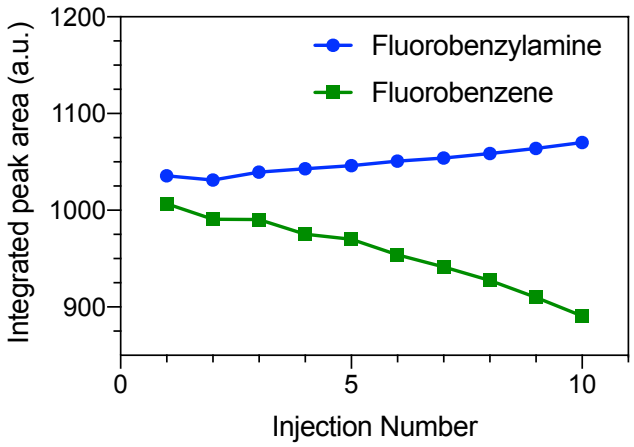

Figure 4.2. Plot of integrated peak area from the HPLC chromatograms for 4-fluorobenzylamine (blue) and fluorobenzene (green) over 10 independent injection events (5 h).

4.2.2 Nuclear magnetic resonance spectroscopy system

An NMR based system was next designed to quantify the surface loading of organic molecules on NDs. A new internal standard was selected for ^{1}H NMR as fluorobenzene was determined to be unsuitable in section 4.2.1. Here, caffeine was chosen as the internal standard due to its three methyl groups which provide distinct, high intensity signals in ^{1}H NMR (Figure 4.3). Two of these resonances are well separated from the DIC and Oxyma ^{1}H NMR resonances (Figure 4.3). 4-Fluorobenzylamine was replaced by polyethylene glycol (PEG) as the reagent to be coupled to the nanodiamond surface. Surface attachment of PEG molecules is known to provide colloidal stability for nanomaterials,[21,40] thus PEG molecules are an ideal selection for attachment to NDs. The PEG molecules investigated here ranged in length from one to nine ethylene glycol

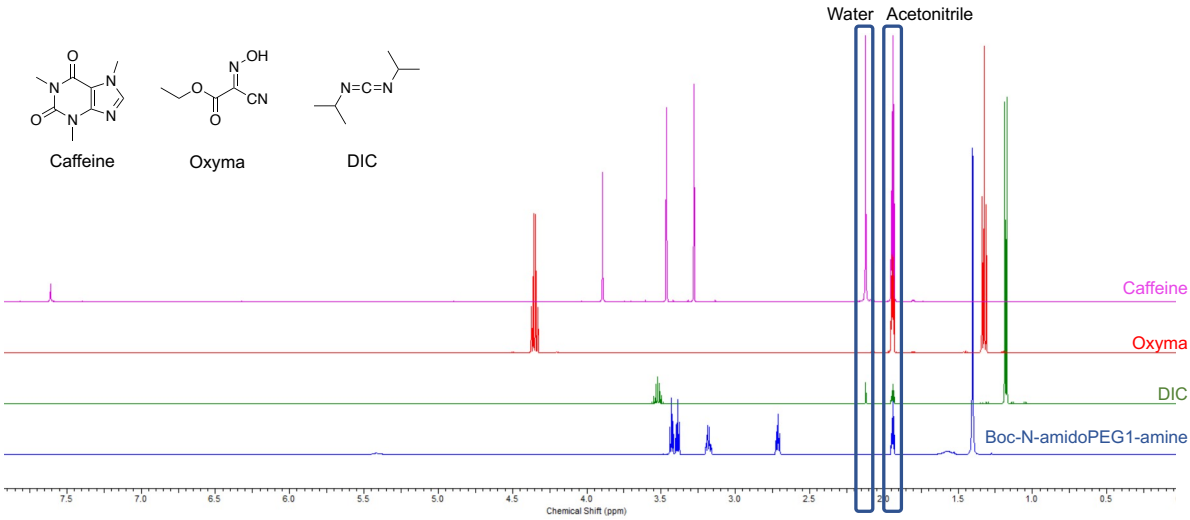

Figure 4.3. ^{1}H NMR spectra for caffeine (pink), Oxyma (red), DIC (green), and Boc-N-amidoPEG1-amine (blue). The caffeine peaks at 3.90 and 3.25 ppm are clearly separated from the DIC and Oxyma. Inset: structures of caffeine, Oxyma, and DIC.

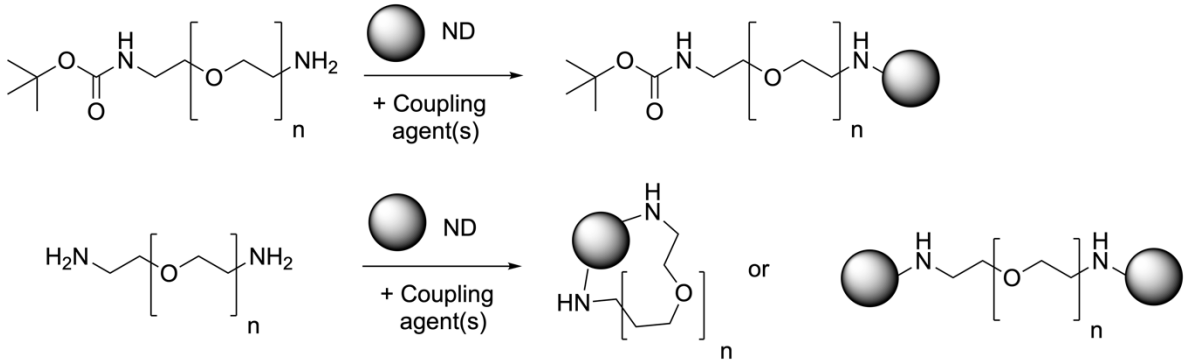

Scheme 4.3. Reaction of diamino-polyethylene glycol (PEG) molecules with nanodiamonds (ND). A mono-protected-PEG (ie one free amine) can only react once with an ND (top), whereas an unprotected diamino-PEG may react twice with one ND, or cross-link two NDs.

units, with a terminal amine at each end. One terminal amine was protected with a tertiary-butylcarbonyl group (Boc) to avoid cross-linking of two NDs, and to ensure that one PEG molecule did not bind twice onto the one ND surface (Scheme 4.3).

Carboxylated HPHT NDs (2.0 mg) were suspended in ACN (500 µL), then DIC, Oxyma, and the PEG reagent added such that all reagents were at a final concentration of 2 mM with a total reaction volume of 2.0 mL (see Experimental section 4.4.4). This reaction suspension was sonicated for 7 h, then stirred at rt overnight. The reaction suspension was centrifuged to pellet the NDs, and an aliquot (400 µL) of the supernatant removed. This was combined with an aliquot of freshly sublimed caffeine (400 µL, 2mM in d_6-ACN) for ^{1}H NMR analysis. The relative integration of the resulting spectra was set using the caffeine resonance at 3.95 ppm, which corresponds to one methyl group (*i.e.*, a 3H integral). The resulting integral of the resonance at

2.7 to 2.9 ppm due to the PEG carbon chain was then used to determine the PEG concentration remaining in the supernatant aliquot, by comparison to the remaining two caffeine integrals at 3.54 and 3.35 ppm. Thus, the amount of PEG reagent attached to the NDs was back-calculated according to Equation 4.1 below. The coupling reactions were repeated three times for each PEG reagent (1, 3, 7, or 9 ethylene glycol units). A control reaction was also performed to account for non-covalent adsorption of PEG reagent on NDs, where NDs were stirred with Boc-N-amido-PEG1amine (*i.e.*, n=1 for the ethylene glycol unit) overnight in the absence of coupling agents. This reaction mixture was submitted to the same NMR quantification protocol as the coupling reaction samples. The amount of Boc-N-amido-PEG1amine bound to NDs due to physical adsorption was found to be approximately 0.1 mmol/g.

$$Moles\ of\ PEG_{on\ NDs} = Moles\ of\ PEG_{initial} - Moles\ of\ PEG_{in\ solution} \qquad (4.1)$$

The amount of each PEG reagent calculated by NMR to be attached to the NDs after the coupling reactions was highly variable - ranging from 0 to 0.2 mmol/g. This variable loading on NDs suggests that either the NMR quantification method is not providing a consistent result, or that the yield of coupling reactions of Boc-N-amido-PEG-amines onto NDs is highly variable, with some reactions resulting in no amide bond formation at all. A potential reason for these inconsistencies is degradation of PEG molecules during the sonication stage. This process is known as sonolysis and has been reported for large PEG-based molecules with an average molecular weight above 1000 Da.[41,42] Sonolysis of the PEG reagents used here (Boc-N-amido-PEG(n)-amine where n=1, 3, 7, or 9) was tested by dissolving each PEG-based molecule in 10% D_2O (700 µL) at a concentration of 1 mg/mL, then sonicating the solution for 6 h. The ^1H NMR spectrum of an untreated PEG-based molecule in 10% D_2O was compared to that of the sonicated sample (Figures 4.4 and 4.5). The spectra were referenced to sodium trimethylsilylpropanesulfonate (DSS), with freshly sublimed caffeine (1 mM) included as an internal standard. No change was observed in the spectra for all PEG-based molecules between untreated and sonicated samples. Thus, sonolysis was ruled out as a cause for the inconsistent ^1H NMR quantification results. Therefore, this suggests that the yield of the ND coupling reactions is highly variable, and that the amidation chemistry requires further optimisation.

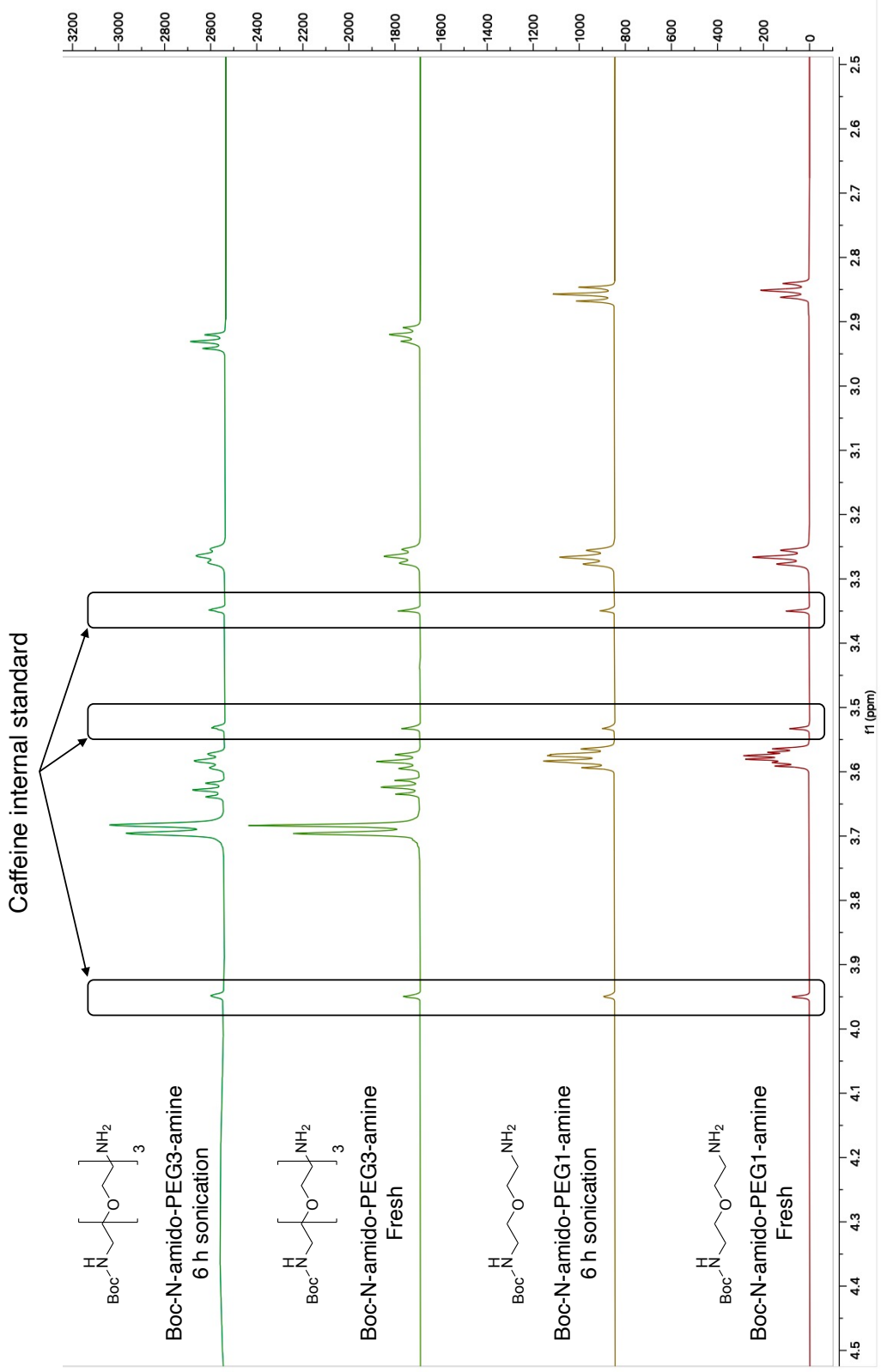

Figure 4.4. ^{1}H NMR spectra for Boc-N-amido-PEG1-amine (red and yellow) and Boc-N-amido-PEG3-amine (light and dark green) collected before and after 6 h of sonication. No change was observed between the spectra obtained before sonication compared to those obtained after sonication.

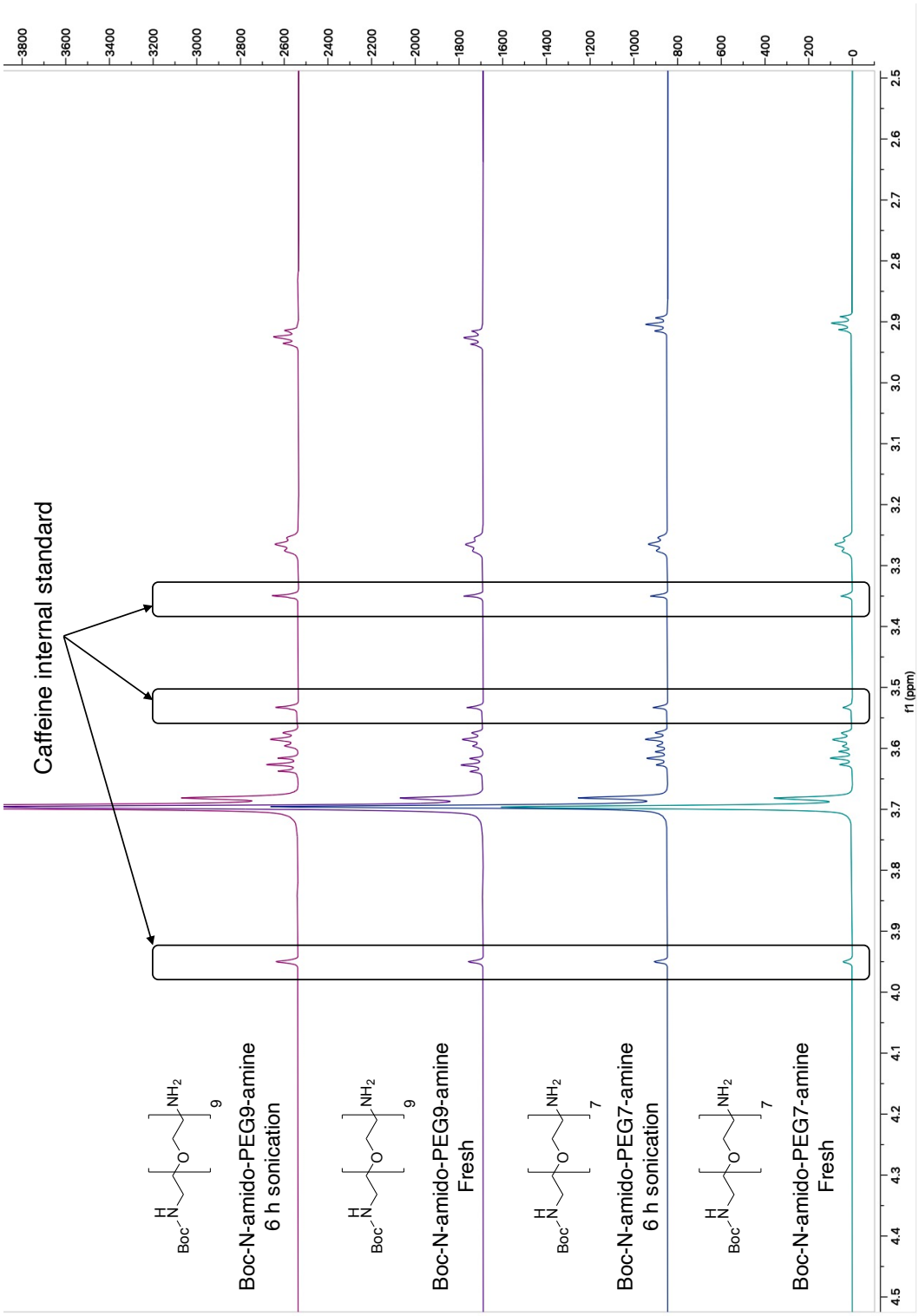

Figure 4.5. ^{1}H NMR spectra for Boc-N-amido-PEG7-amine (light and dark blue) and Boc-N-amido-PEG9-amine (purple and pink) collected before and after 6 h of sonication. No change was observed between the spectra obtained before sonication compared to those obtained after sonication.

4.3 Optimisation of amide bond formation

4.3.1 System design

The quantification of ND functionalisation discussed in section 4.2 did not show consistent surface coverage of the studied compounds on NDs. Hence, the formation of amide bonds on carboxylated NDs was examined in more detail. Reaction conditions employed in the literature for ND functionalisation have included peptide coupling reagents such as DCC and EDC,[16,27] and acyl chloride intermediates.[28] The more recently developed amide coupling agents, such as Oxyma or BTFFH,[30,31,33] have not been investigated to the best of our knowledge. There is a distinct gap in the literature to determine the optimal conditions for amide bond formation on carboxylated NDs, for both DNDs and HPHT NDs.

First, a model amine was designed to study amide bond formation on carboxylated NDs. The design requirements for this model amine were:

1) A primary amine for coupling to the carboxylated ND surface.
2) A characteristic handle for spectroscopic validation of the successfully functionalised material.
3) A linker section to separate the amine and spectroscopic handle.

The first-generation compound designed to fit these three criteria was 4-aminobutanenitrile, where the characteristic CN triple bond can be identified through techniques such as FTIR spectroscopy. The initial synthesis of 4-aminobutanenitrile from 4-bromobutanenitrile following literature conditions was found to be consistently low yielding (see Chapter 6). While this synthesis was successfully optimised, 4-aminobutanenitrile was found to undergo an intramolecular cyclisation under ambient laboratory conditions (also see Chapter 6).[43] Therefore, the butane linker component was replaced with a benzyl linker, to inhibit cyclisation. This provided 4-cyanobenzylamine, which was readily synthesised from the commercial starting material 4-cyanobenzylbromide in two steps, with an overall yield of 63% (Scheme 4.4, see Experimental section 4.4.3).[44]

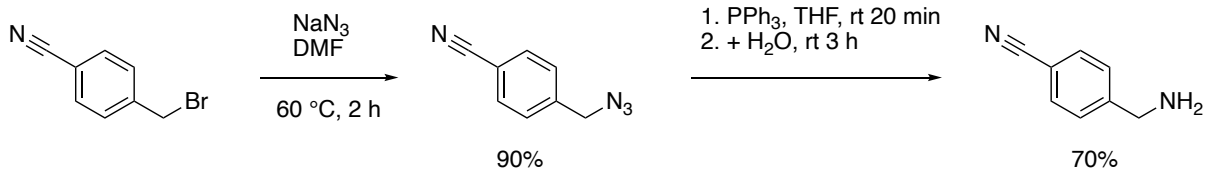

Scheme 4.4. Synthetic procedure to prepare 4-cyanobenzylamine from 4-bromobenzylamine in two steps.

Here, a total of ten reactions to form an amide bond between 4-cyanobenzylamine and a carboxylated DND surface were attempted. DNDs were selected as they are commercially available on a larger scale than HPHT NDs, and were supplied by Adámas Nanotechnologies as a 10 mg/mL suspension in water. A minimum carboxylic acid loading of 0.1 mmol/g for the DNDs was assumed, based on the literature reports ranging from 0.1 to 1.5 mmol/g for functionalised NDs (see Table 4.1 in section 4.1.2). DNDs were solvent exchanged from water to the requisite reaction solvent as described in the Experimental section 4.4.4.

A general procedure was developed for all DND coupling reactions (see Experimental section 4.4.4). The appropriate coupling agent(s) (see Tables 4.5-4.7) were added to the DNDs, followed by 4-cyanobenzylamine and the reaction suspension sonicated for 6 h, then stirred overnight at rt. The DNDs were pelleted by centrifugation and supernatant removed. The DNDs were then resuspended in DMF (20 mL) by sonication. This pellet and resuspension cycle was repeated for DMF (2 × 20 mL), then water (3 × 30 mL). The final aqueous suspension was lyophilised to provide the reacted DNDs as a grey powder.

4.3.2 EDC/NHS or DIC/Oxyma mediated couplings

The first two reactions attempted used a coupling agent cocktail of DIC and Oxyma to form an amide bond between carboxylated DND and 4-cyanobenzylamine (Table 4.5, reactions 1 and 2). These reactions were performed on 20 mg of DND, with an excess of amine and coupling agents used (5 or 10 equivalents) in an attempt to drive the reaction to completion. The resultant DND powders from these reactions were analysed by FTIR and compared to the unreacted DND and 4-cyanobenzylamine starting materials.

Table 4.5. Summary of DIC/Oxyma and EDC/NHS mediated coupling reactions between detonation nanodiamonds and 4-cyanobenzylamine.

Reaction Number	Coupling agent(s)	Nanodiamond (mg)	Amine Equiv.	Solvent
1	DIC/Oxyma	20	5	DMF
2	DIC/Oxyma	20	10	DMF
3	EDC/NHS	20	10	Water
4	EDC/NHS	15	50	DMF
5	EDC/NHS	10	100	ACN

Nanodiamonds have complicated FTIR spectra in the 'fingerprint' region (<1400 cm^{-1}), with a number of overlapping peaks that are assigned to stretching or bending modes of bonds including C-C, C-O-C, C-O, C-H and C-N (due to N impurities in the ND sample).[45] The FTIR spectrum of unreacted DNDs above 1400 cm^{-1} contains two major peaks observed at 1624 and 1767 cm^{-1} (Figure 4.6A). The peak at 1767 cm^{-1} is within the commonly reported range for carboxyl groups and was thus assigned to the carboxyl group of the carboxylic acids on the DND surface. Therefore, the remaining 1624 cm^{-1} peak was assigned to an O-H bending mode due to surface adsorbed water remaining after lyophilisation, rather than a deprotonated carboxyl that has been shifted due to hydrogen bonding between NDs.[46] The remaining spectrum is featureless except for a broad absorbance centred around ~3400 cm^{-1}, which was assigned as an O-H stretching band from a combination of surface adsorbed water and the O-H of the surface carboxylic acids. Overall, the unreacted DNDs spectrum is consistent with a ND surface decorated with carboxylic acids, as expected.

The FTIR spectra of DNDs from reactions 1 and 2, carried out in DMF, are similar to the unreacted DND spectrum, with a 1767 cm^{-1} peak observed (Figure 4.6A-C). The unreacted DND peak observed at 1624 cm^{-1} has shifted to nearly 1650 cm^{-1}, which could be interpreted as a shift from the carboxyl band to the amide I band, and therefore suggest that amide formation was successful. An increase in intensity of the 1650 cm^{-1} peak relative to the 1767 cm^{-1} peak was also observed, along with weak C-H stretching at 2900 cm^{-1}. However, the FTIR spectrum for reaction 3, which was carried out in water, does not contain the observed peak shift from 1624 cm^{-1} to 1650 cm^{-1}, the 2900 cm^{-1} signal, or a change intensity ratio between 1650 cm^{-1} and 1767 cm^{-1}

bands. Instead, the reaction 3 FTIR spectrum is a close match to the unreacted DND spectrum (Figure 4.6A-C). This suggests that reaction 3 was unsuccessful in forming an amide bond, while reactions 1 and 2 may have been successful. However, no peak was observed near 2230 cm^{-1} in the FTIR spectra for all reactions 1-3, which would be expected due to the characteristic nitrile stretching band of 4-cyanobenzylamine if successfully bound to the DNDs. Therefore, the most likely explanation for the peak shift from 1624 cm^{-1} to 1650 cm^{-1} observed for reactions 1 and 2 is residual DMF on the reacted DNDs, as DMF contains an amide bond that could cause this observed peak shift. This conclusion is supported by the increase in intensity of the 1650 cm^{-1} band relative to the 1767 cm^{-1} band, and the observed weak C-H stretching at 2900 cm^{-1} which was assigned to the methyl groups of DMF. Hence, reactions 1-3 were all deemed unsuccessful in attachment of 4-cyanobenzylamine to DNDs.

The effect of residual DMF was investigated further by repeating the EDC/NHS coupling reaction in DMF (Table 4.5, reaction 4). Gaillard *et al*. reported coupling of a peptide nucleic acid using EDC/NHS to carboxylated NDs in DMF,[47] but this was carried out with HPHT NDs rather than DNDs. While it is known that HPHT NDs and DNDs have different surface properties,[14,48] these reported coupling conditions were followed using 4-cyanobenzylamine to allow investigation of the effect of residual DMF on the resultant FTIR spectra. The FTIR spectra of the DND powder obtained from reaction 4 exhibited a peak shift from 1624 cm^{-1} to 1650 cm^{-1} in comparison to the unreacted DNDs, as observed for reactions 1 and 2, with no change in the 1767 cm^{-1} band (Figure 4.6D-F). Therefore, this peak shift can be clearly attributed to residual DMF, and not the desired coupling of 4-cyanobenzylamine to the DNDs.

The final reaction solvent explored was ACN, based on a recent report by Day *et al*. of an EDC/NHS mediated coupling in ACN of two amine-bearing fluorophores onto carboxylated DNDs.[25] The reported conditions were followed using 4-cyanobenzylamine (Table 4.5 reaction 5), however the resultant FTIR spectrum for this reaction (reaction 5, Figure 4.6D-F) appeared extremely similar to the FTIR spectrum of reaction 3 (EDC/NHS in water) and the unreacted DNDs. This suggests that this coupling of 4-cyanobenzylamine was unsuccessful, and confirms that EDC/NHS couplings in ACN or water do not cause the FTIR peak shift from 1624 cm^{-1} to 1650 cm^{-1} observed for EDC/NHS couplings carried out in DMF.

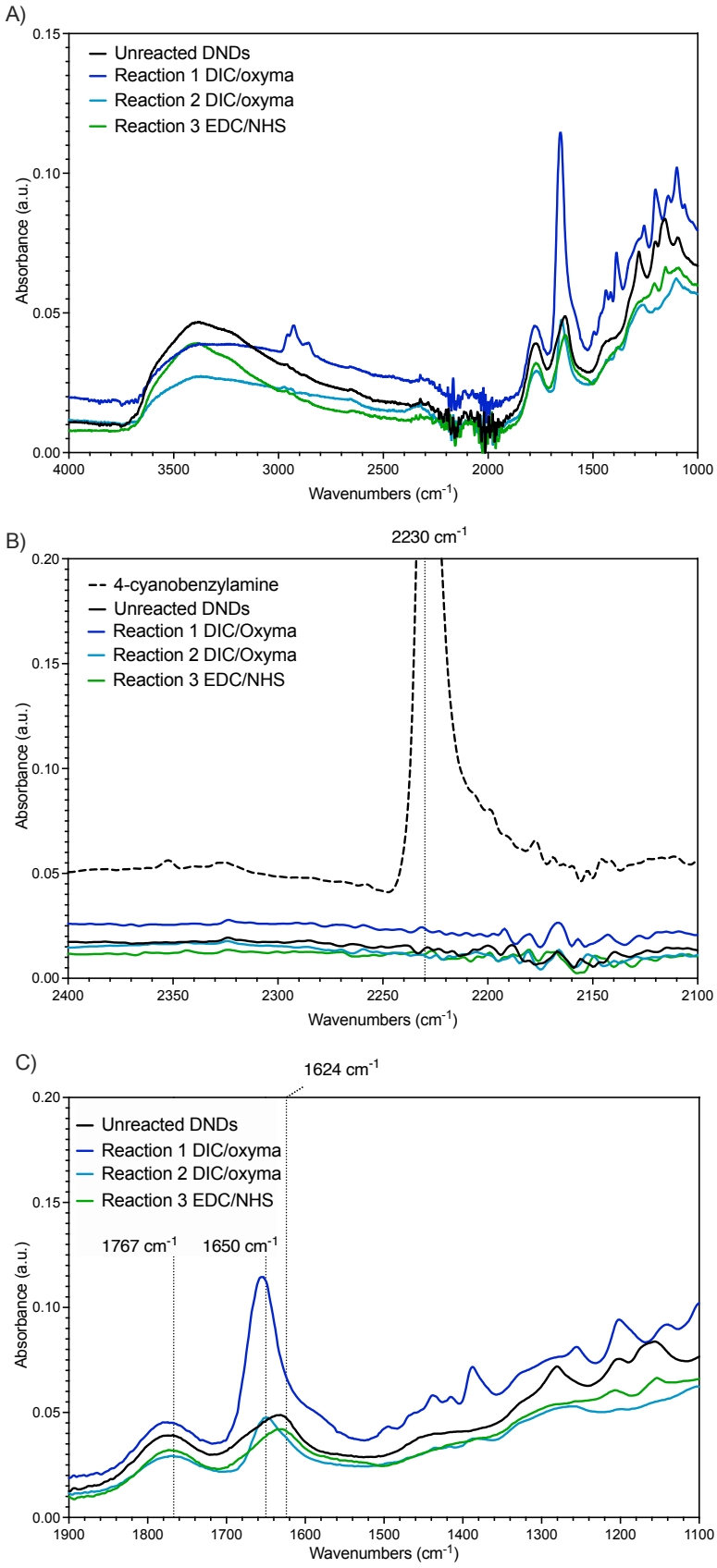

Figure 4.6. FTIR spectra of DNDs after the attempted amide bond formation reactions with 4 cyanobenzylamine. Unreacted DNDs are shown in black on all plots. **A)** Full FTIR spectra for reactions 1 (dark blue), 2 (light blue) and 3 (green). **B)** FTIR spectra for reactions 1-3 between 2400 and 2100 cm^{-1} with 4-cyanobenzylamine (dashed black) included for reference to the characteristic nitrile stretch. **C)** FTIR spectra for reactions 1-3 between 1900 and 1100 cm^{-1}.

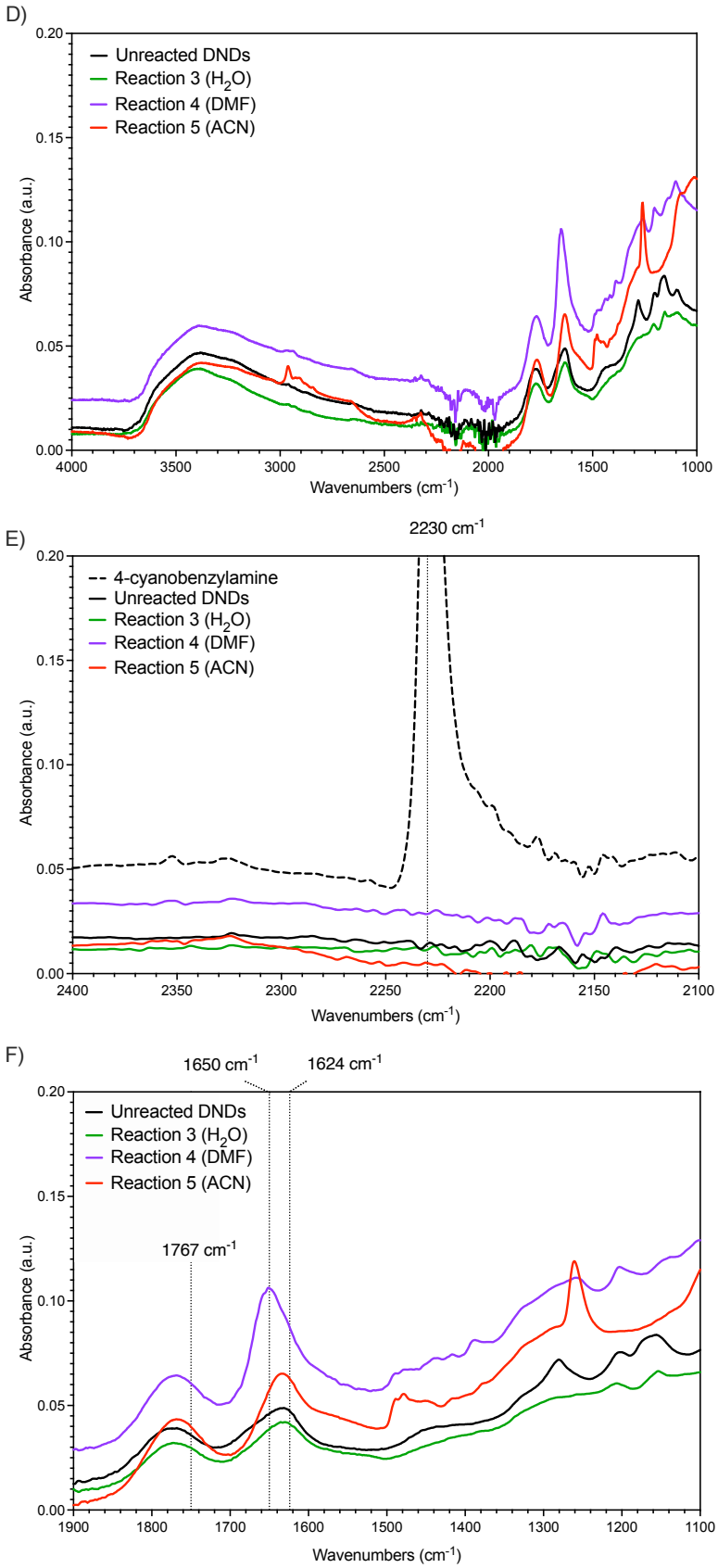

Figure 4.6 Continued. FTIR spectra of DNDs after the attempted amide bond formation reactions with 4-cyanobenzylamine. Unreacted DNDs are shown in black on all plots. **D)** Full FTIR spectra for reactions 3 (green), 4 (purple), and 5 (red). **E)** FTIR spectra for reactions 3-5 between 2400 and 2100 cm^{-1} with 4-cyanobenzylamine (dashed black) included for reference to the characteristic nitrile stretch. **F)** FTIR spectra for reactions 3-5 between 1900 and 1100 cm^{-1}.

4.3.3 HATU, CDI, or T3P mediated couplings

Following the unsuccessful attempts to attach 4-cyanobenzylamine to carboxylated DNDs by EDC/NHS or DIC/Oxyma mediated couplings, three new reactions were attempted using the coupling agents HATU, CDI, or T3P (Table 4.6). These coupling reactions were carried out according to the general procedure as detailed in section 4.3.1. The resultant DND powders were analysed by FTIR in comparison to the unreacted DNDs and the 4-cyanobenzylamine starting materials (Figure 4.7). No peak was observed at 2230 cm^{-1} in the FTIR spectra for all three reactions 6 to 8 (Figure 4.7B). This indicates that 4-cyanobenzylamine was not present on the DND powders obtained from each reaction. The FTIR spectra for reactions 6 and 7 exhibited a peak shift from 1624 cm^{-1} to 1650 cm^{-1} in comparison to the unreacted DNDs, while the peak for reaction 8 remained unchanged at 1624 cm^{-1}. This observation is in agreement with conclusion made for reactions 1 to 5 in section 4.3.2, where the presence of residual DMF causes a peak shift from 1624 cm^{-1} to 1650 cm^{-1}. Reaction 8 was carried out in ethyl acetate and therefore does not exhibit this peak shift. In summary, all three reactions 6 to 8 using coupling agents HATU, CDI, or T3P respectively, did not result in the formation of an amide bond between 4-cyanobenzylamine and DNDs.

Table 4.6. Summary of CDI, HATU, and T3P mediated coupling reactions between detonation nanodiamonds and 4-cyanobenzylamine.

Reaction Number	Coupling agent(s)	Nanodiamond (mg)	Amine Equiv.	Solvent
6	CDI	20	10	DMF
7	HATU	10	10	DMF
8	T3P	10	10	Ethyl acetate

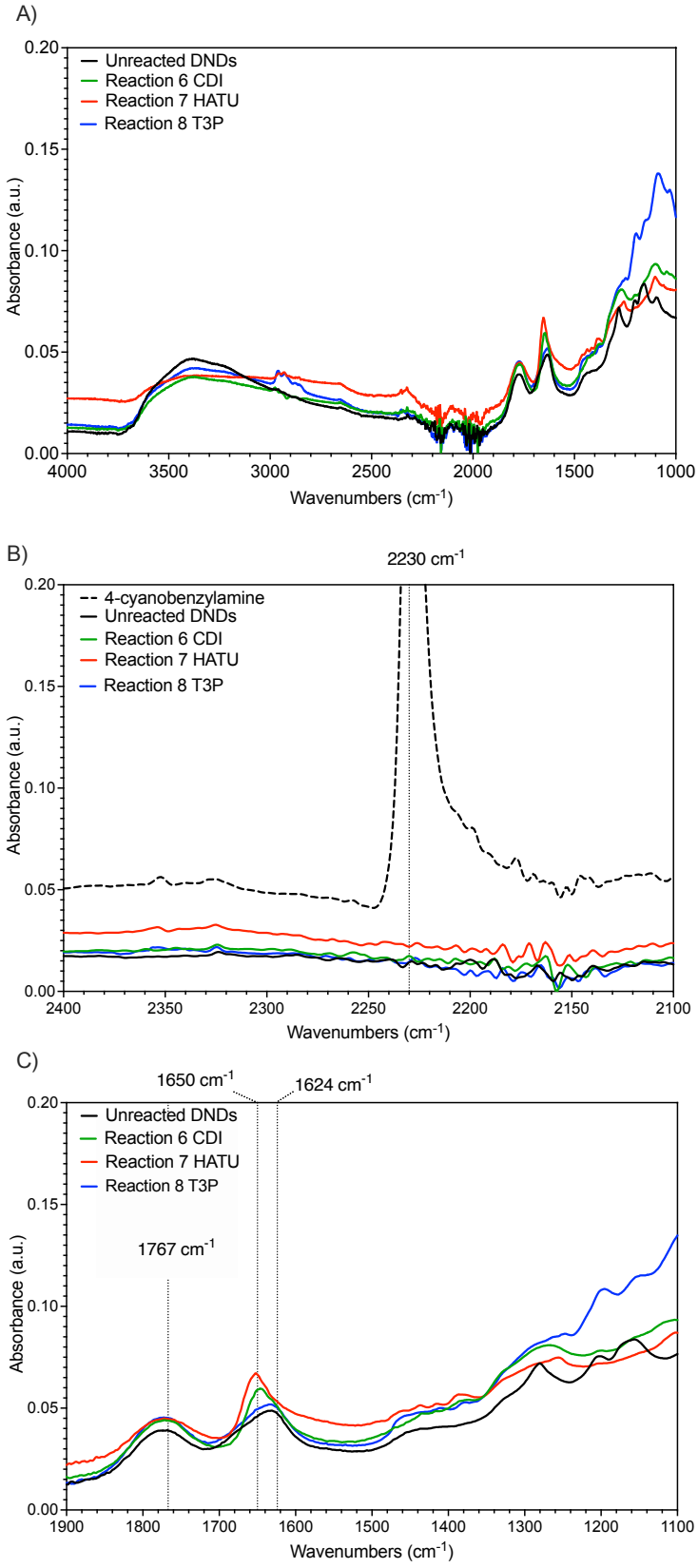

Figure 4.7. FTIR spectra of DNDs after the attempted amide bond formation reactions with 4-cyanobenzylamine 6-8. Unreacted DNDs are shown in black on all plots. **A)** Full FTIR spectra for reactions 6 (green), 7 (red) and 8 (blue). **B)** FTIR spectra for reactions 6-8 between 2400 & 2100 cm^{-1} with 4-cyanobenzylamine (dashed black) included for reference to the characteristic nitrile stretch. **C)** FTIR spectra for reactions 6-8 between 1900 and 1100 cm^{-1}.

4.3.4 Acyl chloride route

An alternative route to attach 4-cyanobenzylamine to NDs *via* an acyl chloride intermediate was attempted given the lack of success with amide coupling reagents in sections 4.3.2 and 4.3.3 (Table 4.7 and Experimental section 4.4.4). This approach was reported by Mochalin *et al*. for the covalent attachment of octadecylamine to carboxylated DNDs.[28] Two reactions were performed according to this literature method to attach either octadecylamine (reaction 9) or 4-cyanobenzylamine (reaction 10) to DNDs.

Mochalin *et al*. confirmed the covalent bond between octadecylamine and DNDs through the presence of amide I and II bands in the FTIR spectra at 1650 cm^{-1} and 1550 cm^{-1} respectively.[28] The DND powders obtained here were also analysed by FTIR spectroscopy (Figure 4.8), however no significant changes were observed in comparison to unreacted DNDs, and no amide I and II bands were observed. The characteristic nitrile peak at 2230 cm^{-1} was not present in the FTIR spectra of DNDs from reaction 10, indicating that 4-cyanobenzylamine was not attached to the DNDs.

Table 4.7. Summary of couplings reactions between detonation nanodiamonds using an acyl chloride intermediate.

Reaction Number	Coupling method	Nanodiamond (mg)	Amine Equiv.	Solvent
9	Acyl chloride	10	370 (octadecylamine)	DMF
10	Acyl chloride	10	370 (4-cyanobenzylamine)	DMF

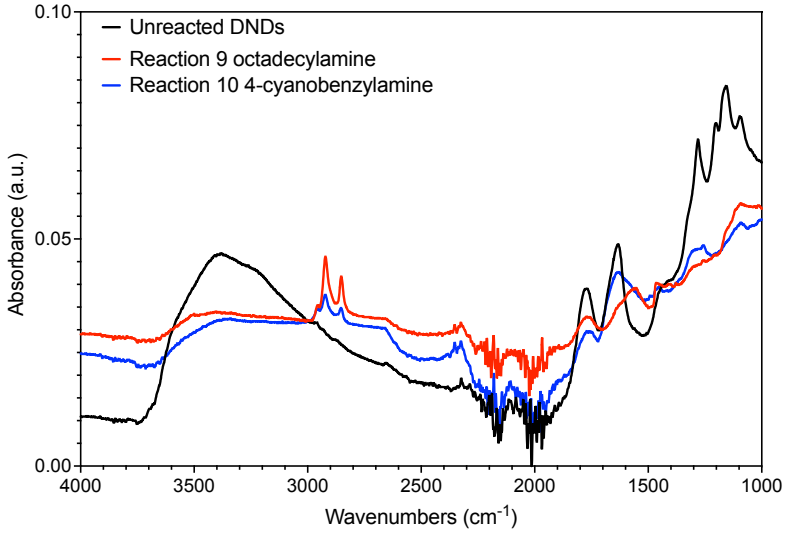

Figure 4.8. FTIR spectra for unreacted DNDs (black) and after attempting attachment of octadecylamine (red) and 4-cyanobenzylamine (blue) through an acyl chloride intermediate.

The supernatants isolated from reactions 9 and 10 during the work-up (see Experimental section 4.4.4) were subjected to a ninhydrin test, a common stain used to detect primary amines in thin-layer chromatography (TLC),[49] to determine if the amine reagents used were present. An aliquot of each reaction supernatant was spotted onto a TLC plate using a 1 µL pipette tip, then the plate dipped in a ninhydrin staining solution. This caused immediate blue colouration of the TLC plate where the supernatant was deposited, consistent with the presence of an amine. Therefore, the presence of octadecylamine and 4-cyanobenzylamine in the respective reaction 9 and 10 supernatants was confirmed. This observation, in conjunction with the FTIR spectra, indicates that the octadecylamine or 4-cyanobenzylamine reagents were not attached to the DNDs through an acyl chloride intermediate pathway.

Overall, all ten attempts to functionalise DNDs through formation of an amide bond were unsuccessful. Furthermore, the RP-HPLC and ^{1}H NMR based quantification systems described in section 4.2 suggested that DIC/Oxyma mediated amidation of 4-fluorobenzylamine or aminoPEG reagents onto NDs was also unsuccessful. Clearly, an alternative route to functionalise NDs is required, which is discussed further in Chapter 5.

4.4 Experimental

4.4.1 General materials

All reagents and solvents were purchased from Merck/Sigma-Aldrich unless otherwise specified, at the highest purity level available. All PEG reagents (Boc-N-amido-PEG(n)-amine; n=1, 3, 5, 7, or 9) were purchased from Broadpharm at 98% purity. DNDs with an average particle size of 5 nm were obtained from Adámas Nanotechnologies as a 10 mg/mL suspension of carboxylated DNDs in water and were used without further treatment. HPHT NDs with an average particle size of 120 nm were purchased from Nabond (Hong Kong) and irradiated, annealed, and oxidised according to previously reported methods.[5] This included a final treatment in concentrated sulfuric acid and nitric acid to provide a carboxylated surface.[28] All ND suspensions were sonicated for 1 h before use in coupling experiments with a 150 W FS-600N ultrasonicator homogeniser (Zhengzhou HenChen Electronic, Henan Province, China) with a 2 s on, 4 s off duty cycle.

4.4.2 Instrumentation

Fourier-Transform Infrared (FTIR) spectroscopy was carried out on a Shimazdu IR Spirit spectrometer in Universal ATR mode. All HPLC analysis was conducted using an Agilent Infinity 1260 analytical HPLC equipped with a Phenomenex Luna^{TM} C18(2) 100 Å 4 × 250 mm column. A gradient of ACN (B) in water (A) with 0.1% trifluoroacetic acid was used as specified for each sample and visualised at 220, 254, or 280 nm. ^{1}H NMR spectra were recorded on an Agilent 500 MHz or a Varian Inova 600 MHz instrument in d_3-ACN, and referenced to TMS at 0 ppm. Chemical shifts are reported in ppm (δ). Resonances are reported as s (singlet), br. s (broad singlet), d (doublet), t (triplet) or m (multiplet, range given). All plots of NMR spectra were generated using MestReNova v14.0.1. Freshly sublimed caffeine (at approximately 178 °C) was used as an internal standard for all quantitative experiments.

4.4.3 Organic synthesis

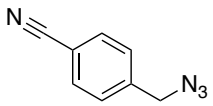

4-cyanobenzylbromide (1.00 g, 5.12 mmol, 1 equiv) was dissolved in DMF (20 mL) and sodium azide (1.66 g, 25.6 mmol, 5 equiv) added. The reaction mixture was stirred at rt until all sodium azide dissolved, then fitted with a condenser and heated to 60 °C for 2 h. The reaction mixture was cooled to rt and diluted with water (200 mL), then extracted with diethyl ether (3 × 50 mL). The combined organic phases were washed with brine (2 × 50 mL), dried over Na_2SO_4, filtered, and solvent removed under reduced pressure to provide 4-cyanobenzylazide as a white solid (0.73 g, 90%). NMR was consistent with literature:[50] ^{1}H NMR (500 MHz, $CDCl_3$) δ 7.69 (d, *J* = 8 Hz, 2H), 7.45 (d, *J* = 8 Hz, 2H), 4.46 (s, 2H) ppm.

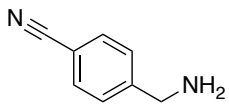

4-cyanobenzylazide (0.73 g, 4.60 mmol, 1 equiv) was dissolved in dry THF (11 mL) and triphenylphosphine (2.60 g, 10 mmol, 2.2 equiv) added, then the reaction mixture was stirred for 20 min at rt under a N_2 atmosphere. Water (1.2 mL) was added and the reaction mixture stirred at rt for a further 3 h. Solvent was removed under reduced pressure and the residue taken up in ethyl acetate (10 mL), dried over Na_2SO_4, filtered, and solvent removed under reduced pressure. The crude product was purified by flash column chromatography on silica (10% (v/v) methanol/dichloromethane) to give 4-cyanobenzylamine as a white solid (0.40 g, 70%). NMR was consistent with literature:[51] ^{1}H NMR (500 MHz, $CDCl_3$) δ 7.64 (d, *J* = 8 Hz, 2H), 7.46 (d, *J* = 8 Hz, 2H), 3.97 (s, 2H) ppm.

4.4.4 Nanodiamond functionalisation reactions

4-fluorobenzylamine attachment

4-fluorobenzylamine (2.7 mM) was added to a suspension of carboxylated HPHT NDs (1.0 mg) and fluorobenzene (2.0 mM), DIC (2.0 mM), and Oxyma (2.0 mM) in ACN (1.0 mL). The reaction was stirred for 6 h. At the 3 h mark, an aliquot (300 µL) was removed and the suspension was centrifuged (14,800 rpm, 20 min) to separate the ND pellet from the supernatant. The isolated supernatant was immediately subjected to analytical RP-HPLC, with three independent injections (20 µL) performed. The remaining suspension after 6 h was also centrifuged and the isolated supernatant analysed by HPLC.

A t_0 sample of the 4-fluorobenzylamine coupling reaction was prepared for comparison to the 3 h and 6 h samples. This was prepared by addition of 4-fluorobenzylamine (2.7 mM) to a solution of fluorobenzene (2.0 mM), DIC (2.0 mM), and Oxyma (2.0 mM) in ACN (1.0 mL). The resultant solution was thoroughly mixed and subjected to analytical RP-HPLC.

Polyethylene glycol attachment

Carboxylated HPHT NDs (2.0 mg) were suspended in ACN (500 µL), then solutions of DIC (8 mM, 500 µL), Oxyma (8 mM, 500 µL), and PEG (n=1, 3, 7 or 9, 8 mM, 500 µL) in ACN were added

such that all reagents were at a final concentration of 2 mM. The reaction mixture was centrifuged to pellet the NDs, and 400 µL of supernatant was removed. This was combined with caffeine (2 mM, 400 µL) in d_6-ACN for ^{1}H NMR analysis.

A t_0 sample of the PEG coupling reactions was prepared for comparison to the reacted sample. Solutions of DIC (8 mM, 100 µL), Oxyma (8 mM, 100 µL), and PEG (n=1, 3, 7, or 9, 8 mM, 100 µL) in ACN were combined and further diluted with ACN (100 µL). Caffeine (2 mM, 400 µL) in d_6-ACN was added and the resulting mixture analysed by ^{1}H NMR.

Coupling agent mediated attachment of 4-cyanobenzylamine

A general procedure was developed for coupling 4-cyanobenzylamine to DNDs. DNDs were solvent exchanged from water to DMF as required by adding DMF to the DND suspension and removing a portion of the solvent removed under reduced pressure. This was done such that the DND concentration did not increase above 10 mg/mL at any stage. This was repeated over three cycles to ensure all water was removed. The same procedure was performed for solvent exchange into ACN or ethyl acetate as required.

First, the DND suspension (10 mg/mL) was further diluted to a final reaction concentration of 1 mg/mL. The solvent used was dependent on the coupling reaction attempted, see Tables 4.5-4.7. Coupling agent(s), followed by 4-cyanobenzylamine were added to the DNDs (variable quantities, see Tables 4.5-4.7) and the reaction suspension sonicated for 6 h, then stirred overnight at rt. The DNDs were pelleted by centrifugation and supernatant removed. The DNDs were then resuspended in the reaction solvent (20 mL) by sonication and the pellet and resuspension cycle repeated for DMF (2 × 20 mL) and water (3 × 30 mL). The final aqueous suspension was lyophilised to provide the reacted DNDs as a grey powder.

Attachment of 4-cyanobenzylamine via an acyl chloride intermediate

The carboxylated DNDs were first lyophilised to provide a grey powder, that was then dried in a 140 °C oven overnight to remove all water. The dried DNDs (10 mg) were suspended in anhydrous toluene (4 mL) by ultrasonication for 45 min, then $SOCl_2$ (3 mL) added slowly at rt, followed by anhydrous DMF (0.1 mL). The suspension was heated to reflux for 24 h. The suspension was then cooled and solvent removed under reduced pressure. The residual DNDs

were resuspended in anhydrous toluene (10 mL) and solvent removed under reduced pressure. This procedure was repeated three more times to ensure full removal of residual $SOCl_2$. The acyl chloride functionalised DNDs were then suspended in anhydrous DMF and octadecylamine (100 mg, 0.37 mmol, reaction 9) or 4-cyanobenzylamine (31 mg, 0.37 mmol, reaction 10) added and the reaction suspension heated at 80 °C overnight. The suspension was then cooled to rt and washed by repeated centrifugation and resuspension cycles with DMF (3 × 10 mL), chloroform (3 × 10 mL), and water (10 mL), then the final DND pellet suspended in water and lyophilised to provide a grey powder.

4.5 References

(1) Guan, B.; Zou, F.; Zhi, J. Nanodiamond as the PH-Responsive Vehicle for an Anticancer Drug. *Small* **2010**, *6* (14), 1514-1519. https://doi.org/10.1002/smll.200902305.

(2) Xiao, J.; Duan, X.; Yin, Q.; Zhang, Z.; Yu, H.; Li, Y. Nanodiamonds-Mediated Doxorubicin Nuclear Delivery to Inhibit Lung Metastasis of Breast Cancer. *Biomaterials* **2013**, *34* (37), 9648-9656. https://doi.org/10.1016/j.biomaterials.2013.08.056.

(3) Jeong, S. H.; Lim, D.; Kim, K.; Kang, E.; Lim, S.; Ricci, J.; Sung, S.; Kwon, M. Comprehensive Evaluation of Carboxylated Nanodiamond as a Topical Drug Delivery System. *Int. J. Nanomedicine* **2016**, 2381. https://doi.org/10.2147/IJN.S104859.

(4) Li, L.; Tian, L.; Wang, Y.; Zhao, W.; Cheng, F.; Li, Y.; Yang, B. Smart PH-Responsive and High Doxorubicin Loading Nanodiamond for in Vivo Selective Targeting, Imaging, and Enhancement of Anticancer Therapy. *J. Mater. Chem. B* **2016**, *4* (29), 5046-5058. https://doi.org/10.1039/C6TB00266H.

(5) Purdey, M. S.; Capon, P. K.; Pullen, B. J.; Reineck, P.; Schwarz, N.; Psaltis, P. J.; Nicholls, S. J.; Gibson, B. C.; Abell, A. D. An Organic Fluorophore-Nanodiamond Hybrid Sensor for Photostable Imaging and Orthogonal, on-Demand Biosensing. *Sci. Rep.* **2017**, *7* (1), 15967. https://doi.org/10.1038/s41598-017-15772-0.

(6) Smith, B. R.; Niebert, M.; Plakhotnik, T.; Zvyagin, A. V. Transfection and Imaging of Diamond Nanocrystals as Scattering Optical Labels. *J. Lumin.* **2007**, *127* (1), 260-263. https://doi.org/10.1016/j.jlumin.2007.02.044.

(7) Chang, B.-M.; Lin, H.-H.; Su, L.-J.; Lin, W.-D.; Lin, R.-J.; Tzeng, Y.-K.; Lee, R. T.; Lee, Y. C.; Yu, A. L.; Chang, H.-C. Highly Fluorescent Nanodiamonds Protein-Functionalized for Cell Labeling and Targeting. *Adv. Funct. Mater.* **2013**, *23* (46), 5737-5745. https://doi.org/10.1002/adfm.201301075.

(8) Su, L.-J.; Wu, M.-S.; Hui, Y. Y.; Chang, B.-M.; Pan, L.; Hsu, P.-C.; Chen, Y.-T.; Ho, H.-N.; Huang, Y.-H.; Ling, T.-Y.; Hsu, H.-H.; Chang, H.-C. Fluorescent Nanodiamonds Enable Quantitative Tracking of Human Mesenchymal Stem Cells in Miniature Pigs. *Sci. Rep.* **2017**, *7* (1), 45607. https://doi.org/10.1038/srep45607.

(9) Fang, C.-Y.; Vaijayanthimala, V.; Cheng, C.-A.; Yeh, S.-H.; Chang, C.-F.; Li, C.-L.; Chang, H.-C. The Exocytosis of Fluorescent Nanodiamond and Its Use as a Long-Term Cell Tracker. *Small* **2011**, *7* (23), 3363-3370. https://doi.org/10.1002/smll.201101233.

(10) Tisler, J.; Reuter, R.; Lämmle, A.; Jelezko, F.; Balasubramanian, G.; Hemmer, P. R.; Reinhard, F.; Wrachtrup, J. Highly Efficient FRET from a Single Nitrogen-Vacancy Center in Nanodiamonds to a Single Organic Molecule. *ACS Nano* **2011**, *5* (10), 7893-7898. https://doi.org/10.1021/nn2021259.

(11) Zhang, X.-Q.; Lam, R.; Xu, X.; Chow, E. K.; Kim, H.-J.; Ho, D. Multimodal Nanodiamond Drug Delivery Carriers for Selective Targeting, Imaging, and Enhanced Chemotherapeutic Efficacy. *Adv. Mater.* **2011**, *23* (41), 4770-4775. https://doi.org/10.1002/adma.201102263.

(12) Zhang, T.; Cui, H.; Fang, C.-Y.; Cheng, K.; Yang, X.; Chang, H.-C.; Forrest, M. L. Targeted Nanodiamonds as Phenotype-Specific Photoacoustic Contrast Agents for Breast Cancer. *Nanomedicine* **2015**, *10* (4), 573-587. https://doi.org/10.2217/nnm.14.141.

(13) Pichot, V.; Guerchoux, M.; Muller, O.; Guillevic, M.; Fioux, P.; Merlat, L.; Spitzer, D. Nanodiamond Coating by Polyethylenimine for Optical Limitation. *Diamond Relat. Mater.* **2019**, *95*, 55-59. https://doi.org/10.1016/j.diamond.2019.04.001.

(14) Krueger, A.; Lang, D. Functionality Is Key: Recent Progress in the Surface Modification of Nanodiamond. *Adv. Funct. Mater.* **2012**, *22* (5), 890-906. https://doi.org/10.1002/adfm.201102670.

(15) Krüger, A.; Liang, Y.; Jarre, G.; Stegk, J. Surface Functionalisation of Detonation Diamond Suitable for Biological Applications. *J. Mater. Chem.* **2006**, *16* (24), 2322-2328. https://doi.org/10.1039/B601325B.

(16) Barras, A.; Szunerits, S.; Marcon, L.; Monfilliette-Dupont, N.; Boukherroub, R. Functionalization of Diamond Nanoparticles Using “Click” Chemistry. *Langmuir* **2010**, *26* (16), 13168-13172. https://doi.org/10.1021/la101709q.

(17) Gaur, P.; Banerjee, S. C-N Cross Coupling: Novel Approach towards Effective Aryl Secondary Amines Modification on Nanodiamond Surface. *Diamond Relat. Mater.* **2019**, *98*, 107468. https://doi.org/10.1016/j.diamond.2019.107468.

(18) Krueger, A.; Stegk, J.; Liang, Y.; Lu, L.; Jarre, G. Biotinylated Nanodiamond: Simple and Efficient Functionalization of Detonation Diamond. *Langmuir* **2008**, *24* (8), 4200-4204. https://doi.org/10.1021/la703482v.

(19) Rehor, I.; Slegerova, J.; Kucka, J.; Proks, V.; Petrakova, V.; Adam, M.-P.; Treussart, F.; Turner, S.; Bals, S.; Sacha, P.; Ledvina, M.; Wen, A. M.; Steinmetz, N. F.; Cigler, P. Fluorescent Nanodiamonds Embedded in Biocompatible Translucent Shells. *Small* **2014**, *10* (6), 1106-1115. https://doi.org/10.1002/smll.201302336.

(20) Krueger, A.; Boedeker, T. Deagglomeration and Functionalisation of Detonation Nanodiamond with Long Alkyl Chains. *Diamond Relat. Mater.* **2008**, *17* (7-10), 1367-1370. https://doi.org/10.1016/j.diamond.2008.01.033.

(21) Zhang, X.; Fu, C.; Feng, L.; Ji, Y.; Tao, L.; Huang, Q.; Li, S.; Wei, Y. PEGylation and PolyPEGylation of Nanodiamond. *Polymer* **2012**, *53* (15), 3178-3184. https://doi.org/10.1016/j.polymer.2012.05.029.

(22) Torelli, M. D.; Rickard, A. G.; Backer, M. V.; Filonov, D. S.; Nunn, N. A.; Kinev, A. V.; Backer, J. M.; Palmer, G. M.; Shenderova, O. A. Targeting Fluorescent Nanodiamonds to Vascular Endothelial Growth Factor Receptors in Tumor. *Bioconjugate Chem.* **2019**, *30* (3), 604-613. https://doi.org/10.1021/acs.bioconjchem.8b00803.

(23) Sotoma, S.; Iimura, J.; Igarashi, R.; Hirosawa, K.; Ohnishi, H.; Mizukami, S.; Kikuchi, K.; Fujiwara, T.; Shirakawa, M.; Tochio, H. Selective Labeling of Proteins on Living Cell Membranes Using Fluorescent Nanodiamond Probes. *Nanomaterials* **2016**, *6* (4), 56. https://doi.org/10.3390/nano6040056.

(24) Genjo, T.; Sotoma, S.; Tanabe, R.; Igarashi, R.; Shirakawa, M. A Nanodiamond-Peptide Bioconjugate for Fluorescence and ODMR Microscopy of a Single Actin Filament. *Anal. Sci.* **2016**, *32* (11), 1165-1170. https://doi.org/10.2116/analsci.32.1165.

(25) Day, A. H.; Adams, S. J.; Gines, L.; Williams, O. A.; Johnson, B. R. G.; Fallis, I. A.; Loveridge, E. J.; Bahra, G. S.; Oyston, P. C. F.; Herrera, J. M.; Pope, S. J. A. Synthetic Routes, Characterization and Photophysical Properties of Luminescent, Surface Functionalized Nanodiamonds. *Carbon* **2019**, *152*, 335-343. https://doi.org/10.1016/j.carbon.2019.05.081.

(26) Dong, Y.; Cao, R.; Li, Y.; Wang, Z.; Li, L.; Tian, L. Folate-Conjugated Nanodiamond for Tumor-Targeted Drug Delivery. *RSC Adv.* **2015**, *5* (101), 82711-82716. https://doi.org/10.1039/C5RA12383F.

(27) Mkandawire, M.; Pohl, A.; Gubarevich, T.; Lapina, V.; Appelhans, D.; Rödel, G.; Pompe, W.; Schreiber, J.; Opitz, J. Selective Targeting of Green Fluorescent Nanodiamond Conjugates to Mitochondria in HeLa Cells. *J. Biophoton.* **2009**, *2* (10), 596-606. https://doi.org/10.1002/jbio.200910002.

(28) Mochalin, V. N.; Gogotsi, Y. Wet Chemistry Route to Hydrophobic Blue Fluorescent Nanodiamond. *J. Am. Chem. Soc.* **2009**, *131* (13), 4594-4595. https://doi.org/10.1021/ja9004514.

(29) Abu Saleh, D.; Shimoni, O.; Sosnik, A. Novel Core-Corona Hybrid Nanomaterials Based on the Conjugation of Amphiphilic Polymeric Diblocks to the Surface of Multifunctional Nanodiamond Anchors. *Mater. Today Chem.* **2017**, *3*, 15-26. https://doi.org/10.1016/j.mtchem.2016.12.001.

(30) El-Faham, A.; Albericio, F. Peptide Coupling Reagents, More than a Letter Soup. *Chem. Rev.* **2011**, *111* (11), 6557-6602. https://doi.org/10.1021/cr100048w.

(31) Hermanson, G. T. Zero-Length Crosslinkers. In *Bioconjugate Techniques*; Elsevier, 2013; pp 259-273. https://doi.org/10.1016/B978-0-12-382239-0.00004-2.

(32) El-Faham, A. NEW SYNTHESES OF *Bis* (TETRAMETHYLENE)FLUOROFORMAMIDINIUM HEXAFLUOROPHOSPHATE (*BTFFH*) AND 1,3-DIMETHYL-2-FLUORO-4,5-DIHYDRO-1H-IMIDAZOLIUM HEXAFLUOROPHOSPHATE (*DFIH*). UTILITY IN PEPTIDE COUPLING REACTIONS. *Org. Prep. Proced. Int.* **1998**, *30* (4), 477-481. https://doi.org/10.1080/00304949809355316.

(33) Prabhu, G.; Narendra, N.; Basavaprabhu, B.; Panduranga, V.; Sureshbabu, V. V. Amino Acid Fluorides: Viable Tools for Synthesis of Peptides, Peptidomimetics and Enantiopure Heterocycles. *RSC Adv.* **2015**, *5* (60), 48331-48362. https://doi.org/10.1039/C4RA16142D.

(34) Jarre, G.; Heyer, S.; Memmel, E.; Meinhardt, T.; Krueger, A. Synthesis of Nanodiamond Derivatives Carrying Amino Functions and Quantification by a Modified Kaiser Test. *Beilstein J. Org. Chem.* **2014**, *10* (1), 2729-2737. https://doi.org/10.3762/bjoc.10.288.

(35) Merz, V.; Lenhart, J.; Vonhausen, Y.; Ortiz-Soto, M. E.; Seibel, J.; Krueger, A. Zwitterion-Functionalized Detonation Nanodiamond with Superior Protein Repulsion and Colloidal Stability in Physiological Media. *Small* **2019**, 1901551. https://doi.org/10.1002/smll.201901551.

(36) Barras, A.; Lyskawa, J.; Szunerits, S.; Woisel, P.; Boukherroub, R. Direct Functionalization of Nanodiamond Particles Using Dopamine Derivatives. *Langmuir* **2011**, *27* (20), 12451-12457. https://doi.org/10.1021/la202571d.

(37) Schmidlin, L.; Pichot, V.; Comet, M.; Josset, S.; Rabu, P.; Spitzer, D. Identification, Quantification and Modification of Detonation Nanodiamond Functional Groups. *Diamond Relat. Mater.* **2012**, *22*, 113-117. https://doi.org/10.1016/j.diamond.2011.12.009.

(38) Cheng, J.; He, J.; Li, C.; Yang, Y. Facile Approach to Functionalize Nanodiamond Particles with V-Shaped Polymer Brushes. *Chem. Mater.* **2008**, *20* (13), 4224-4230. https://doi.org/10.1021/cm800357g.

(39) Magee, J. A.; Herd, A. C. Internal Standard Calculations in Chromatography. *J. Chem. Educ.* **1999**, *76* (2), 252. https://doi.org/10.1021/ed076p252.

(40) Neburkova, J.; Vavra, J.; Cigler, P. Coating Nanodiamonds with Biocompatible Shells for Applications in Biology and Medicine. *Curr. Opin. Solid State Mater. Sci.* **2017**, *21* (1), 43-53. https://doi.org/10.1016/j.cossms.2016.05.008.

(41) Murali, V. S.; Wang, R.; Mikoryak, C. A.; Pantano, P.; Draper, R. Rapid Detection of Polyethylene Glycol Sonolysis upon Functionalization of Carbon Nanomaterials: *Exp. Biol. Med.* **2015**. https://doi.org/10.1177/1535370214567615.

(42) Wang, R.; Murali, V. S.; Draper, R. Detecting Sonolysis of Polyethylene Glycol Upon Functionalizing Carbon Nanotubes. In *Cancer Nanotechnology: Methods and Protocols*; Zeineldin, R., Ed.; Methods in Molecular Biology; Springer: New York, NY, 2017; pp 147-164. https://doi.org/10.1007/978-1-4939-6646-2_10.

(43) Capon, P. K.; Avery, T. D.; Purdey, M. S.; Abell, A. D. An Improved Synthesis of 4-Aminobutanenitrile from 4-Azidobutanenitrile and Comments on Room Temperature Stability. *Synth. Commun.* **2021**, *51* (3), 428-436. https://doi.org/10.1080/00397911.2020.1832527.

(44) Deb, P.; Haldar, T.; Kashid, S. M.; Banerjee, S.; Chakrabarty, S.; Bagchi, S. Correlating Nitrile IR Frequencies to Local Electrostatics Quantifies Noncovalent Interactions of Peptides and Proteins. *J. Phys. Chem. B* **2016**, *120* (17), 4034-4046. https://doi.org/10.1021/acs.jpcb.6b02732.

(45) Petit, T.; Puskar, L. FTIR Spectroscopy of Nanodiamonds: Methods and Interpretation. *Diamond Relat. Mater.* **2018**, *89*, 52-66. https://doi.org/10.1016/j.diamond.2018.08.005.

(46) Tu, J.-S.; Perevedentseva, E.; Chung, P.-H.; Cheng, C.-L. Size-Dependent Surface CO Stretching Frequency Investigations on Nanodiamond Particles. *J. Chem. Phys.* **2006**, *125* (17), 174713. https://doi.org/10.1063/1.2370880.

(47) Gaillard, C.; Girard, H. A.; Falck, C.; Paget, V.; Simic, V.; Ugolin, N.; Bergonzo, P.; Chevillard, S.; Arnault, J. C. Peptide Nucleic Acid-Nanodiamonds: Covalent and Stable Conjugates for DNA Targeting. *RSC Adv.* **2013**, *4* (7), 3566-3572. https://doi.org/10.1039/C3RA45158E.

(48) Reineck, P.; Lau, D. W. M.; Wilson, E. R.; Fox, K.; Field, M. R.; Deeleepojananan, C.; Mochalin, V. N.; Gibson, B. C. Effect of Surface Chemistry on the Fluorescence of Detonation Nanodiamonds. *ACS Nano* **2017**, *11* (11), 10924-10934. https://doi.org/10.1021/acsnano.7b04647.

(49) West, R. Siegfried Ruhemann and the Discovery of Ninhydrin. *J. Chem. Educ.* **1965**, *42* (7), 386. https://doi.org/10.1021/ed042p386.

(50) Ankati, H.; Biehl, E. Microwave-Assisted Benzyne-Click Chemistry: Preparation of 1H-Benzo[d][1,2,3]Triazoles. *Tetrahedron Letters* **2009**, *50* (32), 4677-4682. https://doi.org/10.1016/j.tetlet.2009.06.004.

(51) Maligres, P. E.; Waters, M. S.; Weissman, S. A.; McWilliams, J. C.; Lewis, S.; Cowen, J.; Reamer, R. A.; Volante, R. P.; Reider, P. J.; Askin, D. Preparation of a Clinically Investigated Ras Farnesyl Transferase Inhibitor. *Journal of Heterocyclic Chemistry* **2003**, *40* (2), 229-241. https://doi.org/10.1002/jhet.5570400206.

Chapter 5: Carbon binding peptides for nanodiamond functionalisation

Scope

Given the difficulties encountered in amide bond formation on carboxylated ND surfaces detailed in Chapter 4, an alternative approach to functionalise NDs was clearly required. This chapter describes the identification of a set of four carbon-binding peptides from literature which bind to the carbon allotropes of diamond-like carbon, carbon nanotubes, diamond film, and graphite film and their application to functionalise NDs. This investigation is discussed herein, presented in publication format ahead of submission to the Journal of Physical Chemistry C.

Patrick K. Capon,[1-3] Philipp Reineck,[3,4] Aimee J. Horsfall,[1-3] Wioleta Kowalczyk,[5] Marco D. Torelli,[6] Olga A. Shendarova,[6] Malcolm S. Purdey,[1-3] Andrew D. Abell,[*1-3]

1. School of Physical Sciences, The University of Adelaide, Adelaide, SA, 5005, Australia
2. Institute for Photonics and Advanced Sensing, The University of Adelaide, Adelaide, SA, 5005, Australia
3. Australian Research Council Centre of Excellence for Nanoscale BioPhotonics, Australia
4. Department of Physics, School of Science, RMIT University, Melbourne, VIC, 3000, Australia
5. CSIRO Manufacturing, Clayton South, Victoria, 3169, Australia
6. Adámas Nanotechnologies, Raleigh, North Carolina, 27617, United States of America

Statement of Authorship

Title of Paper	Carbon-binding peptides for nanodiamond functionalisation
Publication Status	☐ Published ☐ Accepted for Publication ☐ Submitted for Publication ☒ Unpublished and Unsubmitted work written in manuscript style
Publication Details	Patrick K. Capon, Philipp Reineck, Aimee J. Horsfall, Wioleta Kowalczyk, Marco D. Torelli, Olga A. Shendarova, Malcolm S. Purdey, Andrew D. Abell*, Carbon-binding peptides for nanodiamond functionalization, manuscript in preparation for submission to Journal of Physical Chemistry C

Principal Author

Name of Principal Author (Candidate)	Patrick Capon		
Contribution to the Paper	Performed absorption, FTIR, TGA, DLS/ZP experiments, attached fluorophore to all peptides, purified peptides, analysed the data, wrote the manuscript.		
Overall percentage (%)	60		
Certification:	This paper reports on original research I conducted during the period of my Higher Degree by Research candidature and is not subject to any obligations or contractual agreements with a third party that would constrain its inclusion in this thesis. I am the primary author of this paper.		
Signature		Date	25/4/2021

Co-Author Contributions

By signing the Statement of Authorship, each author certifies that:

i. the candidate's stated contribution to the publication is accurate (as detailed above);

ii. permission is granted for the candidate in include the publication in the thesis; and

iii. the sum of all co-author contributions is equal to 100% less the candidate's stated contribution.

Name of Co-Author	Philipp Reineck		
Contribution to the Paper	Prepared the HPHT ND material, performed and analysed confocal microscopy experiments, aided design and analysis of FTIR, DLS/ZP experiments. Aided design of figures, edited the manuscript.		
Signature		Date	8 April 2021

Name of Co-Author	Aimee Horsfall		
Contribution to the Paper	Conceptualised and synthesised the carbon-binding peptides, aided with purification of peptides. Aided design of colourimetric assay and edited the manuscript.		
Signature		Date	25 April 2021

Name of Co-Author	Wioleta Kowalczyk		
Contribution to the Paper	Designed and synthesised the carbon-binding peptides, edited the manuscript.		
Signature		Date	16/04/2021

Name of Co-Author	Marco Torelli		
Contribution to the Paper	Provided the DND material used, provided methodology and advice for all DND reactions. Edited the manuscript.		
Signature		Date	26/4/2021

Name of Co-Author	Olga Shendarova		
Contribution to the Paper	Provided the DND material used, provided methodology and advice for all DND reactions. Edited the manuscript.		
Signature		Date	26/4/2021

Name of Co-Author	Malcolm Purdey		
Contribution to the Paper	Provided original concept, oversaw the experimental design, supervised Patrick during PhD candidature.		
Signature		Date	15/04/2021

Name of Co-Author	Andrew Abell		
Contribution to the Paper	Oversaw the experimental design, provided experimental equipment and funding, supervised Patrick during PhD candidature.		
Signature		Date	26/4/2021

5.1 Abstract

Functionalisation of nanodiamonds (NDs) with organic molecules provides a hybrid nanoparticle with advantageous properties for application in drug delivery, cell imaging, or sensing, among others. Here four carbon-binding peptides (**1-DLC**, **2-CN**, **3-DF** and **4-GF**) are employed to non-covalently coat NDs, with coatings confirmed through infrared spectroscopy and thermogravimetric analysis. The retention of each peptide after extensive washing in buffer was assessed by a colourimetric assay, where **1-DLC** was found to be the most well-retained, at 87% and 35% on detonation and high-pressure high-temperature NDs respectively with a K_d of 21 μM between **1-DLC** and DNDs. **1-DLC** was found to bind to NDs predominantly through electrostatic interactions, while **2-CN** bound largely through non-polar interactions. A coating of **1-DLC** or **2-CN** improved the colloidal stability of detonation NDs in aqueous sodium chloride, but did not affect the colloidal stability of high-pressure high-temperature NDs. This study is an important contribution to the ND functionalisation field as it provides a new, highly adaptable approach to functionalise NDs using carbon-binding peptides.

5.2 Introduction

Nanodiamonds (NDs) are a versatile nanomaterial,[1] and are generally accepted as biocompatible due to their low reactivity in biological environments.[2-4] However, the long-term exposure effects are not yet known.[4,5] Reported applications of NDs include cell or tissue labelling,[4,6-8] fluorescence,[9-11] and use as photoacoustic contrast agents.[12] The surface functionalisation of a ND with organic molecules can impart additional advantageous properties. For example, a surface-bound molecule can improve colloidal stability of the ND suspension,[13] or provide fluorescence emission.[14,15] Such functionalisation processes have been reported using silanisation, amidation, and esterification reactions on NDs that bear surface amines,[16-18] alcohols,[19-22] or carboxylic acids.[15,23,24] The resultant hybrid nanomaterials have been applied to drug delivery,[25-29] cell specific targeting of the ND complex,[24,30,31] and tissue engineering.[32]

The addition of an organic fluorophore to a ND containing nitrogen-vacancy (NV) centres is of particular interest as the photostable NV fluorescence provides an opportunity to circumvent

organic fluorophore photobleaching.[10,33] This is achieved by interrogation of the NV centre for nanoparticle tracking and imaging, while the surface bound fluorophore is available for sensing on-demand without having been photobleached by tracking or imaging.[11] We initially attempted to optimise the attachment of fluorescein to carboxylated NV-NDs in an extension of our previous report (see Chapter 4).[11] However, we could not confidently establish the presence of an amide bond through characterisation techniques such as infrared spectroscopy and thermo-gravimetric analysis. The challenges encountered in characterisation of functionalised NDs are well summarised in a recent review from Reina *et al*.[5]

Given the difficulties to prepare covalently functionalised NDs, we sought an alternative method to functionalise carboxylated NDs. Non-covalent coatings are one such option. For example, NDs have been coated with cytochrome c through a layer of poly-L-lysine,[34] coated with organic polymers,[35] or embedded within porous silica shells.[36,37] One approach that is yet to be investigated is the use of solid-binding peptides,[38,39] a class of peptides which can specifically bind to materials including gold,[40] silica,[41] or silk,[42] to name a few. Here, a set of four carbon-binding peptides (CBPs) from literature are used to coat both detonation NDs and high-pressure high-temperature synthesised NDs. The optimal CBP is determined and presented as an effective new option for non-covalent ND functionalisation.

5.3 Results and discussion

5.3.1 Selection of carbon-binding peptides

Carbon-binding peptides (CBPs) that bind to four different carbon allotropes were identified from literature, namely diamond-like carbon (DLC),[43-45] carbon nanotubes (CN),[46] diamond film (DF),[47] and graphite film (GF).[48] These four selected peptides provided a broad scope to investigate the most effective CBP for coating of NDs. All four CBPs were synthesised by standard Fmoc/tBu solid phase peptide synthesis protocols as detailed in Experimental section 5.5.4. Fluorescein was appended to each CBP to allow fluorescence-based visualisation of the peptides when coated on NDs. First, Fmoc-aminohexanoic acid was attached to the *N*-terminus of each CBP by a DIC and Oxyma mediated amide coupling. Subsequent treatment with 20% piperidine removed

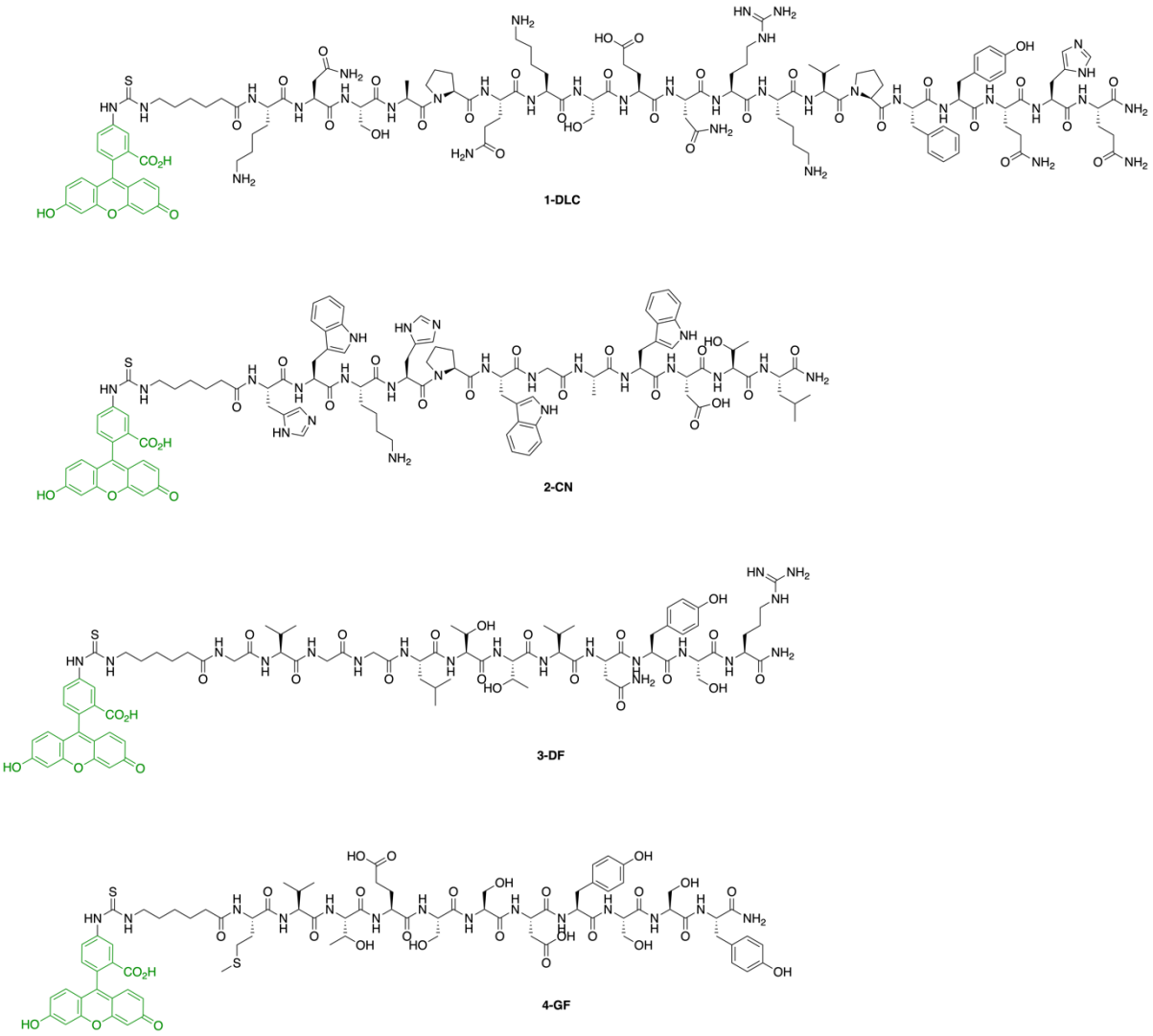

Figure 5.1. Structure of the four carbon-binding peptides (CBPs) used in this study with fluorescein tag highlighted in green. From top to bottom: Diamond-like carbon (**1-DLC**),[43] Carbon nanotubes (**2-CN**),[46] Diamond film (**3-DF**),[47] Graphite film (**4-GF**).[48]

the Fmoc protecting group, then fluorescein isothiocyanate was attached to the peptide *N*-terminus by formation of a thiourea bond to provide the fluorescein tagged analogue of each CBP (**1-DLC**, **2-CN**, **3-DF**, **4-GF**, Figure 5.1).

5.3.2 Colourimetric assay design

A new colourimetric assay to determine the amount of CBP adhered to NDs was developed, based on the 490 nm absorbance of the isolated supernatant after CBP coated NDs were washed with aqueous solvent. The solid ND pellet was separated from the supernatant by centrifugation (Figure 5.2). The supernatant absorbance was then used to calculate the amount of free CBP in solution. A reference sample of each CBP in 50 mM phosphate buffer at pH 8.01 was also prepared and its absorbance at 490 nm collected. This was used to calculate the exact starting

concentration of each CBP upon addition to NDs. The amount of CBP adhered to the washed NDs was therefore calculated from the known initial amount of peptide and the quantity of unbound peptide found in the supernatant, according to *Equation 5.1*.

$$Peptide_{on\ ND} = Peptide_{initial} - Peptide_{supernatant} \quad (5.1)$$

First, a calibration curve of 490 nm absorbance against concentration of 5(6)-carboxyfluorescein was constructed. Standard solutions of 5(6)-carboxyfluorescein were prepared in three phosphate buffer solvents: 50 mM phosphate buffer at pH 8.01 (A), 50 mM phosphate buffer with 1 M NaCl at pH 8.01 (B), and 50 mM phosphate buffer at pH 8.01 with 5% v/v DMSO (C). The absorbance of these standard solutions was collected on a plate reader and plotted against concentration of 5(6)-carboxyfluorescein (see Experimental section 5.5.3 and Supporting Information section S5.2). Next, each CBP was added to a suspension of NDs in 50 mM phosphate buffer at pH 8.01 (buffer A), for a final ND concentration of 1 mg/mL and peptide concentration of ~40 μM. The resulting mixture was sonicated for 30 min, then separated into 3 × 300 μL aliquots. All three aliquots were centrifuged (14,800 rpm, 45 min) and the supernatant separated from the ND pellet and set aside for later analysis (Figure 5.2). The CBP loaded ND pellets were resuspended in one of the three phosphate buffers (300 μL, A, B, or C) by sonication, then submitted to five further pellet and resuspension cycles. This provided five supernatant aliquots (5 × ~300 μL) for each washing buffer, along with the original reaction supernatant, and the remaining CBP loaded ND pellets (see Figure 5.2). The absorbance of each supernatant aliquot was measured by plate reader and the CBP concentration calculated with reference to the prepared 5(6)-carboxyfluorescein calibration curves (see Supporting Information Figure S5.13).

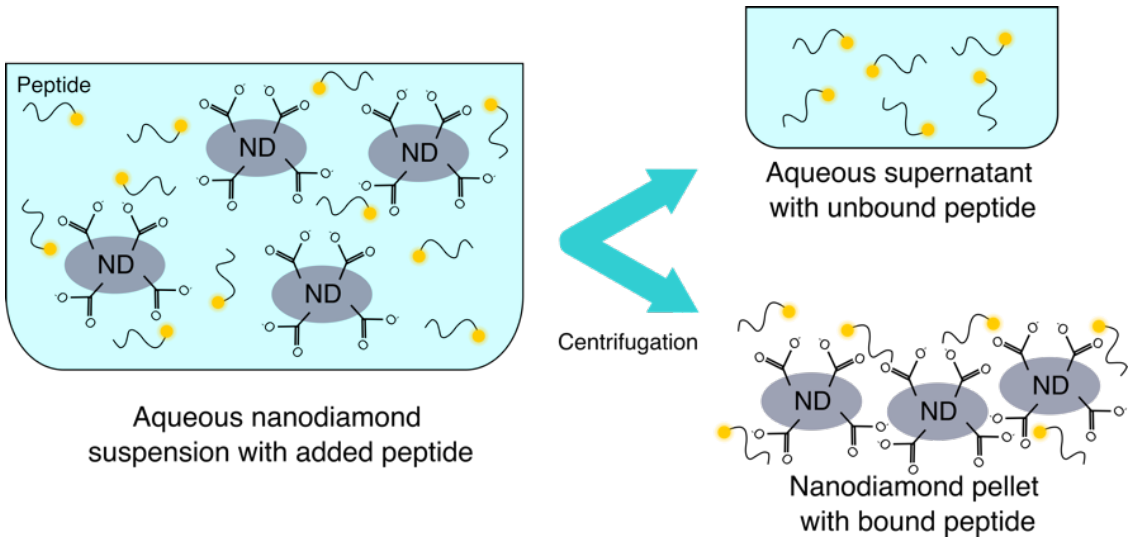

Figure 5.2. Diagram of the nanodiamond (ND) washing procedure used during the colourimetric assay. The peptide-loaded NDs are separated from unbound peptide by centrifugation, which provides a ND pellet and supernatant containing the unbound peptide. The amount of unbound peptide remaining in the supernatant can therefore be used to back-calculate the peptide loaded on the NDs as per equation 5.1. The NDs are then washed by repeated re-suspension and centrifugation cycles.

5.3.3 Colourimetric assay results

The described colourimetric determination of the amount of CBPs loaded on NDs was performed for NDs prepared by detonation (DNDs) and by high-pressure high-temperature synthesis (HPHT NDs), in order to determine if our approach to functionalise NDs through addition of CBPs was generalisable to multiple ND types. The ~5 nm carboxylated DNDs were provided by Adámas Nanotechnologies, while the ~120 nm HPHT NDs were purchased from Nabond (Hong Kong) and treated to provide a carboxylated surface as detailed in the Experimental section 5.5.1.

The colourimetric assay revealed that the most retained CBP on NDs was **1-DLC** for both DNDs and HPHT NDs, with 87% and 35% of **1-DLC** remaining adhered to the NDs respectively (Figure 5.3A, purple). This high level of **1-DLC** retention on NDs was expected given the peptide was originally identified to bind to diamond-like carbon, an amorphous carbon material with a mixture of sp^3 and sp^2 hybridised carbon atoms.[43] Detonation NDs in particular are known to have deposits of amorphous carbon on the surface,[49] which is a potential cause for the observed higher retention of **1-DLC** on DNDs over HPHT NDs when treated at the same ND concentration of 1 mg/mL.

The second most retained peptide on NDs was **2-CN**, with 48% and 18% peptide remaining respectively on DNDs and HPHT NDs (Figure 5.3A, red). This suggests that **2-CN** can

bind moderately to the diamond allotrope of carbon, as well as the described binding to carbon nanotubes.[46] There was limited retention of peptide **3-DF** observed for both ND types, with only 16% and 4% peptide remaining on DNDs and HPHT NDs respectively (Figure 5.3A, blue). No retention of the final peptide, **4-GF**, was observed for either ND type (Figure 5.3A, green). The poor retention of both **3-DF** and **4-GF** is not unexpected, as the DNDs and HPHT NDs before exposure to CBPs bear little resemblance to 2-dimensional films (see Supporting Information Figures S5.14 and S5.15 for scanning electron microscopy images).[50,51]

Lastly, a negative control was conducted where 5(6)-carboxyfluorescein was added to NDs, in order to demonstrate that the CBP sequence is required for binding to NDs. Free 5(6)-carboxyfluorescein (40 μM) was added to NDs and the NDs washed according to the centrifugation protocol described earlier for the CBPs. The isolated supernatants were subjected to the colourimetric assay, where no 5(6)-carboxyfluorescein was observed to remain on either ND type after washing (Figure 5.3A, black). This indicates that 5(6)-carboxyfluorescein alone cannot bind to carboxylated DNDs or carboxylated HPHT NDs. Hence, the CBP sequence is critical to coat NDs, with **1-DLC** the most well-retained peptide.

The binding affinity between **1-DLC** and DNDs was determined by a fluorescence polarisation assay to further characterise the most well-retained CBP. This was carried out by adding **1-DLC** (2 μM) to DNDs (0 to 2.5 mg/mL) and measuring the resultant fluorescence polarisation (see Supporting Information section S5.3 and Figure 5.3B). A carboxylic acid loading of 0.1 mmol/g on the NDs was assumed as a minimum loading, based on literature reports which vary from 0.1 to 1.0 mmol/g.[22,52-55] This was used to convert the DND concentrations from mg/mL to mM, and dissociation constant, K_d, of 21 μM was calculated using GraphPad Prism 9 software (95% confidence interval 11.9 to 36.2 μM). This is in agreement with the surface binding affinities reported for a range of other solid-binding peptides in literature.[38] As such, **1-DLC** is well adhered to the DNDs. The binding affinity of 1-DLC to HPHT NDs was not able to be determined due to excessive levels of light scattering interrupting the fluorescence polarisation measurements.

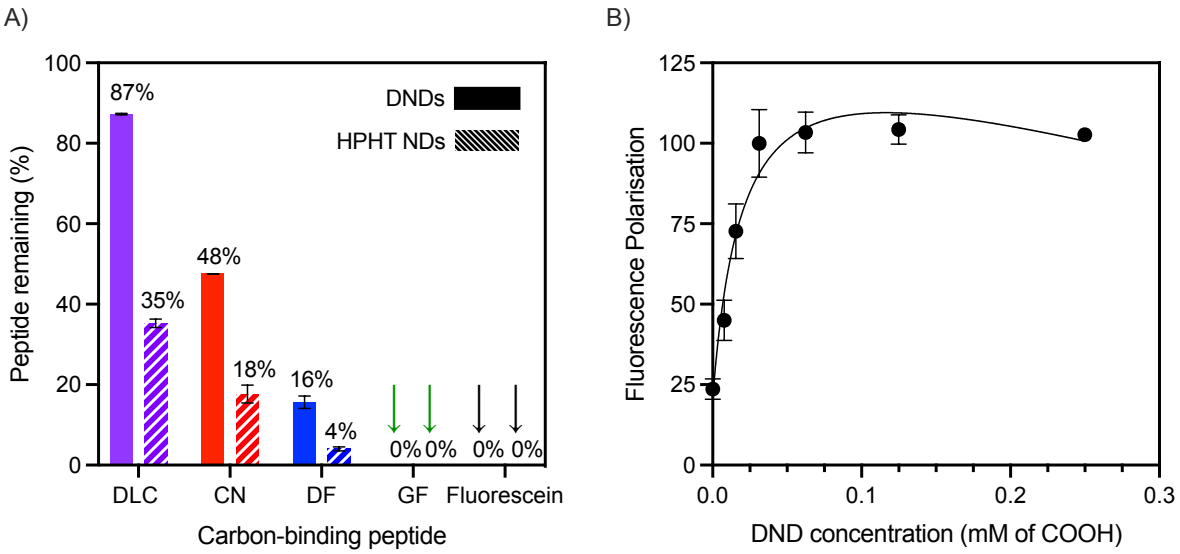

Figure 5.3. A) Peptide remaining (%) on nanodiamonds (NDs) as calculated by colourimetric assay. Detonation NDs are shown by the solid bars and high-pressure high-temperature NDs by the striped bars. **1-DLC**, purple; **2-CN**, red; **3-DF**, blue; **4-GF**, green; 5(6)-carboxyfluorescein, black. **B)** Fluorescence polarisation of **1-DLC** added to DNDs with a calculated K_d of 21 μM. Error bars are standard deviation.

5.3.4 Washing buffer comparison

The three washing buffers A (50 mM phosphate buffer at pH 8.01), B (50 mM phosphate buffer with 1 M NaCl at pH 8.01), and C (50 mM phosphate buffer at pH 8.01 with 5% v/v DMSO) were compared in order to investigate the interaction between ND surface and CBP. This comparison was limited to peptides **1-DLC** and **2-CN** due to the low retention on NDs observed for **3-DF** and **4-GF**. As described earlier, the amount of CBP present in the supernatant was calculated by 490 nm absorbance with reference to a calibration curve of 5(6)-carboxyfluorescein. Figure 5.4 depicts this for each washing buffer A, B, or C. The majority of peptide was removed from the NDs in the reaction supernatant and first wash in all cases. The absorbance calculated for the remaining washes was similar to the blank, which indicates minimal peptide removal from the NDs.

1-DLC was removed from both DNDs and HPHT NDs most effectively by washing with phosphate buffer containing additional 1 M sodium chloride (buffer B, Figure 5.4A and 5.4B, respectively). This suggests that **1-DLC** predominantly binds to NDs through electrostatic interactions. The isoelectric point (pI) of **1-DLC** was calculated to be 10.63 using GenScript's online peptide property calculator,[56] with an approximate net charge of +2 at pH 8 (see Experimental section 5.5.1). Therefore, it is likely that this net positive charge of **1-DLC** plays a

significant role when binding to the negatively charged carboxylated NDs (reported pK_a 4.2).[54] This conclusion is consistent with the observations of Gabryelczyk *et al*., who found that the positive charge of **1-DLC** was important for binding to diamond-like carbon.[44] However, they suggested that the binding event is more complex than electrostatic interactions alone and is dependent on the overall conformation of the peptide.[44] This is consistent with the observation here that washing with phosphate buffer alone (A) or with 5% DMSO (C) also removed any unbound **1-DLC** from NDs.

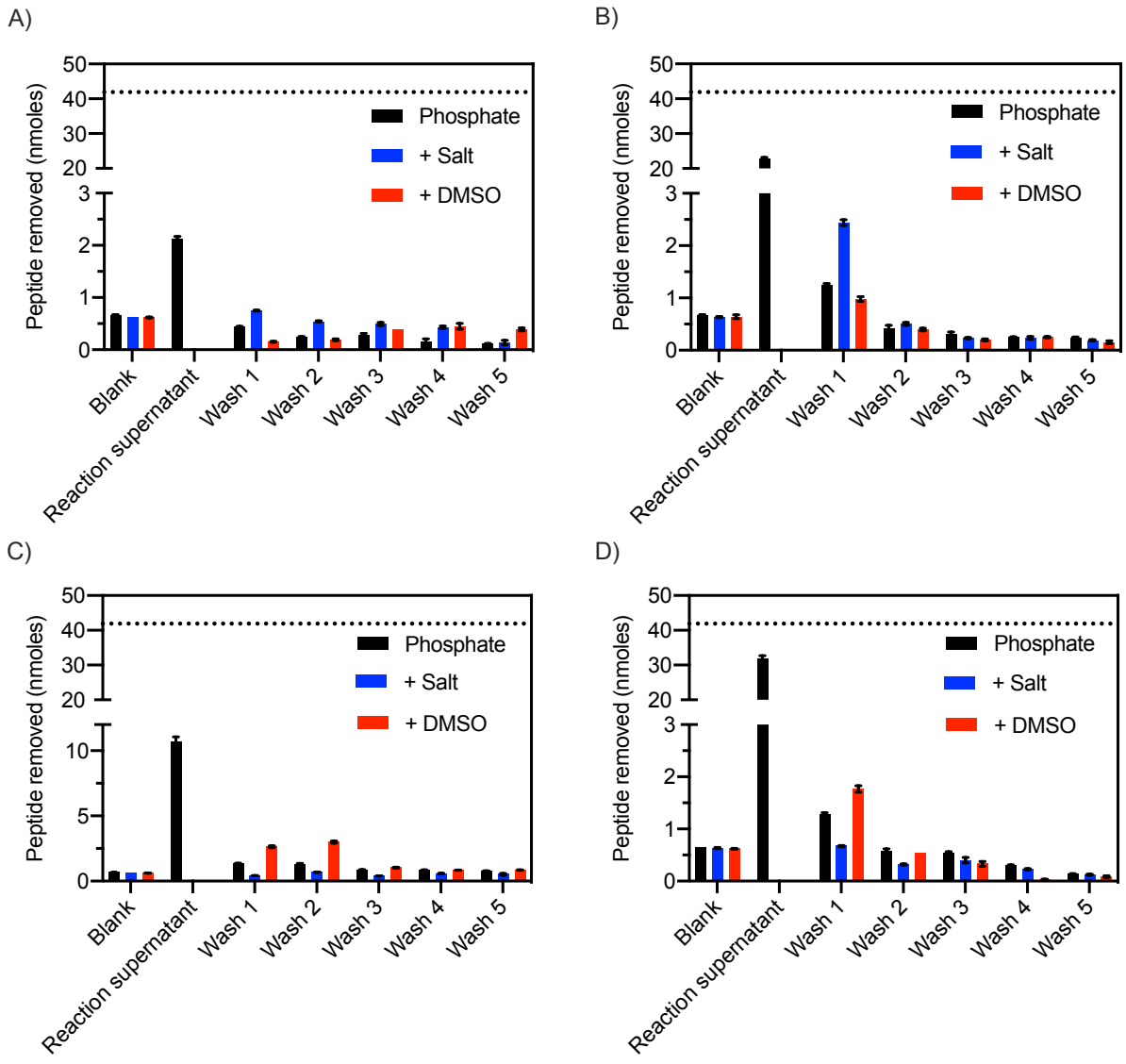

Figure 5.4. Carbon-binding peptide removed from NDs by washing with 50 mM phosphate buffer at pH 8.01 (black), 50 mM phosphate buffer with 1 M NaCl at pH 8.01 (blue), or 50 mM phosphate buffer at pH 8.01 with 5% v/v DMSO (red). Note that only a blue bar is shown for the reaction supernatant as all reactions were initially in 50 mM phosphate at pH 8.01. The dotted line represent the initial amount of peptide added to the NDs. **A)** Plot for **1-DLC** loaded DNDs, **B)** Plot for **1-DLC** loaded HPHT NDs, **C)** Plot for **2-CN** loaded DNDs), **D)** Plot for **2-CN** loaded HPHT NDs. All error bars are standard deviations.

2-CN was removed from both DNDs and HPHT NDs most effectively by washing with phosphate buffer containing an additional 5% v/v DMSO (buffer C, Figure 5.4C and 5.4D, respectively). This suggests that **2-CN** largely binds to the ND surface through non-polar interactions, which is consistent with the original suggestion that the binding of **2-CN** to carbon nanotubes was predominantly due to aromatic and hydrophobic interactions.[46] The addition of 1 M sodium chloride (buffer B) resulted in less removal of **2-CN** than phosphate buffer alone (buffer A), which suggests that there are minimal electrostatic interactions between **2-CN** and the ND surface. This is consistent with the calculated pI of 7.26 for **2-CN**, which indicates it will have a net 0 charge at pH 8.[56]

The colourimetric assay indicated that peptides **1-DLC** and **2-CN** are the optimal choice for non-covalent coating of a fluorophore onto DNDs or HPHT NDs. Interestingly, more peptide was retained on DNDs than HPHT NDs for all three peptides (**1-DLC**, **2-CN** and **3-DF**) found to bind to NDs. However, there is a large particle size difference between the DNDs (5 nm) and HPHT NDs (120 nm) which should be taken into account, as this size difference affects the available surface area for CBP adherence. The surface area of the DNDs and HPHT NDs used here was calculated relying on the assumption that all NDs are spherical on average (see Supporting Information section S5.5). This assumption is generally accepted for DNDs,[57] but has been shown to be inaccurate for HPHT NDs.[51] These surface area calculations return 24× more available surface area in 1 mg of DNDs compared to 1 mg of HPHT NDs. However, the retention of CBPs on DNDs compared to HPHT NDs was only 2-3× greater. This suggests that there is more dense packing of the CBPs on the surface of HPHT NDs, however a greater overall quantity of CBP was adhered to DNDs when both ND samples were used at a concentration of 1 mg/mL. Further computational modelling is clearly required to understand the different CBP loadings between DNDs and HPHT NDs, including a better approximation for the average volume of a HPHT ND. This modelling is beyond the scope of this preliminary study.

5.3.5 Characterisation of CBP loaded NDs

Confocal microscopy

Confocal microscopy was used to confirmed the presence of **1-DLC** or **2-CN** on both DNDs and HPHT NDs. The peptide loaded NDs were drop-cast onto a glass slide and irradiated at 476 and 554 nm to excite the fluorescein and nitrogen-vacancy (NV) centres respectively. The subsequent fluorescence emission was collected between 498 and 541 nm and 719 and 770 nm respectively, with the resultant false colour images shown in Figure 5.5 for the HPHT NDs. Note that only the HPHT NDs contain NV centres, as such the DNDs were not fluorescent under 476 nm excitation. The green fluorescence originating from the fluorescein-bearing CBPs was observed to fully overlap with the red fluorescence of the NV centres, which indicates that the CBPs are co-localised with the HPHT NDs. A similar pattern of green fluorescence was observed for the CBP loaded DNDs (see Supporting Information Figure S5.16). Overall, confocal microscopy confirmed the presence of both **1-DLC and 2-CN** on DNDs and HPHT NDs.

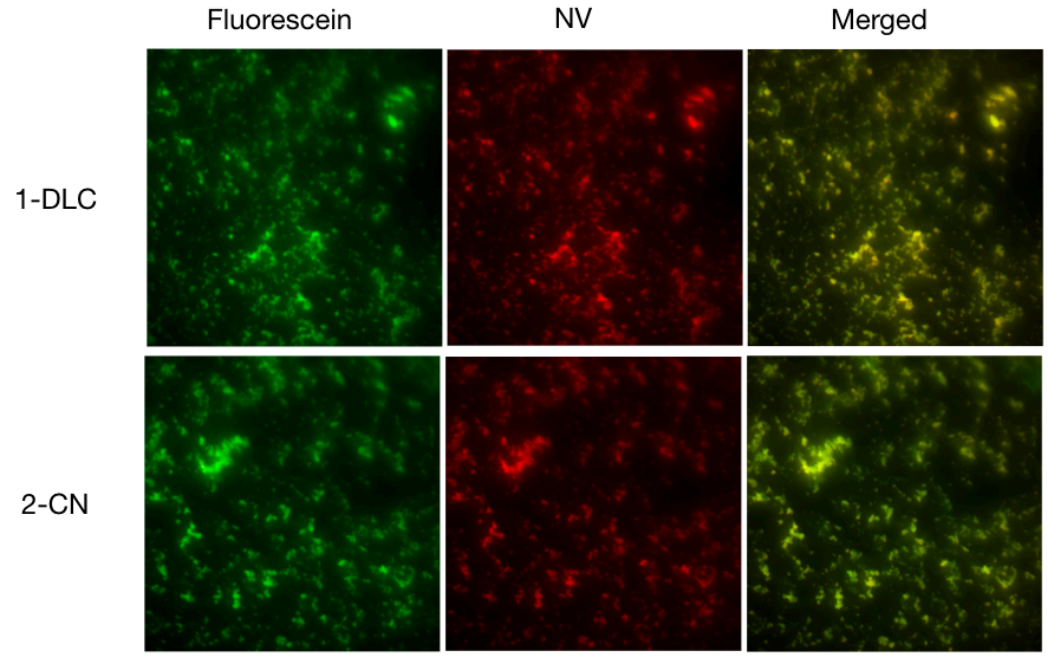

Figure 5.5. Confocal microscopy images of HPHT NDs with adhered **1-DLC** (top row) and **2-CN** (bottom row). **Left,** the fluorescein channel, ex. 476 nm, em. 498-541 nm. **Middle,** the NV channel ex. 554 nm em. 719-770 nm. **Right,** Merged image of the fluorescein and NV channels showing complete overlap between the fluorescein and NV fluorescence.

Infrared spectroscopy

The CBP loaded NDs were analysed by FTIR to confirm the presence of **1-DLC**, **2-CN**, and **3-DF** and to confirm the absence of **4-GF**. The CBP loaded ND pellets obtained by centrifugation during the peptide retention experiments were resuspended in water (1 mg/mL) and lyophilised. FTIR spectra of the lyophilised CBP loaded NDs were collected and compared to FTIR spectra obtained from unreacted NDs and a pure sample of the relevant CBP (see Experimental section 5.5.2).

All CBPs exhibited similar FTIR spectra, with peaks at approximately 3300, 2950, 1650, 1550, and 1450 cm^{-1}, which are assigned to O-H, C-H, C=O (amide I), C=O (amide II), and C-H functional groups respectively (Figure 5.6).[58] Two major peaks were observed in the unreacted DND FTIR spectrum at 1624 and 1767 cm^{-1} which are common for nanodiamond material (Figure 5.6A and 5.6C, black).[59,60] Similarly, two major peaks were observed in the unreacted HPHT ND FTIR spectrum at 1490 and 1780 cm^{-1} (Figure 5.6B and 5.6D, black). The FTIR spectra of **1-DLC** coated DNDs and HPHT NDs were observed to contain additional peaks at 1550 and 1450 cm^{-1} when compared to the respective unreacted ND samples (Figure 5.6A and 5.6B, purple). Furthermore, the fingerprint region (below 1400 cm^{-1}) of the **1-DLC** loaded NDs was consistent with to the fingerprint region of pure **1-DLC** (Figure 5.5A and 5.5B). These additional peaks indicate the presence of **1-DLC** adhered to both DNDs and HPHT NDs, in agreement with the colourimetric assay.

The FTIR spectrum of **2-CN** coated DNDs was observed to contain new peaks at 1550, 1450, and 1100 cm^{-1} in comparison to unreacted DNDs (Figure 5.6C). Together these three additional peaks confirm the presence of **2-CN** on DNDs. The fingerprint region of the **2-CN** coated HPHT NDs FTIR spectrum contained additional peaks in comparison to the unreacted HPHT ND spectrum, which indicates the presence of **2-CN** on HPHT NDs in agreement with the colourimetric assay. However, no additional amide I or II peaks were observed at 1550 or 1450 cm^{-1} for the **2-CN** loaded HPHT NDs (Figure 5.6D). This is likely due to the low loading of **2-CN**, as calculated by the colourimetric assay, resulting in low intensity peaks that could not be resolved from the background noise in the FTIR spectra.

The FTIR spectra for **3-DF** coated DNDs and HPHT NDs, and for NDs after reaction with **4-GF** (found to not bind to NDs) are shown in the Supporting Information (Figure S5.17). These spectra suggest the presence of **3-DF** on DNDs, through a peak match at 1100 cm^{-1}, but are inconclusive for **3-DF** on HPHT NDs. This is likely due to the low loading of **3-DF**, as seen for **2-CN** loaded HPHT NDs. The absence of **4-GF** on both ND types was confirmed by the observation of unchanged FTIR spectra for NDs after **4-GF** was added compared to the FTIR spectra of untreated NDs. Overall, FTIR analysis was consistent with the colourimetric assay results and confirmed the presence of **1-DLC**, **2-CN**, and **3-DF** on NDs, and confirmed the absence of **4-GF** on NDs.

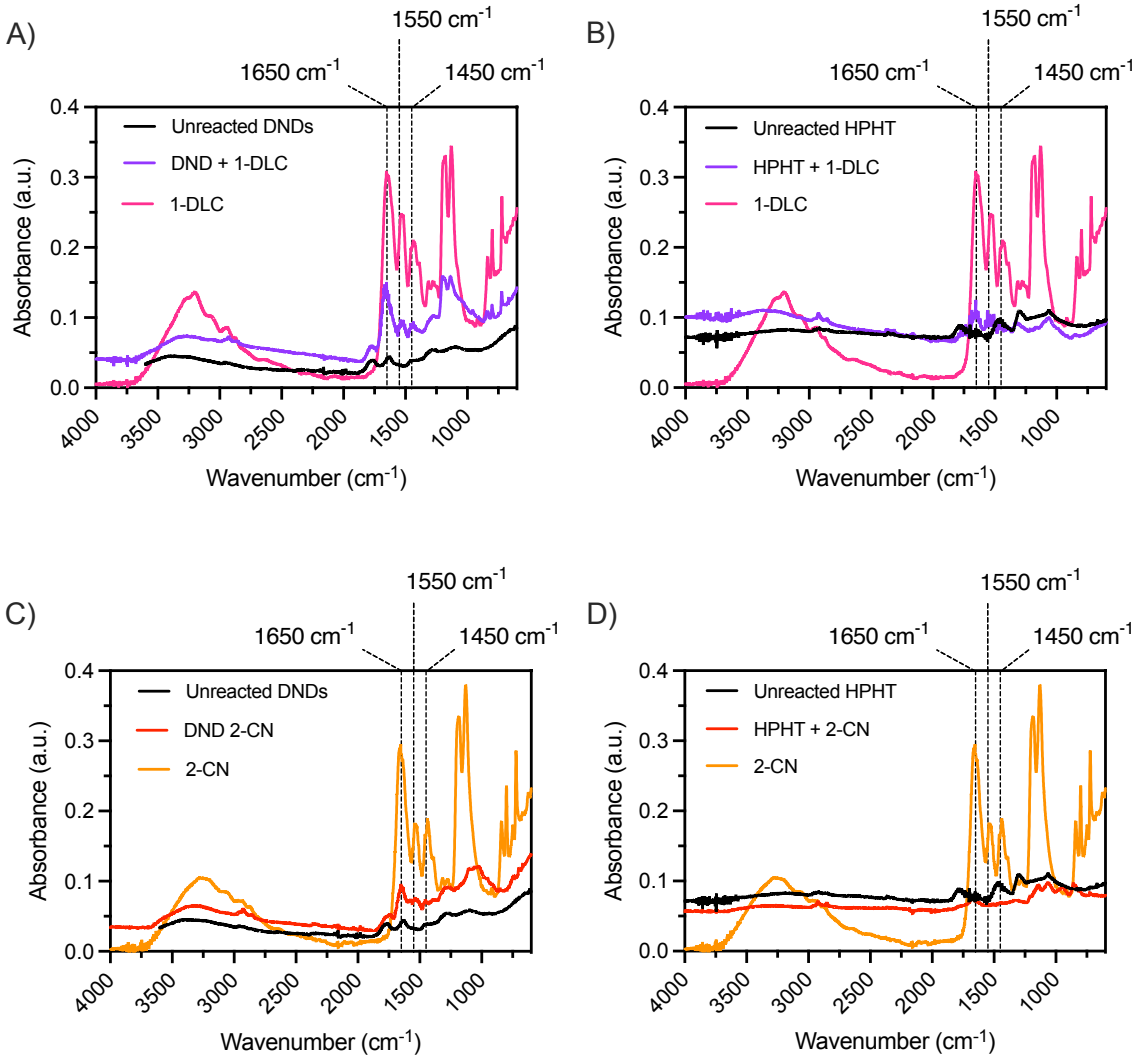

Figure 5.6. FTIR spectra for diamond-binding peptide (CBP) loaded nanodiamonds (NDs). **A)** FTIR spectra for unreacted DNDs (black), **1-DLC** loaded DNDs (purple), and pure **1-DLC** (pink). **B)** FTIR spectra for unreacted HPHT NDs (black), **1-DLC** loaded HPHT NDs (purple), and pure **1-DLC** (pink). **C)** FTIR spectra for unreacted DNDs (black), **2-CN** loaded DNDs (red), and pure **2-CN** (orange). **D)** FTIR spectra for unreacted HPHT NDs (black), **2-CN** loaded HPHT NDs (red), and pure **2-CN** (orange).

Colloidal stability

A suspension of bare ND particles is known to be destabilised by salt in aqueous media, which causes the NDs to aggregate. Therefore, the colloidal stability of **1-DLC** and **2-CN** loaded NDs was investigated by dynamic light scattering (DLS) to determine whether the peptide coating imparted additional stability. Nanoparticle aggregation is experimentally observable through an increase in DLS mean particle size and an increase (less negative) in zeta potential.[61] Here, sodium chloride was added at concentrations of 0.01, 0.1, 0.25, 0.5, and 1.0 mM to aqueous suspensions of NDs, and the DLS size and zeta potential of **1-DLC** and **2-CN** loaded NDs were compared to unreacted NDs, for both DNDs and HPHT NDs (Figure 5.7).

The zeta potential of all **1-DLC** or **2-CN** loaded DNDs remained more negative than the unreacted DNDs at all salt concentrations tested (Figure 5.7A). This indicates a small stabilisation effect against aggregation for the peptide loaded DNDs. The average size of unreacted DNDs also increased significantly from 41 nm to 3500 nm when the salt concentration was increased from 0.01 mM to 0.1 mM, which shows that the unreacted DNDs aggregate severely in 0.1 mM salt (Figure 5.7B). However, the average size of the peptide loaded DNDs remained steady around 1000 $\pm$ 500 nm at all salt concentrations tested. This indicates that **1-DLC** and **2-CN** initially cause the DNDs to form large aggregates (1800 and 700 nm respectively), but these aggregates are stabilised against the further aggregation seen for the unreacted DNDs at 0.1 mM salt concentration, up to 1.0 mM.

The **1-DLC** or **2-CN** loaded HPHT NDs exhibited similar zeta potentials to the unreacted HPHT NDs across all salt concentrations tested (Figure 5.7C). This suggests that there is no stabilisation effect on HPHT NDs from peptide coating. The DLS particle size results confirmed the lack of stabilisation effect for **1-DLC** and **2-CN** loaded HPHT NDs, which had an initial particle size of 310 and 240 nm, respectively, compared to the unreacted HPHT NDs at 180 nm (Figure 5.7D). A small increase in particle size was observed for the unreacted HPHT NDs up to 229 nm as salt concentration increased, while the **1-DLC** loaded HPHT NDs reduced to 260 nm and the **2-CN** loaded HPHT NDs increased to 350 nm. All of these particle size changes were within error (see Supporting Information Figure S5.18). In summary, a coating of peptide **1-DLC** or **2-CN**

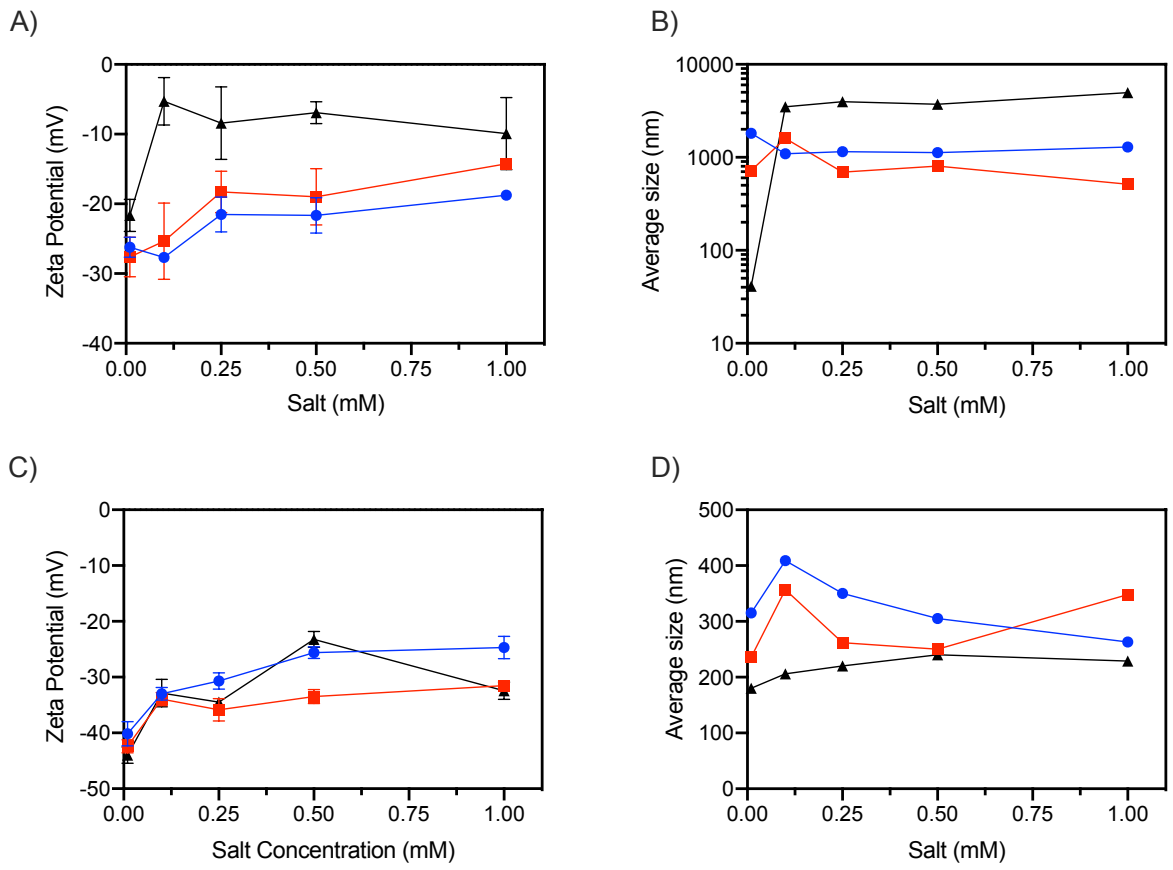

Figure 5.7. Dynamic light scattering data for unreacted (black), **1-DLC** loaded (blue), and **2-CN** loaded (red) NDs. Zeta potential for **A)** DNDs and **C)** HPHT NDs, and the average DLS particle size for **B)** DNDs and **D)** HPHT NDs. Error bars are standard deviations. No error bars are shown for the size data as the high (near 1) polydispersity index of partially aggregated samples causes a large error which obscures the average size data. A plot containing the error bars is provided in the Supporting Information Figure S5.18.

displayed a small stabilising effect on DNDs against salt-induced aggregation, but did not affect the colloidal stability of HPHT NDs.

Thermogravimetric analysis

Thermogravimetric analysis (TGA) of **1-DLC** loaded NDs was carried out in order to quantify the peptide loading at a larger scale. 10 mg of NDs were loaded with **1-DLC** under the same procedure as for the colourimetric assay, and TGA performed with a quadrupole mass spectrometer (QMS) attached to the exhaust line (see Experimental section 5.5.2). First, a pure sample of **1-DLC** was heated at 5 °C/min from 40 to 550 °C to determine the key mass loss steps (Figure 5.8A), with the attached QMS set to scan between 1 and 60 atomic mass units (amu). Three major mass loss steps were observed (Figure 5.8A), with the first an 8.0% mass loss between 40 and 200 °C. This was assigned to water that remained adsorbed to **1-DLC** after

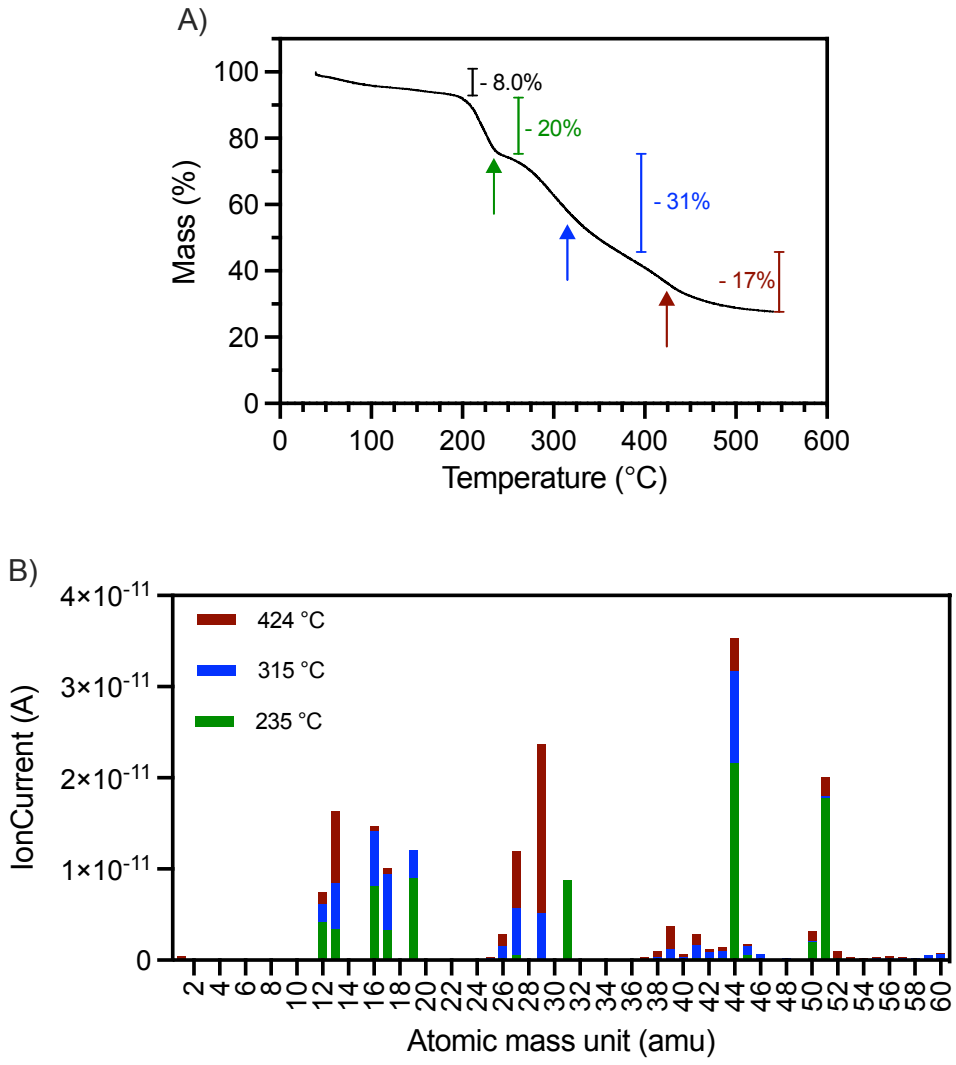

Figure 5.8. A) Plot of mass (%) against temperature during thermogravimetric analysis (TGA) of **1-DLC**. Key mass loss points are shown by the coloured arrows. **B)** Stacked plot of the emitted masses observed through a mass spectrometer attached to the TGA instrument, colour corresponds to spectra obtained at each mass loss event marked in A.

lyophilisation.[19] A two-stage mass loss of 51% occurred between 200 and 380 °C, with a small flattening of the curve at approximately 260 °C. A final 12.7% mass loss occurred from approximately 400 to 500 °C. The attached QMS collected a mass spectrum at each mass loss step, which were plotted to determine the key masses emitted at each stage (Figure 5.8B). The carrier gas N_2 (28 amu) was excluded, and the masses observed were 12, 13, 16, 17, 18, 19, 27, 29, 31, 41, 44, 45, 50, and 51 amu.

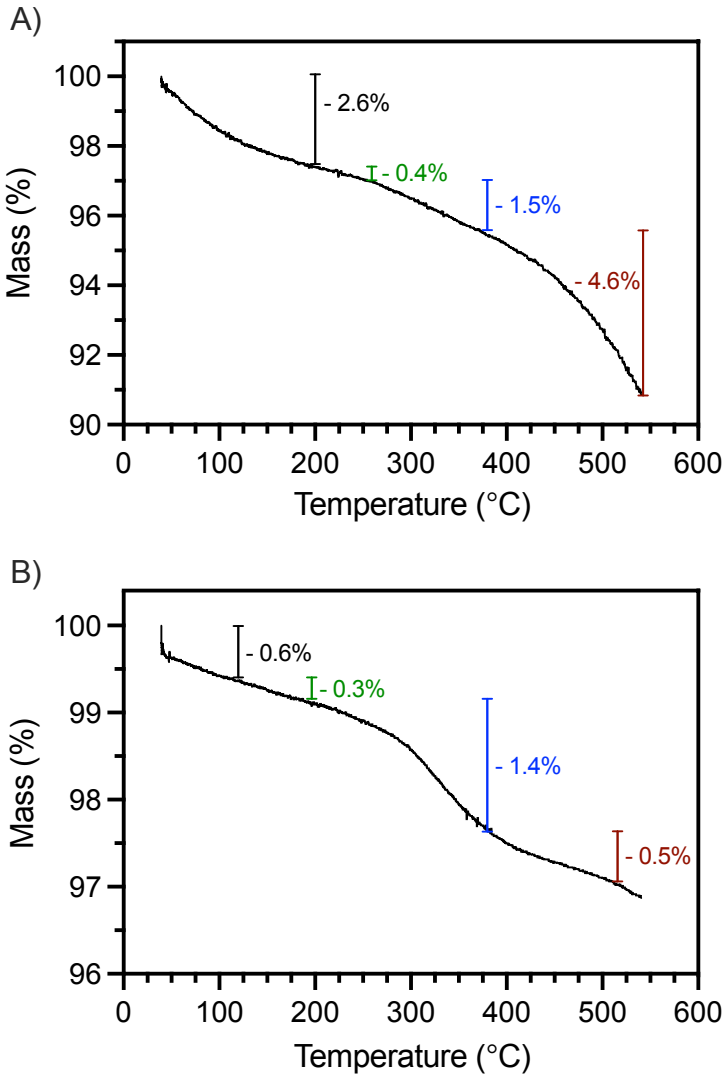

Figure 5.9. Plot of mass (%) against temperature with key mass loss steps marked for **A) 1-DLC** loaded DNDs and **B) 1-DLC** loaded HPHT NDs.

Next, TGA was conducted on samples of **1-DLC** loaded DNDs and HPHT NDs, under the same conditions as pure **1-DLC** (Figure 5.9A and 5.9B). Given that pure **1-DLC** decomposed between 200 and 380 °C, the mass loss of **1-DLC** loaded DNDs was calculated in this region and found to be 1.9%. This suggests that 1.9 mg of **1-DLC** was loaded on the DNDs, which is 0.87 mg more than the expected 1.03 mg based on the 87% retention calculated by the colourimetric assay. Similarly, the TGA curve of **1-DLC** loaded HPHT NDs had a mass loss of 1.4% from 200 to 380 °C, which suggest a loading of 1.4 mg of **1-DLC**. This is 1.0 mg more than the 0.4 mg expected from the colourimetric assay. The increased loading calculated by TGA for both DNDs and HPHT NDs can be attributed to error in estimation of the mass loss events, which makes TGA based quantification less reliable.[52] Jarre *et al*. have reported that cleavage of strongly bound

organic species from the ND surface occurs at elevated temperatures, which can cause overlap with early sublimation of carbon material and results in difficultly determining the precise mass loss step positions.[52]

Mass spectra were collected while the **1-DLC** loaded DNDs and HPHT NDs were analysed by TGA. The QMS was set to search for the masses previously observed during TGA of pure **1-DLC** (12, 13, 16, 17, 18, 19, 27, 29, 31, 41, 44, 45, 50, and 51 amu). The intensity of the 44 amu signal was observed to steadily increase from approximately 300 °C onwards for both ND samples, which is indicative of CO_2 release (see Supporting Information Figures S5.19 and S5.20). However, no change was observed for all other set masses. This indicates that any gaseous emissions (other than CO_2) due to combustion of the **1-DLC** coating are below the detection limit of the QMS. Mass spectra were next collected while untreated DNDs and HPHT NDs were analysed by TGA under the same conditions, as a control to determine the masses that were emitted in the absence of **1-DLC**. The major emissions from these unreacted NDs were 13, 19, and 44 amu (see Supporting Information Figure S5.21). Therefore, the 44 amu emission observed for **1-DLC** loaded NDs was assigned to CO_2 released from sublimation of carbon material on the ND surface,[52] and not from the **1-DLC** peptide itself.

Finally, a visual inspection of the ND samples before and after TGA revealed a colour change from grey-yellow to black (Figure 5.10). This colour change suggests that any peptide present has combusted and resulted in black ‘soot’ deposition on the NDs. No colour change was observed for the untreated DND or HPHT ND samples before and after TGA (Supporting Information Figures S5.22 and S5.23). Overall, TGA of **1-DLC** loaded NDs confirmed the presence of **1-DLC** by an observed mass loss between 180 and 300 °C, but an accurate quantification of the **1-DLC** loading was not possible. Gas emission from the combustion of the **1-DLC** coating on NDs was not able to be confirmed, likely due to the low peptide loading of approximately 1% total mass of the ND samples (calculated by the colourimetric assay) causing the emission to be below the QMS detection limit.

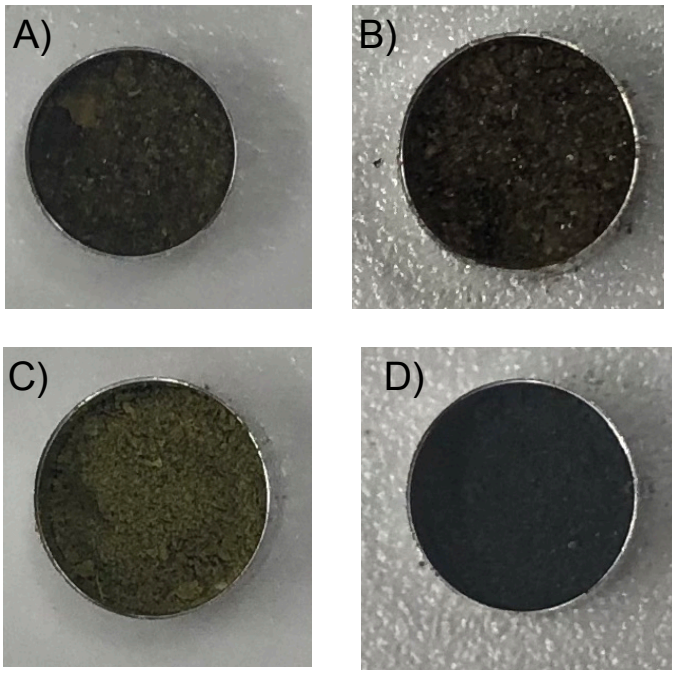

Figure 5.10. Pictures of **1-DLC** loaded DNDs **A)** before and **B)** after TGA, and pictures of **1-DLC** loaded HPHT NDs **C)** TGA and **D)** after TGA.

5.4 Conclusion

Nanodiamond surface functionalisation is a rapidly expanding field with the potential for application in drug delivery, cell imaging, and biological sensing. However, the requisite functionalisation chemistry is not well understood and continues to require reaction optimisation on a case by case basis. Here, carbon-binding peptides (CBPs) are presented as an effective new route to non-covalently functionalise carboxylated NDs.

A fluorescein tag was added to each CBP through *N*-terminal attachment of an aminohexanoic acid linker followed by 5(6)-carboxyfluorescein in order to visualise the peptides when attached to NDs. This provided the CBPs **1-DLC**, **2-CN**, **3-DF**, and **4-GF**. A colourimetric assay was developed to determine the amount of CBP adhered to NDs, where the absorbance of the residual supernatant was measured after the CBP loaded NDs were separated from solution by centrifugation. The presence (or absence for **4-GF**) of the CBPs on NDs was confirmed by FTIR. This assay revealed that the peptide **1-DLC** was the most well retained CBP on both DNDs and HPHT NDs, and a K_d of 21 μM between **1-DLC** and DNDs was calculated by a fluorescence polarisation assay. Interestingly, all three peptides **1-DLC**, **2-CN**, and **3-DF** were retained in greater quantity on DNDs than on HPHT NDs, when both ND samples were held at

1 mg/mL. The binding interactions between CBP and ND were investigated by washing the CBP loaded NDs with phosphate buffer containing additional sodium chloride or DMSO. This revealed that **1-DLC** is predominantly adhered via electrostatic interactions, while **2-CN** is largely adhered through non-polar or hydrophobic interactions.

Overall, these findings present CBPs as a promising non-covalent route to functionalise both DNDs and HPHT NDs. In particular, **1-DLC** was the best candidate of the four peptides investigated. Furthermore, our approach to use CBPs is amenable to the attachment of other organic molecules of interest at the peptide *N*-terminus, in place of the fluorescein tag used in this study. This will allow the CBP coatings to be used in a wide range of applications, dependent on the molecule(s) attached to the CBP.

5.5 Experimental

5.5.1 General materials

All reagents and solvents were purchased from Merck/Sigma-Aldrich unless otherwise specified, at the highest purity level available. Detonation nanodiamonds (DNDs) with an average particle size of 5 nm were obtained from Adámas Nanotechnologies as a 10 mg/mL suspension of carboxylated DNDs in water and were used without further treatment. High-pressure high-temperature (HPHT) synthesised nanodiamonds with an average size of 120 nm were purchased from Nabond (Hong Kong) and irradiated, annealed, and oxidised according to previously reported methods.[11] This included a final treatment in concentrated sulfuric acid and nitric acid to provide a carboxylated surface.[58] All ND suspensions were sonicated for 1 h before use in coupling experiments with a 150 W FS-600N ultrasonicator homogeniser (Zhengzhou HenChen Electronic, Henan Province, China) with a 2 s on, 4 s off duty cycle. Isolectric points (pI) for all peptides were calculated using the online GenScript peptide molecular weight calculator.[56]

5.5.2 Instrumentation

Fourier-Transform Infrared (FTIR) spectroscopy was carried out on a Shimazdu IR Spirit spectrometer in Universal ATR mode. Thermogravimetric analysis (TGA) was performed on a

Netzsch Jupiter 449 F3 Simultaneous Thermal Analyzer with an Aëolos 403 Quadro quadrupole mass spectrometer (QMS) attached to the exhaust line. All samples were heated from 40 °C to 550 °C at a heating rate of 5 °C per minute. Photos of the ND samples before and after TGA were taken on an iPhone 8. Dynamic light scattering and zeta potential measurements of ND samples were collected on a Malvern Zetasizer Nano ZS at a concentration of 0.01 mg/mL in water.

5.5.3 Absorbance calibration curves

Solutions of 5(6)-carboxyfluorescein were prepared at a concentration of 62.50, 31.25, 15.63, 7.813, and 3.906 μM in three phosphate buffers: 50 mM phosphate buffer at pH 8.01 (A), 50 mM phosphate buffer with 1 M NaCl at pH 8.01 (B), and 50 mM phosphate buffer at pH 8.01 with 5% v/v DMSO (C). Each of these fluorescein standard solutions was plated in triplicate (80 μL) black polystyrene, clear bottomed, tissue culture treated polystyrene 96-well plates (Corning Inc. costar® 3605) and absorbance spectra collected using a BioTeK Synergy H4 Plate Reader, using a Xenon light source.

5.5.4 Synthesis & characterisation of peptides

Unless otherwise indicated, all starting materials were purchased from commercial sources and used without further purification. All peptides were synthesised by the Fmoc/tBu solid-phase peptide synthesis using one of three protocols detailed below, with all L-amino acids (unless otherwise specified) purchased from Chem-Impex International: Fmoc-Ala-OH, Fmoc-Arg(Pbf)-OH, Fmoc-Asp(tBu)-OH, Fmoc-Asn(Trt)-OH, Fmoc-Cys(Trt)-OH, Fmoc-Gln(Trt)-OH, Fmoc-Glu(tBu)-OH, Fmoc-Gly-OH, Fmoc-His(Trt)-OH, Fmoc-Ile-OH, Fmoc-Leu-OH, Fmoc-Lys(Boc)-OH, Fmoc-Met-OH, Fmoc-Thr(tBu)-OH, Fmoc-Tyr(tBu)-OH, Fmoc-Trp(Boc)-OH, Fmoc-Ser(tBu)-OH, Fmoc-Phe-OH, Fmoc-Pro-OH, Fmoc-Val-OH and Fmoc-Ahx-OH. Purity of all compounds was confirmed by analytical RP-HPLC on an Agilent 1260 HPLC equipped with a Phenomenex Luna C18(2) column (250 × 4.6 mm) over a gradient of 5-50% B (15 min) and visualised at 220 nm. High-resolution mass spectra were collected using an Agilent 6230 ESI-TOF via direct injection in ACN with 0.1% formic acid as the running buffer. Characterisation data for all peptides is recorded in Table S5.1.

General Procedure for Peptide Synthesis:

All peptides were synthesised by the Fmoc/tBu solid-phase peptide synthesis protocol on a CEM Liberty Blue Automated Microwave Peptide Synthesiser (CEM Corp., Matthews, NC, USA) using the standard manufacturer's conditions. The peptides were assembled on 0.25 mmol scale on Chem Impex International Rink Amide AM resin (0.47 mmol/g) or Mimotopes Rink Amide resin (0.456 mmol/g). The resin was initially swollen in DCM (15 mL, 15 min) and then the resin washed with DMF (2 × 8 mL). The resin-bound Fmoc-groups were deprotected with a mixture of 20% piperidine and 0.1 M OxymaPure in DMF using the standard microwave deprotection method with a maximum temperature of 90 °C. Couplings were performed with Fmoc-protected amino-acids (0.2 M in DMF, 5 equiv), OxymaPure (1 M in DMF, 5 equiv) and DIC (0.5 M in DMF, 5 equiv) under the 'Standard Coupling' microwave method with a maximum temperature of 90 °C, except for coupling of Fmoc-His(Trt)-OH which was coupled using a maximum 50°C 10 min coupling procedure; and Fmoc-Arg(Pbf)-OH which used the default 'Arginine Double Coupling' microwave method which included two couplings steps - the first at room temperature and the second at a maximum of 75 °C. Following assembly of the desired sequence the N-terminal protecting group was removed. The resin was then removed from the synthesiser, washed with DCM (3 × 8 mL) and then diethyl ether (3 × 8 mL) and air dried with suction.

The resin-bound peptide (0.025 mmol) was reswollen in 1:1 DCM/DMF (5 mL) for 15 min, the solution drained and the resin washed with DMF (3 × 5 mL). A solution of fluorescein isothiocyanate (2 equiv, 0.5 mmol, 22 mg) and DIPEA (4 equiv, 0.1 mmol, 17.5 µL) in DMF (1 mL) was added to the resin and reacted for 1.5 h, with intermittent stirring. The solution was drained and the resin thoroughly washed with DMF (3 × 5 mL), then DCM (3 × 5 mL), diethyl ether (3 × 5 mL) and air dried with suction. The peptide was subsequently cleaved from the resin and the side-chain protecting groups simultaneously globally deprotected by treatment of the resin with 92.5/2.5/2.5/2.5 TFA:TIPS:DODT:H_2O (5 mL) for 2 h. The cleavage solution was pipetted from the resin and concentrated under a stream of nitrogen to 0.5-1 mL. The peptide was then precipitated by addition of diethyl ether (10 mL) and the mixture cooled at -20 °C. The precipitate was pelleted by centrifugation (7600 rpm, 10 min), and the supernatant decanted. The pellet was

dried under a nitrogen stream, and then dissolved in 1:1 ACN/H_2O, then syringe filtered (0.2 µm) and lyophilised to yield the crude peptide as a fluffy white powder. The peptide was purified by semi-preparative RP-HPLC on a Gilson GX-Prep system using a Phenomenex Aeris Peptide C18 column (10 × 250 mm), over a linear ACN/H_2O gradient optimised for each peptide sample. RP-HPLC solvents were (A) H_2O with 0.1% TFA and (B) ACN with 0.1% TFA. The product containing fractions were pooled and lyophilised. The identity of the final compounds was confirmed by High Resolution Mass Spectrometry on an Agilent 6230 ESI-TOF LCMS. Purity of the peptides was confirmed by analytical RP-HPLC on an Agilent 1260 HPLC equipped with a Phenomenex Luna C18(2) column (250 × 4.6 mm) over a gradient of 5-50% B (15 min) and visualised at 220 nm. Characterisation data for all peptides in recorded in Table S5.1.

5.6 References

(1) Mochalin, V. N.; Shenderova, O.; Ho, D.; Gogotsi, Y. The Properties and Applications of Nanodiamonds. *Nat. Nanotech.* **2012**, *7* (1), 11-23. https://doi.org/10.1038/nnano.2011.209.

(2) Hemelaar, S. R.; Nagl, A.; Bigot, F.; Rodríguez-García, M. M.; de Vries, M. P.; Chipaux, M.; Schirhagl, R. The Interaction of Fluorescent Nanodiamond Probes with Cellular Media. *Microchim. Acta* **2017**, *184* (4), 1001-1009. https://doi.org/10.1007/s00604-017-2086-6.

(3) Hemelaar, S.; Saspaanithy, B.; L'Hommelet, S.; Perona Martinez, F.; van der Laan, K.; Schirhagl, R. The Response of HeLa Cells to Fluorescent NanoDiamond Uptake. *Sensors* **2018**, *18* (2), 355. https://doi.org/10.3390/s18020355.

(4) Chipaux, M.; Laan, K. J. van der; Hemelaar, S. R.; Hasani, M.; Zheng, T.; Schirhagl, R. Nanodiamonds and Their Applications in Cells. *Small* **2018**, *14* (24), 1704263. https://doi.org/10.1002/smll.201704263.

(5) Reina, G.; Zhao, L.; Bianco, A.; Komatsu, N. Chemical Functionalization of Nanodiamonds: Opportunities and Challenges Ahead. *Angew. Chem. Int. Ed.* **2019**, *58* (50), 17918-17929. https://doi.org/10.1002/anie.201905997.

(6) Smith, B. R.; Niebert, M.; Plakhotnik, T.; Zvyagin, A. V. Transfection and Imaging of Diamond Nanocrystals as Scattering Optical Labels. *J. Lumin.* **2007**, *127* (1), 260-263. https://doi.org/10.1016/j.jlumin.2007.02.044.

(7) Fang, C.-Y.; Vaijayanthimala, V.; Cheng, C.-A.; Yeh, S.-H.; Chang, C.-F.; Li, C.-L.; Chang, H.-C. The Exocytosis of Fluorescent Nanodiamond and Its Use as a Long-Term Cell Tracker. *Small* **2011**, *7* (23), 3363-3370. https://doi.org/10.1002/smll.201101233.

(8) Su, L.-J.; Wu, M.-S.; Hui, Y. Y.; Chang, B.-M.; Pan, L.; Hsu, P.-C.; Chen, Y.-T.; Ho, H.-N.; Huang, Y.-H.; Ling, T.-Y.; Hsu, H.-H.; Chang, H.-C. Fluorescent Nanodiamonds Enable Quantitative Tracking of Human Mesenchymal Stem Cells in Miniature Pigs. *Sci. Rep.* **2017**, *7* (1), 45607. https://doi.org/10.1038/srep45607.

(9) Tisler, J.; Reuter, R.; Lämmle, A.; Jelezko, F.; Balasubramanian, G.; Hemmer, P. R.; Reinhard, F.; Wrachtrup, J. Highly Efficient FRET from a Single Nitrogen-Vacancy Center in Nanodiamonds to a Single Organic Molecule. *ACS Nano* **2011**, *5* (10), 7893-7898. https://doi.org/10.1021/nn2021259.

(10) Reineck, P.; Francis, A.; Orth, A.; Lau, D. W. M.; Nixon-Luke, R. D. V.; Rastogi, I. D.; Razali, W. A. W.; Cordina, N. M.; Parker, L. M.; Sreenivasan, V. K. A.; Brown, L. J.; Gibson, B. C. Brightness and Photostability of Emerging Red and Near-IR Fluorescent Nanomaterials for Bioimaging. *Adv. Opt. Mater.* **2016**, *4* (10), 1549-1557. https://doi.org/10.1002/adom.201600212.

(11) Purdey, M. S.; Capon, P. K.; Pullen, B. J.; Reineck, P.; Schwarz, N.; Psaltis, P. J.; Nicholls, S. J.; Gibson, B. C.; Abell, A. D. An Organic Fluorophore-Nanodiamond Hybrid Sensor for Photostable Imaging and Orthogonal, on-Demand Biosensing. *Sci. Rep.* **2017**, *7* (1), 15967. https://doi.org/10.1038/s41598-017-15772-0.

(12) Zhang, T.; Cui, H.; Fang, C.-Y.; Cheng, K.; Yang, X.; Chang, H.-C.; Forrest, M. L. Targeted Nanodiamonds as Phenotype-Specific Photoacoustic Contrast Agents for Breast Cancer. *Nanomedicine* **2015**, *10* (4), 573-587. https://doi.org/10.2217/nnm.14.141.

(13) Duffy, E.; Mitev, D. P.; Thickett, S. C.; Townsend, A. T.; Paull, B.; Nesterenko, P. N. Assessing the Extent, Stability, Purity and Properties of Silanised Detonation Nanodiamond. *Appl. Surf. Sci.* **2015**, *357*, 397-406. https://doi.org/10.1016/j.apsusc.2015.09.002.

(14) Meinhardt, T.; Lang, D.; Dill, H.; Krueger, A. Pushing the Functionality of Diamond Nanoparticles to New Horizons: Orthogonally Functionalized Nanodiamond Using Click Chemistry. *Adv. Funct. Mater.* **2011**, *21* (3), 494-500. https://doi.org/10.1002/adfm.201001219.

(15) Day, A. H.; Adams, S. J.; Gines, L.; Williams, O. A.; Johnson, B. R. G.; Fallis, I. A.; Loveridge, E. J.; Bahra, G. S.; Oyston, P. C. F.; Herrera, J. M.; Pope, S. J. A. Synthetic Routes, Characterization and Photophysical Properties of Luminescent, Surface Functionalized Nanodiamonds. *Carbon* **2019**, *152*, 335-343. https://doi.org/10.1016/j.carbon.2019.05.081.

(16) Hens, S. C.; Cunningham, G.; Tyler, T.; Moseenkov, S.; Kuznetsov, V.; Shenderova, O. Nanodiamond Bioconjugate Probes and Their Collection by Electrophoresis. *Diamond Relat. Mater.* **2008**, *17* (11), 1858-1866. https://doi.org/10.1016/j.diamond.2008.03.020.

(17) Barras, A.; Szunerits, S.; Marcon, L.; Monfilliette-Dupont, N.; Boukherroub, R. Functionalization of Diamond Nanoparticles Using "Click" Chemistry. *Langmuir* **2010**, *26* (16), 13168-13172. https://doi.org/10.1021/la101709q.

(18) Gaur, P.; Banerjee, S. C-N Cross Coupling: Novel Approach towards Effective Aryl Secondary Amines Modification on Nanodiamond Surface. *Diamond Relat. Mater.* **2019**, *98*, 107468. https://doi.org/10.1016/j.diamond.2019.107468.

(19) Krüger, A.; Liang, Y.; Jarre, G.; Stegk, J. Surface Functionalisation of Detonation Diamond Suitable for Biological Applications. *J. Mater. Chem.* **2006**, *16* (24), 2322-2328. https://doi.org/10.1039/B601325B.

(20) Krueger, A.; Stegk, J.; Liang, Y.; Lu, L.; Jarre, G. Biotinylated Nanodiamond: Simple and Efficient Functionalization of Detonation Diamond. *Langmuir* **2008**, *24* (8), 4200-4204. https://doi.org/10.1021/la703482v.

(21) Krueger, A.; Boedeker, T. Deagglomeration and Functionalisation of Detonation Nanodiamond with Long Alkyl Chains. *Diamond Relat. Mater.* **2008**, *17* (7-10), 1367-1370. https://doi.org/10.1016/j.diamond.2008.01.033.

(22) Barras, A.; Lyskawa, J.; Szunerits, S.; Woisel, P.; Boukherroub, R. Direct Functionalization of Nanodiamond Particles Using Dopamine Derivatives. *Langmuir* **2011**, *27* (20), 12451-12457. https://doi.org/10.1021/la202571d.

(23) Mkandawire, M.; Pohl, A.; Gubarevich, T.; Lapina, V.; Appelhans, D.; Rödel, G.; Pompe, W.; Schreiber, J.; Opitz, J. Selective Targeting of Green Fluorescent Nanodiamond Conjugates to Mitochondria in HeLa Cells. *J. Biophoton.* **2009**, *2* (10), 596-606. https://doi.org/10.1002/jbio.200910002.

(24) Dong, Y.; Cao, R.; Li, Y.; Wang, Z.; Li, L.; Tian, L. Folate-Conjugated Nanodiamond for Tumor-Targeted Drug Delivery. *RSC Adv.* **2015**, *5* (101), 82711-82716. https://doi.org/10.1039/C5RA12383F.

(25) Ho, D. Beyond the Sparkle: The Impact of Nanodiamonds as Biolabeling and Therapeutic Agents. *ACS Nano* **2009**, *3* (12), 3825-3829. https://doi.org/10.1021/nn9016247.

(26) Guan, B.; Zou, F.; Zhi, J. Nanodiamond as the PH-Responsive Vehicle for an Anticancer Drug. *Small* **2010**, *6* (14), 1514-1519. https://doi.org/10.1002/smll.200902305.

(27) Xiao, J.; Duan, X.; Yin, Q.; Zhang, Z.; Yu, H.; Li, Y. Nanodiamonds-Mediated Doxorubicin Nuclear Delivery to Inhibit Lung Metastasis of Breast Cancer. *Biomaterials* **2013**, *34* (37), 9648-9656. https://doi.org/10.1016/j.biomaterials.2013.08.056.

(28) Jeong, S. H.; Lim, D.; Kim, K.; Kang, E.; Lim, S.; Ricci, J.; Sung, S.; Kwon, M. Comprehensive Evaluation of Carboxylated Nanodiamond as a Topical Drug Delivery System. *Int. J. Nanomedicine* **2016**, 2381. https://doi.org/10.2147/IJN.S104859.

(29) Li, L.; Tian, L.; Wang, Y.; Zhao, W.; Cheng, F.; Li, Y.; Yang, B. Smart PH-Responsive and High Doxorubicin Loading Nanodiamond for in Vivo Selective Targeting, Imaging, and Enhancement of Anticancer Therapy. *J. Mater. Chem. B* **2016**, *4* (29), 5046-5058. https://doi.org/10.1039/C6TB00266H.

(30) Gaillard, C.; Girard, H. A.; Falck, C.; Paget, V.; Simic, V.; Ugolin, N.; Bergonzo, P.; Chevillard, S.; Arnault, J. C. Peptide Nucleic Acid-Nanodiamonds: Covalent and Stable Conjugates for DNA Targeting. *RSC Adv.* **2013**, *4* (7), 3566-3572. https://doi.org/10.1039/C3RA45158E.

(31) Chang, B.-M.; Lin, H.-H.; Su, L.-J.; Lin, W.-D.; Lin, R.-J.; Tzeng, Y.-K.; Lee, R. T.; Lee, Y. C.; Yu, A. L.; Chang, H.-C. Highly Fluorescent Nanodiamonds Protein-Functionalized for Cell Labeling and Targeting. *Adv. Funct. Mater.* **2013**, *23* (46), 5737-5745. https://doi.org/10.1002/adfm.201301075.

(32) Zhang, Q.; Mochalin, V. N.; Neitzel, I.; Knoke, I. Y.; Han, J.; Klug, C. A.; Zhou, J. G.; Lelkes, P. I.; Gogotsi, Y. Fluorescent PLLA-Nanodiamond Composites for Bone Tissue Engineering. *Biomaterials* **2011**, *32* (1), 87-94. https://doi.org/10.1016/j.biomaterials.2010.08.090.

(33) Doherty, M. W.; Manson, N. B.; Delaney, P.; Jelezko, F.; Wrachtrup, J.; Hollenberg, L. C. L. The Nitrogen-Vacancy Colour Centre in Diamond. *Physics Reports* **2013**, *528* (1), 1-45. https://doi.org/10.1016/j.physrep.2013.02.001.

(34) Huang, L.-C. L.; Chang, H.-C. Adsorption and Immobilization of Cytochrome *c* on Nanodiamonds. *Langmuir* **2004**, *20* (14), 5879-5884. https://doi.org/10.1021/la0495736.

(35) Jiao, Y.; Liu, S.; Sun, Y.; Yue, W.; Zhang, H. Bioinspired Surface Functionalization of Nanodiamonds for Enhanced Lubrication. *Langmuir* **2018**, *34* (41), 12436-12444. https://doi.org/10.1021/acs.langmuir.8b02441.

(36) Rehor, I.; Slegerova, J.; Kucka, J.; Proks, V.; Petrakova, V.; Adam, M.-P.; Treussart, F.; Turner, S.; Bals, S.; Sacha, P.; Ledvina, M.; Wen, A. M.; Steinmetz, N. F.; Cigler, P. Fluorescent Nanodiamonds Embedded in Biocompatible Translucent Shells. *Small* **2014**, *10* (6), 1106-1115. https://doi.org/10.1002/smll.201302336.

(37) Neburkova, J.; Vavra, J.; Cigler, P. Coating Nanodiamonds with Biocompatible Shells for Applications in Biology and Medicine. *Curr. Opin. Solid State Mater. Sci.* **2017**, *21* (1), 43-53. https://doi.org/10.1016/j.cossms.2016.05.008.

(38) Care, A.; Bergquist, P. L.; Sunna, A. Solid-Binding Peptides: Smart Tools for Nanobiotechnology. *Trends Biotechnol.* **2015**, *33* (5), 259-268. https://doi.org/10.1016/j.tibtech.2015.02.005.

(39) Bansal, R.; Care, A.; Lord, M. S.; Walsh, T. R.; Sunna, A. Experimental and Theoretical Tools to Elucidate the Binding Mechanisms of Solid-Binding Peptides. *New Biotechnol.* **2019**, *52*, 9-18. https://doi.org/10.1016/j.nbt.2019.04.001.

(40) Tamerler, C.; Oren, E. E.; Duman, M.; Venkatasubramanian, E.; Sarikaya, M. Adsorption Kinetics of an Engineered Gold Binding Peptide by Surface Plasmon Resonance Spectroscopy and a Quartz Crystal Microbalance. *Langmuir* **2006**, *22* (18), 7712-7718. https://doi.org/10.1021/la0606897.

(41) Oren, E. E.; Tamerler, C.; Sahin, D.; Hnilova, M.; Seker, U. O. S.; Sarikaya, M.; Samudrala, R. A Novel Knowledge-Based Approach to Design Inorganic-Binding Peptides. *Bioinformatics* **2007**, *23* (21), 2816-2822. https://doi.org/10.1093/bioinformatics/btm436.

(42) Nomura, Y.; Sharma, V.; Yamamura, A.; Yokobayashi, Y. Selection of Silk-Binding Peptides by Phage Display. *Biotechnol. Lett.* **2011**, *33* (5), 1069-1073. https://doi.org/10.1007/s10529-011-0519-6.

(43) Gabryelczyk, B.; Szilvay, G. R.; Salomäki, M.; Laaksonen, P.; Linder, M. B. Selection and Characterization of Peptides Binding to Diamond-like Carbon. *Colloids Surf., B* **2013**, *110*, 66-73. https://doi.org/10.1016/j.colsurfb.2013.04.002.

(44) Gabryelczyk, B.; Szilvay, G. R.; Linder, M. B. The Structural Basis for Function in Diamond-like Carbon Binding Peptides. *Langmuir* **2014**, *30* (29), 8798-8802. https://doi.org/10.1021/la502396p.

(45) Gabryelczyk, B.; Szilvay, G. R.; Singh, V. K.; Mikkilä, J.; Kostiainen, M. A.; Koskinen, J.; Linder, M. B. Engineering of the Function of Diamond-like Carbon Binding Peptides through Structural Design. *Biomacromol.* **2015**, *16* (2), 476-482. https://doi.org/10.1021/bm501522j.

(46) Wang, S.; Humphreys, E. S.; Chung, S.-Y.; Delduco, D. F.; Lustig, S. R.; Wang, H.; Parker, K. N.; Rizzo, N. W.; Subramoney, S.; Chiang, Y.-M.; Jagota, A. Peptides with Selective Affinity for Carbon Nanotubes. *Nat. Mater.* **2003**, *2* (3), 196-200. https://doi.org/10.1038/nmat833.

(47) Swaminathan, S.; Cui, Y. Recognition of Diamond with Phage Display Peptides. *RSC Adv.* **2016**, *6* (54), 49127-49129. https://doi.org/10.1039/C6RA06582A.

(48) Penna, M. J.; Mijajlovic, M.; Tamerler, C.; Biggs, M. J. Molecular-Level Understanding of the Adsorption Mechanism of a Graphite-Binding Peptide at the Water/Graphite Interface. *Soft Matter* **2015**, *11* (26), 5192-5203. https://doi.org/10.1039/C5SM00123D.

(49) Reineck, P.; Lau, D. W. M.; Wilson, E. R.; Fox, K.; Field, M. R.; Deeleepojananan, C.; Mochalin, V. N.; Gibson, B. C. Effect of Surface Chemistry on the Fluorescence of Detonation Nanodiamonds. *ACS Nano* **2017**, *11* (11), 10924-10934. https://doi.org/10.1021/acsnano.7b04647.

(50) Barnard, A. S.; Sternberg, M. Crystallinity and Surface Electrostatics of Diamond Nanocrystals. *J. Mater. Chem.* **2007**, *17* (45), 4811-4819. https://doi.org/10.1039/B710189A.

(51) Reineck, P.; Trindade, L. F.; Havlik, J.; Stursa, J.; Heffernan, A.; Elbourne, A.; Orth, A.; Capelli, M.; Cigler, P.; Simpson, D. A.; Gibson, B. C. Not All Fluorescent Nanodiamonds Are Created Equal: A Comparative Study. *Part. Part. Syst. Charact.* **2019**, *36* (3), 1900009. https://doi.org/10.1002/ppsc.201900009.

(52) Jarre, G.; Heyer, S.; Memmel, E.; Meinhardt, T.; Krueger, A. Synthesis of Nanodiamond Derivatives Carrying Amino Functions and Quantification by a Modified Kaiser Test. *Beilstein J. Org. Chem.* **2014**, *10* (1), 2729-2737. https://doi.org/10.3762/bjoc.10.288.

(53) Merz, V.; Lenhart, J.; Vonhausen, Y.; Ortiz-Soto, M. E.; Seibel, J.; Krueger, A. Zwitterion-Functionalized Detonation Nanodiamond with Superior Protein Repulsion and Colloidal Stability in Physiological Media. *Small* **2019**, 1901551. https://doi.org/10.1002/smll.201901551.

(54) Schmidlin, L.; Pichot, V.; Comet, M.; Josset, S.; Rabu, P.; Spitzer, D. Identification, Quantification and Modification of Detonation Nanodiamond Functional Groups. *Diamond Relat. Mater.* **2012**, *22*, 113-117. https://doi.org/10.1016/j.diamond.2011.12.009.

(55) Cheng, J.; He, J.; Li, C.; Yang, Y. Facile Approach to Functionalize Nanodiamond Particles with V-Shaped Polymer Brushes. *Chem. Mater.* **2008**, *20* (13), 4224-4230. https://doi.org/10.1021/cm800357g.

(56) Peptide property molecular weight calculator-GenScript https://www.genscript.com/tools/peptide-molecular-weight-calculator (accessed Feb 2, 2021).

(57) Chang, S. L. Y.; Dwyer, C.; Ōsawa, E.; Barnard, A. S. Size Dependent Surface Reconstruction in Detonation Nanodiamonds. *Nanoscale Horiz.* **2018**, *3* (2), 213-217. https://doi.org/10.1039/C7NH00125H.

(58) Mochalin, V. N.; Gogotsi, Y. Wet Chemistry Route to Hydrophobic Blue Fluorescent Nanodiamond. *J. Am. Chem. Soc.* **2009**, *131* (13), 4594-4595. https://doi.org/10.1021/ja9004514.

(59) Tu, J.-S.; Perevedentseva, E.; Chung, P.-H.; Cheng, C.-L. Size-Dependent Surface CO Stretching Frequency Investigations on Nanodiamond Particles. *J. Chem. Phys.* **2006**, *125* (17), 174713. https://doi.org/10.1063/1.2370880.

(60) Petit, T.; Puskar, L. FTIR Spectroscopy of Nanodiamonds: Methods and Interpretation. *Diamond Relat. Mater.* **2018**, *89*, 52-66. https://doi.org/10.1016/j.diamond.2018.08.005.

(61) Wilson, E. R.; Parker, L. M.; Orth, A.; Nunn, N.; Torelli, M.; Shenderova, O.; Gibson, B. C.; Reineck, P. The Effect of Particle Size on Nanodiamond Fluorescence and Colloidal Properties in Biological Media. *Nanotechnology* **2019**, *30* (38), 385704. https://doi.org/10.1088/1361-6528/ab283d.

Supporting Information

S5.1 Characterisation data for carbon-binding peptides

Table S5.1. Analytical data for all four carbon-binding peptides.

Peptide	Sequence	Formula	MW (g/mol)	Calc. X+ $[M+XH]^{X+}$	Found	Purity % 220 nm
1-DLC	FITC-Ahx-KNSAPQKSENRKVPFYQHQ-NH_2	$C_{127}H_{179}N_{35}O_{35}S_1$	2786.3024	3+ 929.7753	929.7746	91
2-CN	FITC-Ahx-HWKHPWGAWDTL-NH_2	$C_{102}H_{119}N_{23}O_{21}S_1$	2033.8672	3+ 678.9635	678.9629	92
3-DF	FITC-Ahx-GVGGLTTVNYSR-NH_2	$C_{79}H_{109}N_{19}O_{23}S_1$	1723.7664	2+ 862.8910	862.8917	84
4-GF	FITC-Ahx-MVTESSDYSSY-NH_2	$C_{80}H_{100}N_{14}O_{28}S_2$	1768.6273	2+ 885.3215	885.3225	84

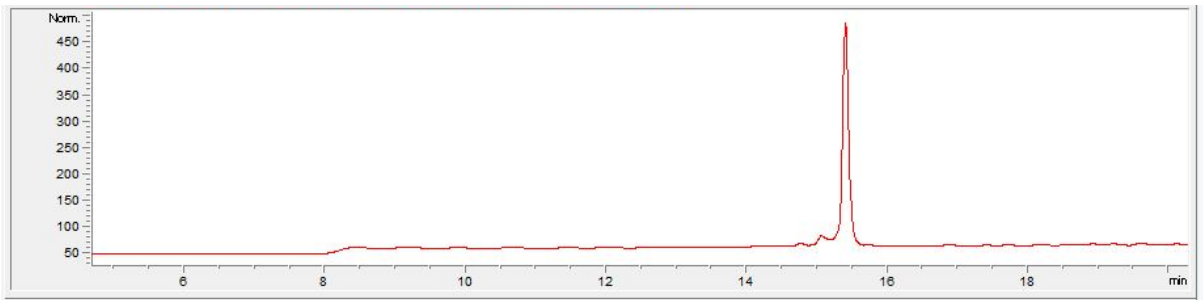

Figure S5.9. Analytical HPLC trace for **1-DLC** over a gradient of 5-50% (15 min) ACN in water with 0.1% TFA, visualised at 220 nm.

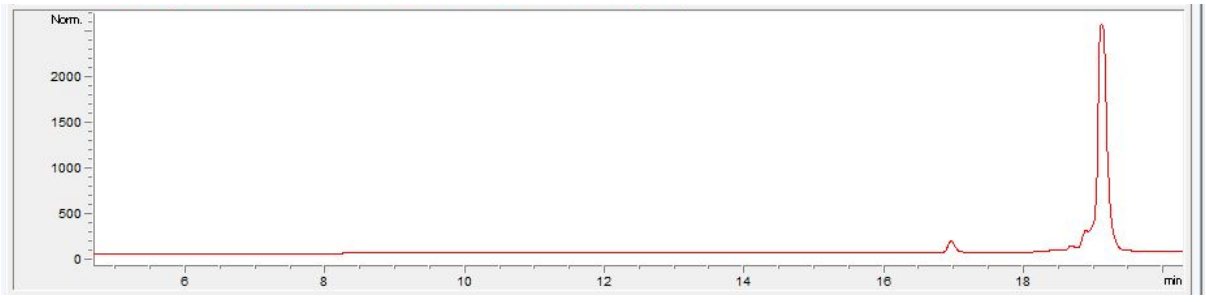

Figure S5.10. Analytical HPLC trace for **2-CN** over a gradient of 5-50% (15 min) ACN in water with 0.1% TFA, visualised at 220 nm.

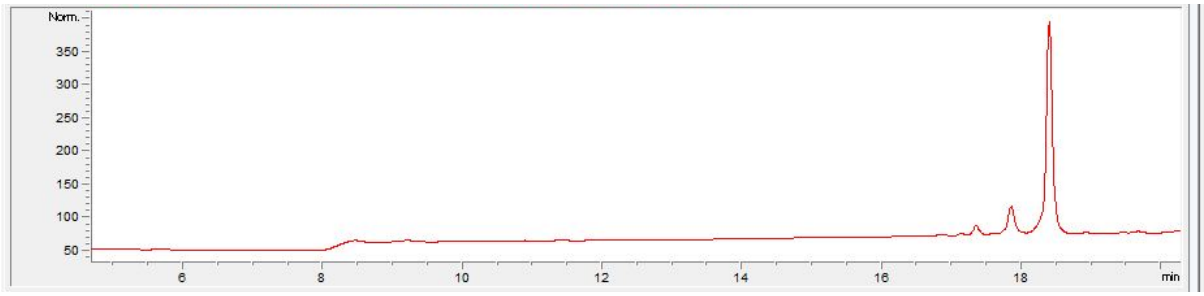

Figure S5.11. Analytical HPLC trace for **3-DF** over a gradient of 5-50% (15 min) ACN in water with 0.1% TFA, visualised at 220 nm.

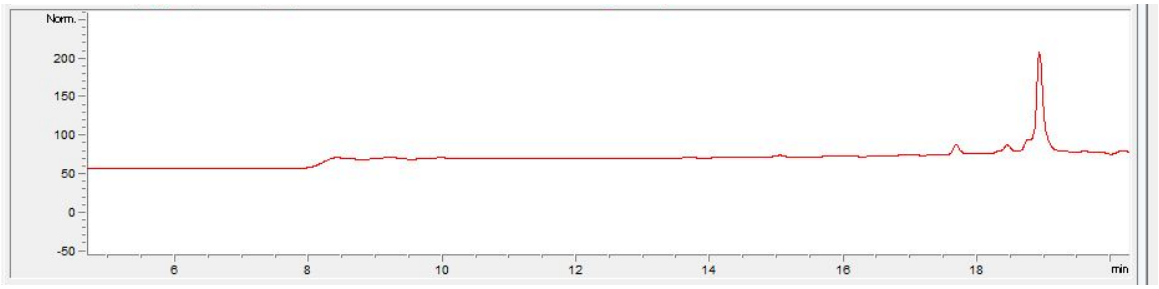

Figure S5.12. Analytical HPLC trace for **4-GF** over a gradient of 5-50% (15 min) ACN in water with 0.1% TFA, visualised at 220 nm.

S5.2 Fluorescein calibration curves

The 490 nm absorbance of solutions of 5(6)-carboxyfluorescein was collected on a plate reader, as detailed in the Experimental section 5.5.3, and a calibration curve constructed of absorbance vs concentration in each of the solvents A (50 mM phosphate buffer at pH 8.01), B (50 mM phosphate buffer with 1 M NaCl at pH 8.01), and C (50 mM phosphate buffer at pH 8.01 with 5% v/v DMSO).

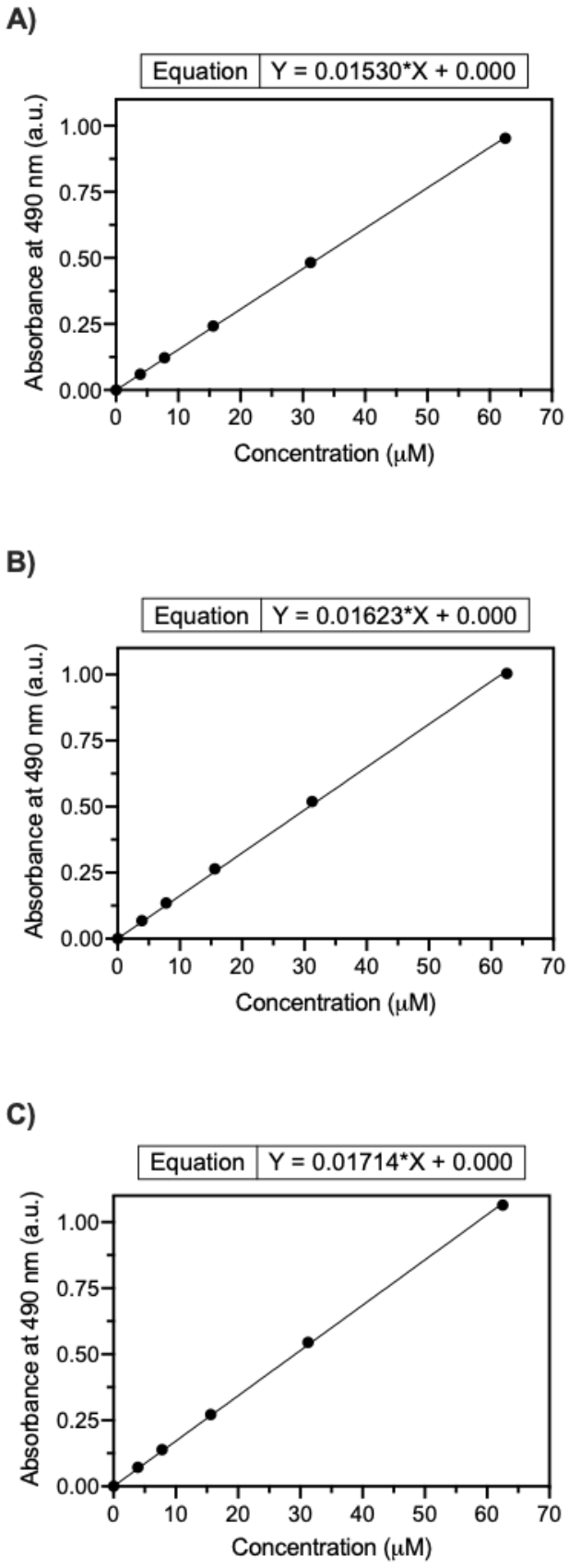

Figure S5.13. Calibration curves for the absorbance of 5(6)-carboxyfluorescein at 490 nm against concentration (μM). **A)** Calibration curve in washing solvent A 50 mM phosphate at pH 8.01. **B)** Calibration curve in washing solvent B 50 mM phosphate at pH 8.01 with 1 M NaCl. **C)** Calibration curve in washing solvent C 50 mM phosphate at pH 8.01 with 5% v/v DMSO.

S5.3 Fluorescence polarisation assay

The dissociation constant (K_d) between 1-DLC and DNDs was determined by measurement of **1-DLC** fluorescence polarisation as a function of DND concentration. All fluorescence polarization values were measured (from the top) with a BioTeK Synergy H4 Plate Reader using a filter set with an excitation wavelength of 485 ± 20 nm and emission wavelength of 620 ± 40 nm, with a Xenon light source and gain set to 70. The plate used was a black polystyrene, clear bottomed, tissue culture treated polystyrene 96-well plate (Corning Inc. costar® 3605).

DNDs were mixed with **1-DLC** (2 μM) at carboxylic acid concentrations of 0.250, 0.125, 0.0625, 0.0313, 0.0156, and 0.00781 mM. The carboxylic acid concentrations were converted from DND concentration in mg/mL based on an average carboxylic acid content of 0.1 mmol/g. The mixture was plated in triplicate (80 μL) into the 96-well plate fluorescence polarization data collected. A one site model, including a non-specific adsorption factor, was used to fit the fluorescence polarization data with GraphPad Prism 8 software, to give a calculated K_d of 21 μM for **1-DLC** to DNDs (95% confidence interval 11.9 to 36.2 μM).

S5.4 Scanning electron microscopy images

SEM images were collected of lyophilised samples of unreacted DNDs and HPHT NDs. The ND particles bear little resemblance to 1-D films which is a likely cause for the low retention of peptides **3-DF** and **4-GF**.

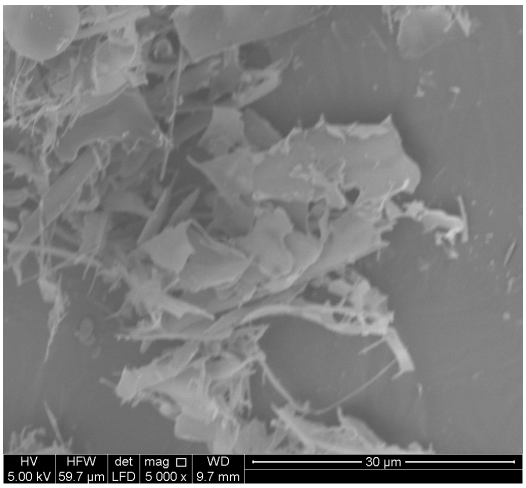

Figure S5.14. Scanning electron microscopy image of lyophilised detonation nanodiamonds.

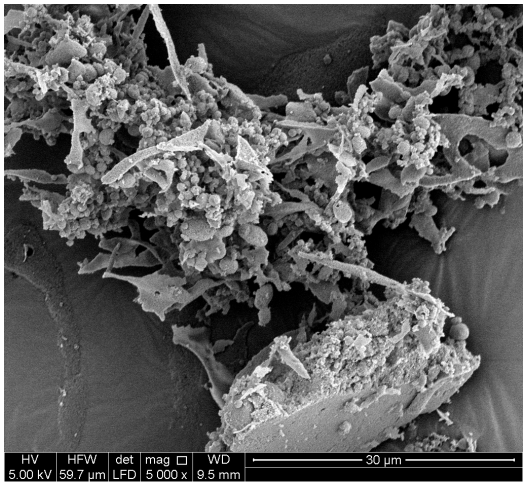

Figure S5.15. Scanning electron microscopy image of lyophilised high-pressure high-temperature nanodiamonds.

S5.5 Surface area calculations

The approximate surface area available in 1 mg of 5 nm DNDs and 120 nm HPHT NDs was calculated according to the following equations, assuming a ND density of 3.51 g/cm^3 and that the NDs are approximately spherical.

$$Volume\ of\ one\ ND = \frac{4}{3}\pi r^3$$

$$Mass\ of\ one\ ND = Density \times Volume$$

$$= 3.51\ \frac{g}{cm^3} \times \frac{4}{3}\pi r^3$$

$$Number\ of\ NDs\ in\ 1\ mg = \frac{1\ mg}{Mass\ of\ one\ ND}$$

$$= \frac{1\ mg}{3.51\ \frac{g}{cm^3} \times \frac{4}{3}\pi r^3}$$

$$\therefore Surface\ area\ in\ 1\ mg\ of\ NDs = 4\pi r^2 \times \frac{1\ mg}{3.51\ \frac{g}{cm^3} \times \frac{4}{3}\pi r^3}$$

These calculations provide an approximate surface area of 3.42 × 10^{17} nm^2 and 1.42 × 10^{16} nm^2 for 1 mg of DNDs and HPHT NDs respectively. This suggests that there is approximately 24× more surface area available for the CBPs to bind to DNDs than to HPHT NDs.

S5.6 Confocal microscopy

Confocal microscopy was conducted on both HPHT NDs and DNDs loaded with **1-DLC** and **2-CN** as described in the main text. The false colour images for the HPHT NDs are shown in Figure 5.5. Only the fluorescein (green) channel is shown here for the DNDs as they do not contain NV centres.

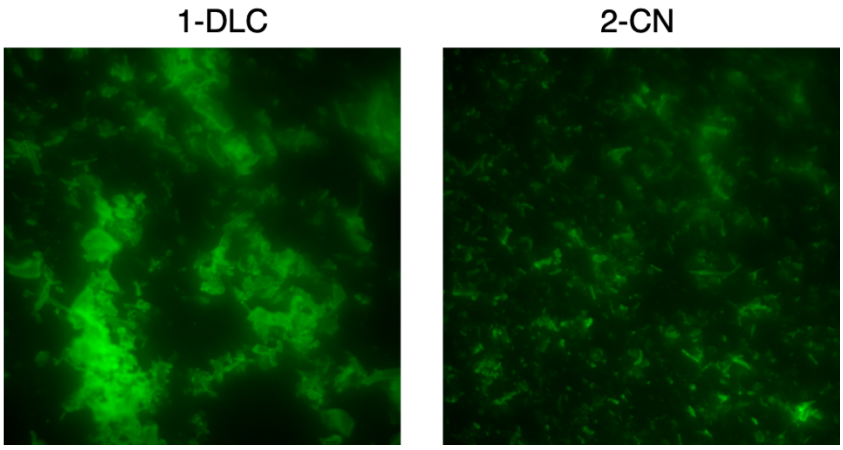

Figure S5.16. Confocal microscopy images of DNDs with adhered **1-DLC** (left) and **2-CN** (right) ex. 476 nm, em. 498-541 nm.

S5.7 Infrared spectroscopy

FTIR spectra of **3-DF** and **4-GF** were collected and compared to those for unreacted DNDs or HPHT NDs in the same manner as described for **1-DLC** and **2-CN** in section 5.3.5. These confirmed the presence of **3-DF** on DNDs through a peak match at 1100 cm^{-1} and the absence of **4-GF** on both DNDs and HPHT NDs, but were inconclusive for the presence of **3-DF** on HPHT NDs.

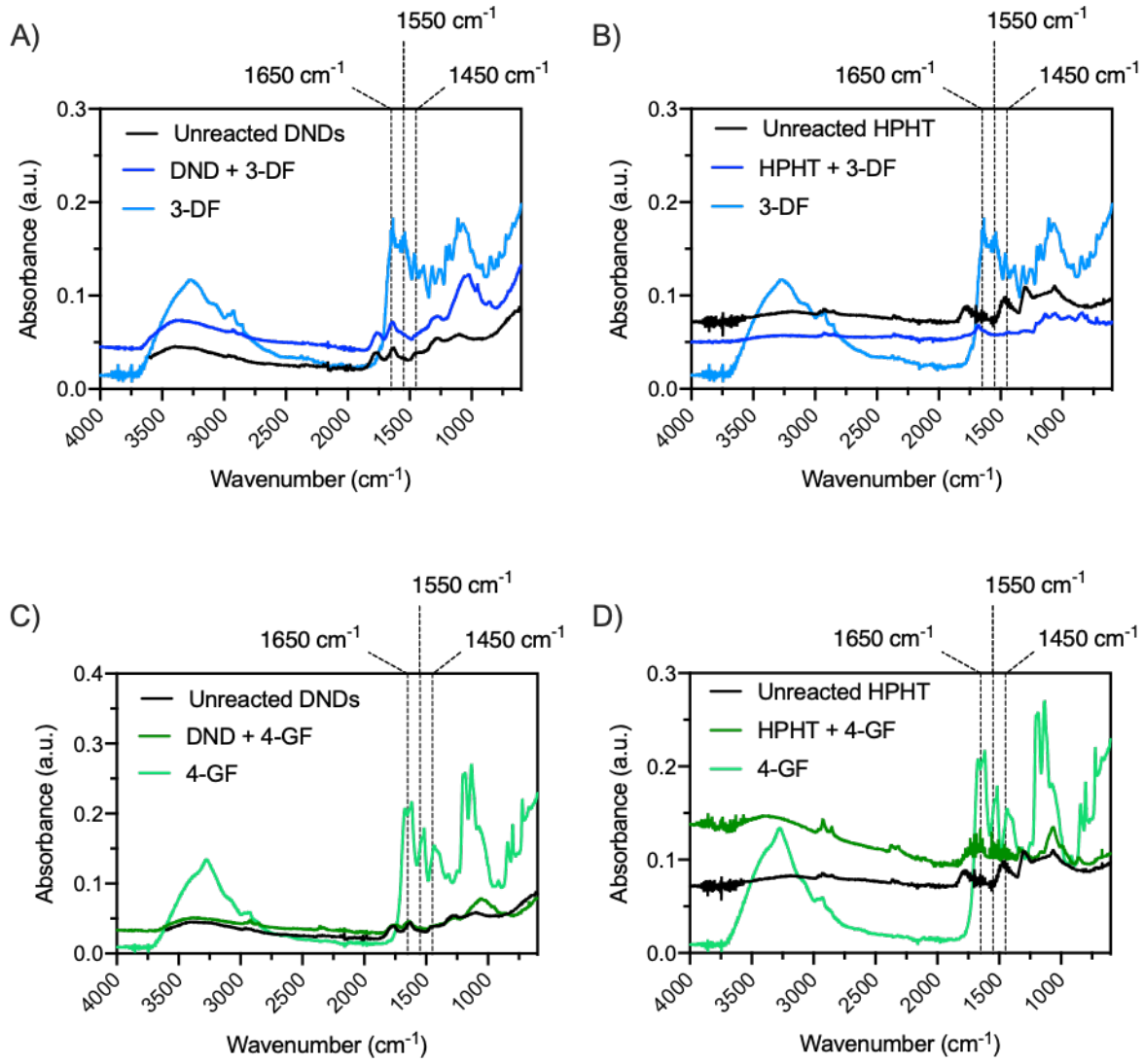

Figure S5.17. FTIR spectra for diamond-binding peptide (DBP) loaded nanodiamonds (NDs). **A)** FTIR spectra for unreacted DNDs (black), **3-DF** loaded DNDs (blue), and pure **3-DF** (light blue). **B)** FTIR spectra for unreacted HPHT NDs (black), **3-DF** loaded HPHT NDs (blue), and pure **3-DF** (light blue). **C)** FTIR spectra for unreacted DNDs (black), **4-GF** loaded DNDs (green), and pure **4-GF** (light green). **D)** FTIR spectra for unreacted HPHT NDs (black), 4-GF loaded HPHT NDs (green), and pure **4-GF** (light green).

S5.8 Dynamic light scattering

As described in the main text, dynamic light scattering (DLS) was performed on 1-DLC and 2-CN loaded NDs to investigate their colloidal stability when exposed to increasing concentrations of aqueous sodium chloride. The DLS particle size plotted in Figure 5.6 does not contain error bars as the partially aggregated ND suspensions result in a high polydispersity index (PdI), which skews the standard deviation to large values according to the below, where SD is standard deviation and d is the particle size:

$$PdI = \left(\frac{SD}{d}\right)^2$$

$$\therefore SD = \sqrt{PdI} \times d$$

The DLS size and zeta potential plots are provided below with the error bars for DLS size included.

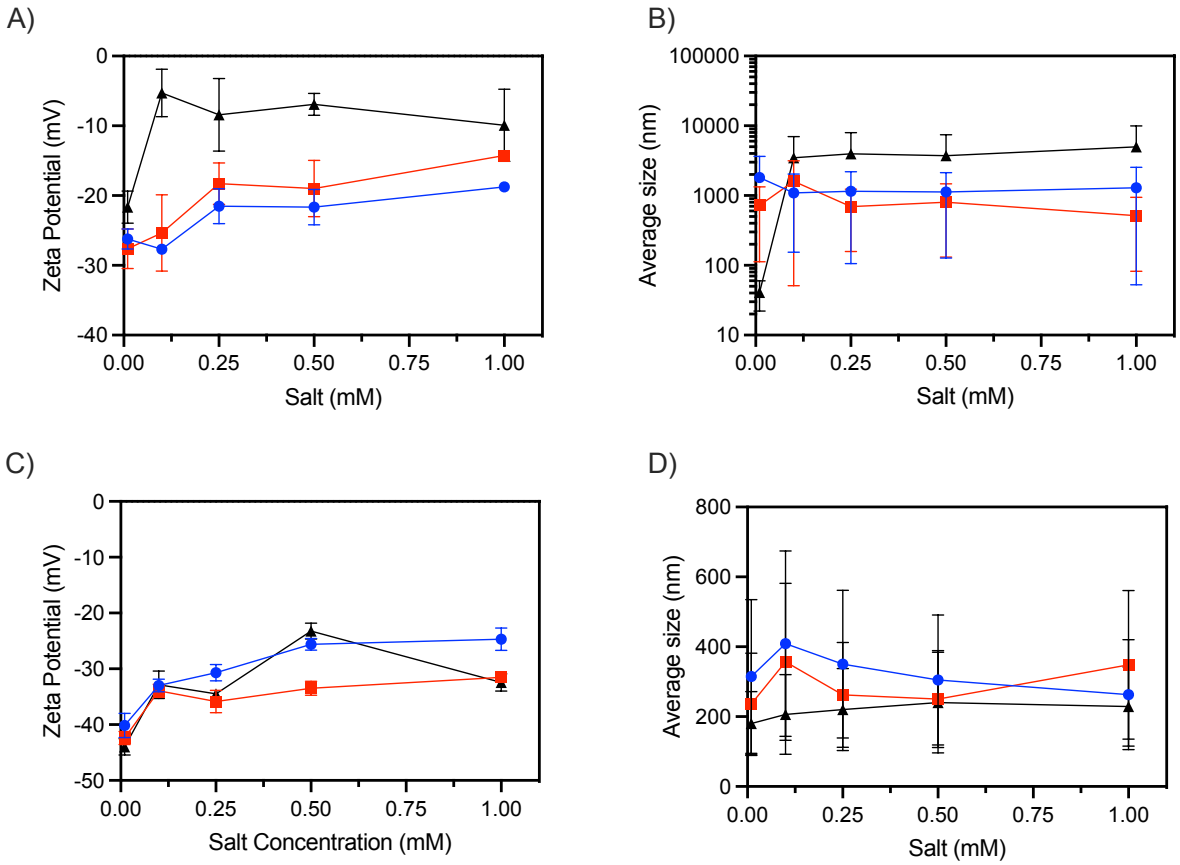

Figure S5.18. Dynamic light scattering data for unreacted (black), **1-DLC** loaded (blue), and **2-CN** loaded (red) NDs. Zeta potential for **A)** DNDs and **C)** HPHT NDs, and the average DLS particle size for **B)** DNDs and **D)** HPHT NDs. Error bars are standard deviations.

S5.9 Thermogravimetric analysis

Additional ion current vs temperature plots obtained during TGA of **1-DLC** loaded DNDs and HPHT NDs are provided, along with the mass spectra obtained from unreacted DNDs and HPHT NDs during TGA and photographs on the ND materials before and after TGA was conducted.

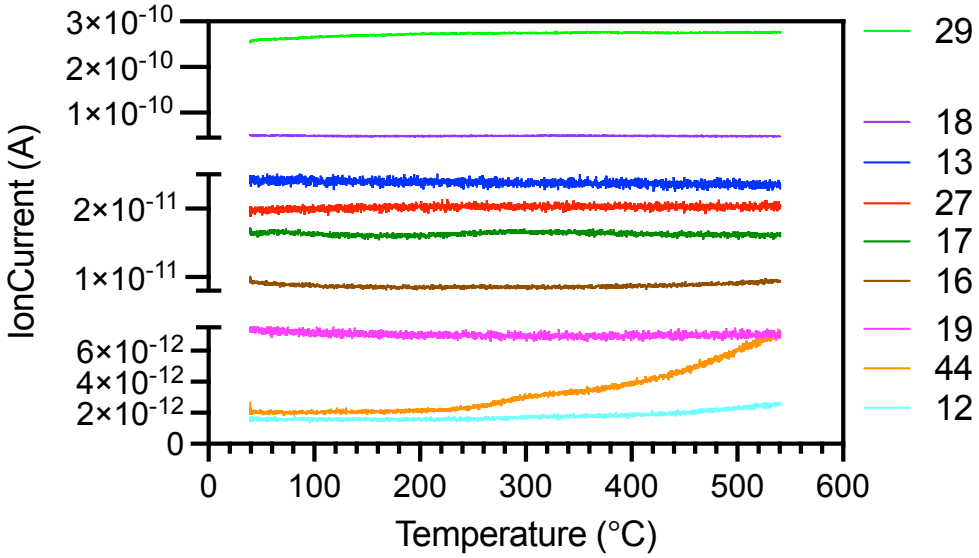

Figure S5.19. Plot of ion current against temperature for **1-DLC** loaded DNDs collected using the quadrupole mass spectrometer set to search for masses 12, 13, 16, 17, 18, 19, 27, 29, 31, 41, 44, 45, 50, and 51 amu. Masses 31, 41, 45, 50, and 51 were all found to have negligible signal (less than $1x10^{-13}$) and are not shown here.

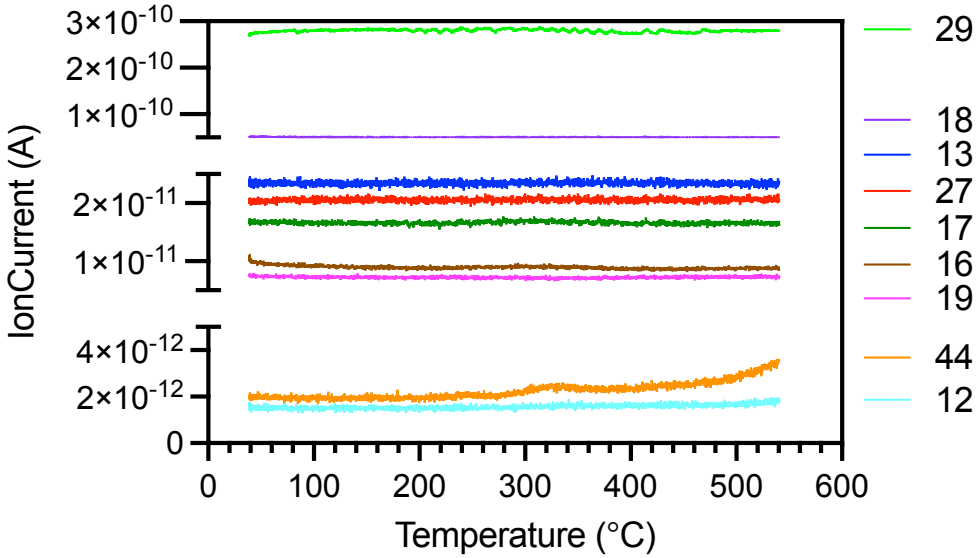

Figure S5.20. Plot of ion current against temperature for **1-DLC** loaded HPHT NDs collected using the quadrupole mass spectrometer set to search for masses 12, 13, 16, 17, 18, 19, 27, 29, 31, 41, 44, 45, 50, and 51 amu. Masses 31, 41, 45, 50, and 51 were all found to have negligible signal (less than $1x10^{-13}$) and are not shown here.

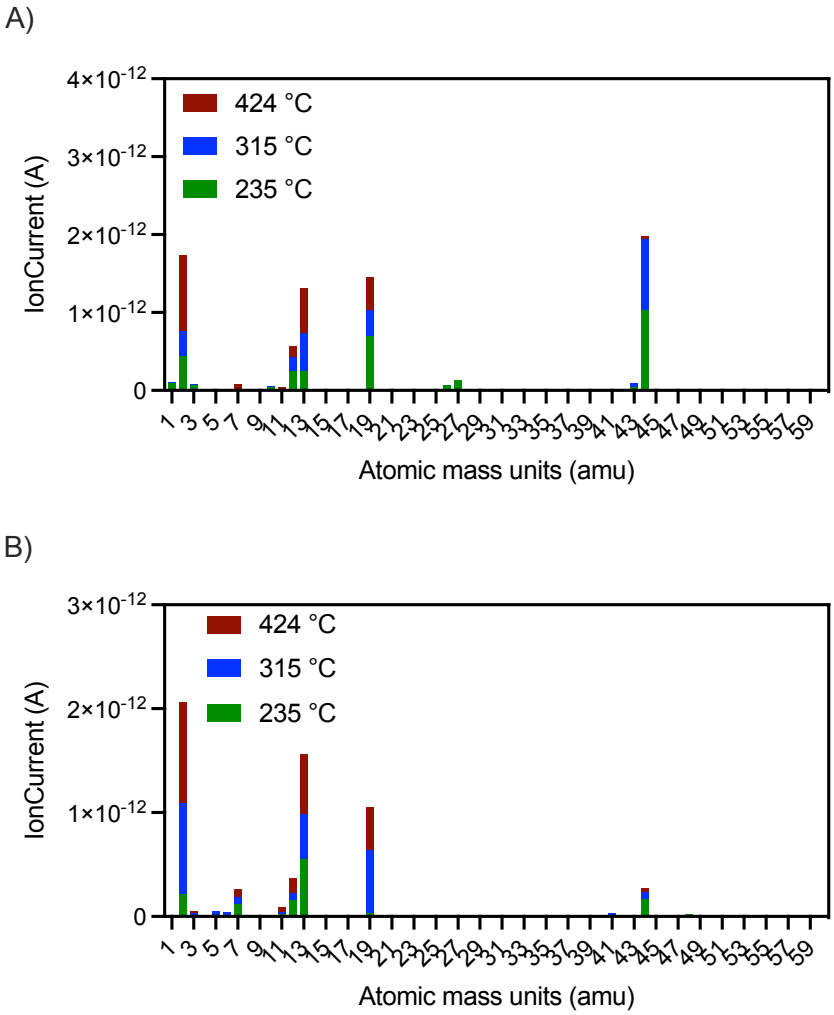

Figure S5.21. Mass spectra obtained for **A)** unreacted DNDs and **B)** unreacted HPHT NDs at the key mass loss events of 235 °C (green), 315 °C (blue), and 424 °C (red).

Figure S5.22. Picture of unreacted DNDs before (left) and after (right) submission to TGA.

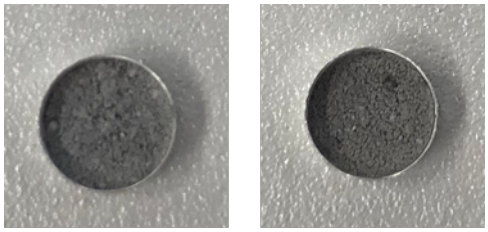

Figure S5.23. Picture of unreacted HPHT NDs before (left) and after (right) submission to TGA.

Chapter 6: An improved synthesis of 4-aminobutanenitrile from 4-azidobutanenitrile and comments on room temperature stability

This chapter consists of a publication submitted to Synthetic Communications in September 2020 and accepted in December 2020. The publication is entitled “An improved synthesis of 4-aminobutanenitrile from 4-azidobutanenitrile and comments on room temperature stability”.

Synthetic Communications, 51 (3), 428-436

Patrick K. Capon, Thomas D. Avery, Malcolm S. Purdey, Andrew D. Abell

Statement of Authorship

Title of Paper	An improved synthesis of 4-aminobutanenitrile from 4- azidobutanenitrile, and comments on room temperature stability
Publication Status	☒ Published ☐ Accepted for Publication ☐ Submitted for Publication ☐ Unpublished and Unsubmitted work written in manuscript style
Publication Details	Patrick K. Capon, Thomas D. Avery, Malcolm S. Purdey & Andrew D. Abell (2020) An improved synthesis of 4-aminobutanenitrile from 4-azidobutanenitrile and comments on room temperature stability, Synthetic Communications, DOI: 10.1080/00397911.2020.1832527

Principal Author

Name of Principal Author (Candidate)	Patrick Capon		
Contribution to the Paper	Conducted the research, wrote the manuscript, revised the manuscript.		
Overall percentage (%)	80		
Certification:	This paper reports on original research I conducted during the period of my Higher Degree by Research candidature and is not subject to any obligations or contractual agreements with a third party that would constrain its inclusion in this thesis. I am the primary author of this paper.		
Signature		Date	13/01/2021

Co-Author Contributions

By signing the Statement of Authorship, each author certifies that:

i. the candidate's stated contribution to the publication is accurate (as detailed above);

ii. permission is granted for the candidate in include the publication in the thesis; and

iii. the sum of all co-author contributions is equal to 100% less the candidate's stated contribution.

Name of Co-Author	Thomas Avery		
Contribution to the Paper	Advised and assisted with the synthetic procedure optimisation, edited the manuscript		
Signature		Date	13/01/2021

Name of Co-Author	Malcolm Purdey		
Contribution to the Paper	Conceived the research, edited the manuscript, supervised Patrick during PhD degree.		
Signature		Date	13/01/2021

Name of Co-Author	Andrew Abell		
Contribution to the Paper	Conceived and provided troubleshooting for the research, edited the manuscript, revised the manuscript. Provided project resources and supervised Patrick during PhD degree.		
Signature		Date	13/01/2021

6.1 Abstract

4-Aminobutanenitrile (**1**) is an important synthetic intermediate for neurological disorder therapeutics including Parkinson's and Alzheimer's diseases, and is an industrial precursor to pyrroline and pyrrolidine. Synthesis of **1** by Co(II) catalysed reduction of 4-azidobutanenitrile (**2**) with $NaBH_4$, or by a one-pot Staudinger reduction of **2** in THF, was low yielding. ^{1}H-NMR analysis of the Staudinger reduction revealed formation of iminophosphorane intermediate (**3**) after 22 h at rt, and that increasing the reaction temperature from rt to 40 °C promoted hydrolysis of **3** to **1**. A modified Staudinger reduction of **2** involving pyridine as solvent, addition of water 3 h after triphenylphosphine, and a temperature increase to 40 °C, gave rise to **1** in 69% yield. **1** is unstable at rt, thus the hydrochloride salt of **1** (**1.HCl**) was prepared by bubbling $HCl_{(g)}$ through a solution of **1** in chloroform. **1.HCl** is stable at rt and is hence the preferred form for storage.

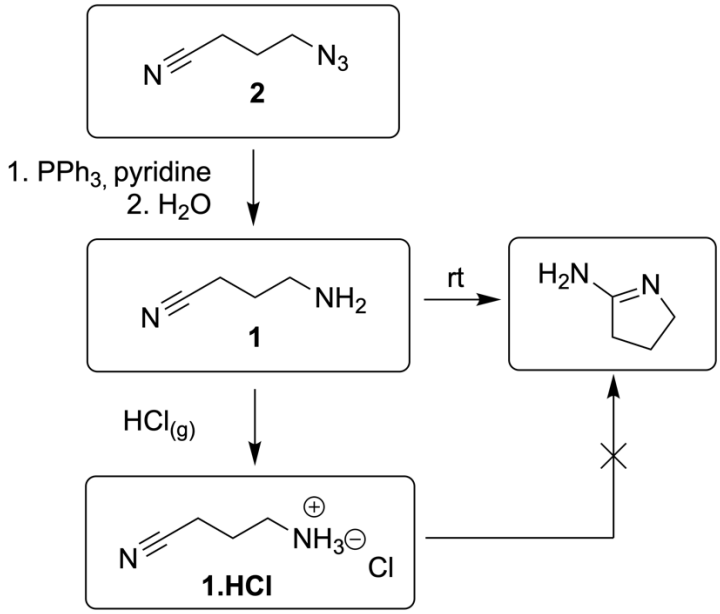

Reaction conditions to improve the synthesis of 4-aminobutanenitrile are discussed alongside room temperature stability.

6.2 Introduction

Aminonitriles are common structural features in a wide range of bioactive compounds, as was recently reviewed by Fleming *et al*.[1] Specifically, 4-aminobutanenitrile (**1**, see Figure 6.1) is an important synthetic intermediate of neurological disorder therapeutics including those treating Parkinson's and Alzheimer's diseases,[2] and in the industrial production of pyrroline and pyrrolidine.[3,4] Furthermore, **1** is commonly used in epoxy resins or as an oil additive,[5] and the characteristic spectroscopic signature of its component nitrile (infrared and Raman spectroscopy bands in the 2250 to 2230 cm^{-1} range)[6,7] provides an opportunity for spectroscopic identification. For example, **1** can be used to functionalise carboxylic acid decorated nanomaterials *via* amide bond formation, with the nitrile available for spectroscopic validation of functionalisation (see Chapter 4).

In this paper we investigate the synthesis and subsequent stability of 4-aminobutanenitrile (**1**). Its synthesis has been reported previously by reduction of the corresponding azide, 4-azidobutanenitrile (**2**). A Staudinger reduction of **2** to **1** was reported by Yuan and Silverman in 2006,[2] while Fringuelli *et al*.[8] reported a cobalt(II) catalysed reduction of **2** to **1** with $NaBH_4$ in water. In our hands these procedures were not reproducible, with little to no product formation observed. Furthermore, in the cases when **1** was obtained, we found it to be unstable at rt in the laboratory, with pure samples forming a complex mixture over two to three days. Here we discuss these issues in detail, and report an improved Staudinger reduction of **2** to provide **1**, including formation of the hydrochloride salt, **1.HCl**.

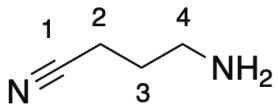

4-aminobutanenitrile (**1**)

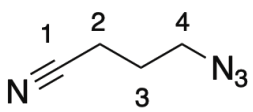

4-azidobutanenitrile (**2**)

Figure 6.1. Structures of 4-aminobutanenitrile (**1**) and key starting material 4-azidobutanenitrile (**2**) with carbon atoms numbered.

6.3 Results and discussion

6.3.1 Synthesis design and optimisation

The key starting material 4-azidobutanenitrile (**2**) was obtained from 4-bromobutanenitrile on reaction with sodium azide (see Supporting Information section S6.1),[2] and subsequent reduction to **1** was attempted under a variety of conditions as shown in Table 6.1 (reactions Cobalt #1-#3). Attempted reduction with a cobalt(II) chloride hexahydrate catalyst and $NaBH_4$, in water at rt, gave rise to quantitative recovery of **2**, contrary to the literature report[8] of a 98% yield of **1** after 10 min (Scheme 6.1, top route). Extension of the reaction time up to one hour did not result in any formation of **1**. The addition of surfactant cetyltrimethylammonium bromide (CTABr), as described in the original manuscript[8] for use with hydrophobic azides (**2** is insoluble in water), also returned starting material **2** without evidence of amine **1**. Finally, cobalt(II) catalyst crushed into a fine powder with a mortar and pestle was used in the reduction to provide increased catalyst surface area, however this reaction also returned **2** only.

Next the Staudinger reduction of **2** to **1** was attempted as per literature conditions (Table 6.1, entry Staudinger #1 and Scheme 6.1, central route).[2] Azide **2** was stirred in THF with 2% (v/v) water and one equivalent of triphenylphosphine at rt overnight. The literature work up was followed, with solvent removed and the residue taken up in ethyl acetate, followed by extraction of the organic layer with 1M HCl, adjustment of the aqueous layer to pH 12 with 1 M NaOH, and extraction with ethyl acetate, then finally solvent removal to isolate **1** in only 5% yield. The fact that **1** was obtained, albeit in low yield, prompted further investigation of the reaction progress.

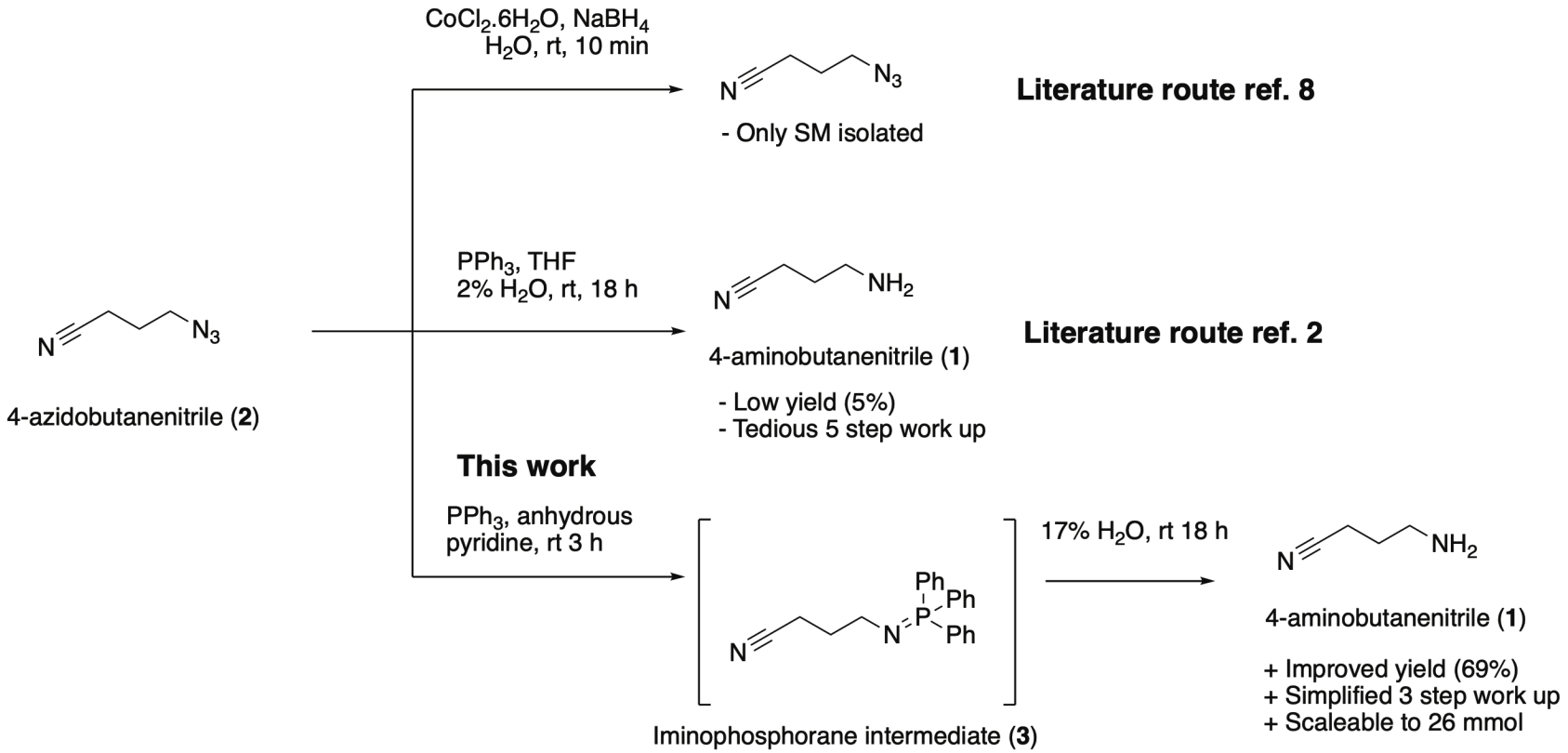

Scheme 6.1. Reduction reactions of 4-azidobutanenitrile (**2**) to 4-aminobutanenitrile (**1**). Co(II) catalysed reaction resulted in recovery of **2**, while the Staudinger reduction in THF was repeatedly low yielding and required a tedious work up. New conditions were developed for the Staudinger reduction in anhydrous pyridine to obtain product **1** in >69% yield. The new conditions contain a simplified work up and have been scaled up to 26 mmol of starting material **2**.

Table 6.1. Summary of the literature reactions attempted to reduce 4-azidobutanenitrile (**2**) to 4-aminobutanenitrile (**1**).

Reaction	Conditions	Result
Cobalt #1 (as per literature)[8]	$NaBH_4$ (2 equiv), $CoCl_2.6H_2O$ (0.1 equiv), water, rt, 10 min to 1 h	Recovered starting material (**2**)
Cobalt #2	$NaBH_4$ (2 equiv), $CoCl_2.6H_2O$ (0.1 equiv), CTABr (0.1 equiv) water, rt, 10 min	Recovered starting material (**2**)
Cobalt #3	$NaBH_4$ (2 equiv), $CoCl_2.6H_2O$ (0.1 equiv, crushed into a fine powder), water, rt, 10 min	Recovered starting material (**2**)
Staudinger #1 (as per literature)[2]	Triphenylphosphine (1 equiv), water (2% v/v), THF, rt, 18 h	5% yield of **1**

In particular, azide **1** and one equivalent of triphenylphosphine were dissolved in $CDCl_3$ (700 µL) and the ensuing reaction was monitored by ^{1}H NMR spectroscopy at rt over three days (Figure 6.2 and Table 6.2). The ^{1}H NMR spectrum after 18 h revealed two new resonances at δ3.20 and 1.84 ppm (Figure 6.2, blue) when compared to that of **2** (Figure 6.2, purple, top) and **1** (Figure 6.2, red, bottom). These new resonances are attributed to the iminophosphorane intermediate (**3**, see Scheme 6.1), a known intermediate in the Staudinger reduction.[9-11] Partial consumption of starting material **2** was observed by the lower integration of its assigned C(4)H_2 and C(2)H_2 resonances at δ3.50 and 1.90 ppm, respectively, compared to integration of the new resonances assigned to **3** (δ3.20 and 1.84 ppm). A minor resonance was also observed at δ2.85 ppm (Figure 6.2, blue), consistent with production of a small quantity of **1**.

D_2O (2% v/v) was next added to the NMR tube to hydrolyse **3** to the desired product **1**, and the reaction mixture stood at room temperature for a further 22 h. The ^{1}H NMR spectrum was recorded to reveal resonances occurring again at δ3.20 and 1.84 ppm due to C(4)H_2 and C(2)H_2 of **3** respectively (Figure 6.2, green). Two new resonances were observed at δ2.85 and 1.80 ppm, and were assigned to C(4)H_2 and C(2)H_2 of product **1** respectively. The product **1** and intermediate **3** were present in a ratio of 2:5 based on integration of the C(4)H_2 resonances of **1** and **3**.

Finally, the NMR tube reaction was heated at 40 °C for 22 h in an attempt to complete hydrolysis of **3** to **1** (Figure 6.2, yellow). This gave rise to further **1**, with **1** and **3** now present in a

ratio of 4:1. However, it should be noted that some of azide **2** remained unreacted, as shown by the presence of the C(2)H_2, C(3)H_2, and C(4)H_2 resonances for **2** in all spectra through the course of the NMR reaction study.

Based on the results of the NMR spectroscopy study, in a separate reaction, azide **2** was first stirred in anhydrous THF with triphenylphosphine (1 equiv) for 3 h, then 2% v/v H_2O added and the reaction mixture heated at 40 °C for 18 h. This was done in order to separate the iminophosphorane formation and hydrolysis steps, as was done in the NMR study. NMR analysis on this reaction mixture, prior to work up, revealed the presence of **1** in a 2:5 ratio to **2**. Further water up to a final concentration of 8% v/v was added and the reaction heated at 40 °C over 72 h in an attempt to complete hydrolysis of **3** to **1**. The reaction mixture was cooled to rt and worked up by the literature procedure described earlier,[2] to give **1** in 13% yield.

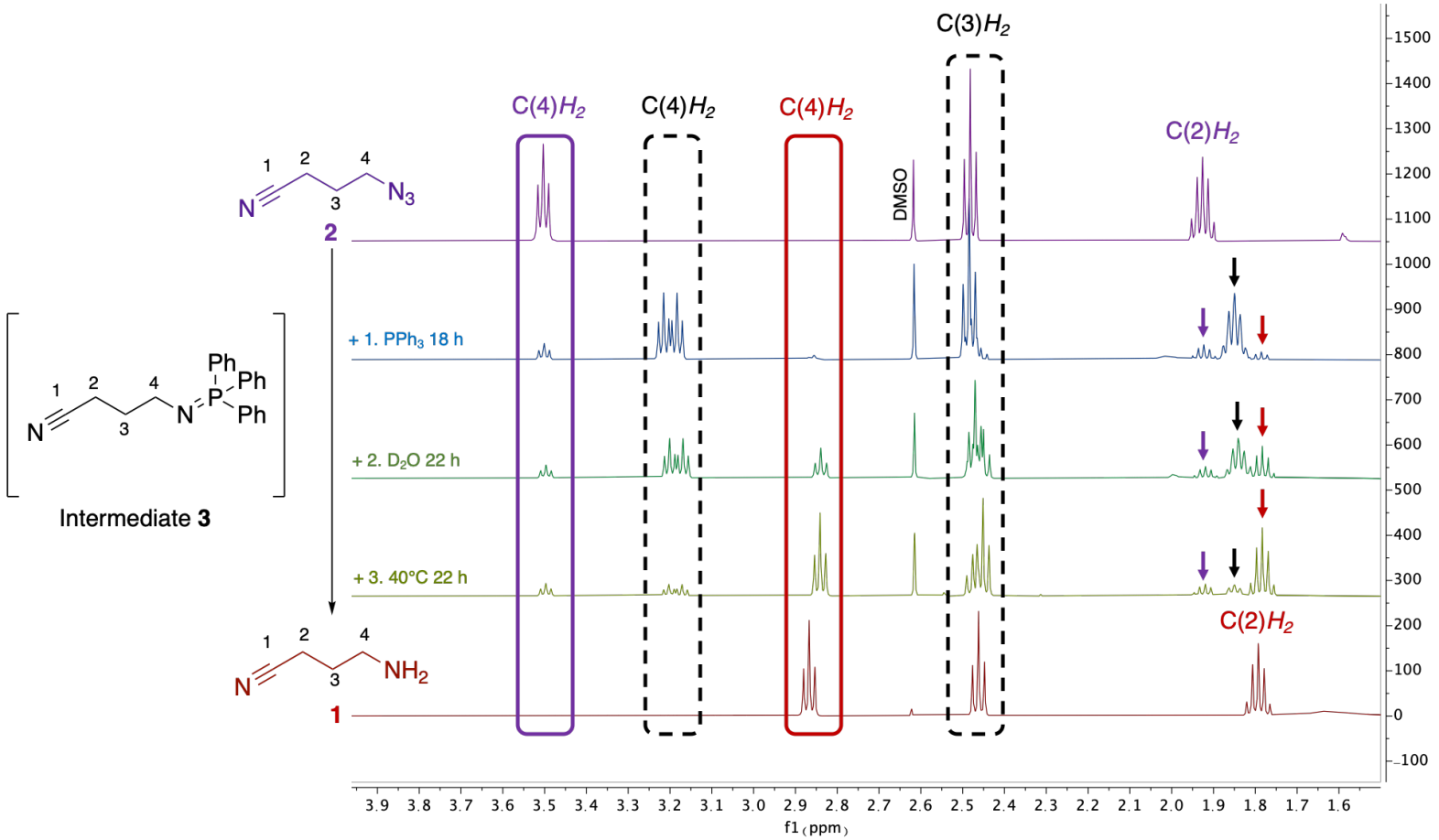

Figure 6.2. ^{1}H NMR spectra following the reduction reaction of 4-azidobutanenitrile (**2**) with triphenylphosphine in $CDCl_3$. From top to bottom: **2** (purple), 18 h at rt after triphenylphosphine addition (blue), 22 h after D_2O addition (green), 22 h after heating at 40 °C (yellow), and pure 4-aminobutanenitrile (**1**) (red). Signals in solid boxes correspond to the $C(4)H_2$ signal for **2** (purple), and **1** (red). The $C(4)H_2$ signal for the iminophosphorane intermediate (**3**) and $C(3)H_2$ signal for all compounds are marked by black dashed boxes. Changes to the $C(2)H_2$ signal are marked by coloured arrows, where the arrow for **2** is purple, intermediate **3** is black, and **1** is red.

Table 6.2. Summary of the reduction of 4-azidobutanenitrile (**2**) to 4-aminobutanenitrile (**1**) followed by ^{1}H NMR spectroscopy in $CDCl_3$ at key intervals.

Conditions	Result
Azide 2 (1 equiv), triphenylphosphine (1 equiv), and $CDCl_3$ (700 µL), rt, 18 h	Iminophosphorane intermediate **3** observed by ^{1}H NMR
D_2O (2% v/v) added, rt, 22 h	**1** and **3** observed in a 2:5 ratio by ^{1}H NMR
Reaction increased to 40 °C, 22 h	**1** and **3** observed in a 4:1 ratio by ^{1}H NMR

Next, the Staudinger reduction was repeated, using anhydrous pyridine instead of anhydrous THF, based on the authors' prior experience with Staudinger reductions performed on similar substrates. Azide **2** was stirred with triphenylphosphine (1.15 equiv) in anhydrous pyridine for 3 h, then water was added at 17% v/v and the reaction mixture stirred at rt overnight (Scheme 6.1, bottom route). In this instance the reaction mixture was worked up by dilution with water, then **1** separated from the triphenylphosphine oxide by-product by washing the aqueous mixture with ethyl acetate. Water was removed under reduced pressure to give **1** in a 69% yield. This compares to a yield of 5% using the reported literature Staudinger conditions.[2] The new workup removes the need for the aqueous extraction, basification, and organic extraction required in the literature workup.[2]

This new Staudinger reduction of **2** was next carried out on a larger 26 mmol scale, given the importance of **1** as a precursor to pyrroline and pyrrolidine. The 14-fold increased reaction scale required only a 3.3-fold increase in ethyl acetate for work up, with **1** isolated in 71% yield. A purity of 94% was calculated by qHNMR using the "*100% method*" as described by Pauli *et al*.[12] (see Supporting Information Figure S6.3), without the need for chromatographic purification.

6.3.2 Stability of **1**

A sample of thus prepared **1** (an oil) was stored on the bench for one week at rt, then the ^{1}H NMR spectrum was collected to reveal multiple new resonances, with those at δ3.51, 2.34, and 1.89 ppm consistent with 2-aminopyrroline (Figure 6.3, red arrows).[13] We propose that **1** cyclises to give 2-aminopyrroline as has been previously reported for **1** (and the related compound 1,4-butanediamine) under nickel catalysed hydrogenation,[3,4,14] however to the best of our

knowledge this is the first report of its occurrence at rt. The original sample of **1**, still dissolved in $CDCl_3$, was re-analysed by ^1H NMR after one week and the resultant spectrum was unchanged relative to the first spectrum obtained (Figure 6.3). This sample had thus not cyclised, likely due to formation of the hydrochloride salt of **1** due to residual HCl in the $CDCl_3$ (Scheme 6.2).

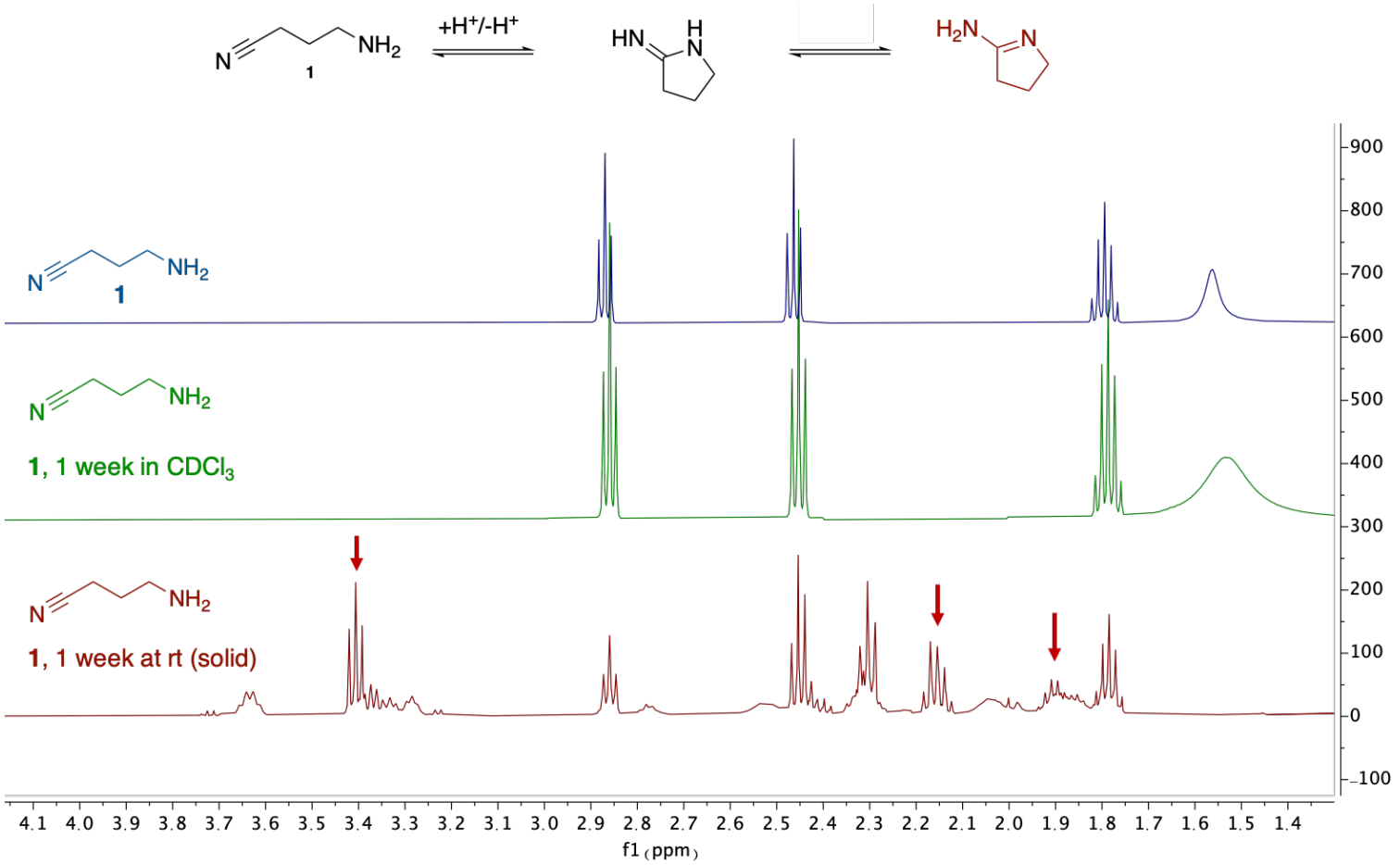

Figure 6.3. Top; Production of 2-aminopyrroline from 4-aminobutanenitrile (**1**). Bottom; NMR in $CDCl_3$ of **1** freshly synthesised (blue), after a week in $CDCl_3$ solution (green), and after a week on the lab bench at ambient conditions (red). Peaks corresponding to 2-aminopyrroline[13] are marked by red arrows.

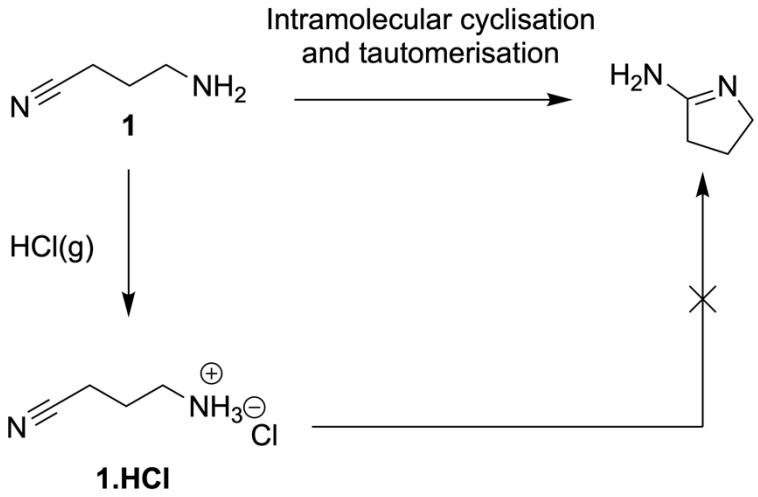

Scheme 6.2. Proposed cyclisation of 4-aminobutanenitrile (**1**) to 2-aminopyrroline, and synthesis of the corresponding hydrochloride salt (**1.HCl**).

The hydrochloride salt of amine **1** (**1.HCl**) was prepared by bubbling HCl gas through a solution of **1** (obtained by the new Staudinger reduction conditions) in chloroform, to give a white precipitate (see Supporting Information section S6.2). A gravimetric titration of **1.HCl** with $AgNO_3$ revealed that it to be the mono-hydrochloride salt, rather than the di-hydrochloride salt (see Supporting Information section S6.2). **1.HCl** was also characterised by ^{1}H NMR (Figure 6.4, blue), where a broad singlet was observed at δ8.2 ppm and assigned to the NH_3^+ group. The methylenes at the C2, C3, and C4 positions were observed to have shifted downfield relative those of **1**. The C(4)H_2 resonance for **1.HCl** (2.85 ppm) was also more complex compared to that of **1** (2.55 ppm, see Figure 6.4 purple and blue).

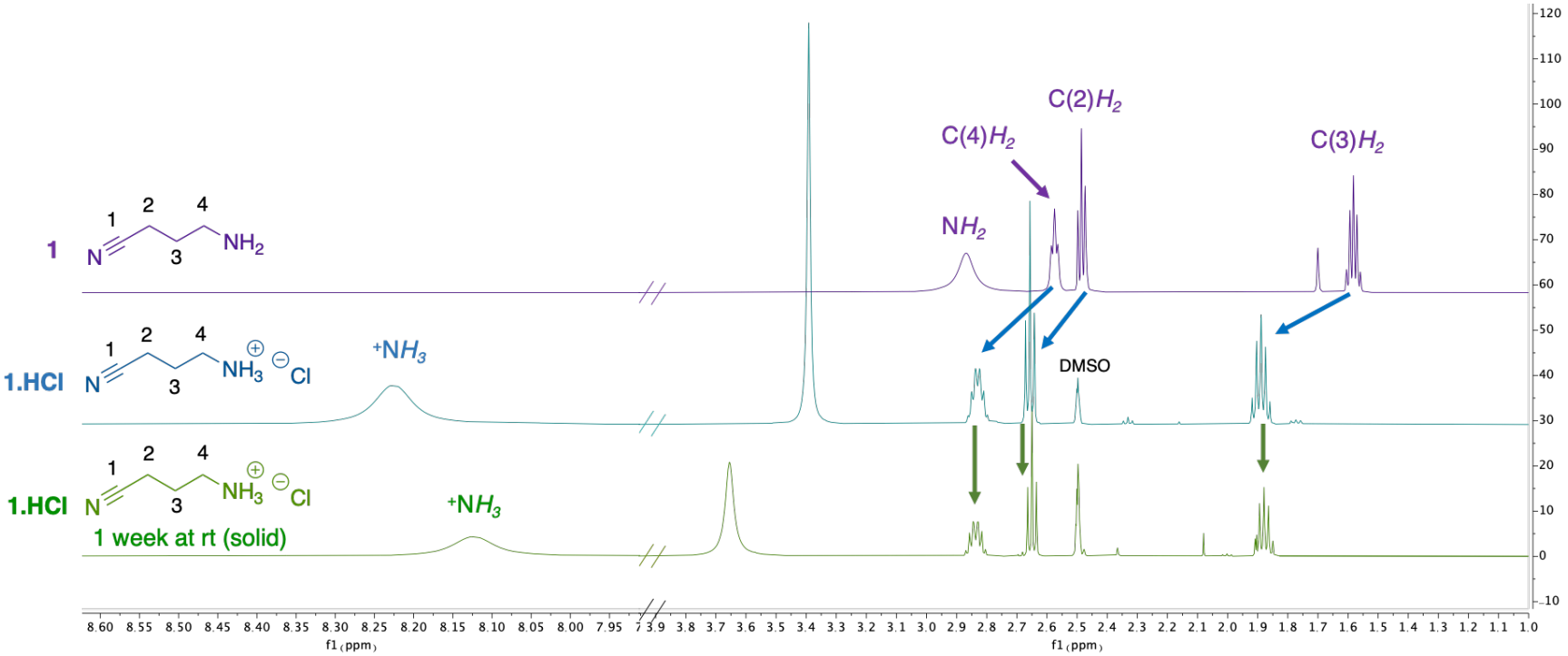

Figure 6.4. ^{1}H NMR spectra in DMSO-d_6 for 4-aminobutanenitrile (**1**) as synthesised (purple), with changes in chemical shift on hydrochloride salt formation highlighted (**1.HCl**, blue). **1.HCl** remains stable for one week on the lab bench under ambient conditions (green). A -$^{+}$NH$_3$ resonance was observed for freshly synthesised **1.HCl** (blue) and after one week (green) at 8.1 to 8.3 ppm, shifted from 2.8 ppm for the -NH$_2$ resonance in **1** (purple). There is a break in the x axis between 3.9 and 7.9 ppm, with no resonances observed in this range.

Finally, the stability of **1.HCl** was investigated by leaving a sample (solid) exposed to air over 7 days at rt. The sample was analysed by ^{1}H NMR, with no changes observed (Figure 6.4, green). The **1.HCl** thus has improved stability compared to the free amine and is as such the preferred method of storage (Scheme 6.2). The free amine **1** is liberated on treatment with a base such as triethylamine.

6.4 Experimental

Synthesis of 4-aminobutanitrile (**1**)

2 (200 mg, 1.82 mmol, 1 equiv) was dissolved in anhydrous pyridine (3.64 mL) under a nitrogen atmosphere. Triphenylphosphine (548 mg, 2.09 mmol, 1.15 equiv) was added and the reaction stirred at rt for 3 h. Water (0.58 mL) was added and the reaction mixture stirred for a further 16 h at rt. The reaction mixture was diluted with water (15 mL) and the aqueous mixture washed with ethyl acetate (3 × 10 mL). Solvent was removed under reduced pressure to yield **1** as a colourless oil (106 mg, 69%). ^{1}H NMR in $CDCl_3$ was consistent with literature[2]: ^{1}H NMR (500 MHz, $CDCl_3$) δ 2.86 (t, *J* = 6.7 Hz, 2H), 2.45 (t, *J* = 7.1 Hz, 2H), 1.87 - 1.74 (m, 2H) ppm. ^{1}H NMR (600 MHz, DMSO-d_6) δ 2.61 (t, *J* = 6.7 Hz, 2H), 2.52 (t, *J* = 7.2 Hz, 2H), 1.61 (p, *J* = 6.9 Hz, 2H) ppm. ^{13}C NMR (151 MHz, DMSO-d_6) δ 120.81, 40.00, 28.34, 13.64 ppm. FTIR (ATR mode): 3370 (N-H), 3297 (N-H), 3183 (N-H), 2939 (C-H), 2870 (C-H), 2245 (CN), 1599 (N-H) cm^{-1}. HRMS (ESI+) expected $[M+H]^+$ 84.0690 for $C_4H_8N_2$, found 84.0687.

6.5 Conclusion

In conclusion, we report an improved synthesis of 4-aminobutanenitrile (**1**), from 4-azidobutanenitrile (**2**). The reaction involves treating **2** with triphenylphosphine in pyridine rather than THF, with the reaction stirred for 3 h to allow for formation of the iminophosphorane intermediate (**3**) prior to the addition of water (17% v/v). The optimum workup involves dilution with water and washing with ethyl acetate to give a 69% yield of **1**. This compares to a yield of 5% using the reported literature Staudinger conditions.[2] We show that this new procedure is amenable to scale up to 26 mmol of **2**, to give **1** in 71% yield at 94% purity without chromatographic purification (qHNMR, 100% method). Finally, we have also shown that **1**

cyclises to 2-aminopyrroline at rt over a period of several days. The corresponding hydrochloride salt **1.HCl**, prepared by bubbling $HCl_{(g)}$ through a solution of **1**, is however stable and is the preferred form for storage.

6.6 Acknowledgements

The authors acknowledge support from the Australian Research Council Centre of Excellence for Nanoscale Biophotonics (CE140100003). PKC would like to acknowledge PhD scholarship support from the MF and MH Joyner Scholarship in Science, and the Norman and Patricia Polglase Supplementary Scholarship. The authors would like to thank Philip Clements for assistance with NMR collection and analysis. This work was performed in part at the Optofab node of the Australian National Fabrication Facility utilizing Commonwealth and SA State Government funding.

6.7 References

(1) Fleming, F. F.; Yao, L.; Ravikumar, P. C.; Funk, L.; Shook, B. C. Nitrile-Containing Pharmaceuticals: Efficacious Roles of the Nitrile Pharmacophore. *J. Med. Chem.* **2010**, *53* (22), 7902-7917. https://doi.org/10.1021/jm100762r.

(2) Yuan, H.; Silverman, R. B. New Substrates and Inhibitors of γ-Aminobutyric Acid Aminotransferase Containing Bioisosteres of the Carboxylic Acid Group: Design, Synthesis, and Biological Activity. *Bioorg. Med. Chem.* **2006**, *14* (5), 1331-1338. https://doi.org/10.1016/j.bmc.2005.09.067.

(3) Hoffer, B. W.; Schoenmakers, P. H. J.; Mooijman, P. R. M.; Hamminga, G. M.; Berger, R. J.; van Langeveld, A. D.; Moulijn, J. A. Mass Transfer and Kinetics of the Three-Phase Hydrogenation of a Dinitrile over a Raney-Type Nickel Catalyst. *Chem. Eng. Sci.* **2004**, *59* (2), 259-269. https://doi.org/10.1016/S0009-2509(03)00303-8.

(4) Serra, M.; Salagre, P.; Cesteros, Y.; Medina, F.; Sueiras, J. E. Nickel and Nickel-Magnesia Catalysts Active in the Hydrogenation of 1,4-Butanedinitrile. *J. Catal.* **2001**, *197* (1), 210-219. https://doi.org/10.1006/jcat.2000.3084.

(5) Reissner, Thomas; Altenhoff, Ansgar Gereon; Mueller, Christian; Fischer, Rolf-Hartmuth. Method for the Preparation of Polyamines From Dinitriles and/or Amino Nitriles. 20190218341, July 18, 2019.

(6) Lin-Vien, D.; Colthup, N. B.; Fateley, W. G.; Grasselli, J. G. CHAPTER 8 - The -C≡N and -N≡C Groups. In *The Handbook of Infrared and Raman Characteristic Frequencies of Organic Molecules*; Lin-Vien, D., Colthup, N. B., Fateley, W. G., Grasselli, J. G., Eds.; Academic Press: San Diego, 1991; pp 105-115. https://doi.org/10.1016/B978-0-08-057116-4.50014-6.

(7) Deb, P.; Haldar, T.; Kashid, S. M.; Banerjee, S.; Chakrabarty, S.; Bagchi, S. Correlating Nitrile IR Frequencies to Local Electrostatics Quantifies Noncovalent Interactions of Peptides and Proteins. *J. Phys. Chem. B* **2016**, *120* (17), 4034-4046. https://doi.org/10.1021/acs.jpcb.6b02732.

(8) Fringuelli, F.; Pizzo, F.; Vaccaro, L. Cobalt(II) Chloride-Catalyzed Chemoselective Sodium Borohydride Reduction of Azides in Water. *Synthesis* **2000**, *2000* (05), 646-650. https://doi.org/10.1055/s-2000-6389.

(9) Staudinger, H.; Meyer, J. Über Neue Organische Phosphorverbindungen III. Phosphinmethylenderivate Und Phosphinimine. *Helv. Chim. Acta* **1919**, *2* (1), 635-646. https://doi.org/10.1002/hlca.19190020164.

(10) Gololobov, Yu. G.; Zhmurova, I. N.; Kasukhin, L. F. Sixty Years of Staudinger Reaction. *Tetrahedron* **1981**, *37* (3), 437-472. https://doi.org/10.1016/S0040-4020(01)92417-2.

(11) Gololobov, Y. G.; Kasukhin, L. F. Recent Advances in the Staudinger Reaction. *Tetrahedron* **1992**, *48* (8), 1353-1406. https://doi.org/10.1016/S0040-4020(01)92229-X.

(12) Pauli, G. F.; Chen, S.-N.; Simmler, C.; Lankin, D. C.; Gödecke, T.; Jaki, B. U.; Friesen, J. B.; McAlpine, J. B.; Napolitano, J. G. Importance of Purity Evaluation and the Potential of Quantitative 1H NMR as a Purity Assay. *J. Med. Chem.* **2014**, *57* (22), 9220-9231. https://doi.org/10.1021/jm500734a.

(13) Gratchev, M. K.; Kurochkina, G. I.; Negrebetsky, V. V.; Nifantyev, E. E. The Synthesis and Structure of P(III)-Phosphorylated 2-Aminopyrrolines. *Phosphorus Sulfur Silicon Relat. Elem.* **1994**, *88* (1-4), 257-269. https://doi.org/10.1080/10426509408036930.

(14) Laval, S.; Dayoub, W.; Pehlivan, L.; Métay, E.; Favre-Reguillon, A.; Delbrayelle, D.; Mignani, G.; Lemaire, M. Straightforward Access to Cyclic Amines by Dinitriles Reduction. *Tetrahedron* **2014**, *70* (4), 975-983. https://doi.org/10.1016/j.tet.2013.11.101.

(15) Tian, L.; Gao, S.; Wang, R.; Li, Y.; Tang, C.; Shi, L.; Fu, J. Copper-Catalyzed Ring-Opening C(Sp3)-N Coupling of Cycloketone Oxime Esters: Access to 1°, 2° and 3° Alkyl Amines. *Chem. Commun.* **2019**, *55* (37), 5347-5350. https://doi.org/10.1039/C9CC02030F.

Supporting Information

S6.1 General experimental details

All reagents and solvents were purchased from Merck/Sigma-Aldrich unless otherwise specified, at the highest purity level available. ^{1}H NMR spectra were recorded on an Agilent 500 MHz or a Varian Inova 600 MHz instrument in d_6-DMSO or $CDCl_3$ as indicated, and referenced to TMS at 0 ppm. Chemical shifts are reported in ppm (δ). Resonances are reported as s (singlet), br. s (broad singlet), d (doublet), t (triplet) or m (multiplet, range given). All plots of NMR spectra were generated using MestReNova v14.0.1. Fourier Transform Infrared (FTIR) spectroscopy was performed using a Perkin Elmer S400 Infrared spectrometer in Universal ATR mode. High-resolution mass spectra were collected using an Agilent 6230 ESI-TOF LCMS.

S6.2 Synthetic procedures

Synthesis of 4-azidobutanitrile (**2**)

4-Bromobutanitrile (1.21 mL, 12.2 mmol, 1 equiv) was dissolved in DMSO (20 mL), followed by addition of sodium azide (1.20 g, 18.5 mmol, 1.55 equiv) and the reaction mixture stirred at rt for 16 h. Water (50 mL) was added and the aqueous mixture extracted with diethyl ether (3 × 40 mL). The combined organic phases were washed with brine (40 mL), dried over $MgSO_4$, filtered, and solvent removed from the filtrate under reduced pressure to yield **2** as a colourless oil (0.90 g, 68%). NMR was consistent with literature:[2] ^{1}H NMR (500 MHz, $CDCl_3$) δ 3.50 (t, *J* = 6.3 Hz, 2H), 2.48 (t, *J* = 7.1 Hz, 2H), 1.93 (p, *J* = 6.8 Hz, 2H) ppm. ^{1}H NMR (500 MHz, DMSO-d_6) δ 3.44 (t, *J* = 6.6 Hz, 2H), 2.56 (t, *J* = 7.2 Hz, 2H), 1.88 - 1.78 (m, 2H) ppm. ^{13}C NMR (151 MHz, DMSO-d_6) δ 119.98, 49.40, 24.33, 13.82 ppm FTIR (ATR mode): 2939 (C-H), 2867 (C-H), 2250 (CN), 2096 (N=N=N) cm^{-1}.

Synthesis of 4-aminobutanenitrile (**1**) on a large scale

2 (2.86 g, 26.0 mmol, 1 equiv) was dissolved in anhydrous pyridine (52.0 mL) under a nitrogen atmosphere. Triphenylphosphine (7.83 g, 30.0 mmol, 1.15 equiv) was added and the reaction stirred at rt for 3 h. Water (8.32 mL) was added and the reaction mixture stirred for a further 16 h at rt. The reaction mixture was diluted with water (150 mL) and the aqueous mixture washed with ethyl acetate (2 × 50 mL). Solvent was removed under reduced pressure to yield **1** as a colourless oil (1.55 g, 71%). NMR data was consistent with the small scale reaction and literature:[2] ^{1}H NMR (500 MHz, $CDCl_3$) δ 2.86 (t, *J* = 6.7 Hz, 2H), 2.45 (t, *J* = 7.1 Hz, 2H), 1.79 (p, *J* = 6.9 Hz, 2H) ppm.

Synthesis of 4-aminobutanenitrile hydrochloride (**1.HCl**)

1 (116 mg, 1.38 mmol, 1 equiv) was dissolved in chloroform (2 mL) in a two neck round bottom flask equipped with a drying tube. Hydrochloric acid gas was produced through slow addition of H_2SO_4 onto NH_4Cl and bubbled through the reaction solution, carried by a stream of N_2 gas, for 20 mins while cooling at 4 °C. Solvent was removed under an N_2 stream and the residue dried under reduced pressure for 2 h to yield **1.HCl** as a white solid (142 mg, 85%). ^{1}H NMR in D_2O was in agreement with literature:[15] ^{1}H NMR (599 MHz, D_2O) δ 3.13 (t, *J* = 7.6 Hz, 2H), 2.65 (t, *J* = 7.2 Hz, 2H), 2.11 - 2.02 (m, 2H) ppm. ^{1}H NMR (500 MHz, DMSO-d_6) δ 8.13 (s, 3H), 2.89 - 2.77 (m, 2H), 2.65 (t, *J* = 7.2 Hz, 2H), 1.88 (p, *J* = 7.3 Hz, 2H) ppm. ^{13}C NMR (126 MHz, DMSO-d_6) δ 123.02, 40.72, 26.15, 16.97 ppm. FTIR (ATR mode): 3450 (N-H), 3013 (N-H), 2841 (C-H), 2250 (CN), 1656 (N-H) cm^{-1}.

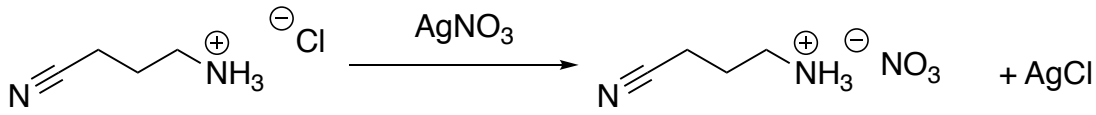

Scheme S6.3. Determination of HCl content through titration with $AgNO_3$

Determination of HCl content in **1.HCl**

The hydrochloride content of **1.HCl** was determined by precipitation of AgCl from **1.HCl** by addition of $AgNO_3$. $AgNO_{3(aq)}$ (0.1 M, 20 mL) was prepared from $AgNO_{3(s)}$ which had been pre-dried for 2 h at 100°C. **1.HCl** (48.5 mg, 0.402 mmol) was dissolved in water (20 mL) and heated to 80°C. $AgNO_{3(aq)}$ (0.1 M, 4 mL) was added and a white precipitate formed immediately. No stirrer bar was used to avoid deposition of AgCl. The solution was heated at 80°C for 30 min, then cooled to rt. The solution was decanted, and the solid washed with 2% v/v $HNO_{3(aq)}$ (50 mL). The solid was dried at 120°C for 1 h, then cooled to rt to yield AgCl as a white solid (55.80 mg). The AgCl was dried for a further 1 h and weighed again (56.00 mg), then dried for 72 h and weighed a third time (56.10 mg) to give an average mass of 55.97 mg, and hence 0.391 mmoles of Cl^- (c.f. 0.402 mmol of starting material). Therefore **1.HCl** was confirmed to be a mono hydrochloride salt.

S6.3 ^{1}H NMR spectra

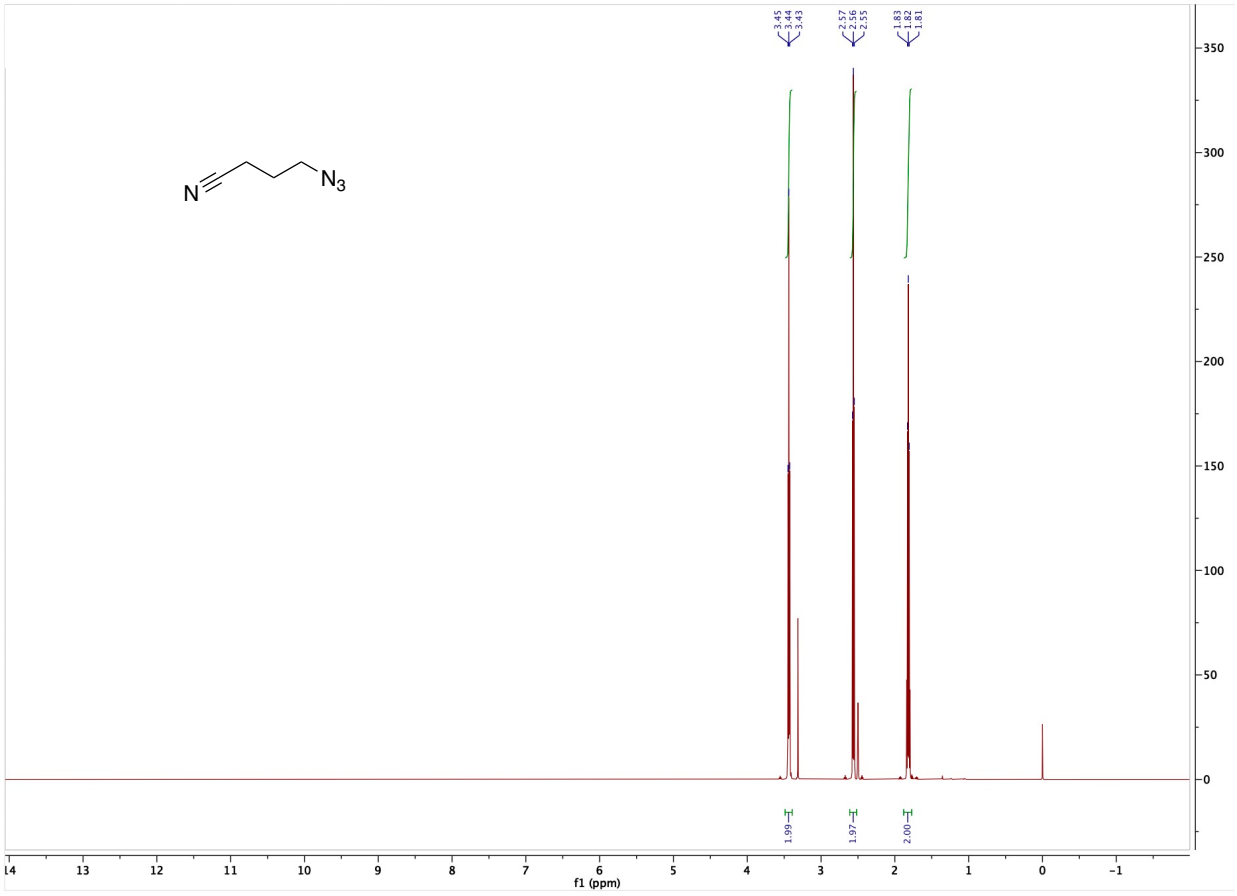

Figure S6.5. ^{1}H NMR spectrum for 4-azidobutanenitrile (2).

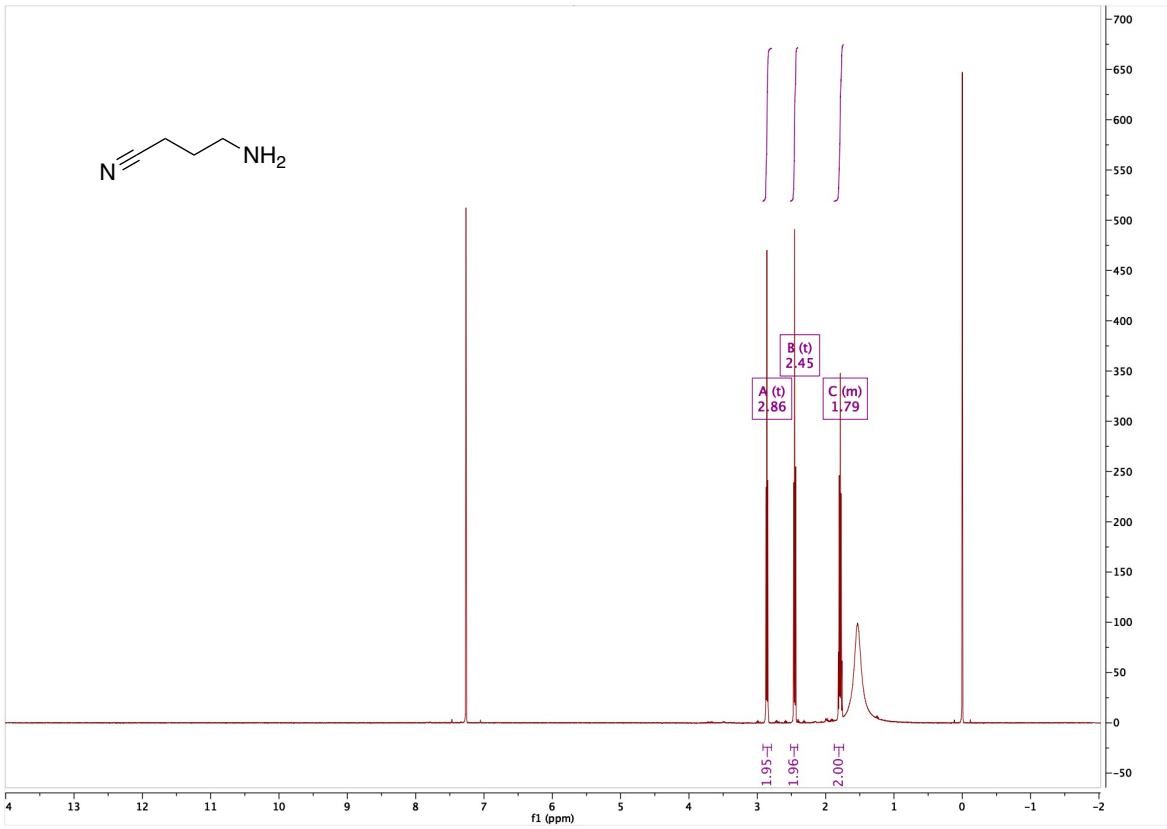

Figure S6.6. ^{1}H NMR spectrum for 4-aminobutanenitrile (1).

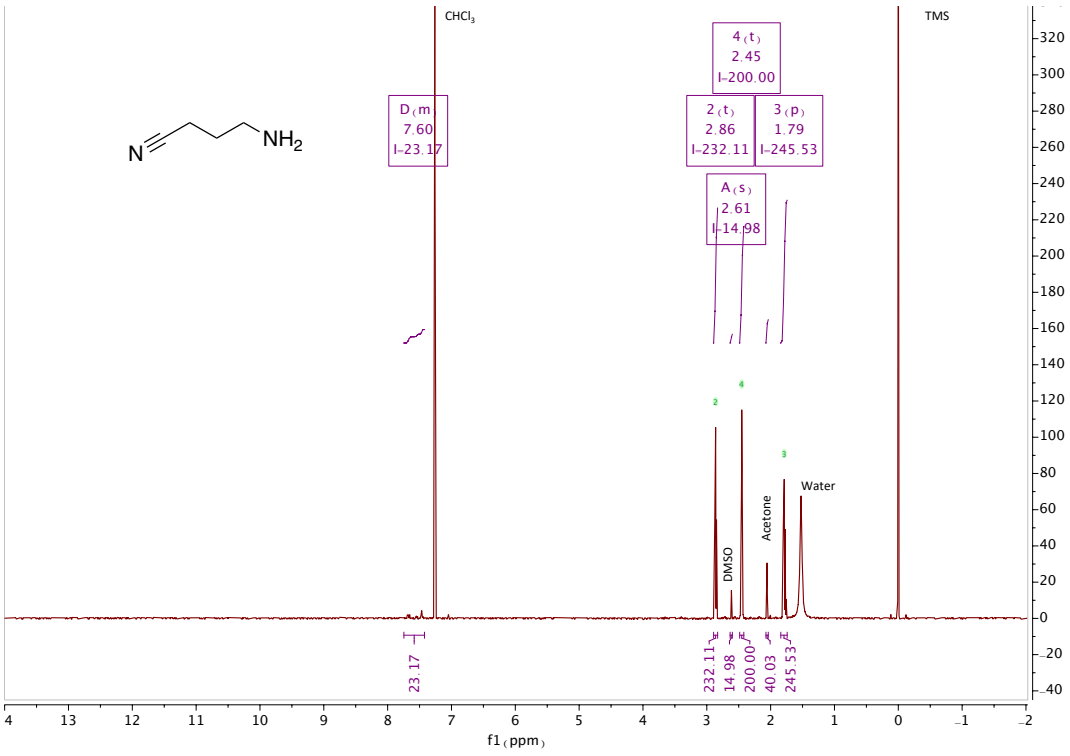

Figure S6.7. NMR spectra for 4-aminobutanenitrile (**1**) obtained on a large scale. Integrals set and purity calculated to be 94.3% by qHNMR using the "100% method" as described by Pauli et al. (Ref. 12 in the manuscript).

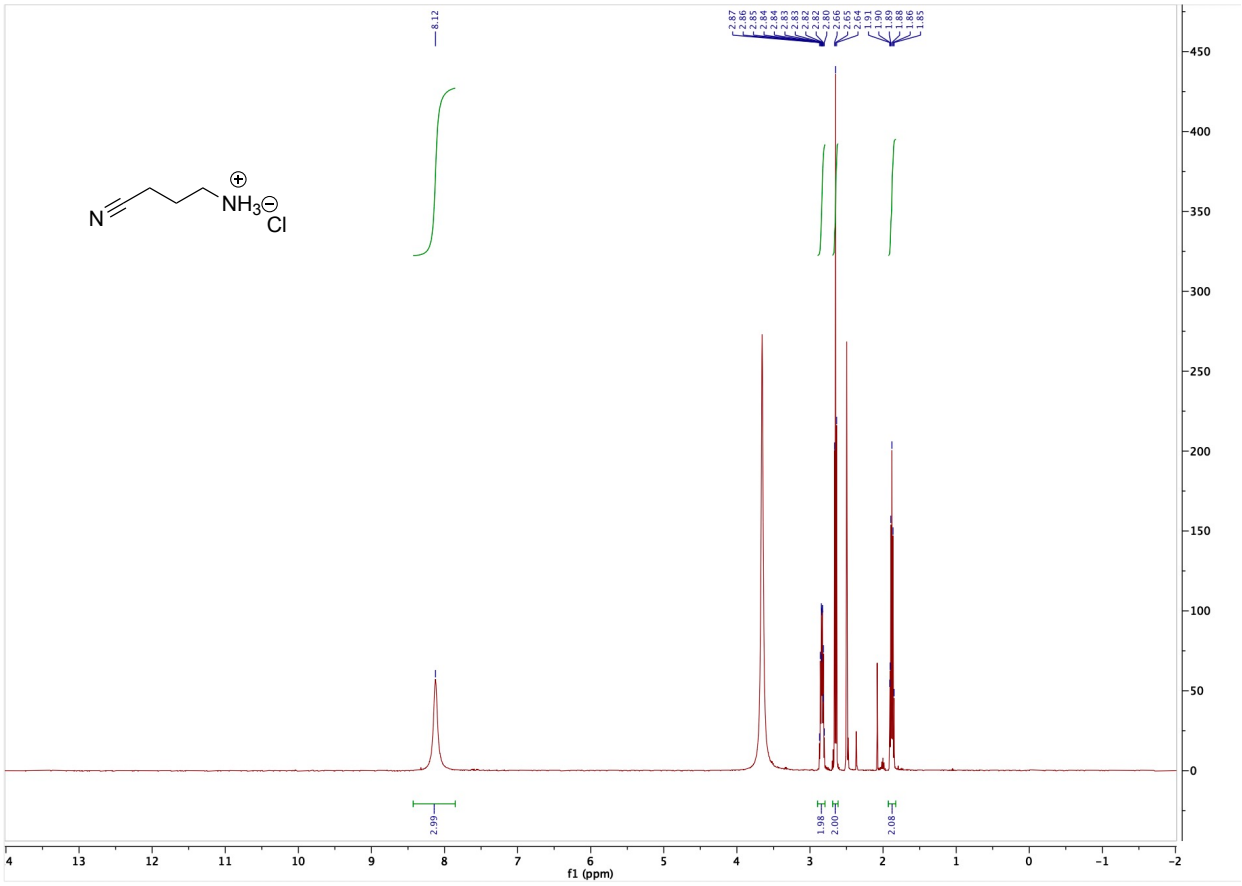

Figure S6.8. ^{1}H NMR spectrum for 4-aminobutanenitrile hydrochloride (1.HCl).

S6.4 ^{13}C NMR spectra

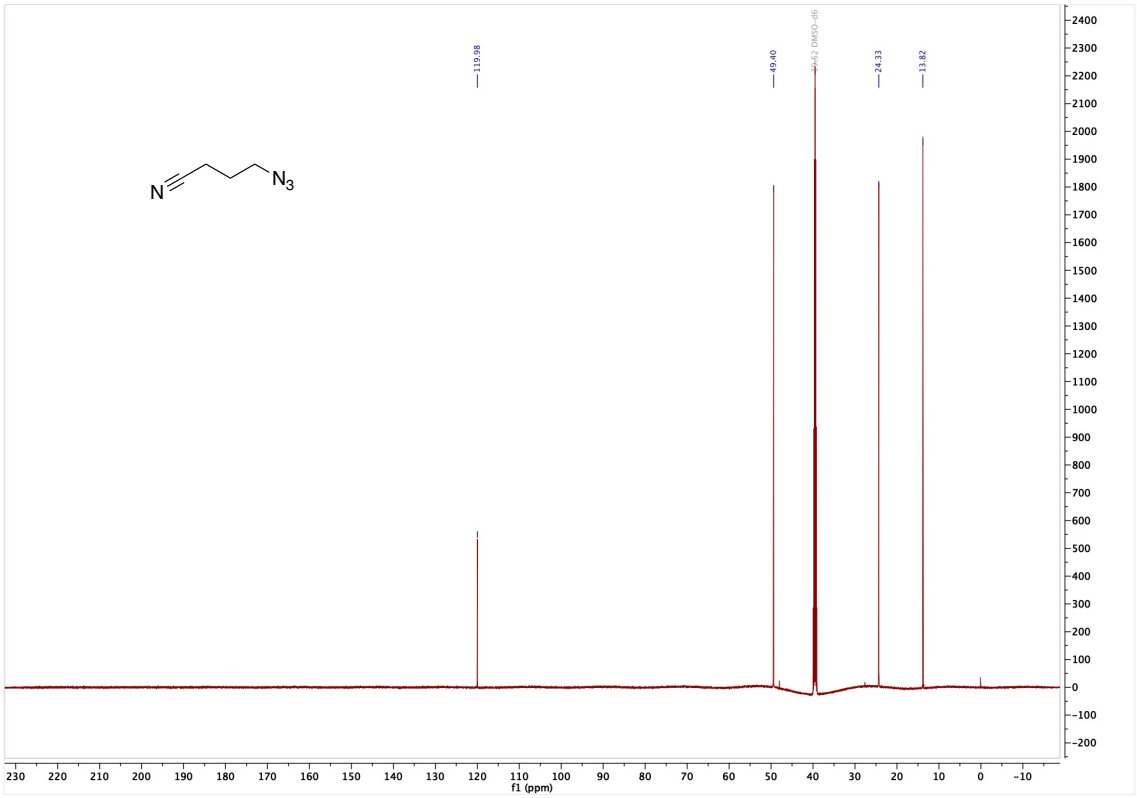

Figure S6.9. ^{13}C NMR spectrum for 4-azidobutanenitrile (2).

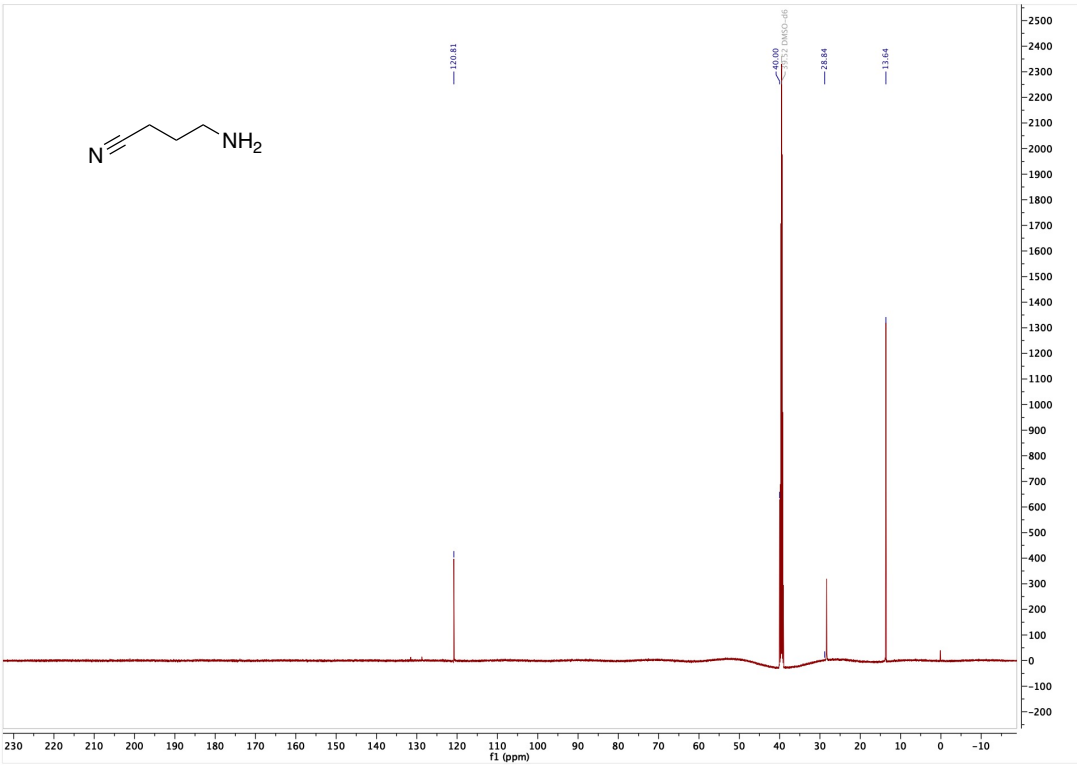

Figure S6.10. ^{13}C NMR spectrum for 4-aminobutanenitrile (1).

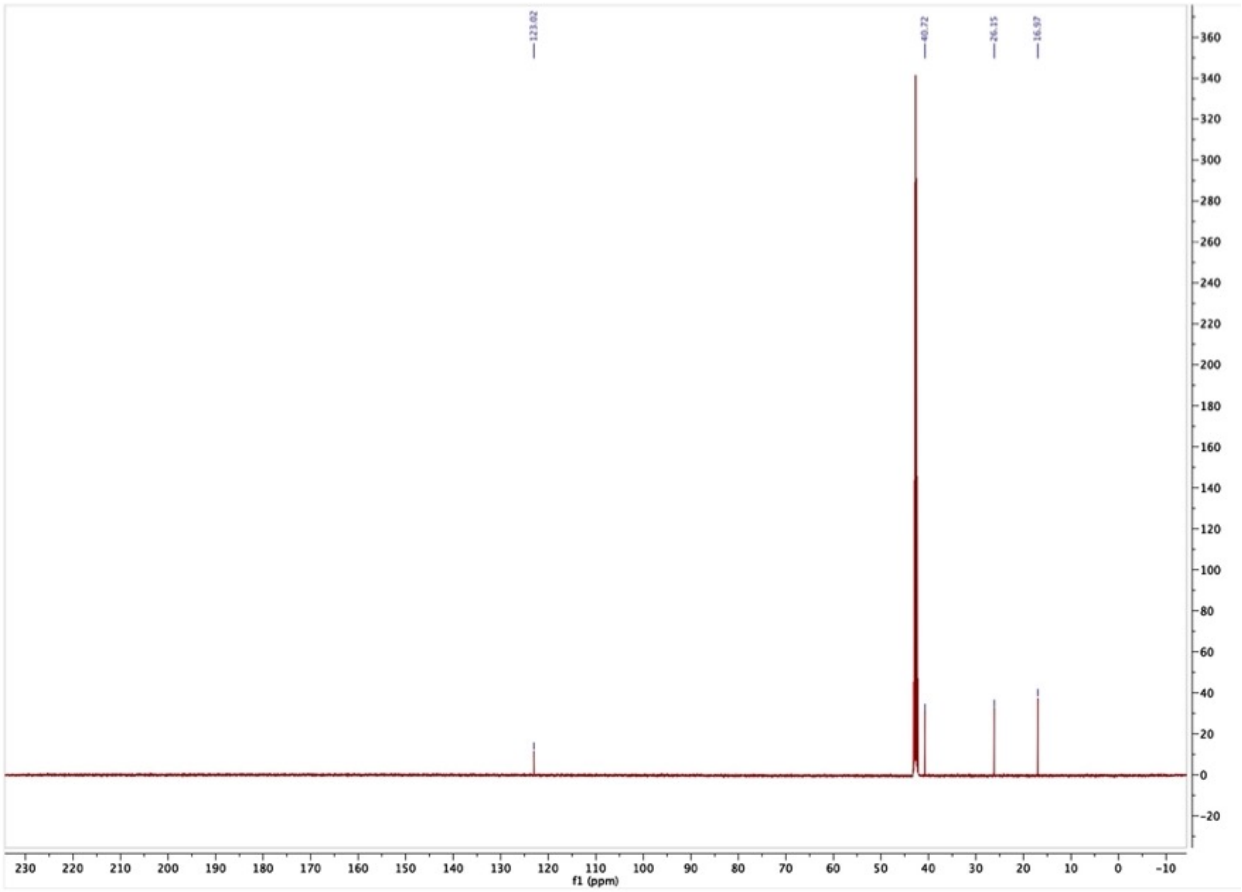

Figure S6.11. ^{13}C NMR spectrum for 4-aminobutanenitrile hydrochloride (1.HCl).

S6.5 HRMS spectra

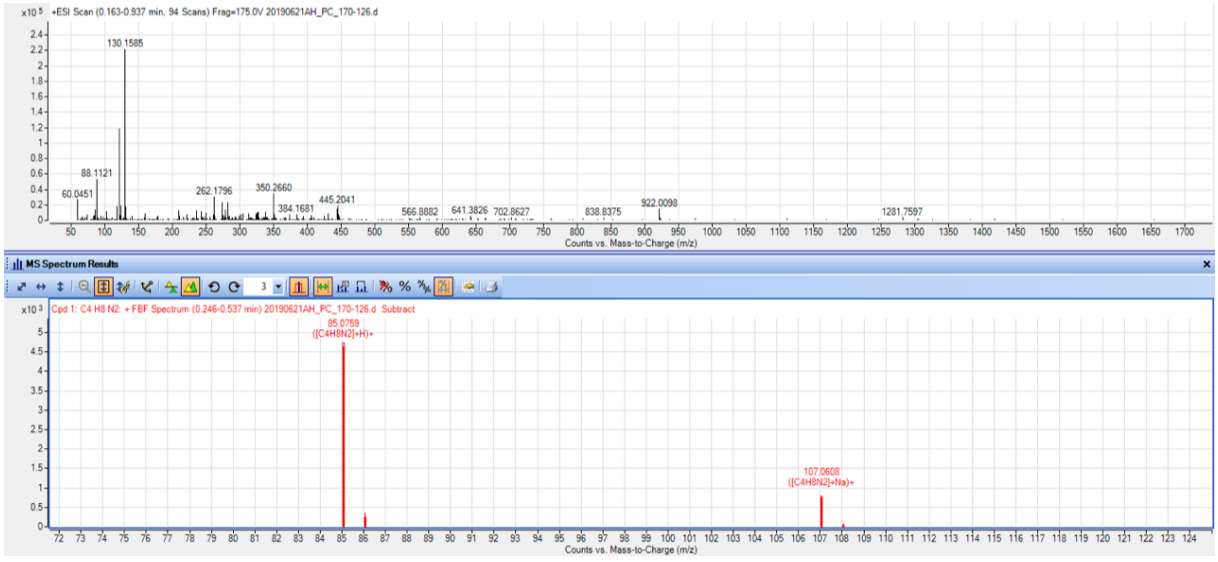

Figure 6.12. HRMS spectrum for 4-aminobutanenitrile (1)

S6.6 FTIR spectra

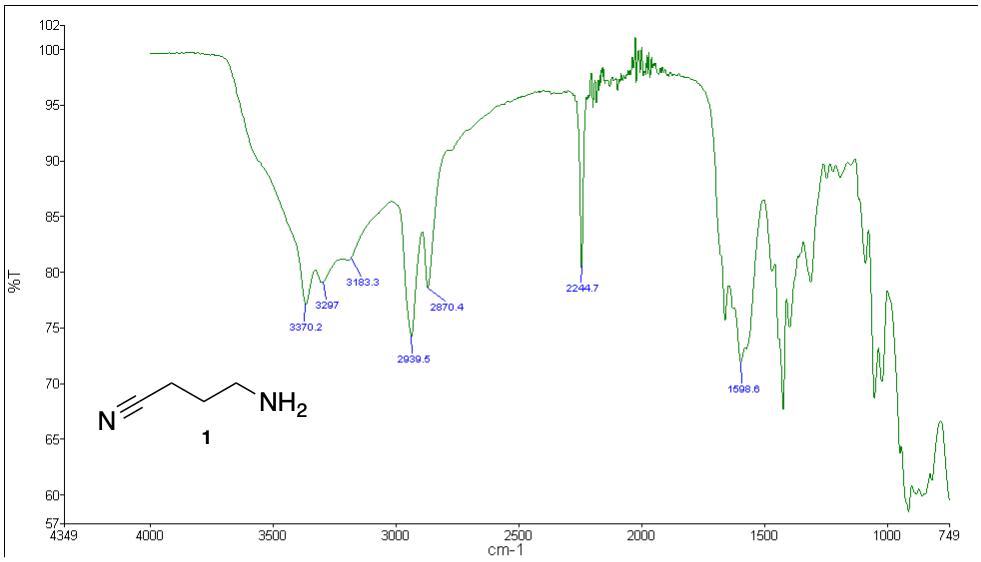

Figure S6.13. FTIR spectrum of 4-aminobutanenitrile (1)

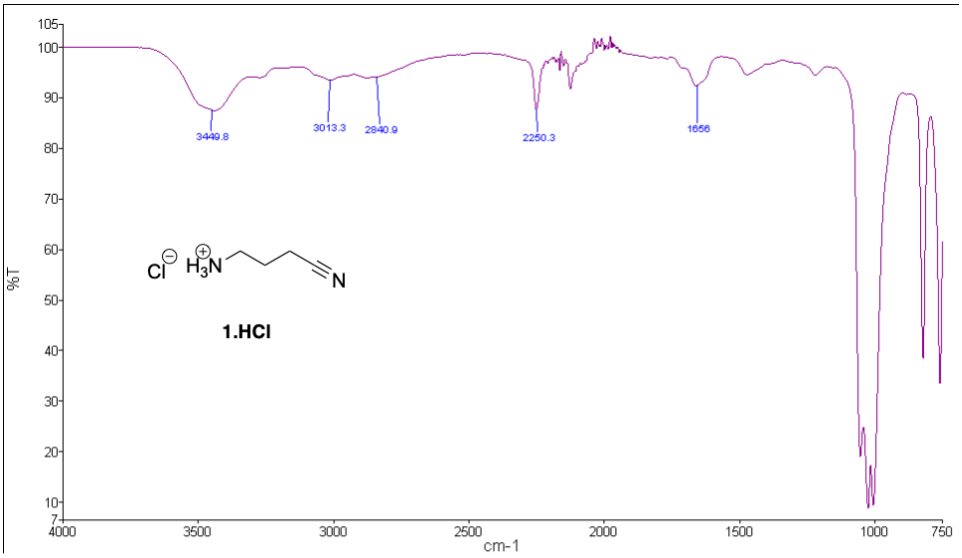

Figure S6.14. FTIR spectrum of 4-aminobutanenitrile hydrochloride (1.HCl)

Chapter 7: Conclusions and future directions

Fluorescence-based sensing is a powerful technique for the detection and quantification of biological analytes. However, a number of challenges remain unresolved including targeting the fluorophore to a specific location, as well as cell permeability and photobleaching of the fluorophore. The extensive research conducted in this thesis has shown that these challenges can be addressed by attaching a fluorophore to solid supports such as optical fibres (Chapters 2 and 3), or nanodiamonds (Chapters 4 and 5), which can provide location-specific targeting, impart cell permeability, or circumvent fluorophore photobleaching. This research has included a thorough investigation of the surface functionalisation methodology to attach fluorophores to such solid supports, in order to provide fluorescence-based sensing devices.

The fibre probes described in **Chapter 2** are compatible with incorporation into aspiration needles commonly used in surgical procedures. This would allow preparation of a device with an overall device diameter less than 0.2 mm, which can be inserted into tissue in a minimally invasive manner. Importantly, this advancement will circumvent the current requirement to excise the sample of interest from the surrounding tissue, which will allow dual imaging and sensing to be performed within the tissue/organism. For example, incorporation of the OCTpH probe described in Chapter 2 within an aspiration needle would provide access to an ovary *in vivo* without the need to excise the ovary from the surrounding tissue. These probes require further *in vivo* studies to determine their viability for clinical use.

Research conducted in **Chapter 3** demonstrated that the precise location of the sensor component with respect to the fibre coating is a critical design consideration in preparation of optical fibre probes for protein sensing. The coating of optical fibres with in-house prepared or commercial silk fibroin was also compared to allow wider access to this fibre coating technology.

It was determined that commercial silk fibroin did not successfully form a coating on optical fibres, however this was rectified by dialysis against water. Analysis by atomic absorption spectroscopy suggested that a low lithium content (≤20 ppm) in the silk solution was an important factor in forming a silk fibroin coating on optical fibres. Thus, all future work using the fibre coating technology presented in Chapter 3 requires the lithium content of all aqueous silk fibroin solutions to be carefully monitored prior to coating optical fibres, and dialysis be performed to reduce the lithium content below 20 ppm.

Both Chapters 2 and 3 presented a new approach to prepare optical fibre probes for fluorescence-based sensing. The sensor-SBP complex can be easily modified for the desired application. For example, SBP-Biotin (Chapter 3) was prepared based on the design of SBP-SNARF (Chapter 2). The simple amidation chemistry employed to bind the sensor component to the *N*-terminus of the SBP allows a plug-and-play approach to future applications, where the desired compound for a specific sensing application can be installed as required.

Chapter 4 discussed the functionalisation of nanodiamonds (NDs) which bear carboxylic acids on the surface through amide bond formation, in order to prepare hybrid nanomaterials. However, numerous attempts involving characterisation techniques including FTIR, NMR, and HPLC concluded that amide bond formation is not an effective strategy for ND functionalisation. Hence, research carried out in Chapter 5 focused on providing an alternative route.

Chapter 4 also contains unsuccessful attempts to replicate literature reports of ND functionalisation. This points to deficiencies in the reproducibility of ND functionalisation strategies between laboratories. These discrepancies may be due to different commercial ND sources which may effect ND functionalisation. However, we note that many studies focus on the application of the reportedly functionalised nanodiamonds without a thorough investigation of the surface chemistry involved. We urge that simple ‘additive’ FTIR characterisation is not sufficient and that future research in this area must characterise the requisite nanomaterials more thoroughly. It is critical to note that uncertainty around the precise surface chemistry of functionalised NDs does not necessarily detract from the demonstrated application, as the material is exhibiting the

described function. For example, a ND-drug conjugate may still work as an effective drug against the intended disease target, regardless of the unknown surface interactions in play.

Chapter 5 presented four carbon-binding peptides (CBPs) as a new strategy to functionalise carboxylated NDs. A fluorescein tag was added to each CBP to allow visualisation of the peptides when attached to NDs, which was achieved through *N*-terminal attachment of an aminohexanoic acid linker followed by 5(6)-carboxyfluorescein. The binding interactions between CBP and ND were determined by colourimetric assay and revealed retention as high as 88% for peptide 1-DLC to DNDs. This approach to use CBPs is amenable to attachment of other organic molecules of interest at the peptide *N*-terminus in place of the fluorescein tag. For example, one can envisage a fluorescent sensor attached to a CBP in a similar manner to the SBPs described in Chapters 2 and 3. This would allow a CBP coating to be used in a wide range of applications, depending on the molecule(s) attached to the CBP. The future focus of this work is to prepare a series of hybrid nanoparticles for application to biological sensing using nitrogen-vacancy containing NDs, which will allow the common problem of fluorophore photobleaching to be circumvented by instead interrogating the photostable NV-NDs.

Chapter 6 focused on optimising the synthesis of 4-aminobutanenitrile, an important synthetic intermediate for neurological disorder therapeutics. Literature methods used to prepare 4-aminobutanenitrile from 4-azidobutanenitrile were found to be extremely low yielding, and the final compound was found to be unstable at room temperature as it cyclised to 2-aminopyrroline over several days. This cyclisation was interrupted by conversion to the hydrochloride salt, which was found to be stable at room temperature. The free amine can be simply liberated from the salt by treatment with a base, such as triethylamine, when required. We therefore suggest that all future syntheses of 4-aminobutanenitrile follow our optimised route and that the preferred long-term storage of 4-aminobutanenitrile is as the hydrochloride salt.